SOME INVESTIGATIONS ON ULTRA-WIDEBAND ANTENNA USING METAMATERIAL AND SUPERSTRATE

Submitted in partial fulfilment of the requirements

for the award of the degree of

Doctor of Philosophy

by

Rahul Singha

(Roll No. 701351)

Under the Guidance of

Dr. D. Vakula

Associate Professor

DEPARTMENT OF ELECTRONICS AND COMMUNICATION ENGINEERING

NATIONAL INSTITUTE OF TECHNOLOGY

WARANGAL – 506004, TELANGANA, INDIA

2018

DECLARATION

This is to certify that the work presented in the thesis entitled "**Some Investigations on Ultra-Wideband Antenna using Metamaterial and Superstrate**" is a bonafide work done by me under the supervision of **Dr. D. Vakula**, Associate Professor, Department of Electronics and Communication Engineering, NIT Warangal, India and is not submitted elsewhere for the award of any degree.

I declare that this written submission represents my ideas in my own words and where others ideas or words have been included; I have adequately cited and referenced the original sources. I also declare that I have adhered to all principles of academic honesty and integrity and have not misrepresented or fabricated or falsified any idea/data/fact/source in my submission. I understand that any violation of the above will be a cause for disciplinary action by the institute and can also evoke penal action from the sources which have thus not been properly cited or from whom proper permission has not been taken when needed.

Date:

Place:

Signature_____

Rahul Singha

Roll No. 701351

Department of Electronics and Communication Engineering

National Institute of Technology

Warangal – 506004, Telangana, India

CERTIFICATE

This is to certify that the thesis entitled "**Some Investigations on Ultra-Wideband Antenna using Metamaterial and Superstrate**" which is being submitted by Mr. Rahul Singha (Roll No. 701351) in partial fulfilment for the award of the degree of Doctor of Philosophy to the Department of Electronics and Communication Engineering of National Institute of Technology Warangal, is a record of bonafide research work carried out by him under my supervision and has not been submitted elsewhere for any degree.

Dr. D. Vakula,
(Supervisor)
Associate Professor,
Dept. of ECE,
National Institute of Technology,
Warangal – 506004,
Telangana, India.

Dedicated to my parents and school teachers

Table of Contents

Acknowledgements

Research on improvement of UWB antenna is very challenging task with entire operating frequency band. I would like to thank my supervisor Dr. D. Vakula, Associate professor, Department of Electronics and Communication Engineering, National Institute of Technology Warangal, for her outstanding guidance and cooperation during my entire PhD journey. I want to express my deep gratitude to her for personal supervision on fabrication and helping me in taking antenna measurement which will be beneficial in my entire life.

I am very grateful to Dr. Anjaneyulu L, Associate Professor and Dr. N.V.S.N. Sarma, Professor of Department of Electronics & Communication Engineering, for their helpful discussions and extensive comments during the course of my doctoral work. I also thank Prof. Bhagwan K Murthy, Professor of Department of Electrical Engineering for his detailed review, valuable suggestions and excellent advice during the course of my research work.

I take this privilege to acknowledge Dr. Bheema Rao N, Head, Department of Electronics and Communication Engineering, for his invaluable assistance and suggestions that he shared during my research presentations and thesis preparation.

I also thank the team of Antenna Wing, Defence Electronics Research Laboratory, Hyderabad and Research Centre Imarat for their help to measure all my antennas. I thank Mr. Srinivas Reddy from Cosmic Enterprises, Hyderabad in supporting the fabrication of UWB antennas.

Finally I thank my parents and all family members for their cheerful support.

Rahul Singha

List of Figures

List of Tables

List of Acronyms

UWB	Ultra-wideband
TSA	Tapered Slot Antenna
AVA	Antipodal Vivaldi Antenna
BAVA	Balanced Antipodal Vivaldi Antenna
CPW	Coplanar Waveguide
PMA	Planar Monopole Antenna
HFSS	High Frequency Structure Simulator
MTM	Metamaterial
EM	Electromagnetics
FCC	Federal Communications Commission
ZIM	Zero Index Metamaterial
GRIN	Gradient Refractive Index Metamaterial
PMC	Perfect Magnetic Conductor
PEC	Perfect Electric Conductor
WLAN	Wireless Local Area Network
ITU	International Telecommunications Union
SRR	Split Ring Resonator
EMI	Electromagnetic Interference
ELC	Electric Field Coupled

Abstract

Wireless communication systems need broad bandwidth for faster connections among various wireless devices, where as narrowband and multiband systems have small bandwidth which limit their applications. The applications of wireless communications can be increased by adopting ultra-wideband technology. Ultra-wideband systems are designed to operate from 3.1 to 10.6 GHz for transmitting low power. Modern wireless communication devices need a compact broadband and low cost antenna. Wireless electronic system such as printer, mouse, smart watch, cell phone etc. require broad bandwidth with high data rate for high speed internet connection.

A compact UWB antennas with directional and omnidirectional characteristics are required for commercial, aerospace and defence industry applications and also for future complex wireless devices. Tapered slot antenna can be operated at broad bandwidth and hence are suitable for UWB directional applications. Vivaldi antennas which are end fire radiators are designed over UWB frequency band with various taper profiles like linear, exponential, elliptical and also corrugated along the antenna edges for performance improvement. In the thesis, the experimental results of the antennas are compared with the published literature. On the other hand, UWB antenna with omnidirectional characteristics are designed using printed monopole antenna with high gain.

Antenna designs are modified to improve the performance in terms of return loss, radiation pattern, gain, efficiency and group delay using superstrate and metamaterial. It has been established that by using fractal structure on the radiating patch, size of the antenna can be reduced with enhanced bandwidth and improved radiation. Moreover, it is also shown that dielectric superstrate can be placed on the fractal monopole antenna to enhance the gain of the antenna. The parallel-line structure metamaterial (MTM) is also used to enhance the performance of the tapered slot antenna and monopole antenna. Gradient refractive index metamaterial lens is designed by using different refractive index unit cell MTM. This helps to focus and make the radiated beam more directional. Hence, the gain of the antenna can be increased. The proposed metamaterial has low material loss covering UWB frequency band and is easy to fabricate. The band notch characteristics are also included to avoid a serious electromagnetic interference within UWB spectrum. The band notch characteristics at WLAN and ITU band are implemented by using split ring resonator and electric field coupled

resonator in UWB tapered slot antenna. Due to the these MTM, the gain of the antenna is also slightly decreased at other frequencies for harmonic effects. The S-shaped unit cell metamaterial are also used to enhance the gain of the antenna. Antennas are simulated using three dimensional High Frequency Electromagnetic Field Simulation (HFSS) Simulator and they are fabricated, tested and also compared with simulation results.

Chapter-1

Introduction

1.1 Overview

The antenna is one of the most fundamental elements in a wireless communication system. It is defined as a device which can transmit and receive electromagnetic energy by converting electric current to radio wave and vice versa [1]. An ideal antenna system requirements are identified to improve the performance of the overall system. Generally, the antenna is designed by a conductor and also utilize dielectric materials. Dielectric resonator antennas (DRAs) is one kind of example which is implemented using ceramic materials. The devices like power lead devices also radiate less electromagnetic energy. Still, they are not considered as an antennas because that electromagnetic energy cannot be transmitted or received in efficient and desired manner.

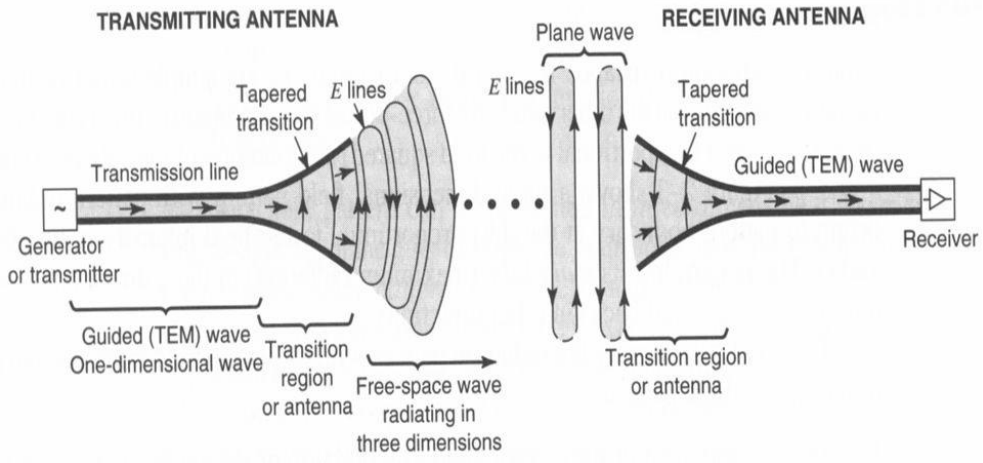

Figure 1.1 A typical radio system

A typical radio communication system, as shown in Figure 1.1. A 50 Ω transmission line is used to connect the generator to antenna. The message signal is modulated to the carrier and amplified. The amplified signal is sent to the antenna via transmission line. The radiated signal is collected by the receiving antenna. The received modulated signal is demodulated to get an original message at the receiver. In this way, the antenna acts as a transducer which

transforms electrical signals i.e. voltages and currents into electromagnetic waves or vice versa.

An antenna is said to be resonant if its input impedance is entirely real. So, the real part of impedance should be matched at the feed line to transfer a maximum power without reflection. However, the operating frequency decides the size of the antenna. Depending on the frequency range, antennas can be classified as narrowband, wideband, and ultra wideband. Narrow band is used for applications like GPS, WLAN, WiMax and Bluetooth etc. Wideband antennas are used for transmitting high data rates for internet applications. Generally, the antenna bandwidth is defined using fractional bandwidth (FBW). The FBW is less than 20% for narrowband antenna. In case of wideband antennas, fractional bandwidth is considered greater than or equal to 20%. The FBW of the ultra-wideband antenna is greater than 50% .

Ultra-wideband (UWB) is a wireless radio technology first proposed by Robert A. Schorton. Ultra-Wideband (UWB) concept has been adopted by the United States Department of Defense in 1989 [2]. In 2002, the United States Federal Communications Commission (FCC) authorized the use of UWB in the frequency range from 3.1 to 10.6 GHz [3]. UWB has a capability to transmit large amounts of data over a wide spectrum with a very low energy level intended for short-range distances. According to the Hartley-Shannon formula, the maximum channel capacity is directly proportional to channel bandwidth and logarithmic function of signal-to-noise ratio (SNR) [4]. Thus, the channel capacity would not significantly change with SNR. Consequently, UWB wireless system has a ability to work in noisy communication channels i.e. low SNRs with large channel capacity. The need for wider bandwidth is rapidly increasing in modern radar, imaging and telecommunications applications.

Classical antennas such as horn antenna, log-periodic antenna, bi-conical antenna, helical antenna and bow tie Antenna, are used in UWB applications. But, the classical 3D UWB antennas are not suitable in compact wireless communication systems due to their large size. Therefore, a two dimensional (2D) printed UWB antenna is widely used in portable wireless devices. Among 2D UWB antennas, the Vivaldi and monopole antennas are widely used in commercial and military applications for their broadband characteristics, low weight, low cost and easily integrable with wireless communication devices. A traditional Vivaldi

antenna is known as a 2D horn antenna. This antenna has another name called tapered slot antenna (TSA) [5], as shown in Figure 1.2. The radiated beam of Vivaldi antenna is unidirectional, means it radiates only in a single direction which is suitable for point to point communication such as ground penetrating radars (GPR) [6], through-wall radar [7], biomedical imaging [8], and radio telescope [9] applications. The impedance bandwidth of the 2D UWB antenna can be controlled by the 50 ohm microstrip feed and shape of the radiating patch. The performance can also be controlled by varying the dimension of ground plane structures [11] and [12].

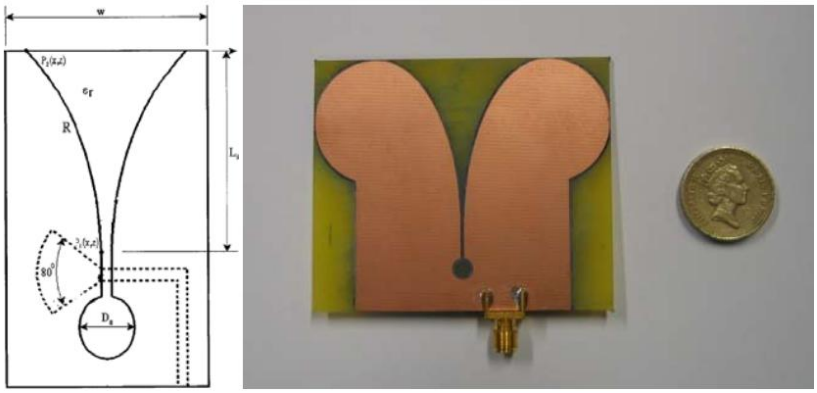

Figure 1.2 Configuration of Vivaldi antenna

The radiation pattern characteristics decide the usage of the antenna in various applications. The isotropic antenna radiates uniformly in all directions. Unfortunately, such type of source cannot be realized in the real world. All portable devices, such as cell phones, FM radios, walkie-talkies, wireless computer networks, cordless phones and GPS are require omnidirectional coverage to receive signal from all possible direction. Therefore, the radio broadcasting systems are require an omnidirectional antennas. Base stations that communicate with mobile radios, such as police and taxi dispatchers and aircraft communications, radiation of radio wave power is to be distributed uniformly in all directions in one plane. For omnidirectional radiation, printed monopole antenna is used in UWB application. The operating bandwidth bandwidth can be increased by fractal structure.

In the past decades, UWB is widely adopted in commercial applications, as shown in Figure 1.3. Some of the peripherals that can connect to a personal computer (PC) are TV, printer, PC, external HDD, portable media players, mobile handset and DSC/DVD. Generally, PCs are either a desktop that is placed at a fixed location or a notebook that is a

laptop and mobile. Traditionally, PC peripherals are connected using USB, Bluetooth, or WiFi.

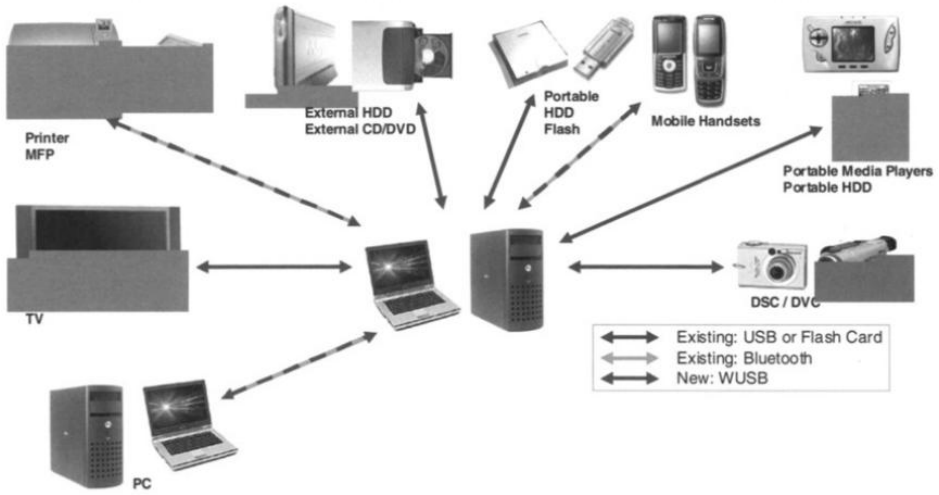

Figure 1.3 UWB offers some compelling applications for linking PCs to peripherals

On the PC, it has limited total throughput because of the inherent limitations of the USB bus. Peripheral Component Interconnect (PCI) and Peripheral Component Interconnect Express (PCIe) implementation is necessary for maximum data transfer. But, a larger aggregate throughput is required when multiple devices are connected at the same time. For a desktop PC, external USB dongle supports both USB high speed and full speed. For these applications UWB technology is more flexible to apply.

In case of notebook PCs with UWB capabilities, the earliest products are PC Card (using the parallel Cardbus 32 interface) and Express Card implementations, as shown in Figure 1.4., because they are easily connected with notebook PC by the end user.

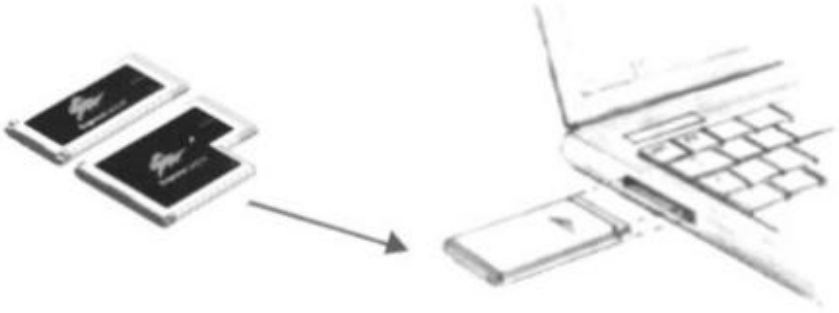

Figure 1.4 PC Card and Express Card implementations of UWB functionality enable notebooks.

In the digital world, almost all electronics systems are converting into a wireless communication system with small size. In real life applications, a UWB antenna is to be designed for fulfill the demands. Hence, the UWB antennas in different applications is always been a compromise over various requirements. UWB communications are divided into two modulation schemes, namely, impulse radio or Direct Sequence UWB (DS-UWB) and the Multiband OFDM (MB-OFDM).

The performance of UWB antenna for impulse radio is also done by observing the time domain characteristics. Group delay measurement is one of the parameter which is used to observe the characteristics of the antenna in time domain. Hence, it is required to measure group delay. in addition to other parameters like return loss, radiation pattern and gain. There are frequency bands fixed for impulse radio by different countries FCC has fixed 7500 MHz for UWB impulse radio. Whereas Europe and otrher countries has set two sub band i.e. 3.1-4.8 GHz and 6.2-10.6 GHz, respectively. The dipole type of UWB antennas are utilized in the first generation of impulse radio systems, as shown in Figure 1.5.

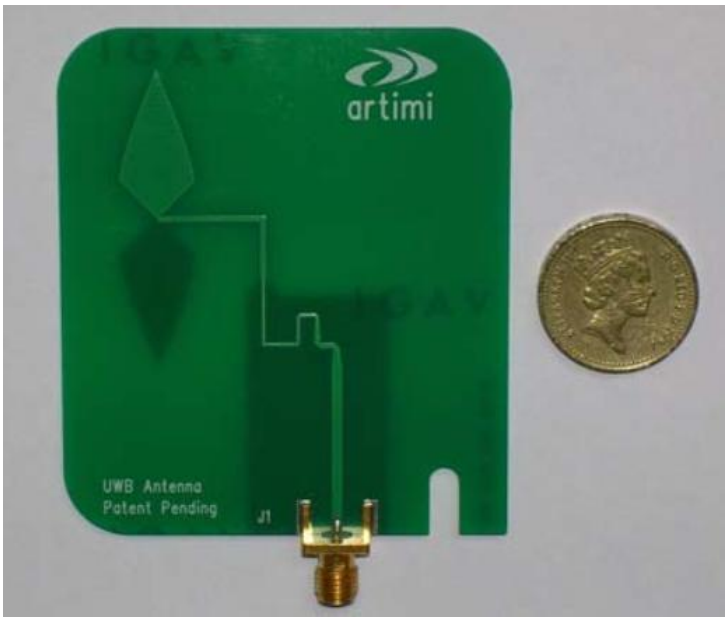

Figure 1.5 UWB dipole antenna.

Generally, UWB dipole antennas actively work in the impulse radio system and operate independent of other hardware or software. Printed UWB monopole antennas are a favorable choice where the balanced feed does not require and also easy to be integrated with the radio unit.

The MB-OFDM scheme is very popular and has been applied in UWB communication systems, e,g. Wireless USB dongles. For this application, numerous kind of compact ultra-wideband monopole antennas are implemented and to suppress the WLAN band around 5.6 GHz. In Multiband-OFDM scheme, UWB frequency band (3.1-10.6 GHz) is further divided into 14 sub-bands and each band is allotted 528 MHz bandwidth.

UWB antennas can also be useful for EM measurements, including different purposes. The detecting antenna should be broadband or ultra wideband to detect and measure for any wide band signal, e.g. a double ridged horn. Antenna radiation pattern or gain can be measured using 8:1 relative bandwidth. EM spectrum is monitored using broadband dicon antenna, which is commonly utilize for this type of application. Other broadband antennas, such as log-periodic antenna which is also utilized to detect the EM emission from any electronic devices.

A compact UWB antenna system can be utilized for an autonomous interference monitoring system (AIMS) to monitor EM spectrum usage in the urban, suburban and rural locations. An UWB antenna with omnidirectional radiation pattern is required for the AIMS system. The antenna system can be divided into two subsystems for low and high frequency band. Each subsystem would consist of two antennas to receive dual polarized signals. The low band antenna operates over the frequency range from 100 MHz to 3 GHz. So, it can receive dual polarized RF signals, particularly for horizontally polarized TV signals around 400 MHz. The high band antenna will be from 3GHz to 10.6 GHz in the UWB antenna sub-system. At the time of scanning the spectrum, the switching of these antennas is done using RF switch.

Now, all kind of modern radar devices are made by installing an UWB antennas, e.g. the impulse radar and the phased array radar. In case of impulse radar, the radar transmit EM wave pulse and the pulse is reflected from the objects to detects by the radar. The concept of impulse radar can be use in ground penetrating radars (GPR) to detect buried landmines, other unexploded bomb and biomedical imaging. Here, the UWB antenna elements must be a minimum amount dispersion of the UWB impulse and similar requirement is applicable for the impulse radio.

UWB radars are also used to monitor vital signs of soldiers. Remote measurement of heart and respiration rates generally require attaching a set of electrodes to the body and carrying a remote wireless link. In early war, the Micropower impulse radar (MIR) is used to monitor vital signs and images of front-line combat soldiers body and casualty assessment. The device is placed under soldiers clothing and body armor to measure their heart and respiration rates.

UWB technology is also used for breast cancer detection. In this application, low power short duration UWB pulses are transmitted and reflected pulses are analyzed for differentiating healthy and cancer tissues. UWB antenna arrays are preferred to improve the resolution of the image.

Electronically scanned satellite antenna can be developed using UWB technology for mobile and fixed platforms. Metamaterials can also be used for satellite-communications which are needed for broadband Internet anywhere in the world. The satellite industry has been waiting for an electronically steered antenna to bring the massive capacity available via satellite to the mobile communications. High-throughput connectivity will now be available to a broad range of markets, including maritime, rail and civilian Armored Vehicles, energy and more by using UWB technology.

1.2 Motivation

As the world is moving towards UWB communications for high speed applications, there is a requirement for UWB systems to suit different applications and in turn antennas for these systems. Antennas are the eyes and ears for wireless devices which are undergoing a versatile change from the earlier long wire type of radio broadcasting for communication links in military applications to modern compact antennas. UWB antenna is widely used for internet, Bluetooth, laptop, mobile communication due to their high data rate within short range wireless applications, e.g. wireless personal area networks (WPANs) [13–15]. So, the ultra-wideband antenna is replacing multiband antenna. The range and the data rate in UWB technology is compromise which makes ideal for a wide array of applications in civil and commercial sector.

In the modern age, wireless communication systems are also designed for a long range complex systems such as aircrafts, radars, missiles and space applications [16]. Because time

modulated UWB pulses has a unique codes in each transmitter/receiver pair. Due to the wide frequency band, time modulation of UWB pulse is giving extremely narrow duration pulses which is provides more security to UWB transmission. Because the detection of picosecond pulses are impossible without knowing code of each transmitter/receiver pair. Thus, UWB system can able to provide highly secure with low probability of intercept and detection (LPI/D) for long range wireless communications which is very important for military operations. For long range wireless system, the directivity of UWB antenna must be high.

Mobile wireless communication products must be easily portable and cheap to do so that they can be attractive to modern people. Hence, there is a need to investigate and develop antennas for Ultra wide band frequencies. An ultra wideband antenna must radiate a low power level at -41.3 dBm for short distance as given by the FCC standards. The commercial UWB frequency range is from 3.1 to 10.6 GHz. Antenna is a resonant structure which can radiate a narrow bandwidth. But an ultra wideband antenna has to radiate from 3.1 to 10.6 GHz. Hence the design of UWB antenna by satisfying all characteristics of transmission is a challenging task.

In recent times, electromagnetic metamaterials are very popular among physicists and engineers to augment EM waves through appropriate arrangements of meta-atoms (unit cells). Low refractive index metamaterial has beam focusing property. So, the directivity and gain can be improved using metamaterials. The non-resonant structure metamaterial has a low material loss with broadband characteristics which is perfect for UWB antenna. By using metamaterial, the performance of Ultra-wideband antenna can be improved. But some narrowband applications such as WIMAX (3.5 GHz), WLAN (5.5 GHz) and ITU (8.5 GHz) are also working within Ultra wide band range. So, serious electromagnetic interference can happen. To avoid the interference, notch characteristic is required at these frequencies.

1.3 Literature Survey

This section deals with brief overview of the published literature on ultra-wideband antennas. The existing techniques are explained in the published works and highlighted their drawbacks on UWB antenna. Moreover, the proposed techniques which are adopted to increase the gain of the UWB antenna are discussed.

W. J. Lui et al presented a compact tapered microstrip slot antenna for ultra-wideband (UWB) applications [17]. The properties of the antenna, including return loss, radiation patterns and gain have been investigated experimentally and compared with simulation results. The operating bandwidth of the antenna is from 2.91 to 12 GHz. But, the measured return loss of the antenna is not below -10 dB at 4.1 GHz and 6.75 GHz (approximately). After installation antenna in the handset, the return loss has become greater than -10 dB at some frequencies.

J. Wu et al designed a Vivaldi antenna with the stepped structure between slotline and tapered patches [18]. The measured results show the impedance bandwidth of the proposed antenna is 3-15.1 GHz which is improved uisng stepped structure. The antenna size is 41×48 mm^2. Measured gain is fluctuating from 5-6 dBi over the operating frequency band. The side lobe level is fluctuating and above -10 dB, which is not good for many applications.

R. Azim et al presented a compact tapered slot antenna with microstrip line-fed for ultrawideband application [19]. The antenna is constructed with tapered-shaped slot and rectangular stub. The FR4 substrate is used to design of antenna and also fabricated with the dimension of 22×24 mm2. The experimental results show that the proposed antenna provides a good impedance bandwidth, gain, better radiation patterns over the frequency band of 3-11.2 GHz. But the cross polarization effect is more at high frequencies.

A. Z. Hood et al proposed a compact antipodal Vivaldi antenna for ultra-wideband (UWB) applications [20]. The antenna operates across the entire UWB spectrum with low cross-polarization levels. The gain is varying up to 5 dBi over the operating frequency band. The return loss is greater than -10 dB at 10 GHz for FR4 and at 5 GHz for antenna with roger substrate. Therefore, the group delay is also notched at 3.5 GHz and 8.6 GHz with FR4 and Roger RO 3006 substrates, respectively.

F. Jolani et al designed and optimized a compact directive balanced antipodal Vivaldi antenna for ultra-wideband applications [22]. The particle swarm optimization is applied in conformal finite difference time domain method. The size of the miniaturized antipodal Vivaldi antenna is 32×35×1.6 mm3. But the antenna gain is below 5 dBi.

J. Bai et al presented a novel way of enhancing low-frequency performance of Antipodal Vivaldi antennas [23]. The antenna impedance bandwidth at low frequency is improved by

using a slot in circular loaded area. This modified antenna has an impedance bandwidth of over 25:1. It also exhibits symmetric radiation patterns in both the E and H-planes. The gain is varying from 3 to 12.5 dBi in the frequency band of 4-50 GHz.

P. Fei et al miniaturized an antipodal Vivaldi antenna by making slot at the edge of antipodal Vivaldi antenna [24]. The proposed tapered slot edge structure has the capacity to extend the low-end operating frequency and improve the radiation characteristics at lower frequencies. The lower end frequency of the original antenna is changed to 2.8 GHz from 3.3 GHz by using tapered slot edge. However, the side lobe level and back radiation of the antennas are high.

The printed Vivaldi antenna or tapered slot antenna suffers from low directivity. To increase the gain of the antenna, E. W. Reid et al designed a 2D antenna array with 324-elements for radio astronomy application with sensitive two mutually orthogonal polarizations [9]. The Vivaldi antenna array provides a symmetrical radiation pattern with main beam of 87.5^0 at 3 GHz and 44.2^0 at 6 GHz. The proposed array can able to operate without the formation of grating lobes at the frequency of 5.4 GHz.

Low Z. N. et al presented a low-cost knight's helm shaped double-sided printed monopole antenna of size 3×3 cm2 [25]. The antenna is working on UWB frequency range with constant group delay and constant gain over the operating frequency band. Satisfactory performance is obtained using FR4 substrate, allowing low cost of production. It is noticed that the gain is decreasing at high frequencies, it means the antenna losses are high at that frequency.

The microstrip feed printed antenna is suffering from higher dispersion with high radiation losses. To reduce these characteristics, the CPW feed is widely used for UWB printed monopole antenna. CPW feed antenna provides a wider bandwidth, lower dispersion with lower radiation loss than microstrip antennas. CPW feed makes monopole antenna easy in parallel and series connection with active and passive elements. CPW feed is required for impedance matching, gain improvement and ease of integration with monolithic microwave integrated circuits [26].

Angelopoulos E.S. et al presented a novel circular monopole with coplanar waveguide fed slot and elliptical monopole with microstrip-fed antenna targeting the 3.1-10.6 GHz band

[27]. The antennas are comprised of elliptical or circular stubs that excite similar-shaped slot apertures. Compared to microstrip fed, the CPW-fed antennas are showing more impedance bandwidth for return loss below -10 dB. In the same year, Denidni and Habib designed a broadband printed CPW-fed circular slot with circular patch antenna [28]. Measured results show that the proposed design offers an ultra-wide bandwidth of 143.2% (from 2.3 to 13.9 GHz). The size of the antenna is large and gain is not mentioned in the article.

Fallahi H. et al investigated a multiresonance technique to achieve ultra-wideband characteristics in a CPW-fed monopole antenna [29]. Smaller fractal elements are added at the corners of a polygon patch. The pentagon based fractal antennas are working from 2.8 to 11.3 GHz and a hexagon based fractal elements are working from 3 to 11.5 GHz.

The longest electrical path or current distribution in the patch and the ground plane conductor are also helpful to enhance the bandwidth of the antenna. So, the fractal structures are widely adopted in UWB antennas. K. R. Chen et al proposed a planar microstrip-fed wideband monopole antenna [30]. A semi-elliptical fractal complementary slot with asymmetrical ground plane provides a -10 dB bandwidth of 172% (1.44-18.8 GHz) and bandwidth ratio of 12:1. Due to the diversified electric current distribution on the antenna, the cross-polarization level rises with increasing frequency at 6 and 9 GHz.

J. Pourahmadazar et al designed a novel modified microstrip-fed printed Pythagorean tree fractal monopole antenna for ultra-wideband application [10]. Broader impedance bandwidth has been achieved using pythagorean tree fractal on the radiating patch. A new resonances are created with increasing the number of tree fractal iterations. The compact size is acheived using tree frcatal that is $25\times25\times1$ mm^3 which is giving the frequency band from 2.6 to 11.12 GHz. The gain is below 2 dBi at the operating frequency band.

S. Tripathi et al investigated a design approach to achieve multi resonance phenomena in ultra-wideband bandwidth by using fractal geometry [31]. The Koch fractal structure is introduced in radiating patch and also in the ground plane for the additional resonance in antennas, which helps to achieve entire UWB operational bandwidth. Therefore, the bandwidth is increased up to 122% and also stable radiation pattern is obtained. But the gain is decreased in the range 5.5-10 GHz. M. Ding et al also proposed an ultra-wideband CPW-fed fractal monopole antenna [32]. A fractal is designed in circular disc patch to create a

longer electrical path. So, the antenna is covered from 2.28 to 12 GHz, which is larger than 6:1 bandwidth ratio. The simulated gain is not linearly increasing over the operating frequency band.

From the above literature, the bandwidth of monopole antenna is enhanced by using CPW-fed for UWB application. Still, gain improvement of monopole antenna is a major issue. The superstrate is a well known technique which is used to enhance the gain of the compact monopole antenna. Further, one of the early researchers, Y. Sugio et al have used dielectric layers on the antennas [33]. Later, Jackson and Alexopoulos analyzed and derived asymptotic formulas at resonance conditions for a substrate-superstrate printed antenna geometry which has large antenna gain [34]. In the last decades, among the existing literature, a simple dielectric superstrate is unable to enhance the gain of the antenna within the UWB frequency band.

Metamaterial is widely used to design superstrate [35]. J. Ju et al proposed a high-gain antenna using a single layer metamaterial superstrate with a zero refractive index (n) [36]. The size of the unit cell MTM is 7.16×7.16 mm^2. The MTM superstrate is composed of 7×7 unit cells and is placed 14 mm above the feed. Both the simulation and measurement results show that the gain of the proposed antenna is increased by about 5 dBi at 10.32-11.66 GHz. The material loss exists in the designed metamaterial and also MTM is working at narrow frequency band.

H. Attia et al presented a magnetic superstrate designed to enhance the gain and efficiency of a microstrip patch antenna [37]. The modified split ring resonator is used in the design of the magnetic superstrate. The size of the proposed antenna is 85×85×16 mm^3 to operate in the frequency band 2190-2210 MHz. The broadside gain of the antenna is increased by 3.4 dB and the efficiency is improved by 17%. The magnetic superstrate is working at narrow frequency band.

Shaw T. et al illustrated a technique to enhance the broadside gain of a CPW fed slot antenna using a single layer metamaterial superstrate [38]. An array of 3×3 ring unit cells is designed on both sides of a dielectric substrate. The gain enhancement is obtained using the zero-index property of the metamaterial. The broadside gain enhancement for the proposed antenna is 7.4 dB more in comparison with reference slot antenna. The proposed

metamaterial superstrate loaded antenna provides a minimum overall thickness. A high efficiency of about 93.2% is obtained at resonating frequency. The antenna size is large and metamaterial is working on narrow band with high losses.

M. Sun et al proposed a zero-index metamaterial to enhance the gain of an antipodal tapered slot antenna (ATSA) for the frequency bands of 57-66 GHz [39]. Metamaterial loaded ATSA is provides gain improvement up to 10 dBi. ZIM loaded ATSA array with 2 element is giving gain from 12-13.2 dBi for the frequency band of 57-66 GHz. But, the gain is not uniformly increased by using metamaterial.

B. Zhou et al proposed an anisotropic zero-index metamaterials to enhance the directivity of the Vivaldi antenna for ultra-wideband application [40]. Anisotropic ZIM is designed using resonant meander-line structures and integrated with the Vivaldi antenna. Measurement results show that the directivity and gain of the Vivaldi antenna have been enhanced significantly in the designed bandwidth (9.5-10.5 GHz), but the gain is not improved in other frequency bands (2.5-9.5 GHz and 10.5-13.5 GHz). Here, the antenna size is too large and metamaterial is working on narrow band.

S. Wu et al presented a zero indexed metamaterial structure for the gain enhancement of the TSA [41]. The ZIM cell is designed by a resonant metal structure with an inductor between two resonant structures. This structure is able to operate at low frequencies with one component of permittivity tensor reaching zero. By changing the inductance value of the inductor component, the zero point of the permittivity tensor of the ZIM is obtained. The gain of the TSA has been enhanced by 0.9-2.48 dB with ZIM cells. In this design, metamaterial is working over a wide frequency band. Moreover, the antenna gain is not uniformly increased i.e. gain is not enhanced significantly at high frequencies.

H. X. Xu et al proposed a three-dimensional gradient-refractive-index (GRIN) lens which has a capability to focus the radiated beam and also beam steering over the operating frequencies [42]. The omnidirectional source antenna is placed centre of four 3D gradient-refractive-index (GRIN) lenses and each lens kept at certain distance. GRIN metamaterial is designed using non-uniform fractal structure. Due to the non-resonant fractal structure, the 3D GRIN lens is provide wide bandwidth i.e. 3 to 7.5 GHz. The radiation pattern is directed in four directions. The peak gain is observed to be 15 dBi across the whole band. The area of

proposed lens installed in the antenna setup is large and side lobes are increased by using metamaterial.

From the published literature, it can be established that the printed antenna is suitable as a low profile antenna. Printed antennas have simple structures that are easily manufactured at a low cost, light weight and are suitable to integrate with any wireless electronic device. But the patch antenna has a narrow bandwidth and low gain. Printed monopole and Vivaldi antennas are famous for their broadband characteristics. The printed monopole antenna has omnidirectional pattern with UWB characteristics. So, it can be used for short range wireless communication, such as Bluetooth and WiFi.

In the present thesis work, it is attempted to investigate various geometries of basic Vivaldi and antipodal Vivaldi antennas for point to point wireless communication in UWB frequencies. It is also proposed to design monopole antennas for omnidirectional radiation.

To make more compact UWB antennae, the dielectric superstrate concept is also very useful to enhance the gain of the monopole antenna. Almost all classical superstrate designs do not work effectively on the UWB frequency band. In the published literature, dielectric superstrate is not able to enhance the gain of the antenna in an entire UWB frequency band. Here, dielectric superstrate is modified and incorporated with monopole antenna. In addition, the fractal structure is also added in the radiating patch to enhance the performance of the antenna. By using this novel superstrate, the fringing field of monopole is enhanced. Ultimately, the gain is increased at the entire UWB frequency band. The proposed monopole is useful for mobile applications.

From the published metamaterial antennas, it can be seen that the gain and size of the antennas are increased by using metamaterial. The designed metamaterial structures are not working over the entire UWB frequency band and also giving high material loss.

In order to overcome these problems, non-resonant structure is very useful in metamaterial for UWB application. In this thesis, unit cell metamaterial is designed by non-resonant parallel-line and S-shaped structure of sub-wavelength dielectric substrate. Here, the proposed metamaterial is used in both printed monopole and tapered slot antennas for UWB applications. The designed parallel-line structure is integrated in front of the tapered slot antenna. The propagating surface wave in TSA is influenced by the metamaterial lens

and radiated beam become more focused. Another novel technique is also used with metamaterial in the TSA and printed monopole. Here, Luneburg lens design equation is adopted to implement GRIN lens. This lens is installed on both TSA and monopole antennas. By using GRIN lens, the spherical wave is converted into plane wave and radiated beam becomes more directive.

The UWB antennas are also suffering from serious EM interference within the operating band due to applications, such as WLAN, WiMax and ITU band. So, the split ring resonator (SRR) is used in TSA to suppress the WLAN application within the UWB frequency band. Due to the harmonic effects of SRR resonator, the performance of the antenna degrades in terms of radiation pattern and gain at the other frequencies. So, the S-shaped unit cell MTM is fabricated and integrated in front of TSA for gain improvement except notched frequency.

The selection of simulation tools for antenna is also a very important factor to get more accurate result. So, the three dimensional EM simulator Ansys HFSS 15 and CST studio suite are used which are provide more accurate results.

The performance of antennas is measured in an anechoic chamber. The anechoic chambers with indoor and outdoor antenna ranges is exist. Indoor range is preferable, due to the measurement conditions are controlled in every possible way than outdoor ranges. The EM wave absorbing materials are attached with the walls, ceilings and floor inside the chamber room to get accurate results.

1.4 Research Objectives

The research primarily focuses on achieving the following objectives:

I. Design, fabrication and testing a compact size ultra-wideband (UWB) antenna.
II. Implementation of structural modifications and slots for achieving a compact structure.
III. Addition of superstrate to the radiating patches to gain enhancement.
IV. Improvement of the radiation pattern and gain of UWB antenna by using broadband non-resonant metamaterial.
V. Frequency band suppression in UWB ranges to avoid interference with existing services in the UWB region.

VI. To compare the simulation with experimental result of the above designed antenna. Also compare with the existing published work.

1.5 Thesis Outline

The thesis presents the state of the art ultra wide band antennas, analysis and design of UWB antennas and performance improvement in terms of compact size, gain enhancement, low side lobe and band notch characteristics. The results are improved using metamaterial and superstrate.

Chapter1: Introduction

This chapter presents an introduction to the UWB antenna and its applications. A detailed survey of published literature is illustrated. It also includes drawbacks of the existing UWB antennas. A thorough discussion is presented for the design of UWB antennas. Some of the novel methods to overcome the existing drawbacks are mentioned. A brief outline of the thesis is presented.

Chapter2: Vivaldi antenna for UWB Applications

In this chapter, a brief introduction of Vivaldi antenna is discussed. The design and geometry of the different types of Vivaldi antennas with various taper profiles are explained for UWB applications. The linear and exponential Vivaldi antennas are designed with the frequency band 3.5-11 GHz and 2.5-11 GHz, respectively. Both antennas have equal size of 40×60 mm2. The unbalanced antipodal Vivaldi antenna is designed for exponential and elliptical tapered profile with an operating frequency range 3-11 GHz and 3.2-11 GHz, respectively. The corrugated balanced antipodal Vivaldi antenna is designed with size 40×80 mm2. The reflection coefficient of the antenna is below -10 dB over the frequency band 3.2-11 GHz. The gain of the all Vivaldi antennas vary from 1 to 11 dB (approximately).

Chapter 3: Compact UWB Fractal Monopole Antenna and Superstrates

An analysis and design of compact printed monopole antennas has been explained. The fractal concept is applied for radiation pattern improvement in the monopole antenna. Gain enhancement of antenna is established by applications of superstrates. The reflection

coefficient (S_{11}) of the proposed antenna is controlled to be less than -10 dB in the UWB frequency band. The gain of the antenna is increased by 2 dB.

Chapter 4: UWB antenna with Metamaterial

This chapter deals with the design and improvement of UWB antenna using parallel-line metamaterial. Generally, the metamaterials have narrow bandwidth with high loss. Here, the proposed metamaterial has non-dispersive characteristics with broadband and low material loss. The gradient refractive index (GRIN) metamaterial is designed by arranging different refractive indices in a periodic fashion. The GRIN is incorporated with UWB monopole and Vivaldi antenna. The gains of the antennas are increased successfully without destroying UWB characteristics. The side lobe level is also reduced by using the gradient refractive index (GRIN) Metamaterial.

Chapter 5: Band notch characteristics with artificial material integrated UWB TSA

Here, the band notch characteristics are discussed to suppress the WLAN bands within the UWB frequency band. The notch is implemented using split ring resonator (SRR). Due to the SRR harmonic effects, the gain of the antenna can be slightly decreased. So, the artificial material is used in tapered slot antenna for gain enhancement. The dual band notch tapered slot antenna is also designed using SRR and electric-field-coupled (ELC) resonator.

Chapter 6: Conclusions

A consolidation of the results is presented. Compact UWB antennas are designed for commercial applications with better gain, radiation pattern than that is available in the literature. Thus the results obtained indicate that the designed antenna is a good candidate for UWB application.

Future work: To design a novel broadband fractal shape Metamaterial using different fractal geometries. Implementation of a novel UWB antenna with fractal shaped Metamaterial. To design a more compact nano-scale unit cell Metamaterial for solar cell application. Implementation of the solar cell antenna using Metamaterial can be attempted.

1.6 Contribution of Work

The key contributions of this work are summarized as follows:

1. A detailed survey of published literature is explained. It also includes drawbacks of the existing UWB antennas. Some of the novel methods are used to overcome the existing drawbacks.
2. The tapered slot antenna and corrugated TSA are designed with a reflection coefficient below -10 dB over the frequency band 3.5-11 GHz and 2.5-11 GHz, respectively. The gain is varying from 2 to 11 dB over the operating frequency band.
3. The unbalanced antipodal Vivaldi antennas are designed for exponential and elliptical tapered profile with an operating frequency range 3-11 GHz. The corrugated balanced antipodal Vivaldi antennas is also introduced with the frequency band 3.2-11 GHz. The gain is varying from 1-10 dB over the designed frequency band.
4. In order to create a compact monopole antenna, different designs are introduced. Stepped cut and elliptical profiles are applied to monopole antennas. The size of the elliptical monopole of 25×30 mm^2. The gain is varying from 2 to 5 dBi.
5. In order to improve the compactness of the antenna, a fractal is used in monopole antenna with CPW feed for ultra-wideband frequency band 3.1 to 10.6 GHz. A superstrate is used to enhance the gain of the fractal antenna. The peak gain of the conventional monopole antenna has been increased by 1.6 dB at 10 GHz.
6. To increase the gain of the UWB antenna, the gradient refractive index (GRIN) metamaterial is implemented using parallel-line metamaterial.
7. The GRIN lens is installed in monopole antenna. The radiation pattern of the monopole is more directional with GRIN lens. Due to GRIN lens, the peak gain of the basic monopole antenna is increased by 5.3 dB at 8.8 GHz.
8. The GRIN lens is also incorporated in front of the Vivaldi antenna with a distance of 23 mm. The measured normalized radiation patterns are directive and gain of the Vivaldi is increased up to 14 dB.
9. Next, band notch characteristics have been implemented in tapered slot antenna with split ring resonator (SRR) for low electromagnetic interference for WLAN

application. The measured VSWR of basic TSA and artificial material TSA are fluctuating at 1.5 over frequency band 3-11 GHz except at 5.1-5.8 GHz.

10. The dual band notch is implemented with SRR and the electric-field-coupled (ELC) resonator. SRR slot and ELC resonator are placed close to excitation point and inside balun. The notches are created at 5.5 GHz and 8.5 GHz.
11. All antennas are fabricated and experimentally tested in vector network analyzer and anechoic chamber. The simulated and measured results are compared.

1.7 Conclusions

The requirements of complex wireless devices for covering wideband width are discussed. The application areas of ultra-wideband antennas are elaborated. The significance of the research on ultra-wideband antennas is discussed. The published literature is presented on ultra-wideband antennas and different techniques for gain enhancement are discussed. The research objectives of the proposed work is outlined. The antennas are suitable for UWB application. The effects of metamaterial and superstrate on printed UWB antenna for obtaining high gain are explained. A brief summary of the thesis work on ultra--wideband antennas is mentioned. Key contribution of the proposed work are also highlighted.

Chapter-2

Vivaldi Antenna for UWB applications

2.1 Introduction

In the modern world, the demand of directional antenna is very high in UWB frequency band. Basically UWB directional antenna is widely used in radar and other military equipments. Now, the UWB directional antennas are also used in radio telescope by creating focal plane array to get a clear image. These antenna elements are also used to design a Phased Antenna Array for Hybrid Nonlinear Delay Line system with space beam steering capability for radar applications. Further, it is also applicable in radar gun which is used by traffic police to detect the speed of the car. Directional UWB antennas are also used in microwave imaging, ground penetration radar and tumor detection.

In classical ultra-wideband antennas, 3D horn antenna is very useful for its broadband characteristics and high gain. Unfortunately, the 3D horn antenna is not suitable in the modern portable wireless system for its large size. So, the 2D horn antenna is very useful for modern wireless communication which is also called a printed Vivaldi antenna.

In April 1979, tapered slot antennas are first presented by Prasad and Mahapatra with the linear tapered slot antenna in 9th European Microwave Conference [43]. In the same conference, Gibson also proposed the exponentially tapered slot antenna or arial Vivaldi [44]. Later, improvements are done by many researchers, namely in the works of E. Gazit in 1988 [45] and Langley Hall and Newham [46] in 1996.

Yao Y. et al introduced an UWB tapered slot antenna and numerically analyzed using conical and rectangular coordinate systems [47]. The metal parts were modeled in a conical coordinate system with the medium modeled in rectangular coordinates. The tapered profile has been developed by parabola to create a wider bandwidth. The antenna impedance is matched over a wide bandwidth from 2 GHz to 11 GHz. Gopikrishna et al investigated a

compact ultra-wideband linear tapered slot antenna [48]. The antenna possesses wide bandwidth from 2.95-14 GHz for return loss less than -10 dB and a gain of 3 dBi.

Nasser et al proposed a new method to improve the directivity and bandwidth of the antipodal Vivaldi antenna [51]. A parasitic elliptical patch is introduced in the flare aperture of the antenna to enhance the field coupling between the arms. So, it can produce stronger radiation in the end fire direction. The directivity is increased in the 5-32 GHz frequency range. The gain is not uniformly distributed and also decreased monotonically at high frequencies.

Lee et al implemented an array of 25x25 dual-pol flared dipoles or bunny-ears antenna [52]. Schubert et al also designed a double mirrored balanced antipodal Vivaldi antenna array [53]. There are vias that connect the two outer fins of the BAVA in the region near the tips of the BAVA. The impedance anomalies presented by the gaps between the elements. So, these anomalies are removed by applying the mirror symmetries technique in the array of BAVAs. The metallic walls and vias in the substrate have enabled the single polarized antenna to exhibit better bandwidth and wider scan angle.

Vivaldi UWB antennas are mentioned in the published literature with different design techniques. Even though the methods exist to get desired antenna impedance bandwidth, the designed models do not have compact structure with high gain. Moreover, the selection of dielectric substrate and its height also play important role in antenna characteristics.

In this chapter, the design procedure of different tapered profile Vivaldi antennas is discussed and implemented for UWB application. The linear, exponential, and elliptical profiles are used in the Vivaldi antenna. The proposed antennas are analyzed and designed with the help of parametric study with different substrates. Here, hybrid taper profile, i.e. linear mixed with exponential taper profile is used in the tapered slot antenna. The edge of the antenna is corrugated to enhance the impedance bandwidth and to reduce the mutual coupling in array system. The corrugation is also used in balanced antipodal Vivaldi antenna.

2.2. Basic Geometry

The basic construction of a tapered slot antenna or Vivaldi antenna is shown in Figure 2.1.

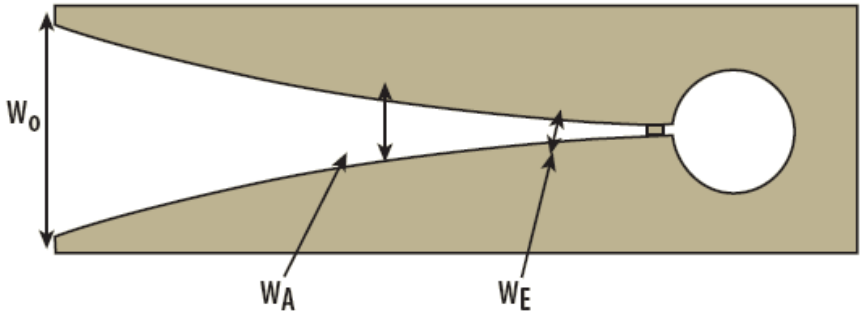

Figure 2.1 Basic construction of Vivaldi antenna with different tapered slot area

TSA is one kind of traveling wave antenna. The travelling-wave antennas are divided into two main groups called the leaky-wave antennas and the surface-wave antennas [54]. In case of leaky wave antenna, the antenna structure propagates a travelling-wave with a phase velocity, V_{ph} greater than the speed of light, and the main beam occurs in the direction different from endfire. Leaky-wave antennas continuously lose energy along the direction of wave propagation.

The EM wave that travels along the surface or at the interface between two media with different refraction indices and radiates when discontinuity appears, such type of antenna is called as slow wave antenna or surface-wave antenna. Tapered slot antennas belong to the surface-wave antennas in which the traveling wave propagation with a phase velocity less than or equal to the speed of light and radiates along end fire direction [54].

The taper slot area is divided into three regions, where high frequency radiates at input slot width WE, WA is the slot width of the radiating area, and W0 is the output slot width designed to radiate at low frequency. Different taper profiles are shown in Figure 2.2.

The basic radiation mechanism is similar for all taper profile. Generally, three basic profiles are existing: (1) constant width (2) linear taper and (3) nonlinear taper (exponential or, elliptic and parabolic). The TSAs with constant width taper profile and transitional step regions taper profile are shown in Figures 2.2(a) and (b). Only the exponential and the linearly tapered slot antenna have been extensively studied over the decades. Among the different profiles, Fermi tapering provides additional degrees of freedom which is allowing more control over radiation characteristics [55]. But, very limited data are available for the other designs.

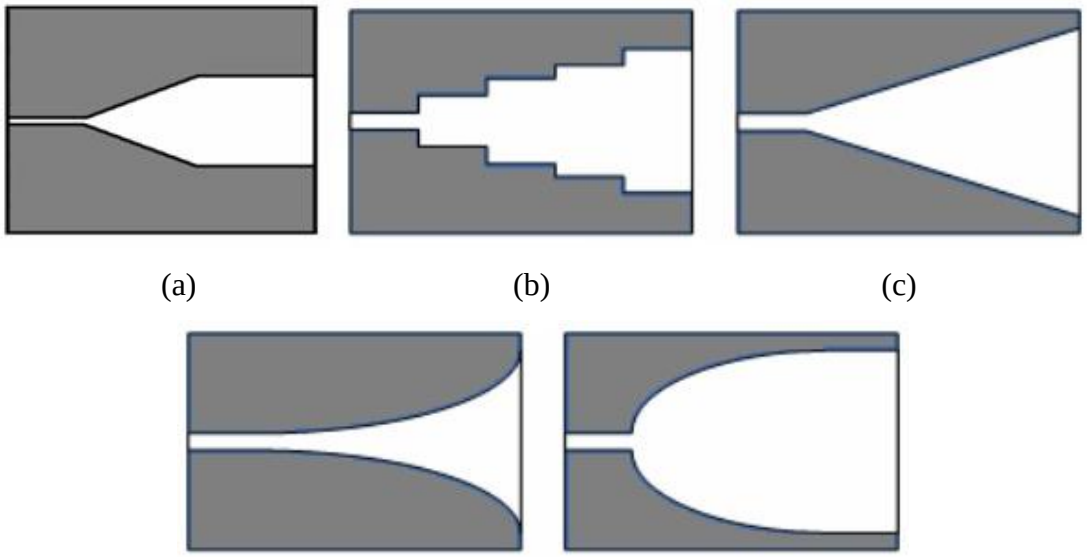

(a) (b) (c)

(d) (e)

Figure 2.2 TSA with different tapered profiles excited by a slotline; (a) Step constant (b) linearly tapered (c) exponentially tapered and (d) Fermi profile, and (e) constant width slot

Basically, Vivaldi antennas are classified as (1) tapered slot antenna (2) unbalanced antipodal Vivaldi antenna (AVA) (3) balanced antipodal Vivaldi antenna (BAVA), as shown in Figure 2.3.

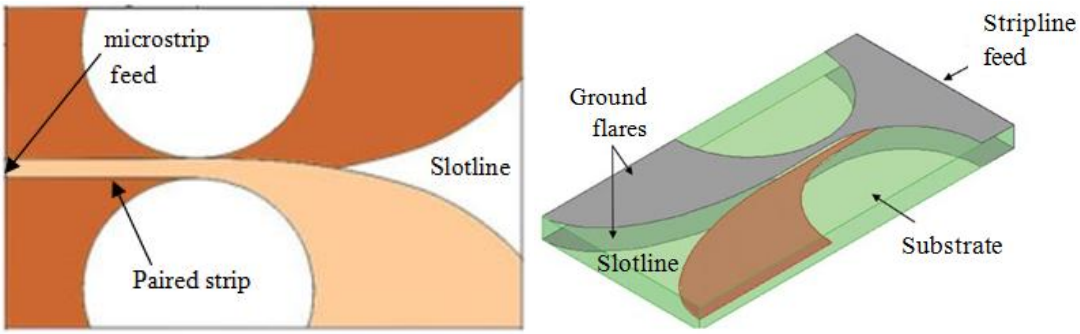

(a) (b)

Figure 2.3 (a) Antipodal slotline transition, (b) Balanced antipodal slotline transition

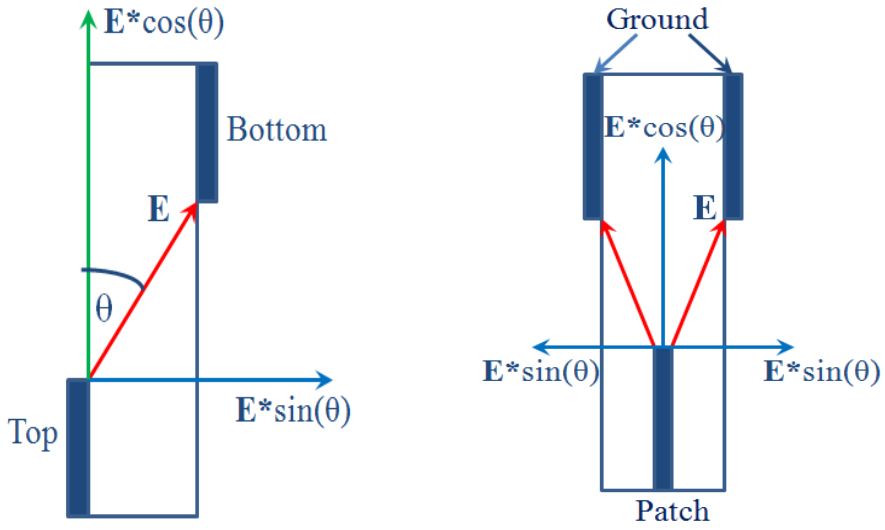

(a) (b)

Figure 2.4 Electric field distribution (a) unbalanced antipodal Vivaldi antenna and (b) balanced antipodal Vivaldi antenna

The electric field distribution of the unbalanced and balanced antipodal Vivaldi antennas are shown in Figure 2.4. The electric field is inclined at an angle θ with respect to surface which results in two orthogonal components. The cross polarization exists in unbalanced AVA for sin(θ) component of electric field, E. In case of balanced antipodal Vivaldi antenna, there are two ground plane which creates two sin(θ) component to cancels each other. Therefore, the balanced AVA has low cross polarization compared to the unbalanced AVA.

2.3 The feeding Techniques

Appropriate selection of feeding techniques is significant for broadband operation. Different feeding techniques for coupling TSA are discussed in this section. Initially, coaxial to slotline transition techniques are used [56]. But coaxial feeding is complicated to implement successfully for the etching difficulties. Coaxial to slotline transition is called as directly coupled transition.

On the other hand, the coupling of signals to the slotline through the fields is called electromagnetically coupled transitions. Microstrip to slotline, stripline to slotline, antipodal slotline and balanced antipodal slotline are the best known types of electromagnetically coupled transitions.

2.3.1 Microstrip to slotline transition

In the last two decades, most of the researchers have used an electromagnetically coupled transition's technique, namely, microstrip to slotline transition [57], as shown in Figure 2.5(a). To improve impedance matching of the TSA, a basic microstrip to slotline transition is realized by etching the slotline on one side of a substrate. On the opposite side of the substrate, a microstrip line crosses perpendicularly to the slotline, so that an electromagnetic signal is passed between the two sides. In order to fulfil this operation with negligible power losses, the microstrip line and the slotline have to be orthogonal to each other. Due to this mechanism, the electromagnetic coupling is exist in between the microstrip and slot line. In practice, the two types of terminations can be accomplished by virtual open and virtual short circuits (open or short-circuited stubs).

A small modification has been done in the basic microstrip to slotline transition techniques to enhance the bandwidth with a simple structure. So, a non-uniform stub is used in both stripline to slotline. To implement the non-uniform stub, the microstrip line is connected to the radial stub. A different type of radial stub can be used with microstrip line. Circular radial stubs are used to extend bandwidth in microstrip to slotline transition as shown in Figure 2.5(b). The conventional coplanar waveguide is also useful to feed TSA [58, 59], as represented in Figure 2.5(c).

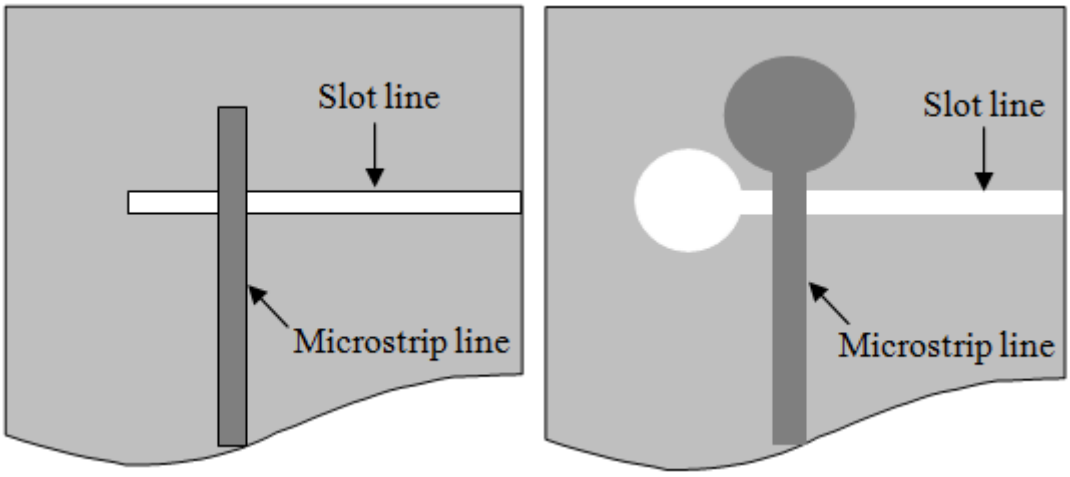

(a) (b)

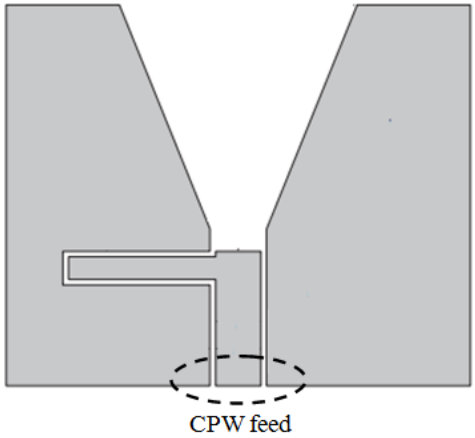

(c)

Figure 2.5 (a) Microstrip to slotline transition (b) Non-uniform stub Microstrip to slotline transition (b) CPW fed tapered slot antenna

2.3.2 Antipodal Slotline

Antipodal slotline transition is first introduced by E. Gazit. Compare to the microstrip to slotline transition, the antipodal slotline is giving more bandwidth. Feed by a microstrip line is directly connected to the antipodal slotline transition as shown in Figure 2.3(a). This slotline techniques will provide high cross-polarization.

2.3.3 Balanced antipodal Slotline

In case of this slotline transition, an additional dielectric and ground metallic layer has been added as represented in Figure 2.3(b). Balanced antipodal slotline is giving low cross-polarization. In this type of transition, antenna is fed by a stripline directly.

2.4 Study and design of tapered slot antenna

The selection of dielectric substrate is also very important to get good result. Generally the low relative permittivity with tangent loss substrate is considered. The selected substrate must have low loss tangent. The dielectric constant and height of the substrate are often design parameter of the antenna which control the propagation of waves in the substrate. Antenna with less dielectric constant substrate have wide bandwidth.

2.4.1 Linear profile TSA

2.4.1.1 Design

The geometry of the linear tapered slot antenna is given in Figure 2.6. There are two linear sections, namely linear 1 and linear 2 as shown in Figure 2.6(a). The linear 1 section is designed at the high frequency region and linear 2 section is implemented at the radiating and low frequency region. The selection of feeding techniques is very important to radiate at the UWB frequency band. In this design, the Rogers RO4003 is chosen as the substrate material (tan δ = 0.0021) with dielectric constant of ε_r=3.55 and height as 0.8 mm.

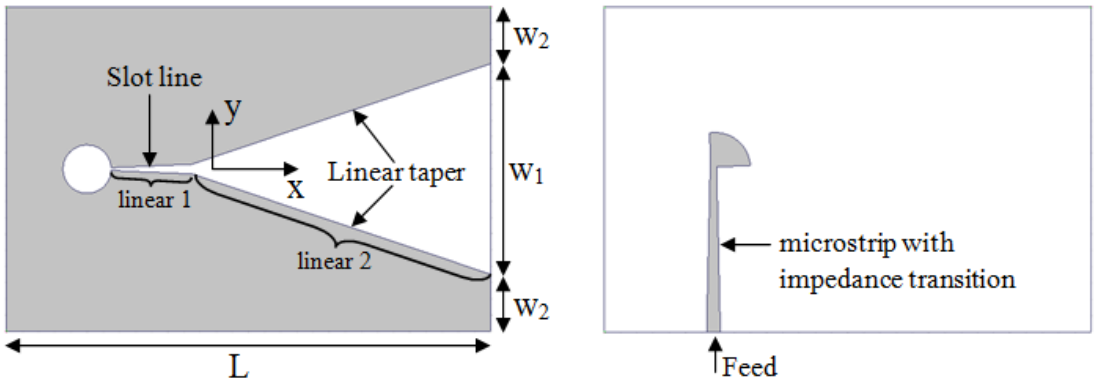

(a) (b)

Figure 2.6 Linear tapered slot antenna structure (a) Top view, (b) Bottom view

Hence, the non-uniform radial stub based microstrip to slotline transition technique is used in the linear profile tapered slot antenna. In the proposed antenna, microstrip line feed is connected to radial stub and slotline is connected to the circular balun. The microstrip to slotline transition design is shown in Figure 2.6(b). The broad and narrow widths of microstrip line are 1.7 mm and 0.8 mm, respectively. The dimensions of the antenna are L=60 mm, W_1=26 mm and W_2=7 mm.

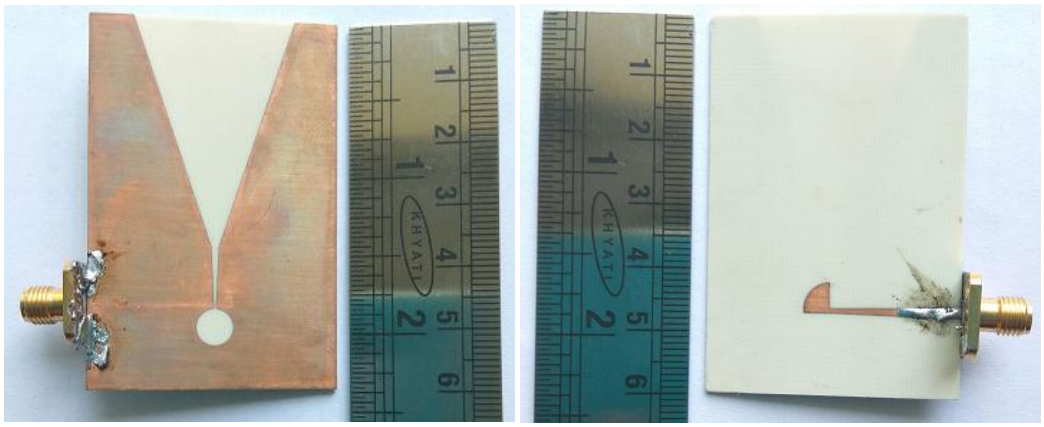

(a) (b)

Figure 2.7 Fabricated linear TSA (a) top and (b) bottom view

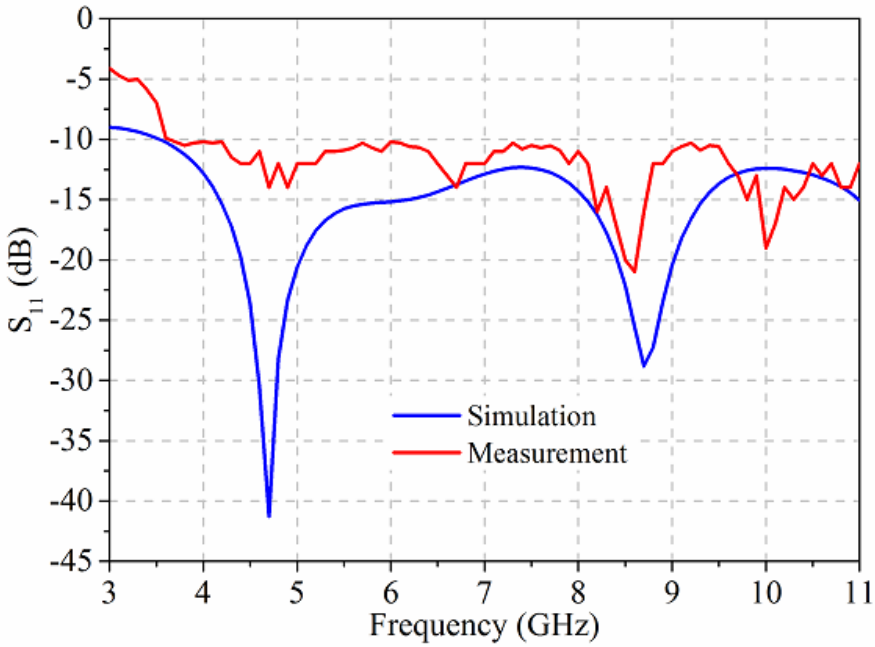

Figure 2.8 Simulated and measured reflection coefficient (S_{11}) of the linear TSA

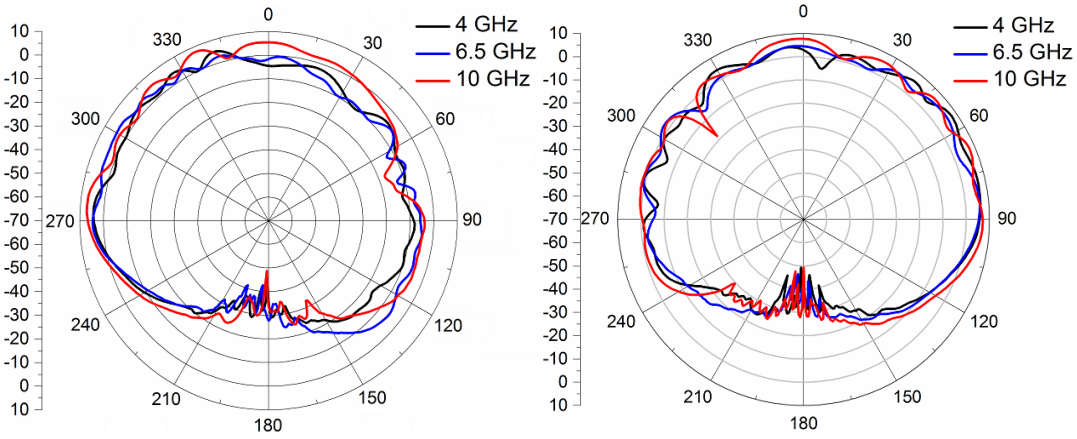

(a) (b)

Figure 2.9 Measured radiation pattern of the linear TSA, (a) E-plane and (b) H-plane

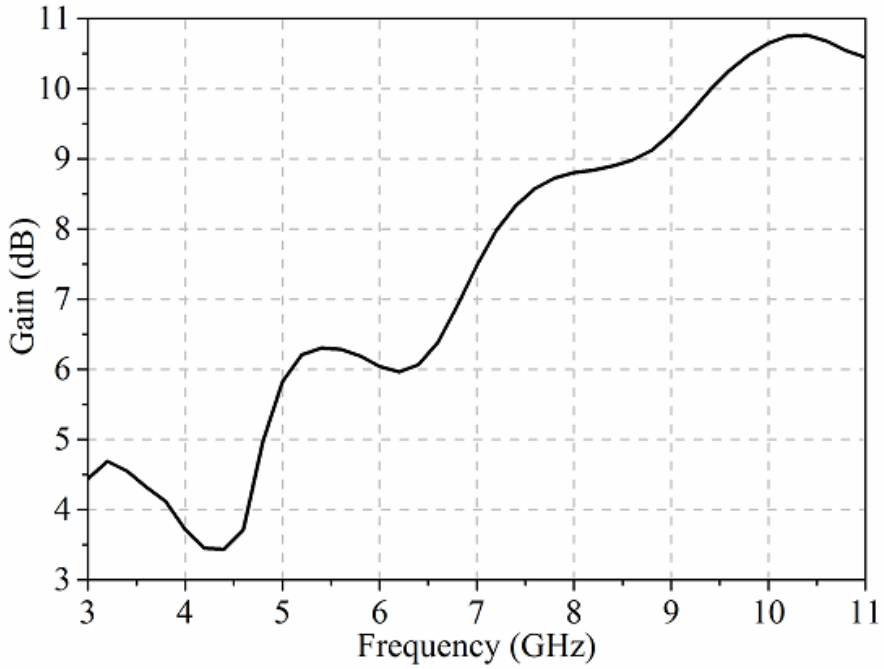

Figure 2.10 Measured gain of the linear TSA

2.4.1.2 Results and Discussions

The fabricated linear TSA is shown in Figure 2.7. The simulated and measured results of reflection coefficient (S_{11}) of the antenna are illustrated in Figure 2.8. It can be seen that the simulation result is varying near –15 dB over the UWB frequency band. The measured S_{11} is below -10 dB and varying near to –10 dB within UWB frequency range. On the other side, both E-plane (xy-plane) and H-plane (xz-plane) radiation patterns measured at the frequency

of 4, 6.5 and 10 GHz are shown in Figure 2.9. The measured gain variation of the antenna over the operating frequency band is presented in Figure 2.10. Moreover, the gain is varying and increasing with respect to the frequency.

2.4.2 Exponential profile TSA

2.4.2.1 Design

In this section, the TSA is designed by using exponential equation. The geometry of the exponential TSA is shown in Figure 2.11. The substrate is selected to be the same as the linear TSA. The taper section is calculated by the expression which is given below, where $p_1(x_1, y_1)$ and $p_2(x_2, y_2)$ are starting and ending points of the taper section. c_1 and c_2 are constants determined from the points p_1 and p_2.

$$y = c_1 e^{Rx} + c_2 \tag{2.1}$$

where, $c_1 = \dfrac{y_2 - y_1}{e^{Rx_2} - e^{Rx_1}}$ and $c_2 = \dfrac{y_1 e^{Rx_2} - y_2 e^{Rx_1}}{e^{Rx_2} - e^{Rx_1}}$

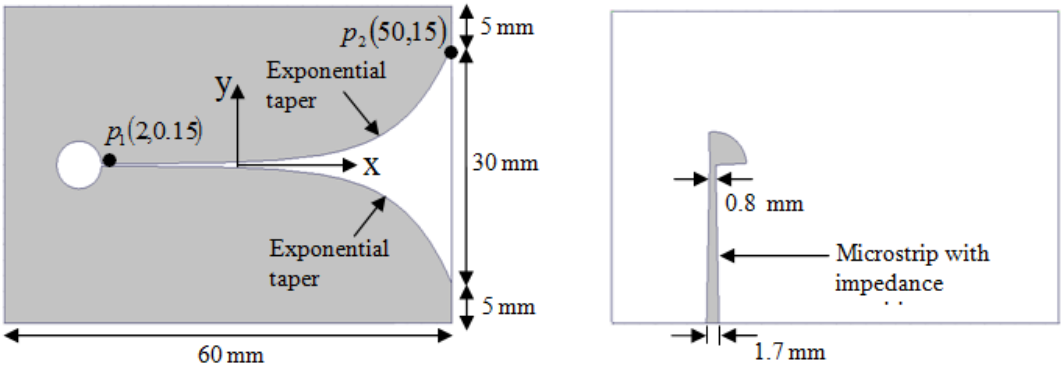

Figure 2.11 Exponential tapered slot antenna structure (a) Top view, (b) Bottom view

The non-uniform stub microstrip to slotline transition design starts with the choice of substrate material and thickness. Microstrip line width (W) with impedance transition (50 Ω to 100 Ω) is calculated using the stripline characteristic impedance formula and is given below:

$$\frac{W}{h} = \frac{8\exp(A)}{\exp(2A)-2} \text{ for } \frac{W}{h} \le 2 \qquad (2.2)$$

where $A = \frac{Z_C}{60}\left\{\frac{\varepsilon_r+1}{2}\right\}^{0.5} + \frac{\varepsilon_r-1}{\varepsilon_r+1}\left\{0.23+\frac{0.11}{\varepsilon_r}\right\}$

where, Z_C is the characteristic impedance of the stripline (Ω), W is the stripline width (mm), h denotes thickness of dielectric substrate (mm), ε_r is the relative permittivity of the dielectric substrate.

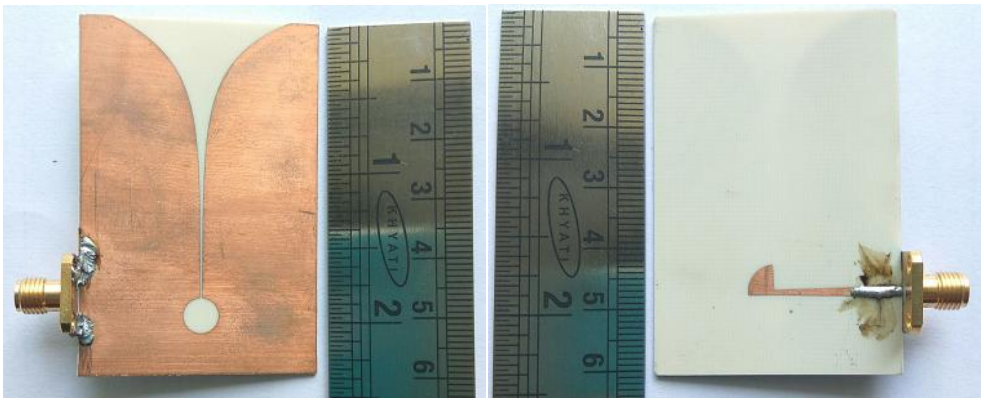

(a) (b)

Figure 2.12 Fabricated exponential TSA (a) top and (b) bottom view

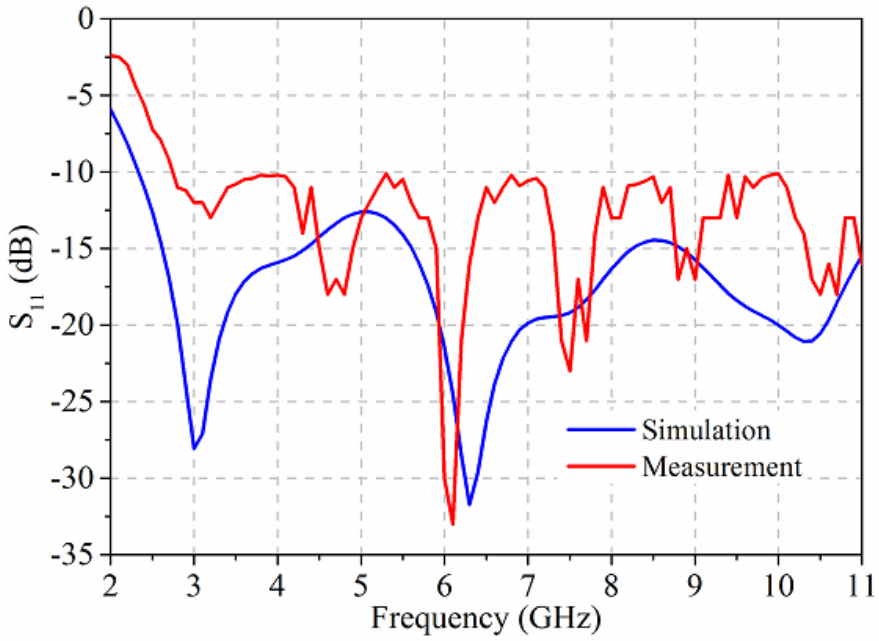

Figure 2.13 Simulated and measured reflection coefficient (S_{11}) of the exponential TSA

2.4.2.2 Results and Discussions

The antenna is fabricated as shown in Figure 2.12 and results are validated through measurements. The simulated and measured results of reflection coefficient (S_{11}) of the antenna are shown in Figure 2.13. It is clear that the simulated reflection coefficient is varying at -15 dB over the UWB frequency band. The measured result also shows that the antenna is working over the frequency band from 2.85-11 GHz which is covering UWB frequency range. The measured E-plane (xy-plane) and H-plane (xz-plane) radiation patterns of the exponential TSA at the frequency of 4, 6.5 and 10 GHz are depicted in Figure 2.14. The measured gain variation of the antenna over the operating frequency band is illustrated in Figure 2.15. Moreover, the gain highly fluctuates and gradually increases from 3 to 11 GHz. Compared to the linear TSA, the exponential TSA is showing wider bandwidth with less gain.

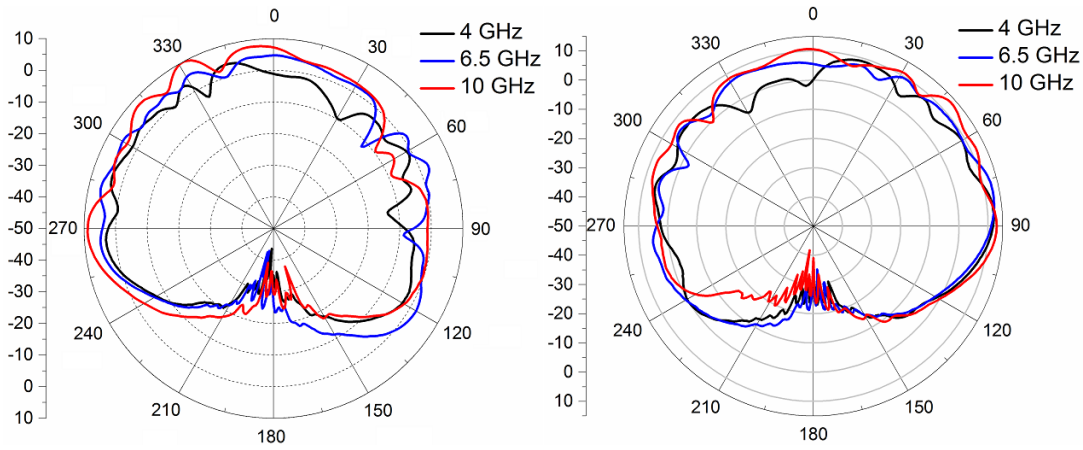

Figure 2.14 Measured radiation pattern of the exponential TSA, (a) E-plane and (b) H-plane

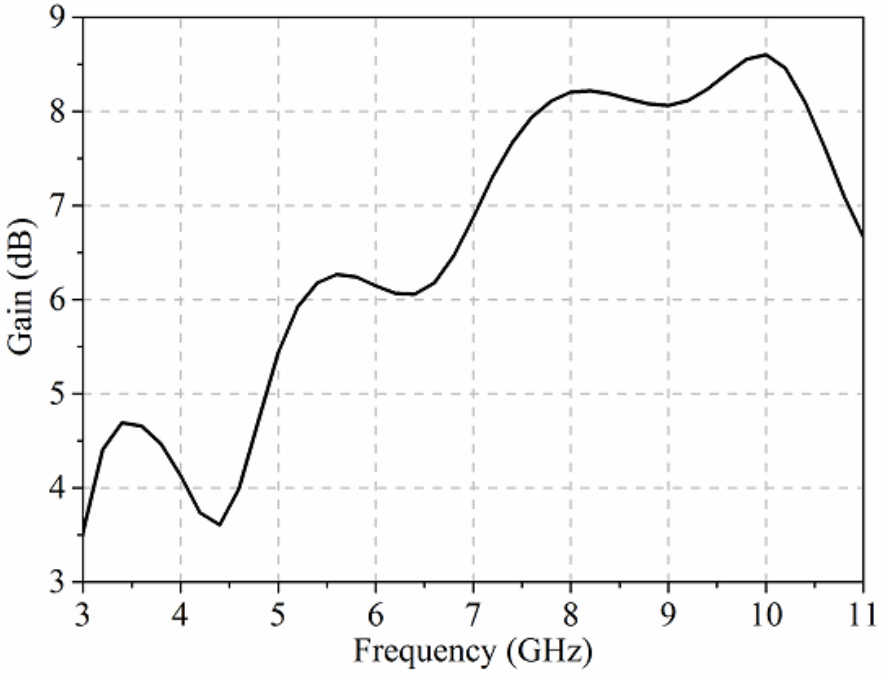

Figure 2.15 Measured gain of the exponential TSA

2.4.3 Corrugated TSA

2.4.3.1 Design

TSA does not radiate from a single point for a given frequency, but from a small section along the line of the flare. The taper profile is designed as a combination of three linear lines, one linear region for high frequency and others are for low frequencies. Linear tapered slot antennas are the best compromise between beam width and side lobe level. If the number of linear lines increases gradually in such a way that the linear taper can be turned into an exponential. At the same time, beam of the radiation pattern becomes narrow.

In this work, corrugation is introduced at the edge of the proposed antenna. By corrugating the edge of the proposed antenna it is possible to suppress surface current along the longitudinal direction and resonant frequency will be reduced. The corrugations will effectively reduce the coupling between two antennas in antenna array.

The geometry of the modified linear Tapered Slot Vivaldi antenna is depicted in Figure 2.16. The antenna is designed by substrates of Roger TMM3 with dielectric constant 3.27, thickness is 0.3807 mm and loss tangent, tanδ = 0.002. It is necessary to transform the impedance of the input feeding microstrip line (50Ω) to the input impedance (100Ω) of the

transition. The tapered slot Vivaldi antenna with feed is shown in Figure 2.16(b). The parameters of the Vivaldi antenna are given in Table 2.1.

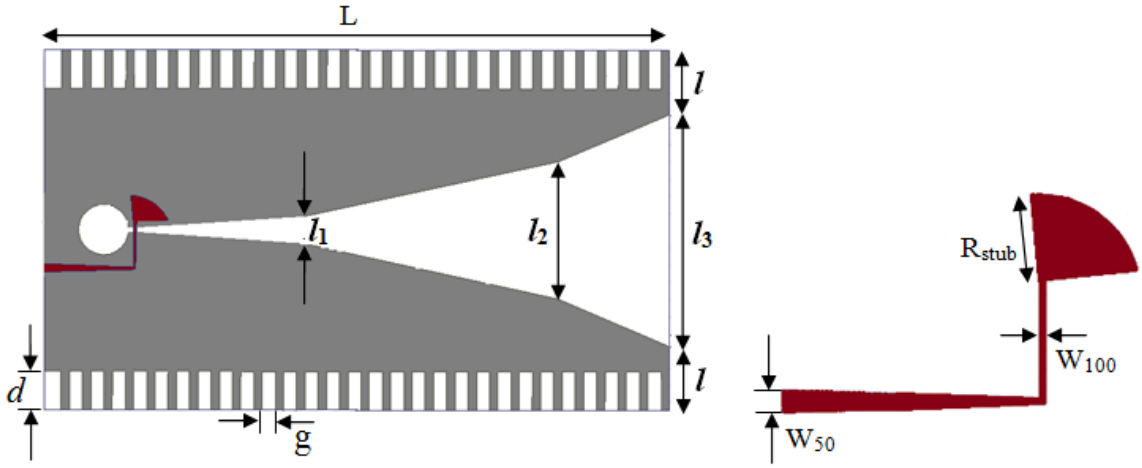

Figure 2.16 (a) Geometry of corrugated tapered slot antenna structure, (b) Microstrip line feed with impedance transition

Table 2.1 Parameters values of corrugated tapered slot Vivaldi antenna

Parameters	Values (mm)
L	72.92
l	7.485
l_1	3
l_2	16
l_3	27
g	1.5
d	5
W_{50}	0.9021
W_{100}	0.2668
R_{stub}	3.5

2.4.3.2 Results and Discussions

The simulation results of antenna are showing very wide bandwidth as shown in Figure 2.17. The reflection coefficient is below -10 dB over the frequency band from 2.85 to 20

GHz. The designed antennas can be used in the entire UWB frequency band with a fractional bandwidth of 146% from 3.1 up to 20 GHz.

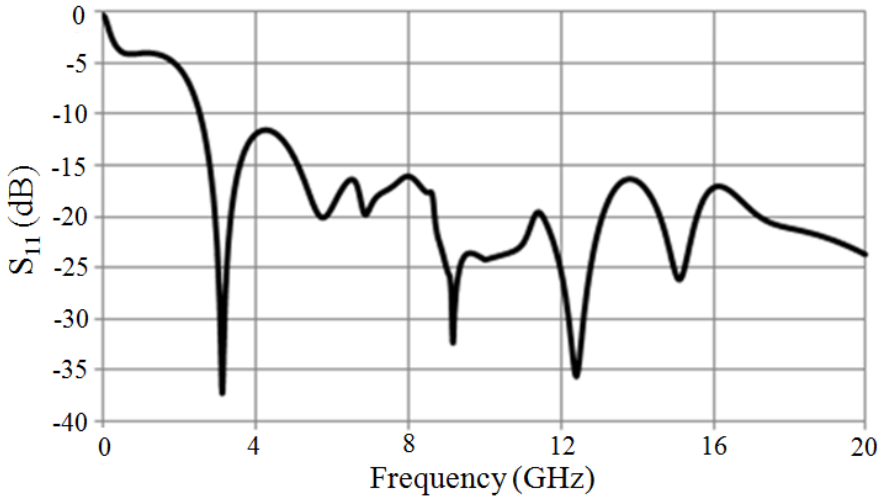

Figure 2.17 Simulated reflection coefficient of corrugated tapered slot Vivaldi antenna

The E-plane and H-plane radiation patterns for the frequencies of 4 GHz, 6.5 GHz and 15 GHz are illustrated in Figure 2.18. According to the design of the antenna, the xy plane and xz plane are considered as an E-plane and H-plane respectively. The gain variation of the corrugated TSA over the operating frequency band is shown in Figure 2.19. The gain is linearly increasing from 2.2 to 10 GHz from 0 to 12 dBi and almost constant at 10 to 20 GHz.

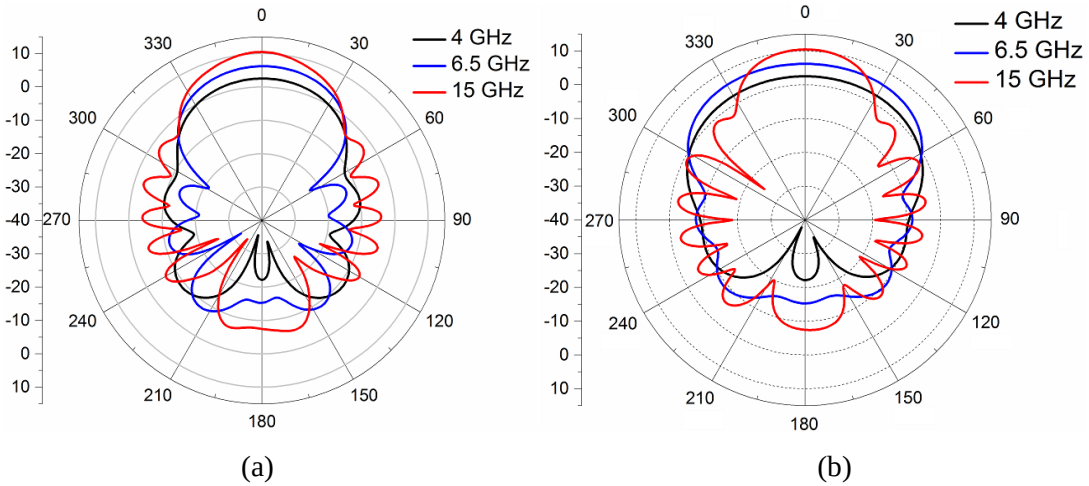

Figure 2.18 Simulated radiation pattern of the corrugated TSA, (a) E-plane and (b) H-plane

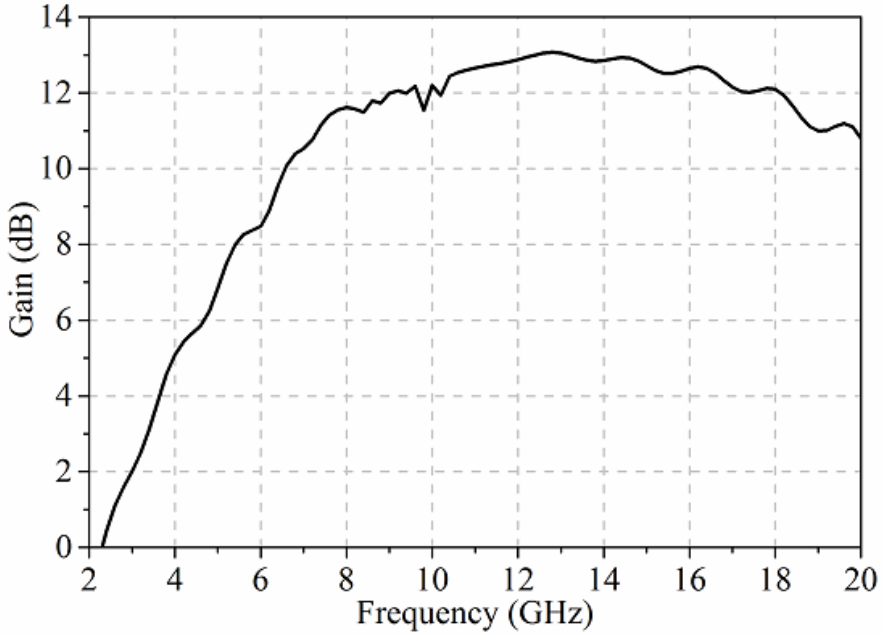

Figure 2.19 Simulated gain of the corrugated TSA

2.4.4 Exponential profile AVA

2.4.4.1 Design

The geometrical structure and dimensions of the exponential antipodal Vivaldi antenna (AVA) are shown in Figure 2.20. The exponential tapered profile is used for the patch and the ground plane of the proposed antenna. The exponential curve is defined by using equation (2.1). To create a better performance, the exponential rate is taken 0.04. After calculating, the final outcome of the equation is given below:

$$y = 1.74e^{0.04x} - 4.24 \qquad (2.3)$$

Antipodal slotline transition is used to feed the antenna. This feeding technique can operate in a multi-octave bandwidth with low cross polarization levels. For maximum power transfer to the antenna 50 Ω microstrip line is used. To determine the width of microstrip line, the calculation has been done by using equation (2.2), obtained at 5 mm.

In the design section of linear TSA, it is mentioned that the low dielectric constant substrates give more efficient design and a wider bandwidth and also provide lower scattering along the antenna with spurious fields. So, the exponential AVA is designed on

the roger RT/duroid 5880 (ε_r= 2.2 and tanδ = 0.0009) substrate with a thickness of 1.575 mm.

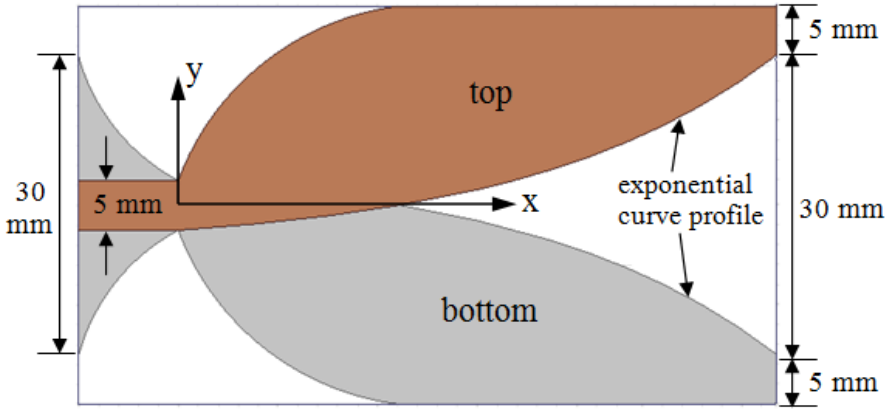

Figure 2.20 Geometry of exponential antipodal Vivaldi antenna (AVA)

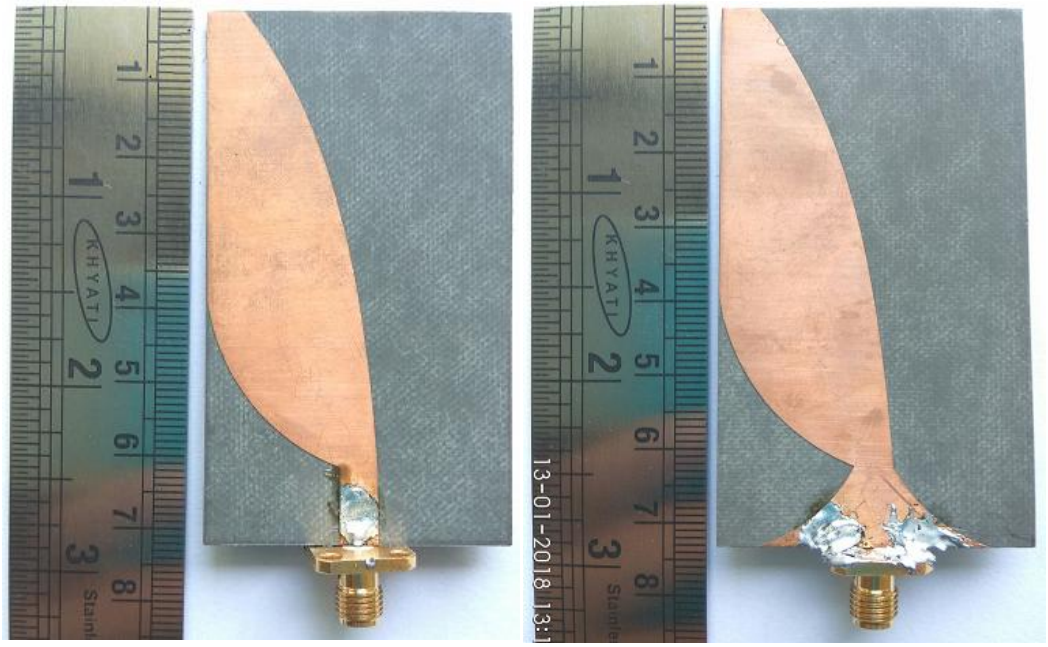

(a) (b)

Figure 2.21 Fabricated exponential AVA (a) top and (b) bottom view

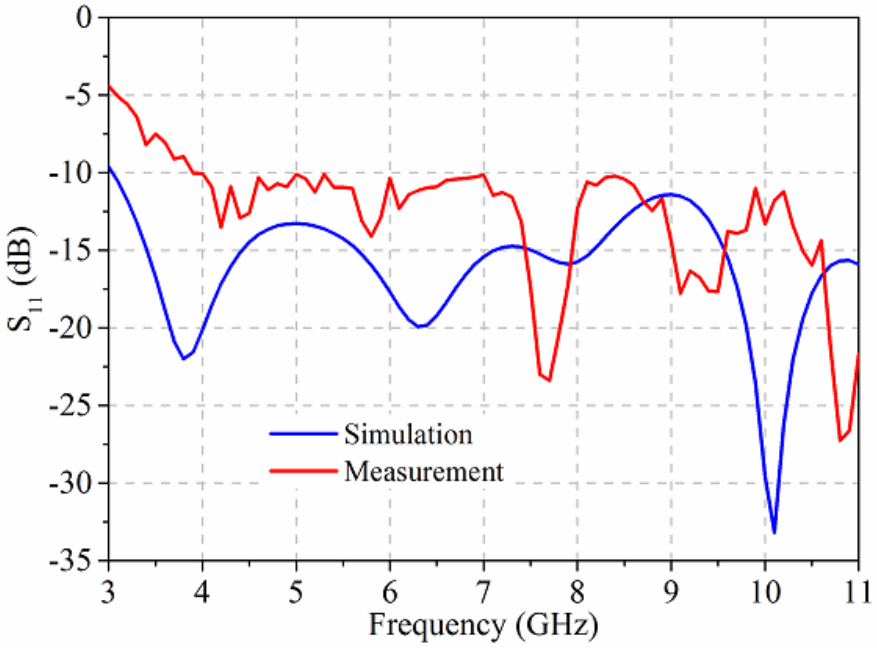

Figure 2.22 Simulated and measured reflection coefficient (S_{11}) of the exponential AVA

2.4.4.2 Results and Discussions

Prototype of the exponential AVA is fabricated and is shown in Figure 2.21. A 50 Ω flat type SMA connector is used to feed the antenna. The variation of simulated and measured reflection coefficient for exponential AVA is depicted in Figure 2.22. From the figure, it is observed that the lower end of S_{11} is 3 GHz and 4 GHz for simulated and measured AVA, respectively. The measured result is slightly different, which is possibly due to the introduction of the SMA connector, the irregularity of soldering or the inaccuracy in fabrication.

The co and cross polarizations of both E and H-plane radiation patterns are plotted at the frequencies 4, 6.5 and 10 GHz which are depicted in Figure 2.23. As the figure reveals, the proposed antenna radiates with the main lobe in the direction of the x-axis. From the patterns, it is clear that the cross polarization level is -5 dB at 10 GHz along the radiated direction of the x-axis. So, unbalanced AVA has a high level of cross polarization. The measured gain is increased up to 9 dB with huge fluctuation over the frequency band from 3-11 GHz as shown in Figure 2.24.

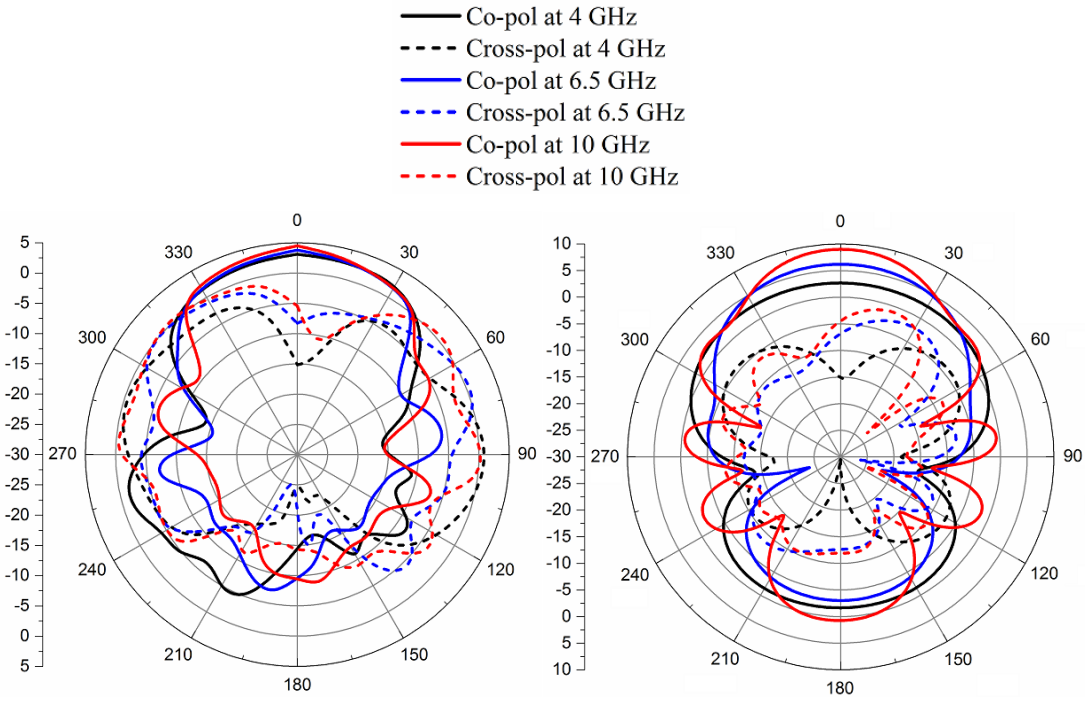

Figure 2.23 Measured co and cross polarization radiation pattern of the exponential AVA, (a) E-plane and (b) H-plane

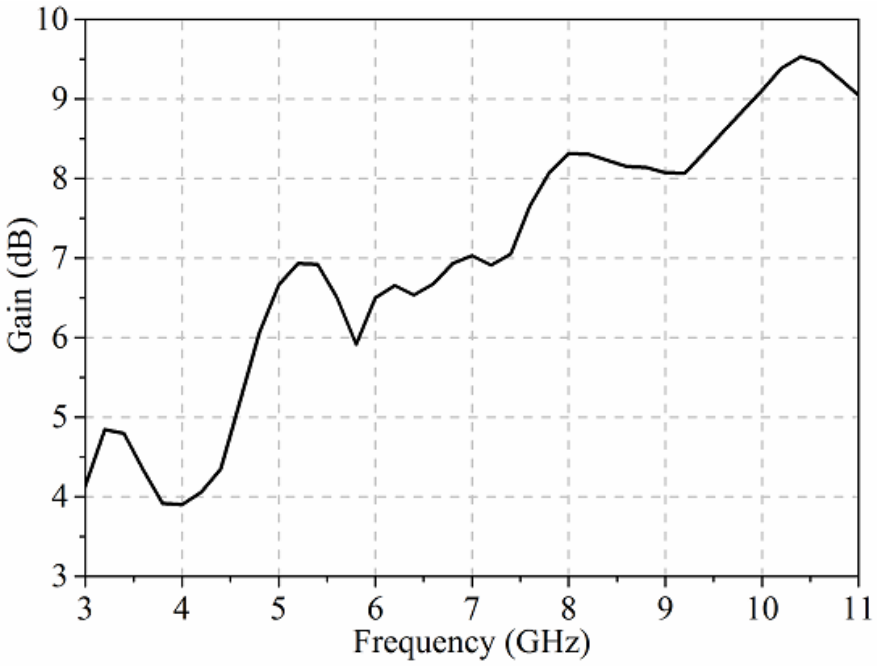

Figure 2.24 Measured gain of the exponential AVA

Table 2.2 Parameters values of elliptical antipodal Vivaldi antenna

Parameters	Values (mm)
$L_{elliptical}$	73
$W_{elliptical}$	37
W_{ground}	40
a	20
b	16
W_f	5

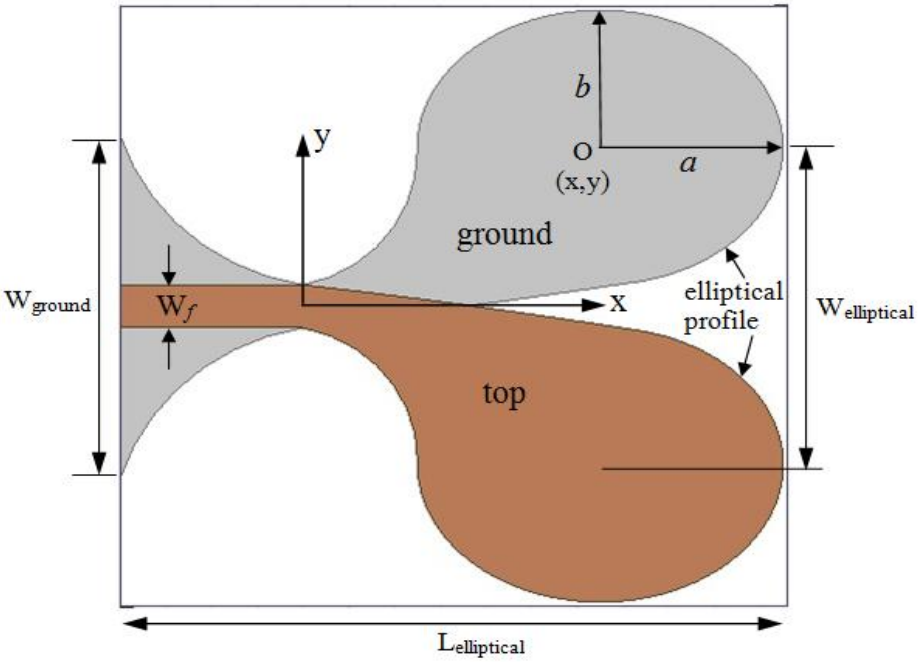

Figure 2.25 Geometry of elliptical antipodal Vivaldi antenna (AVA)

2.4.5 Elliptical profile AVA

2.4.5.1 Design

The geometry and structure of the elliptical antipodal Vivaldi antenna are shown in Figure 2.25. The radiating flare is designed by using elliptic structure. The ash and brown color define ground and top conducting planes. The position of elliptical structure is indicated by the coordinate point O(x,y), that is (52.5, 18.5). The parameters a and b are indicating major axis and minor axis radii, respectively. The feeding has been done by using

50 Ω microstrip line and line width (W_f) is calculated from the equation (2.2). The dimensions of the antenna parameters are given in Table 2.2.

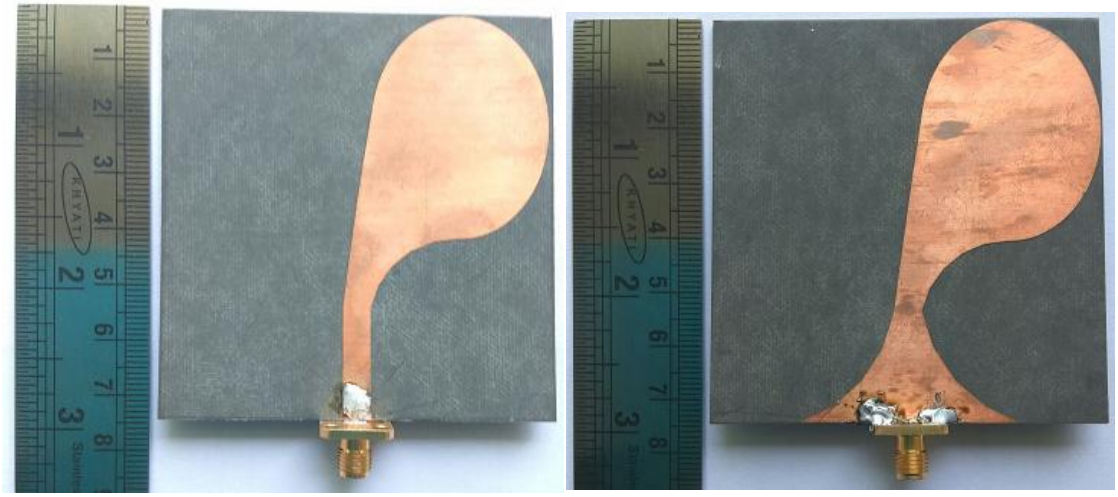

(a) (b)

Figure 2.26 Fabricated elliptical AVA (a) top and (b) bottom view

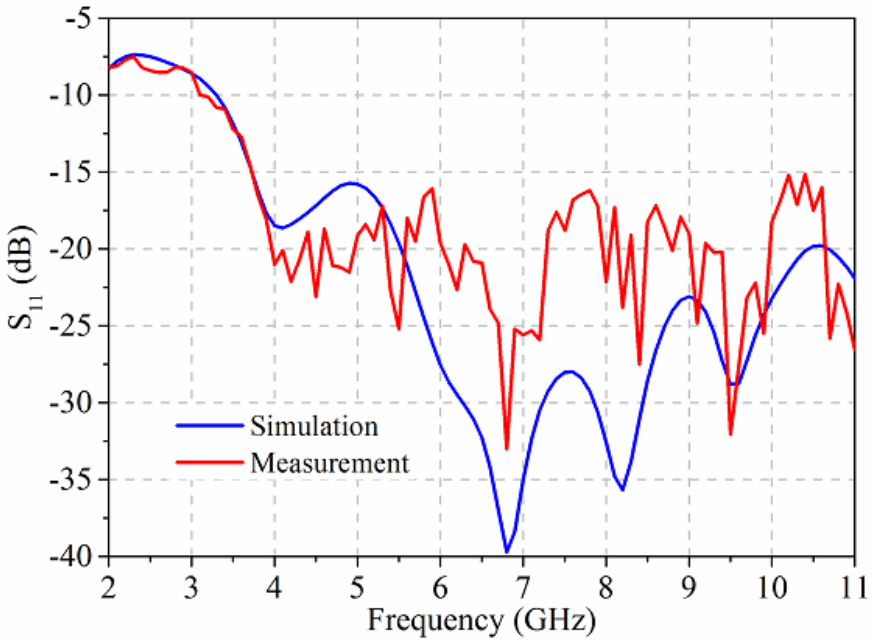

Figure 2.27 Simulated and measured reflection coefficient (S_{11}) of the elliptical AVA

2.4.5.2 Results and Discussions

The elliptical AVA is designed and fabricated on the roger RT/duroid 5880 (ε_r=2.2 and tanδ = 0.0009) substrate with a thickness of 1.575 mm. The fabricated prototype of the

proposed antenna is shown in Figure 2.26. The reflection coefficient (S_{11}) is measured using a vector network analyzer (VNA) over the frequency band from 2 to 11 GHz. The simulated and measured S_{11} values are below –10 dB, plotted and compared as illustrated in Figure 2.27. It is clear that the antenna is working over the frequency band from 3.1-11 GHz. The lowest frequency for both simulated and experimental results are identical.

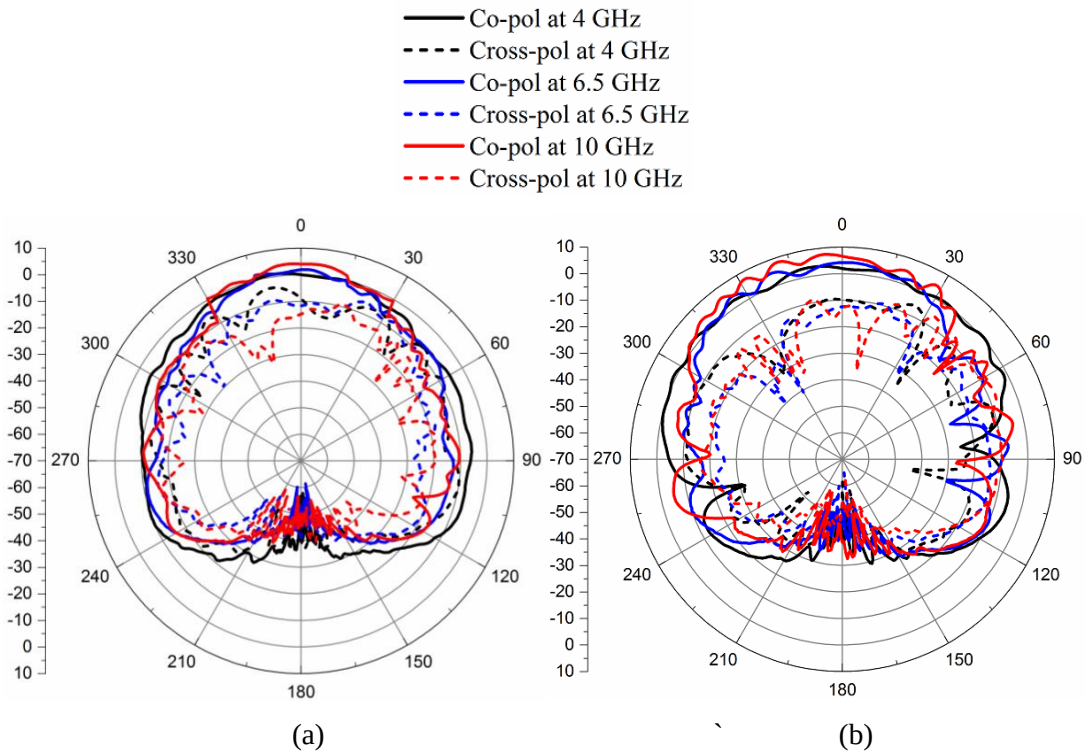

Figure 2.28 Measured co and cross polarization radiation pattern of the elliptical AVA , (a) E-plane and (b) H-plane

In case of elliptical AVA, the E and H-plane radiation patterns are measured with co and cross polarization at 4, 6.5 and 10 GHz are shown in Figure 2.28. The proposed antenna is radiating with a main lobe in the direction of the x-axis. The radiation pattern is showing that the cross polarization levels are -9.9 dB and -14 dB at 4 GHz and 10 GHz, respectively. However, elliptical AVA has slightly low cross polarization level. The measured gain is linearly increasing up to 9 dB over the frequency band from 3-11 GHz as shown in Figure 2.29.

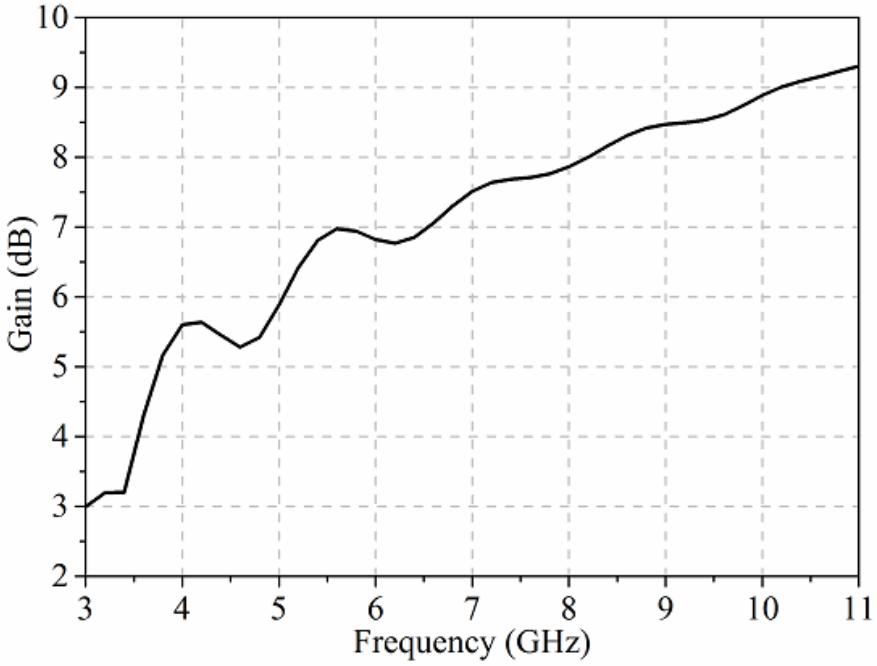

Figure 2.29 Measured gain of the elliptical AVA

2.4.6 Balanced antipodal Vivaldi antenna (BAVA)

2.4.5.1 Design

To overcome this high cross-polarization, another ground plane integrated substrate has been added to form a balanced antipodal Vivaldi as shown in Figure 2.30. The microstrip line feed of the balanced AVA remains the same as unbalanced AVA. The stripline width is calculated from the equation (2.2), that is 5 mm. The resultant electric field in the slot region is now oriented parallel to the ground plane whilst the output transmission medium is tri-plate stripline. The corrugation is used at the edge of both the ground plane and the middle conductor layer to enhance the performance of the antenna. The exponential profile is designed by using the equation (2.1) and the final form of the calculated equation is given below:

$$y = 2.0\,e^{0.035x} - 4.52 \qquad (2.4)$$

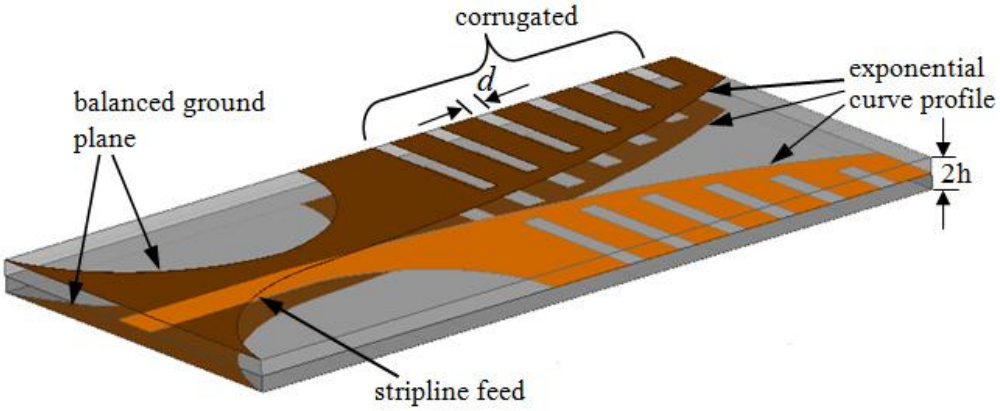

Figure 2.30 Geometry of balanced antipodal Vivaldi antenna (BAVA)

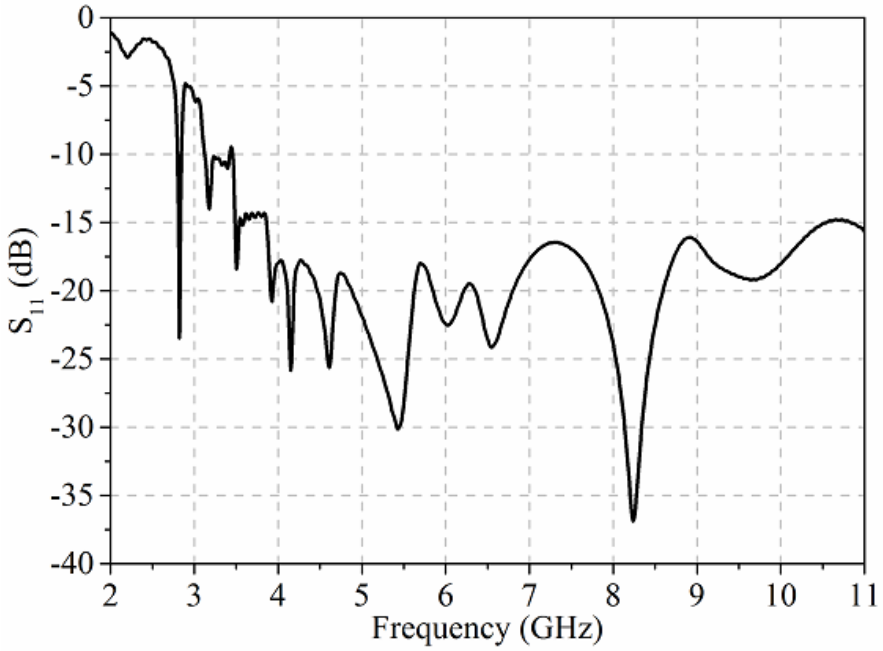

Figure 2.31 Simulated reflection coefficients (S_{11}) of the BAVA vs frequency

2.4.5.2 Results and Discussions

The variation of the simulated reflection coefficient for BAVA is shown in Figure 2.31. It indicated that the S_{11} is below -10 dB from 3-11 GHz. The radiation pattern of the BAVA is depicted in Figure 2.32. In case of BAVA, the cross polarization level is -29.49 dB at 10 GHz along the direction of the x-axis. From the unbalanced AVA, it can be noticed that the cross polarization is high which is not sufficient for some applications. Therefore, BAVA is considered for UWB application. The overlap of two substrates at the time of fabrication is also a very complicated task. The air gap between the substrate can provide poor

performance of the BAVA. Otherwise, the tapered slot antenna can be useful for UWB application. The gain of the BAVA is varying from 4 to 10 dB over the frequency band 3 to 11 GHz as depicted in Figure 2.33. The comparison between the designed antennas and published work is given in Table 2.3. The proposed antennas are giving compact size.

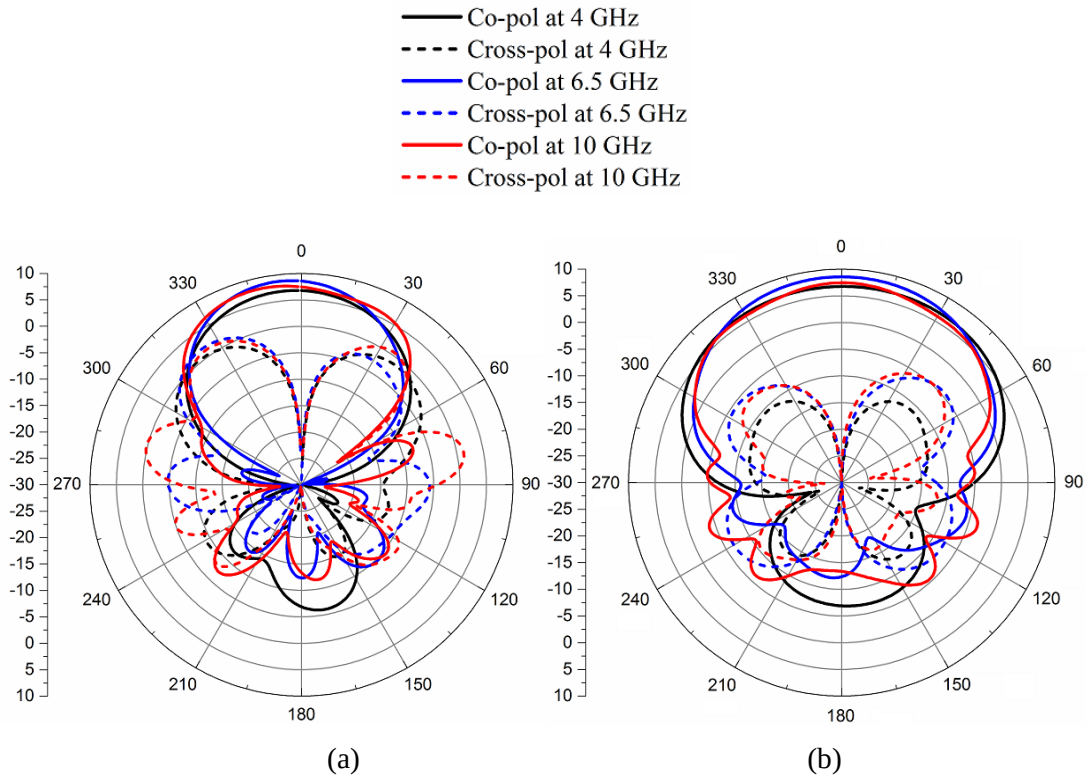

(a) (b)

Figure 2.32 Simulated co and cross polarization radiation pattern of the BAVA, (a) E-plane and (b) H-plane

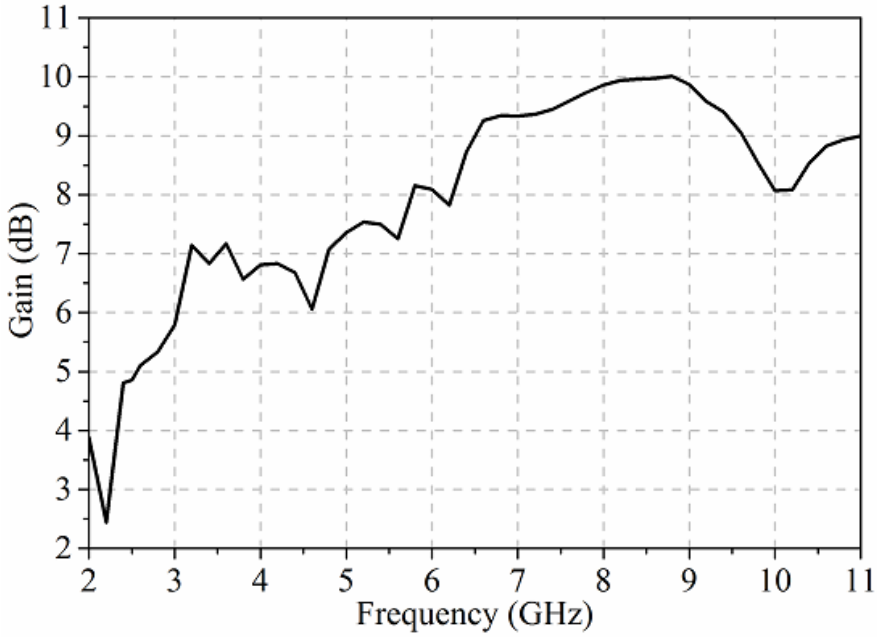

Figure 2.33 Simulated gain of the BAVA

Table 2.3 The comparison between Existing and Proposed work

Reference	**Size (mm^2)**	**Peak Gain (dB)**
[96]	36×36	8
[99]	80×80	8
[100]	50×50	8.5
Linear Vivaldi	40×60	11
Exponential Vivaldi	40×60	9
Corrugated Vivaldi	41.97×72.92	13
Exponential Taper AVA	40×70	10
BAVA	40×80	10

2.5 Conclusions

In this chapter, Vivaldi antennas with different types of taper profiles are designed, such as linear, exponential, elliptical and corrugations for UWB applications. In case of tapered slot antenna, linear and exponential flares have been used. The corrugation in TSA is also introduced for better impedance bandwidth. The reflection coefficient is also measured and compared with simulated results. The exponential and elliptical taper structures are used in unbalanced antipodal Vivaldi antenna. The cross polarization of the unbalanced AVA is

high, which is not suitable for UWB application. So, the balanced antipodal Vivaldi antenna with corrugations is designed and simulated. BAVA is showing very low cross polarization over the entire UWB frequency band. All the designed antennas have improved gain and compact size compared to existing literature.

Chapter-3

Compact UWB Fractal Monopole Antenna and Superstrates

3.1 Introduction

Compact omnidirectional UWB antennas have a tremendous demand in the modern portable system, such as printer, mouse, smart watch, and mobile handset, Bluetooth, WLAN applications. Ultra-wideband (UWB) omnidirectional antenna also finds a place in laptop for wireless communications. In short range communication, the printed monopole antenna is widely used due to the broadband characteristics, light weight, and omnidirectional radiation pattern.

Among omnidirectional antennas, printed monopole antenna is highly suitable for the above applications. The metal rod based classical antennas are used for UWB application. In 1992, Honda et al. designed a circular planar monopole having an 8:1 impedance bandwidth [60]. He investigated on planar monopole with different geometrical shapes, such as the ellipse, rectangle, bow-tie, diamond and trapezoid numerically and experimentally.

Agrawal et al. presented several structures for planar monopole antennas [61] with geometries of circular disc monopole and elliptical disc. These antennas have achieved impedance bandwidth ratio from 2:1 to more than 10:1 with the help of varying the major and minor radii of ellipse. The experimental results provides impedance bandwidth 1.17-12 GHz and 1.21-13 GHz for circular and elliptical monopoles, respectively.

There is no doubt that the planar monopole antenna can provide UWB frequency band. Unfortunately, the size is not suitable for portable wireless systems. The modern antenna has been transformed from simple metal rod to ceramic chip, reconfigurable, active and complicated smart Antenna. Therefore, the 2D or printed monopoles are introduced and designed on the printed circuit board.

J. Liang et al presented an ultra-wideband circular disc shape monopole antenna [62]. The measured return loss bandwidth is from 2.78 to 9.78 GHz while simulated result is from

2.69 to 10.16 GHz. The simulated theta polarization gain in different directions in E plane is verified. The maximum gain is varying from 3.5 to 6.7 dBi at frequencies from 6 to 10 GHz. But the gain is negative within 2.78-5 GHz frequency band.

In 2004, Choi et al. introduced printed monopole antenna with the UWB characteristics [63]. It is constructed by rectangular patch with a single slot on the patch, and a partial ground plane. The antenna is satisfying the UWB frequency band. But the gain is decreasing at high frequencies.

Generally, the printed monopole antenna has a low gain. Many researchers have successfully developed and analyzed dielectric superstrate to increase the directivity of the microstrip antenna. Ehrenspeck et al first conceived the principle of short backfire antennas which are very popular due to the higher directivity [64]. Sugio et al. proposed gain enhancement of multiple-reflection line antenna with dielectric plates [65]. This concept is applied in printed circuit dipole in a grounded substrate by the Jackson and Alexopoulos, to increase gain of antenna [66]. The transmission line analogy and reciprocity theorem are used to derive numerical asymptotic formulas for gain, beamwidth, and bandwidth. Lin et al. first applied the dielectric superstrate concept to the microstrip patch antenna [67]. Unfortunately, the superstrate concept is not applied to the UWB planar antenna which can cover frequency band 3.1 to 10.6 GHz.

In this chapter, compact printed monopole antenna is designed for UWB application. Monopole with step profile, curvature profile, elliptical and concentric ring are designed, simulated and measured for comparison. To achieve a compact size, fractal structure is proposed in CPW-fed monopole antenna for UWB application. A modified dielectric superstrate is also designed to increase the gain of the compact UWB fractal monopole antenna. The fractal parts on the radiating patch reduce the conducting area of the antenna. The current density at the edges of the fractal is increased which is very helpful for improving the antenna radiation. The fractals also play an important role to increase impedance bandwidth..

3.2 UWB monopole antenna

A basic monopole antenna belongs to the radio antennas which is made by a conducting rod and placed perpendicularly on the conductive surface, called ground plane. The feed line

of the connector is connected to the conducting rod and lower end of the connector is connected to the ground plane. The basic monopole antenna and feeding techniques are shown in Figure 3.1. But, a basic monopole is a resonant antenna which can provide a very narrow band. So, it is not suitable for UWB application.

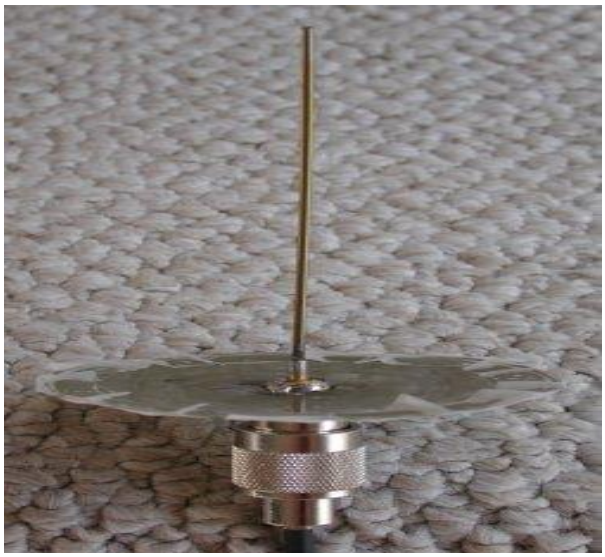

Figure 3.1 basic monopole antenna

Therefore, 3D monopole or Planar Monopole Antenna (PMA) was introduced first by Dubost and Zisler in 1976 [68]. The 3D monopole can able to provide wide impedance bandwidth. Planar monopole is constructed by the metal-plate with different shapes, where the metal-plate is placed perpendicularly on the ground plane and feeding is given by a coaxial probe. The radiation pattern is relatively omnidirectional with low manufacturing cost. The lower frequency limit of the impedance bandwidth is defined by the longest electrical path that the generated currents can travel on the surface of the monopole. The upper limit depends on other factors, such as the shape of the monopole and the separation from the ground plane. Therefore, the PMA can be useful for UWB application. But PMA has large ground plane which has limited its application for compact devices.

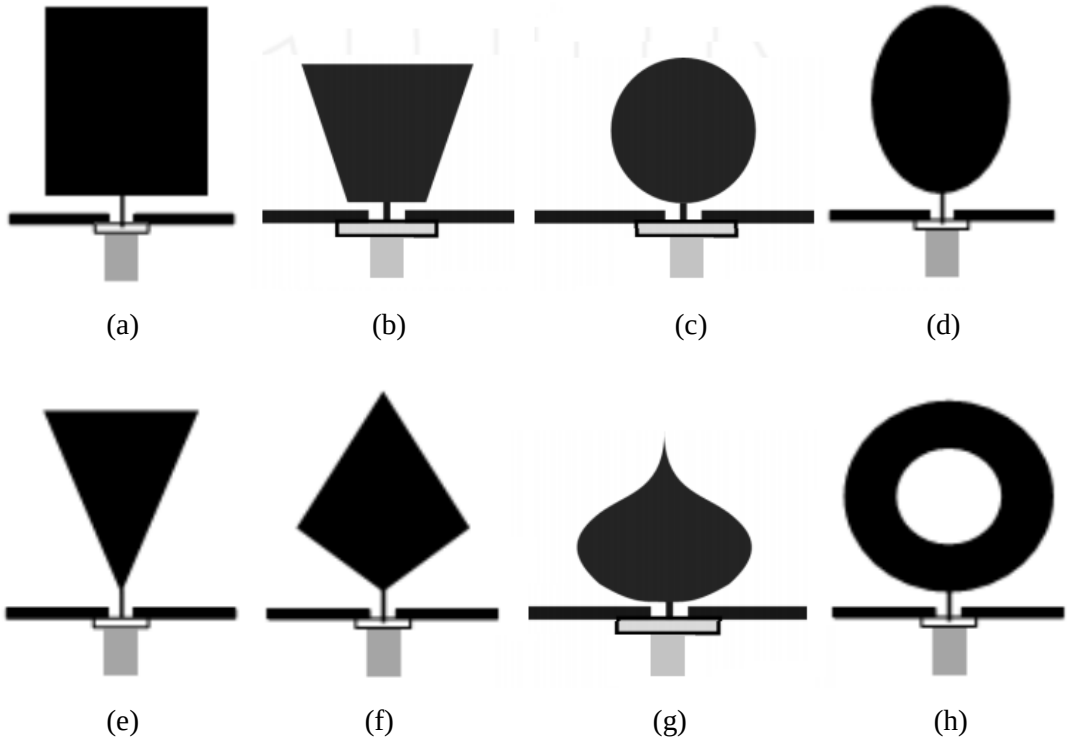

Figure 3.2 Various geometries of planar monopole antennas (a) rectangular (b) trapezoidal (c) circular (d) elliptical (e) triangular (f) polygon (g) planar inverted cone antenna (PICA) (h) circular slot

Now, the limitation can be overcome by printed monopole antenna [69]. It consists of a metal patch on the one side of dielectric substrate and ground plane is located on the opposite side of the the printed circuit board. Generally, microstrip feed line is used to give the excitation of antenna with the same ground plane. The coplanar waveguide feed is used when radiating patch and ground plane are coplanar on the same surface. Different printed monopole antennas are also proposed and studied, such as circular monopole [70], octagon monopole [71], spline-shaped monopole [72], U-shaped monopole [73] and knight's helm shape monopole [74] are shown in Figure 3.3.

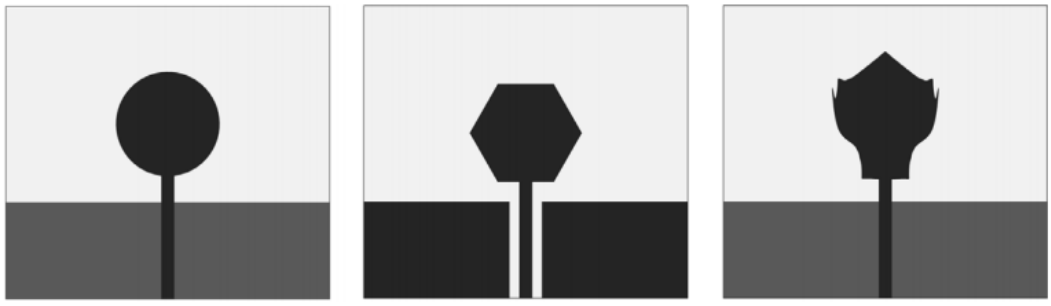

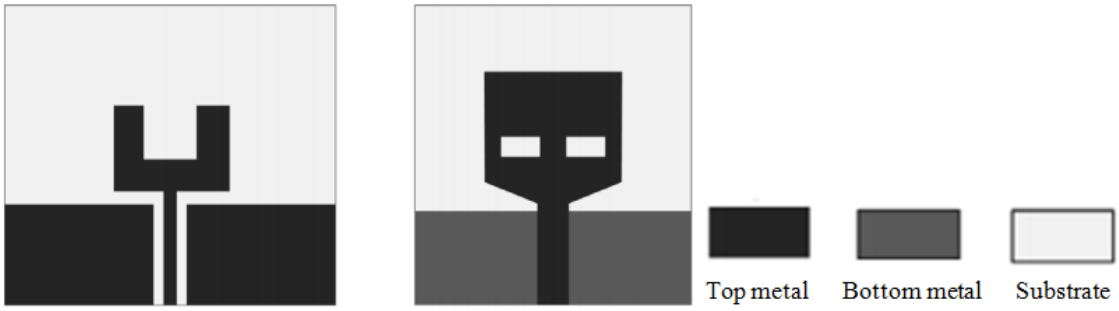

(d) (e)

Figure 3.3 Various monopole structures (a) circular monopole, (b) octagon monopole, (c) spline-shaped monopole, (d) U-shaped monopole, (e)knight's helm shape monopole.

3.3 Design and analysis of monopole antenna

3.3.1 Step profile

3.3.1.1 Design and results

The configuration and dimensions of the stepped gradient profile monopole antenna are shown in Figure 3.4(a). The antenna is printed on Roger RT/Duroid 5880 substrate featuring 1.575 mm thickness, with relative dielectric constant of 2.2. The size of the antenna is obtained as 40×40 mm^2. The CPW feed line is designed by using a rectangular patch to connect to the stepped gradient structure patch of the main radiator. So, the microstrip line is designed with 50 Ω characteristic impedance having 3 mm line width. The microstrip line is printed between two ground planes and is kept at a distance of 0.5 mm on both sides. Both patch and ground plane structures are printed on the same side of the Roger RT/Duroid 5880 substrate.

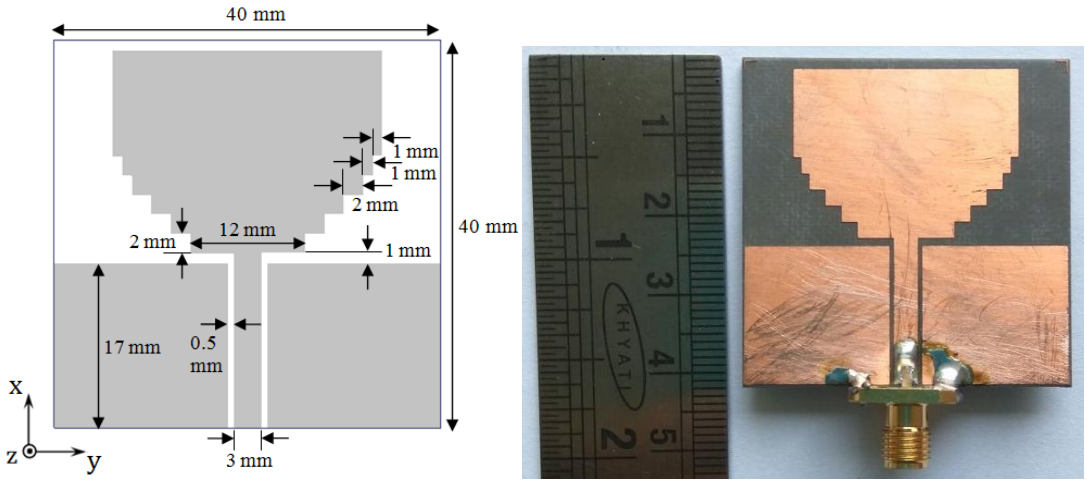

Figure 3.4 (a) Geometry and dimensions of the stepped gradient profile monopole, (b) Fabricated antenna

The fabricated prototype of the proposed antenna is shown is Figure 3.4(b). The simulated and measured reflection coefficients (S_{11}) of the stepped gradient monopole antenna are illustrated in Figure 3.5. It can be noticed that the measured S_{11} is below -10 dB within 3.1-9.5 GHz frequency band.

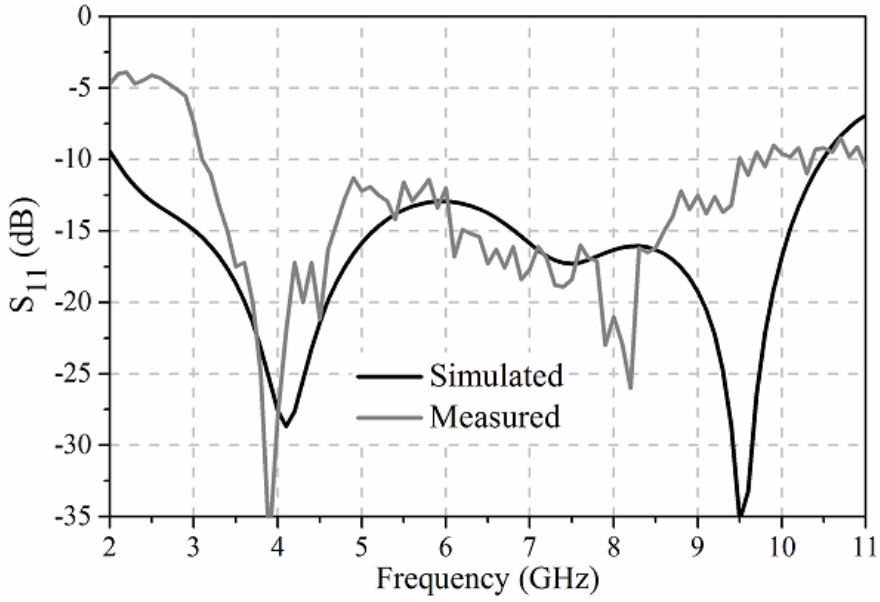

Figure 3.5 Reflection coefficient (S_{11}) of the stepped gradient profile monopole antenna

3.3.2 Elliptical profile

3.3.2.1 Design and results

The geometry of the elliptical patch based printed monopole antenna is shown in Figure 3.6. Here, the radiating patch is designed with overlapping two different dimensions of elliptical disc, namely elliptic 1 and elliptic 2. The antenna is printed on the roger RT/duroid 5880 substrate with dielectric constant 2.2 and thickness, h=0.787 mm. The excitation of the antenna is given by using 50 Ω microstrip line feed with line width W_f = 2.4 mm and bottom layer consists of the partial metallic layer. The impedance matching of feedline depends on the curvature of the elliptic 1. The maximum bandwidth can be implemented by varying elliptical parameter a1, b1.

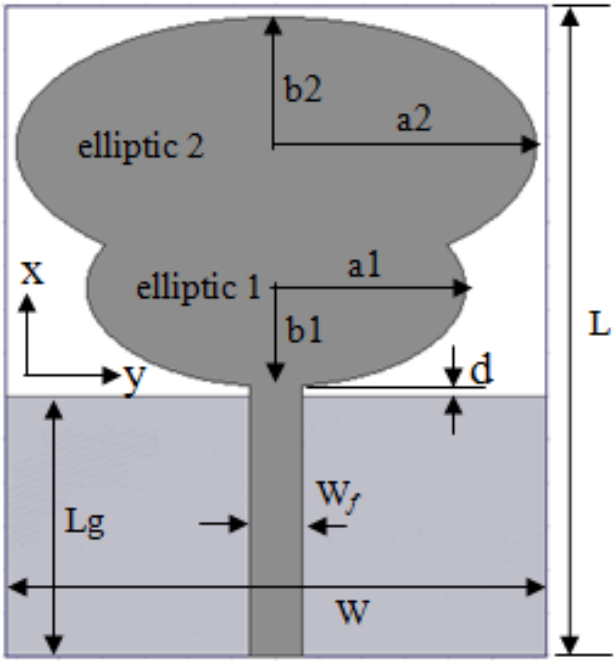

Figure 3.6 Geometrical structure of the elliptical profile monopole

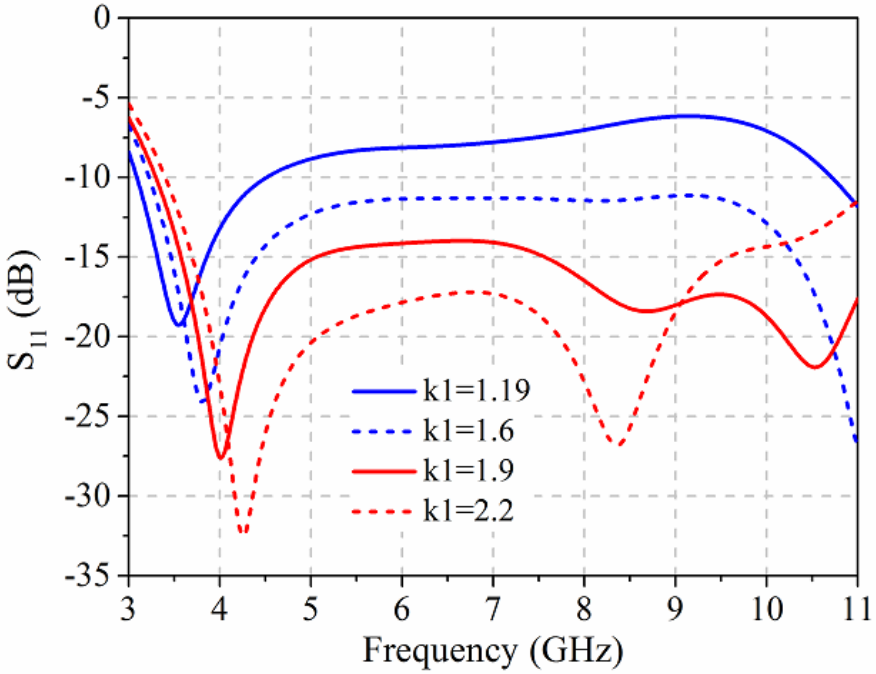

(a)

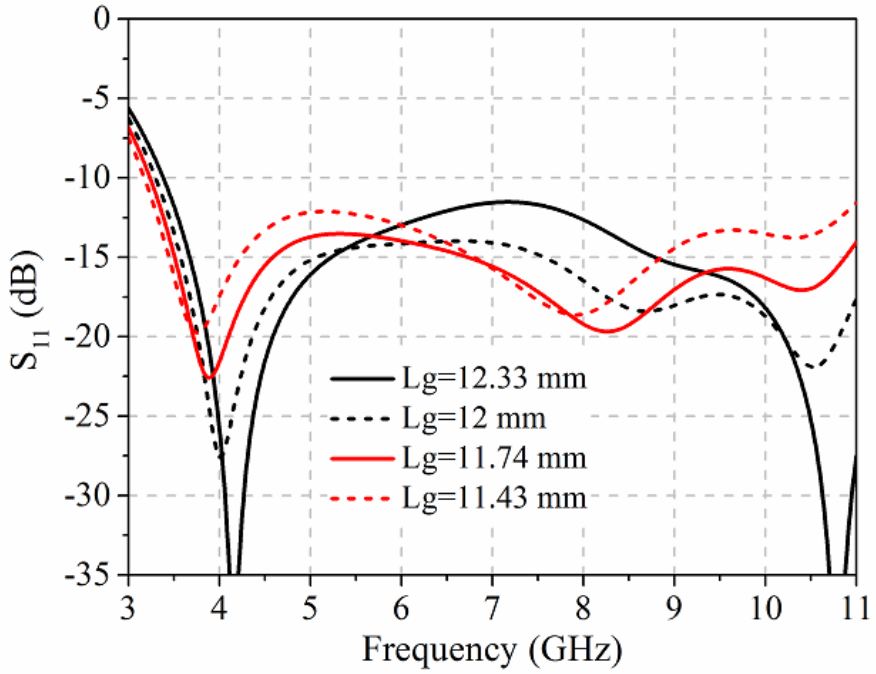

(b)

Figure 3.7 The reflection coefficient (S_{11}) variation of the elliptical monopole antenna with (a) different values of k1, and (b) different values of Lg.

To understand the effects of the parameters on the impedance bandwidth, the parametric analysis of the antenna has been done by simulating a three-dimensional electromagnetic

(EM) simulator CST microwave studio 2016. To satisfy the UWB frequency range, the lowest frequency, f_L and impedance bandwidth of the designed antenna with S_{11}<–10 dB is determined by the ellipticity ratios (a1/b1) k1 [61]. The variation of the S_{11} level and f_L with respect to the k1 is illustrated in Figure 3.7(a). So, it is clear that the fL is reduced with decreasing the value of k1. But the S_{11} is increasing and fluctuating near to -10 dB. At k1=1.9, the value of f_L is 3.3 GHz and fluctuating at S_{11}= –15 dB covering the whole UWB frequency band. The dimensions and simulated reflection coefficient bandwidths for all these cases are summarized in Table 3.1.

Table 3.1 Reflection coefficient (S_{11}) bandwidth of the elliptical monopole

a1 (mm)	**b1 (mm)**	**Frequency range for S_{11}< –10 dB (GHz)**	**Bandwidth ratio**
5.5	4.6	3-4.5	1:1.5
7.5	4.6	3.23-11	1:3.4
8.74	4.6	3.3-11	1:3.3
10.12	4.6	3.4-11	1:3.2
5.5	4.6	3-4.5	1:1.5
7.5	4.6	3.23-11	1:3.4

The reflection coefficient of the antenna is a function of the current distribution on the partial metallic ground plane. The variation of S_{11} for the length Lg is shown in Figure 3.7(b). At Lg=12 mm, the reflection coefficient is showing less than or equal to –15 dB and the value of f_L remains same. The optimized dimensions of the elliptical monopole are shown in Table 3.2.

Table 3.2 Optimal parameters of the elliptical monopole

Parameter	**Value (mm)**	**Parameter**	**Value (mm)**
L	30	W_f	2.4
W	25	d	0.4
Lg	12	h	0.787
L	30	W_f	2.4

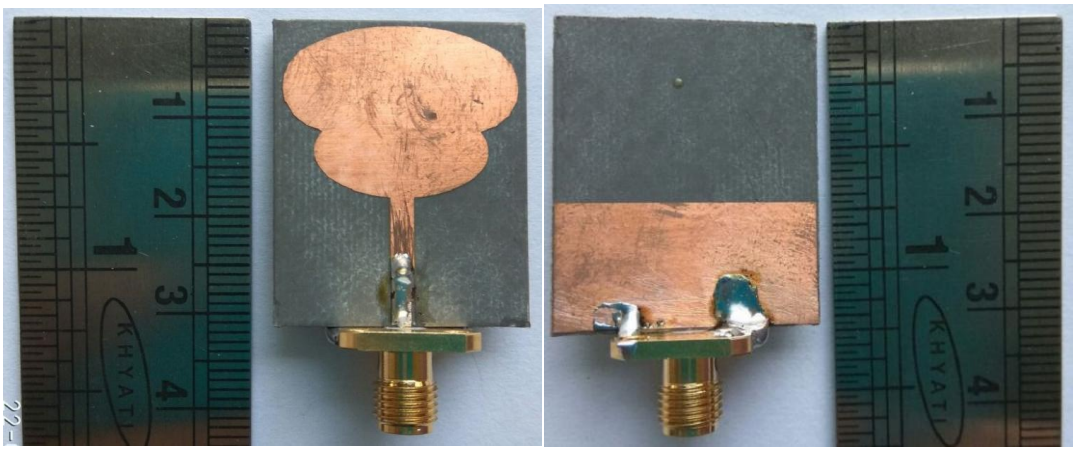

(a) (b)

Figure 3.8 The fabricated prototype of the antenna, (a) Radiating patch, and (b) Ground plane

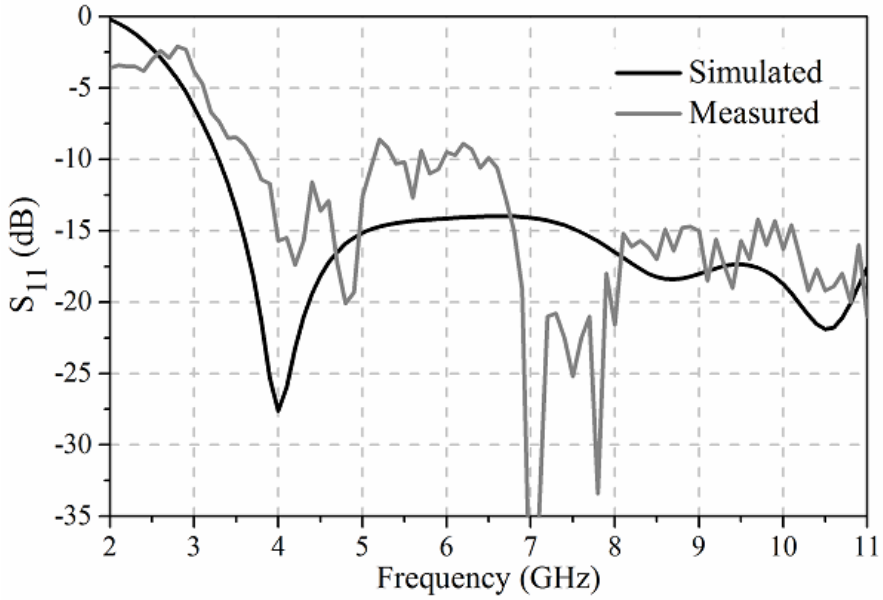

Figure 3.9 Reflection coefficient (S_{11}) of the elliptical profile monopole antenna

The fabricated prototype of the elliptical monopole antenna is shown in Figure 3.8. The simulated and measured reflection coefficient results are plotted and compared in the Figure 3.9. From the simulation result, it can be seen that the S_{11} is varying at -15 dB over the UWB frequency band. While the measurement result is indicating that the reflection coefficient is less than -10 dB at 3.7-5.1 GHz and 6.5 -11 GHz. The variation in S_{11} result can be explained by the overlapping area between two ellipses.

3.3.3 Concentric ring patch

3.3.3.1 Design and results

The printed planar monopole antennas are very popular and are used in compact wireless communication devices. In order to make compact monopole, the topology of the antenna is changed to consist of a impedance transition microstrip line feed and a concentric ring shape radiating patch with the partial metallic ground plane. It is implemented using Rogers RT/duroid 5880 material board which has relative permittivity 2.2 and height 0.787 mm. The geometrical views of the presented antennas are shown in Figure 3.10. The overall size of antenna is 16×12 mm^2. To improve impedance matching, it is necessary for the impedance transition from 50 Ω input to 100 Ω feeding microstrip line.

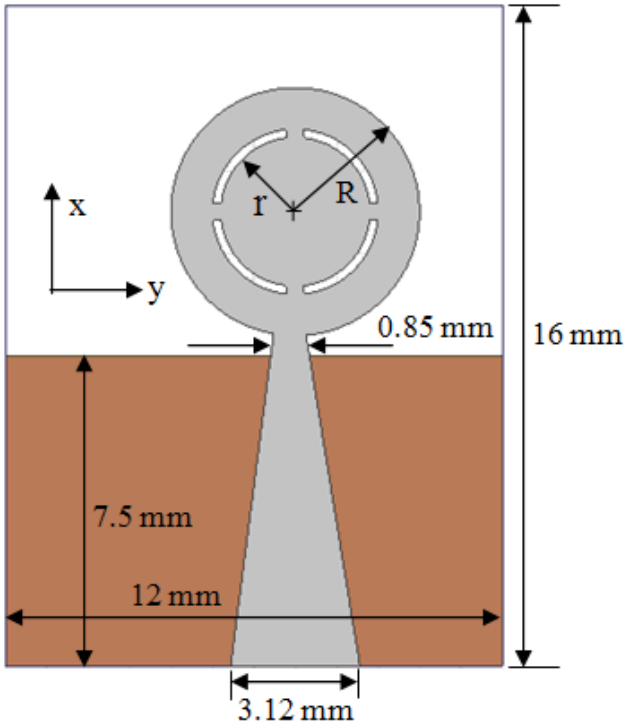

Figure 3.10 Geometrical structure of the concentric ring monopole

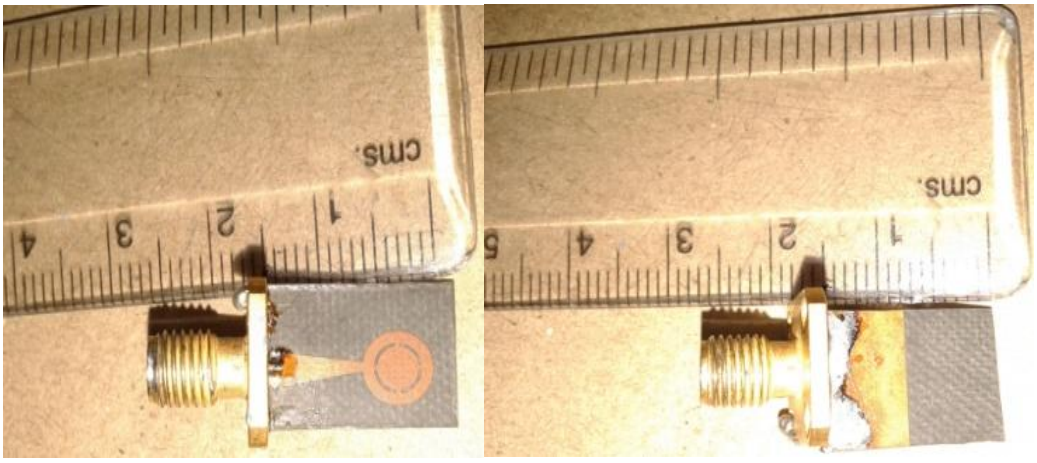

(a) (b)

Figure 3.11 The fabricated antenna picture, (a) Radiating patch, and (b) Ground plane

The simulation of the proposed antenna and optimization is done by using the high frequency structure simulator (HFSS) version 15. The measured and simulated return loss (S_{11}) of the presented antenna are shown in Figure 3.12. The simulated return loss exhibits a wideband performance from 6.5 GHz to beyond 13 GHz for $S_{11}< -10$ dB. The return loss of the antenna is measured from 3 to 13 GHz and it is below -10 dB from the frequency band 6.2-10.2 GHz.

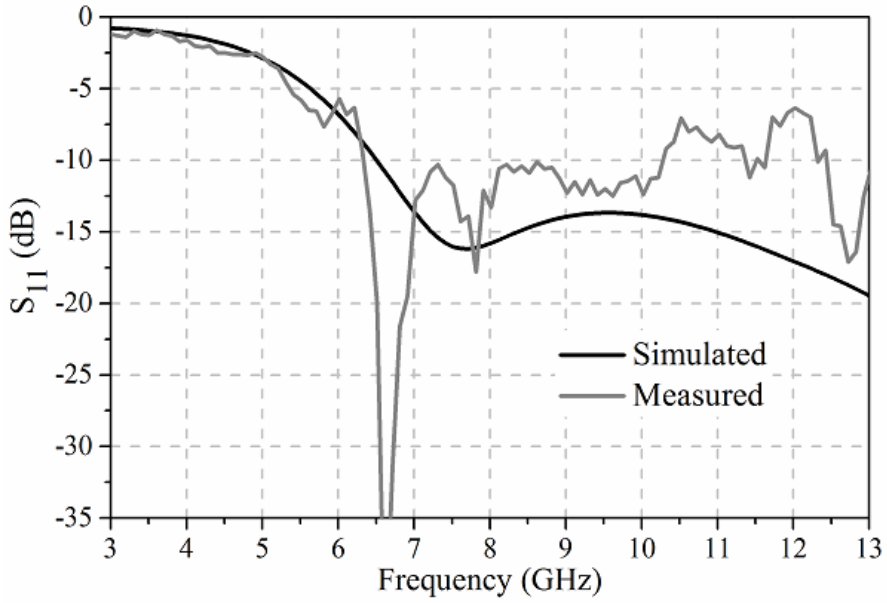

Figure 3.12 Return loss (S_{11}) of the concentric ring monopole antenna

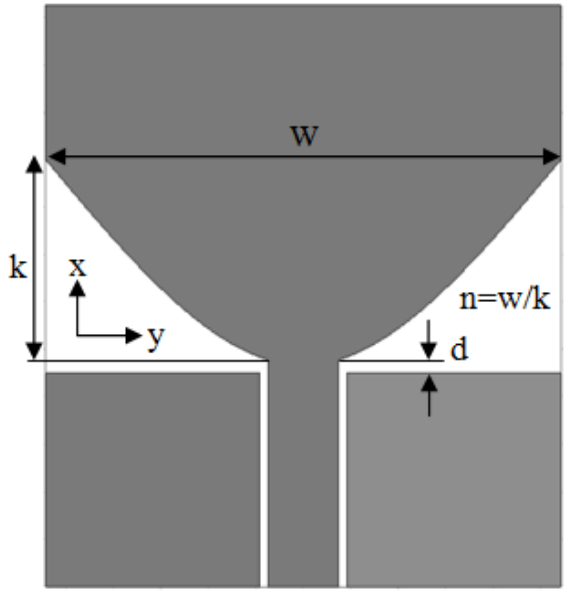

Figure 3.13 Structure of the curvature profile or conventional monopole antenna.

3.3.4 Curvature profile

3.3.4.1 Design and results

A compact printed monopole antenna with CPW feed is selected for ultra-wideband frequency band from 3.1 to 10.6 GHz. The design structure of the conventional monopole antenna is shown in Figure 3.13. It is designed on roger RT/duroid 5880 substrate with dielectric constant (ε_r) 2.2, loss tangent (tanδ) 0.0019 and substrate thickness (h) of 1.575 mm. The designed antenna has 50 Ω CPW transmission line fed with the line width of 3 mm and the symmetric line spacing between the ground plane and transmission line as 0.35 mm.

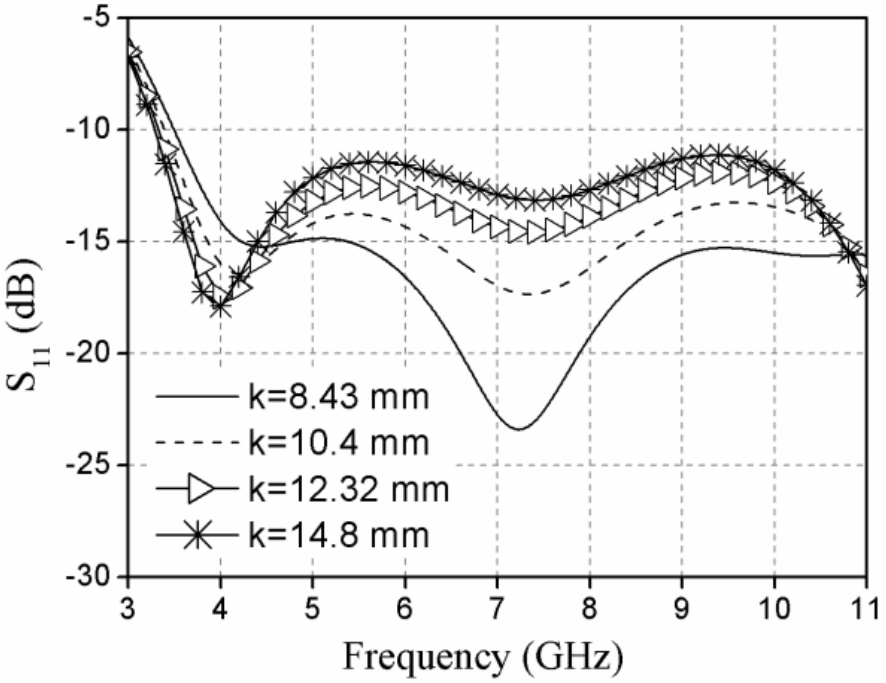
-5
-10
-15
-20
-25
-30
3
4
5
6
7
8
9
10
11
S11 (dB)
Frequency (GHz)
k=8.43 mm
k=10.4 mm
k=12.32 mm
k=14.8 mm

(a)

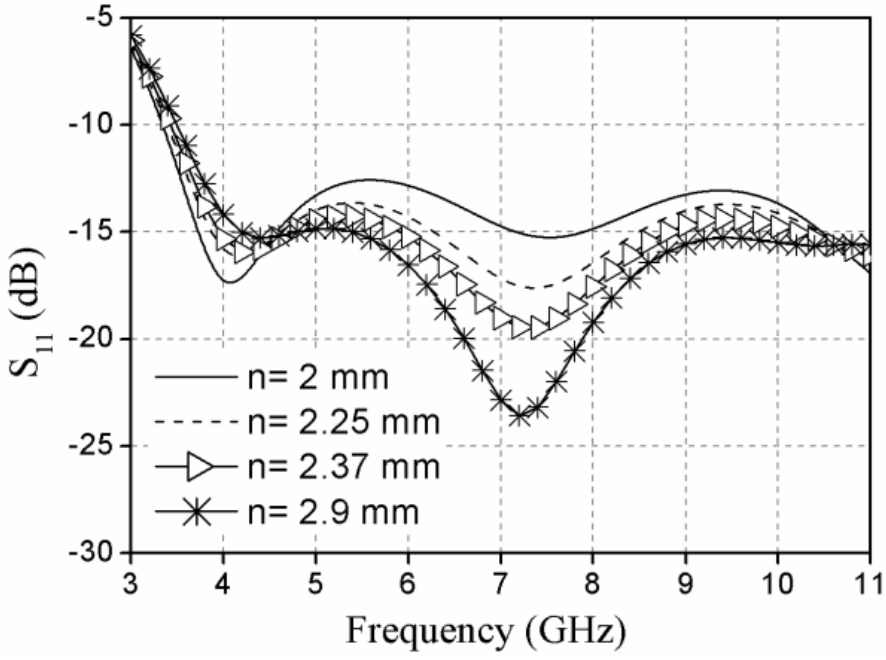
-5
-10
-15
-20
-25
-30
3
4
5
6
7
8
9
10
11
S11 (dB)
Frequency (GHz)
n= 2 mm
n= 2.25 mm
n= 2.37 mm
n= 2.9 mm

(b)

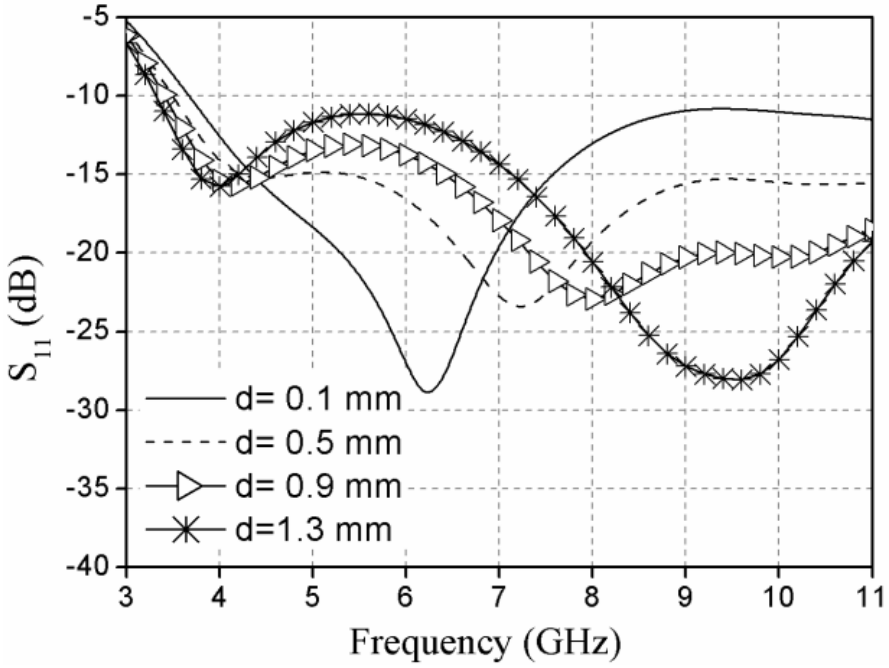

(c)

Figure 3.14 The reflection coefficient (S_{11}) for the conventional monopole antenna design, (a) with different value of *k*, (b) with different value of *n*, (c) with different value of *d*.

In this design, the lowest frequency (f_L) of the antenna depends on the curvature of the radiating patch. This curvature is adjusted by the length, *k*. To satisfy the impedance bandwidth in UWB frequency range, the ratio *n* (*n*=*w*/*k*, where *w* is the width of the antenna) must vary and the ratio is selected for better impedance matching. Moreover, the reflection coefficient can be slightly adjusted by the parameter, *d*, where *d* is the distance between the upper edge of the ground plane and the bottom of the radiating patch. To understand the effects of the parameters on the impedance bandwidth of the conventional antenna, a three-dimensional electromagnetic (EM) simulator Ansys HFSS 15 is used. The changes of the length *k* will affect f_L, as shown in Figure 3.14(a). The frequency, f_L is shifted towards the lower frequency side, when *k* is increased. The simulated value of f_L is 3.3 GHz, when the *k* is fixed at 10.4 mm. In case of parameter *n*, the simulated impedance bandwidth is covering the UWB frequency range when the value of *n* is 2 and 2.25, as shown in Figure 3.14(b). The distance, *d* has also effected the reflection coefficient of the antenna. The larger values of *d* are showing a good impedance match, as illustrated in Figure 3.14(c).

Figure 3.15 The fabricated curvature profile monopole antenna

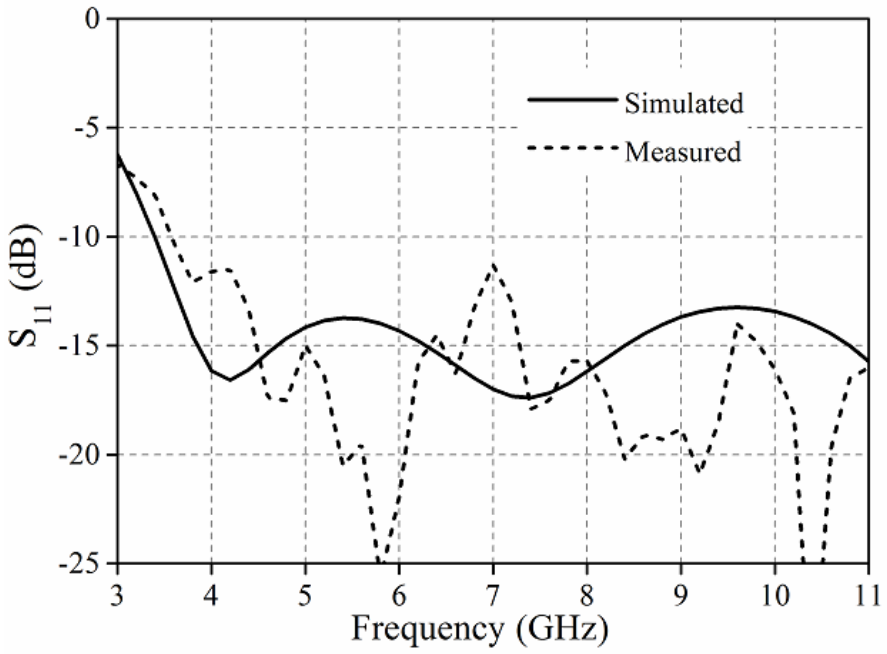

Figure 3.16 Reflection coefficient (S_{11}) of the optimised conventional monopole or curvature profile monopole antenna

The photo of the fabricated curvature profile monopole is illustrated in Figure 3.15. The reflection coefficient is measured in vector network analyzer and compared with simulated results in the plotted graph, as shown is Figure 3.16. The S_{11} result is indicating that the impedance is matched, and the simulation and the measurement data are almost identical

except at the lowest frequency, f_L. The measurement result shows that the lowest resonant frequency is 3.6 GHz.

3.4 Design of fractal monopole

Among the above monopoles, it can be seen that the performance of the curvature profile monopole is better and compact than other monopoles. In order to obtain the complete FCC UWB frequency band, the fractal concept is applied in the radiating patch of the conventional monopole antenna.

3.4.1 Analysis and design procedure of fractal

To design fractal structure, the trapezoidal shaped slot has been created at the radiating patch of the antenna, name as antenna1, as shown in Figure 3.17(a). In the trapezoidal slot, a metallic triangle has been designed and sierpinski fractal is applied at that triangle, named as antenna2 and antenna3 in Figures 3.17(a) and (b), respectively.

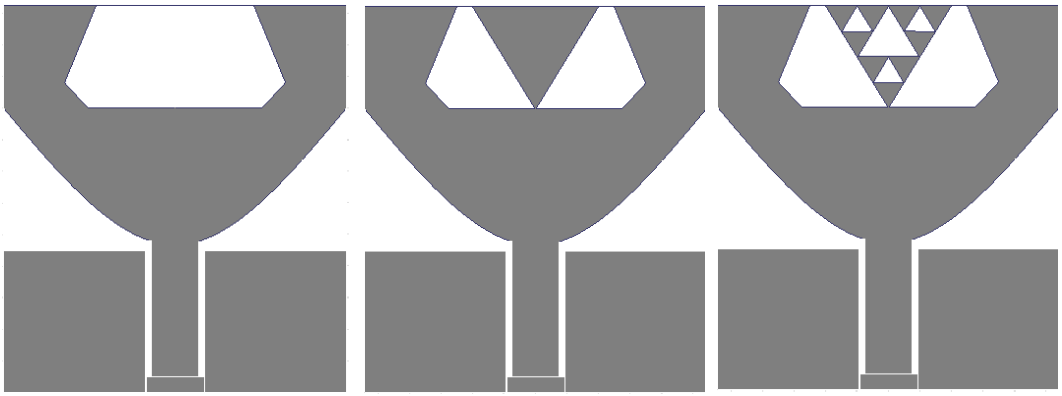

(a) (b) (c)

Figure 3.17 Modified antenna structures with fractal, (a) antenna1, (b) antenna2, and (c) antenna3.

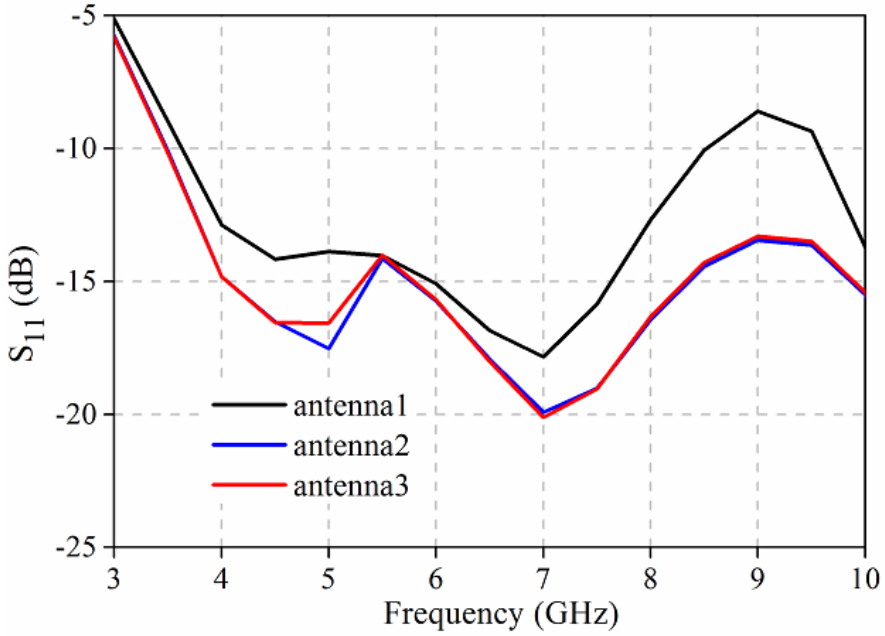

(a)

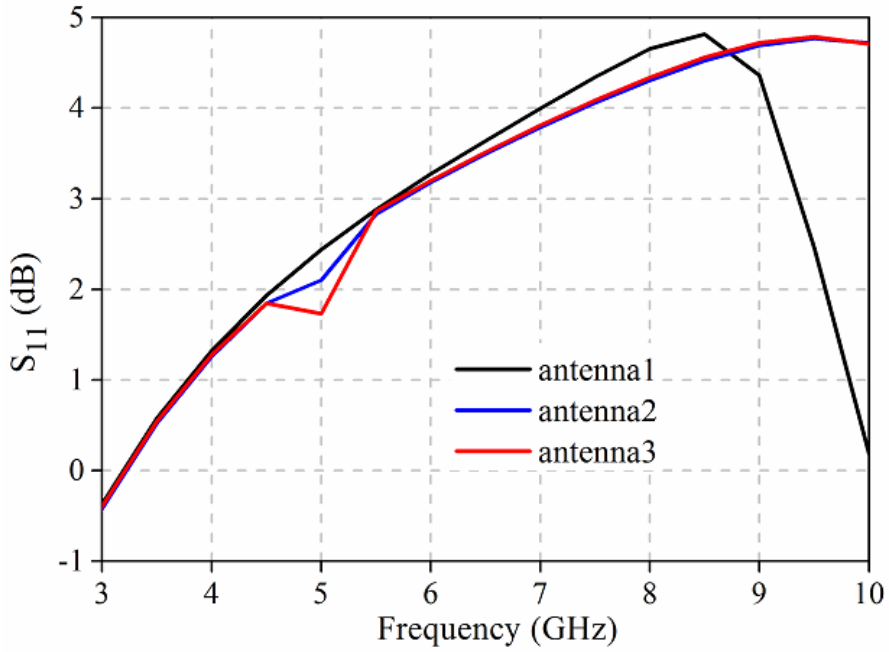

(b)

Figure 3.18 Simulation result of antenna1, antenna2 and antenna3, (a) Reflection coefficient (S_{11}), and (b) gain characteristics

The reflection coefficient (S_{11}) and gain characteristics for antenna1, antenna2 and antenna3 are plotted in Figure 3.18. Compared to antenna2 and antenna3, the S_{11} of the antenna1 is not below -10 dB at the entire operating frequency band. By using metallic

triangle and sierpinski fractal, the reflection coefficient has become more downward at the lowest and highest frequencies. Still, the lowest frequency is not shifted to 3.1 GHz. The gain of the antenna1 is also negative at high frequencies. Therefore, a novel fractal geometry has been proposed with an identical small triangle structure which is described below.

A step by step fractal design procedure is depicted in Figure 3.19. In step 1, the hexagonal structure is shown with different side lengths. It is made by connecting *n* number of points, where *n* varies from 1 to 6. Step 2 shows the triangle a_{12}-a_5-a_4 designed by connecting the points of a_5, a_4 and a_{12}, where a_{12} is the middle point of a_1 and a_2. This triangle is an equilateral triangle with side length, *l*. Now each side of the triangle is divided into three equal sides (*l*/3) as shown in step 3 and the black color is a small equilateral triangle with each side dimension *l*/3. In final step 4, middle points of a_1, a_6 and a_2, a_3 are a_{16} and a_{23}, respectively. They are connected to two points which are shown in step 3. So, the fractal is designed using small equilateral triangles with side length, $t=l/3=2.8$ mm and triangles are separated by $W_1=2.7$ mm. The final optimized dimensions of the designed antenna are shown in Figure 3.20(a).

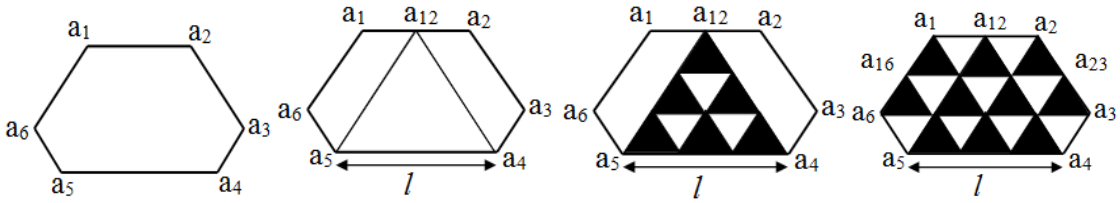

Figure 3.19 Fractal design steps for proposed antenna

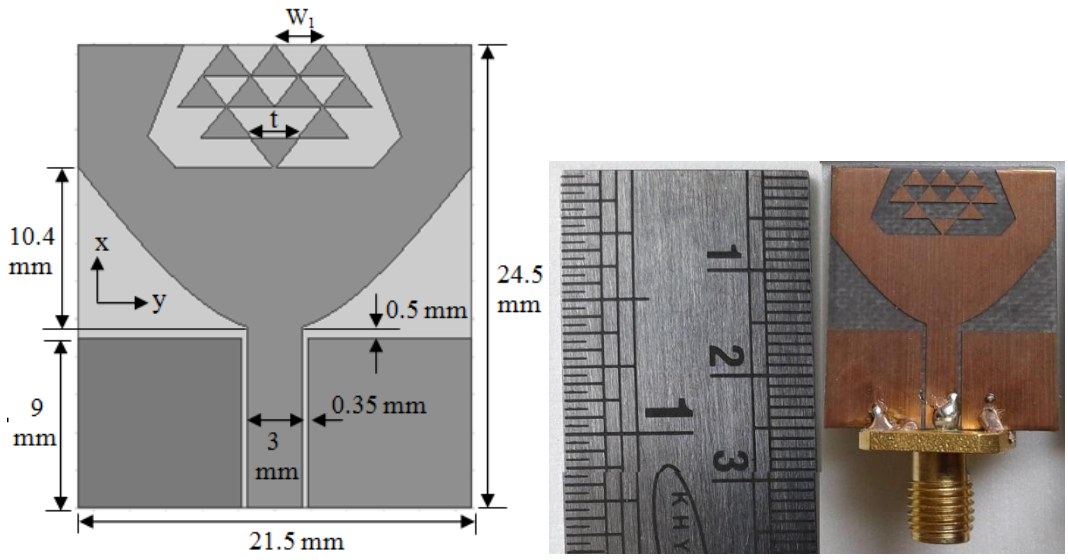

(a) (b)

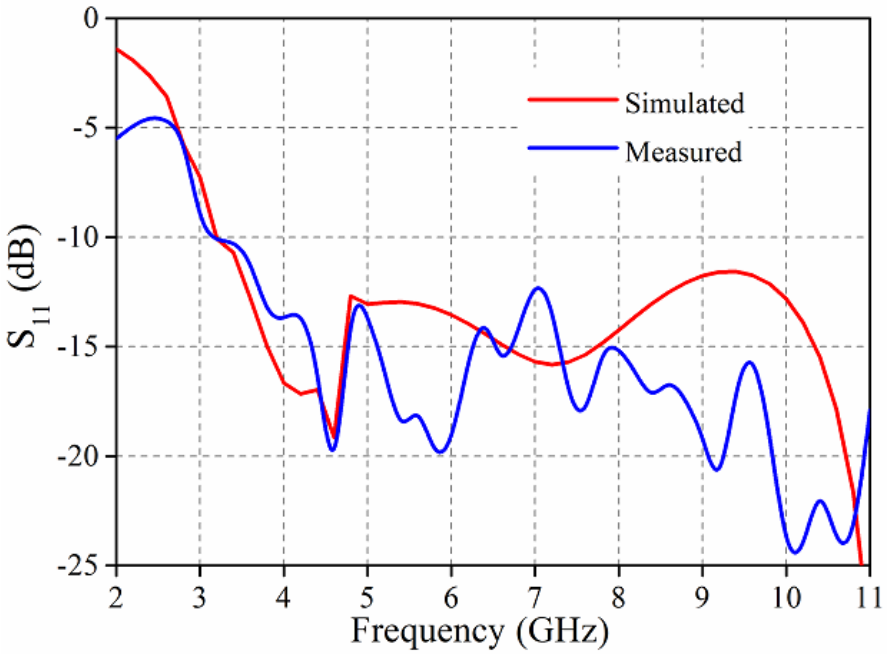

(c)

Figure 3.20 (a) Top view of the optimised fractal antenna (b) Fabricated prototype, (c) Reflection coefficient (S_{11}) optimised fractal antenna.

The optimized fractal monopole is fabricated and is shown in Figure 3.20(b). The simulated and measured S_{11} values for various frequencies are plotted on the same graph and compared, as shown in Figure 3.20(c). From the result, it is clear that both S_{11} results are almost identical and below –10 dB over the FCC based UWB frequency band. So, the bandwidth is increased by etching fractal on the radiating patch and the value of f_L is 3.1 GHz.

In this work, a compact fractal CPW-fed monopole antenna is introduced for UWB application with superstrate layer. The fractal parts of the radiating patch reduce the conducting area of the antenna and the current density at the edges of the fractal is increased which is very helpful for improving the antenna radiation. The fractals also play an important role to increase impedance bandwidth. The proposed antenna has a compact size compared to the other existing works.

3.5 Fractal Monopole with dielectric superstrate

3.5.1 Design procedure

The roger RT/duroid 5880 (height, h=1.575 mm) is used as a dielectric superstrate which consists of a rectangular shaped copper with dimension as L=10 mm and W=21.5 mm. The top and side views of superstrate loaded fractal monopole antenna are shown in Figure 3.21(a). The performance of the antenna is optimized when the dielectric properties of the antenna and superstrate are same, because the direction of internal fringing fields can reflect or refract for the higher or lower dielectric properties in superstrate. According to the electromagnetic field theory, the fringing fields of the fractal antenna will be enhanced along the radiation direction of z-axis using proposed superstrate because the conductor of the superstrate is connected through the ground plane of the antenna. The fringing fields between the superstrate conductor and radiating patch are shown in Figure 3.21(b). Hence, the performance of the antenna is improved.

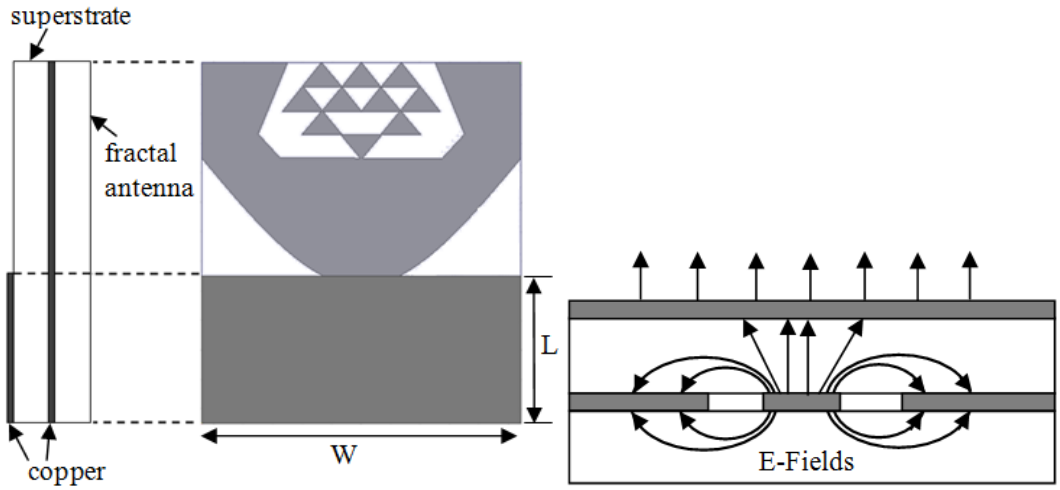

Figure 3.21 (a) Top and side view of the superstrate loaded fractal antenna, (b) electric fields distribution between fractal antenna and superstrate

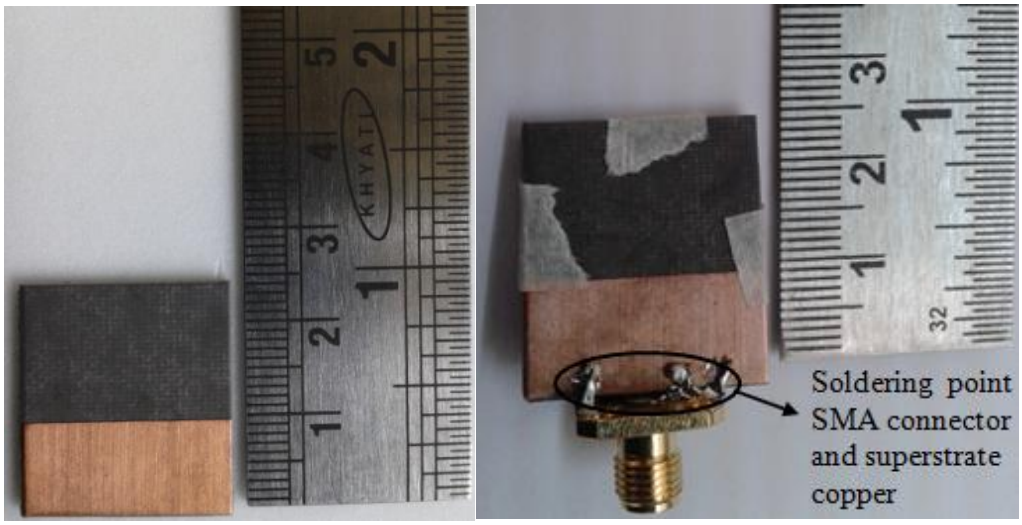

(a) (b)

Figure 3.22 Photograph of the fabricated antennas (a) Top view of dielectric superstrate with rectangular copper, (b) Superstrate on the fractal antenna. Also shown a soldering between ground and superstrate conductor.

Table 3.3 Size comparison between proposed antenna and existed work

Reference	**Size (mm^2)**
[35]	62×62
[76]	100×100
[77]	59.5×59.5
[78]	380×280
Proposed antenna	24.5×21.5

3.5.2 Experimental Results and Discussions

The prototype of conventional, fractal and superstrate loaded fractal antennas are fabricated and shown in Figure 3.22. The size of the proposed antenna is compared with some existing works which are listed in Table 3.3. The proposed antenna has compact size and reduced by 30%. The variation of the measured reflection coefficient (S_{11}) of the three antennas are shown in Figure 3.23. It is indicated that the lowest frequency (f_L) for the fractal monopole antenna is 3.1 GHz and does not change using superstrate. Practically some air gap may be present between the antenna and superstrate which could cause deviation in the performance.

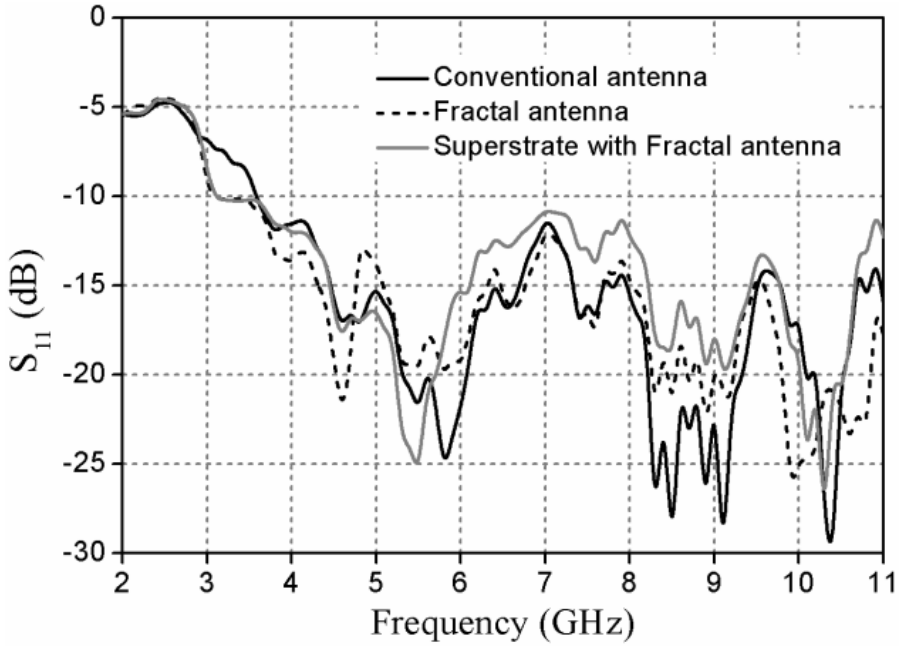

Figure 3.23 Measured reflection coefficient (S_{11}) of the antennas.

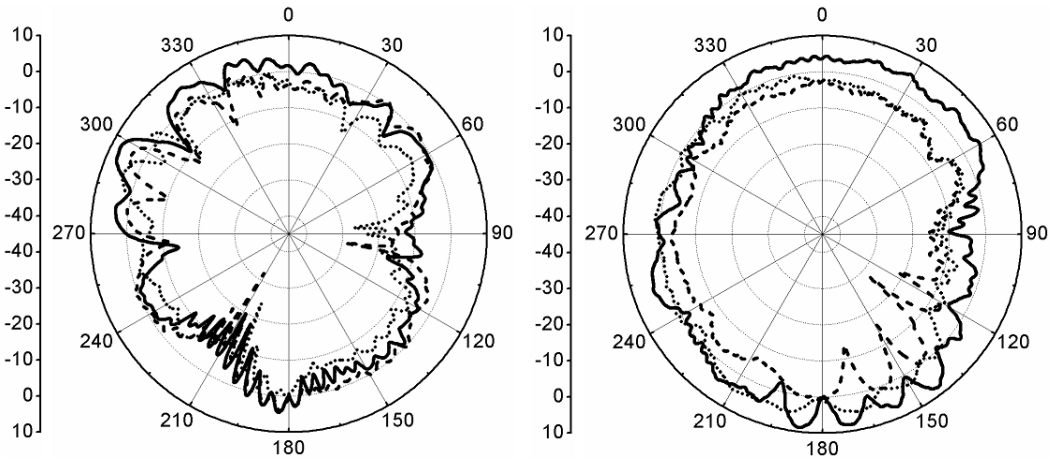

E-plane H-plane

(a)

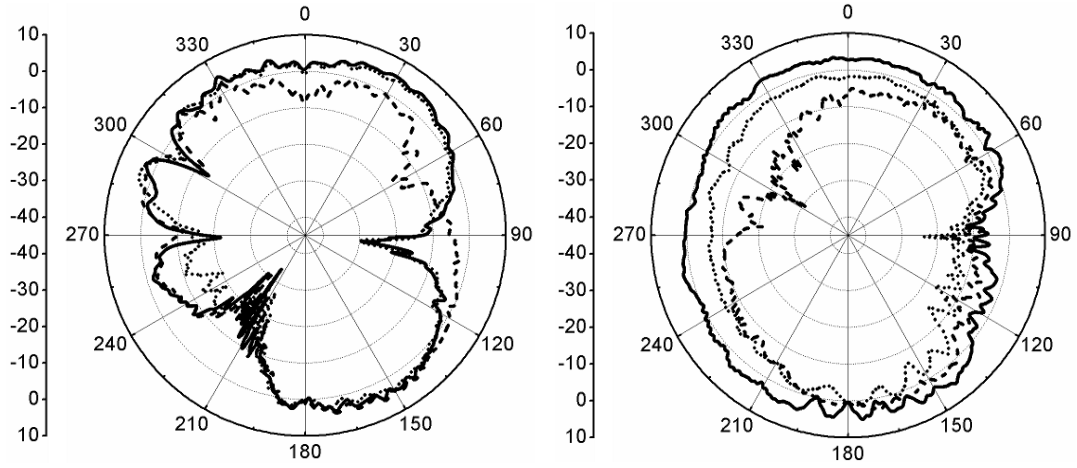

(b)

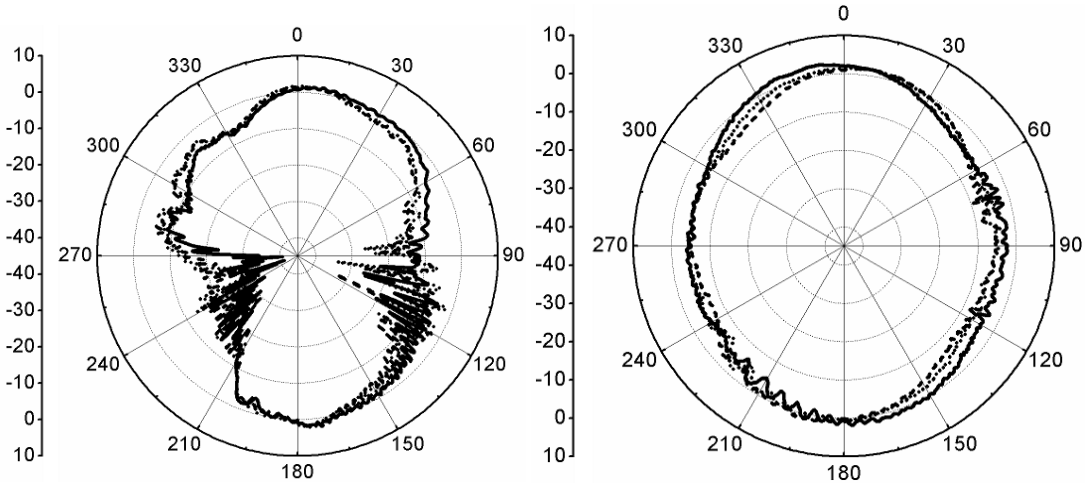

(c)

Conventional antenna
Fractal Antenna
Superstrae loaded antenna

Figure 3.24 Measured E-plane and H-plane radiation patterns at (a) 4 GHz, (b) 6 GHz, (c) 10 GHz.

The measured E-plane (x-z plane) and H-plane (y-z plane) radiation patterns of the antennas are compared at 4 GHz, 6 GHz and 10 GHz as shown in Figure 3.24. It is observed that the radiation pattern is improved by using superstrate over fractal monopole antenna. The antenna exhibits almost omnidirectional radiation patterns over the entire operating bandwidth.

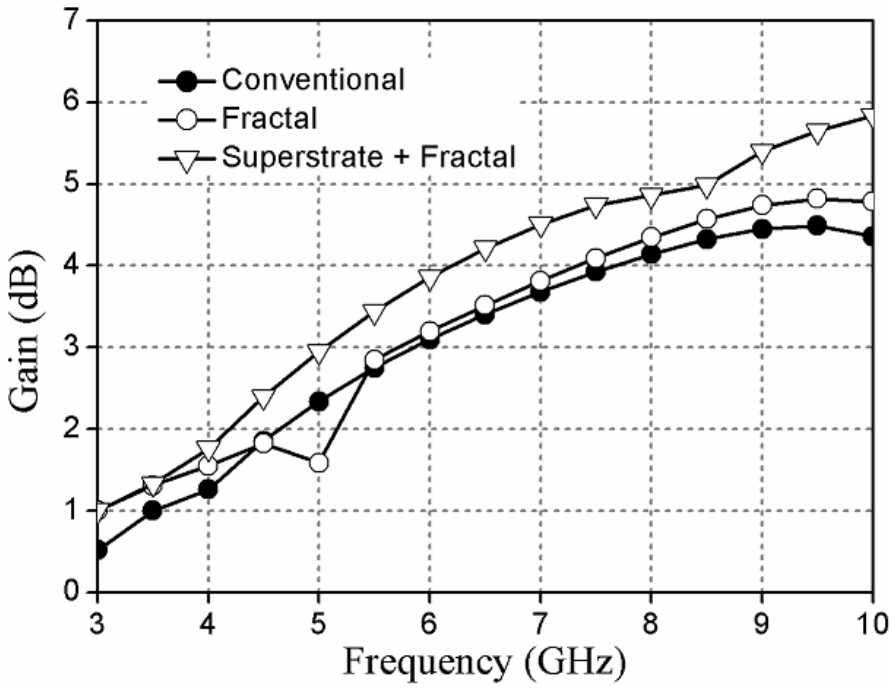

Figure 3.25 Measured gain variation of the conventional, fractal and superstrate loaded fractal monopole antenna.

The measured gain of the conventional, fractal and superstrate loaded fractal antennas are indicated in Figure 3.25. After incorporating superstrate into the fractal antenna, the peak gain of the conventional monopole antenna is increased by 1.6 dB at 10 GHz. The maximum gain is 6 dB at 10 GHz and varying from 1–6 dB over the frequency band of 3−10 GHz.

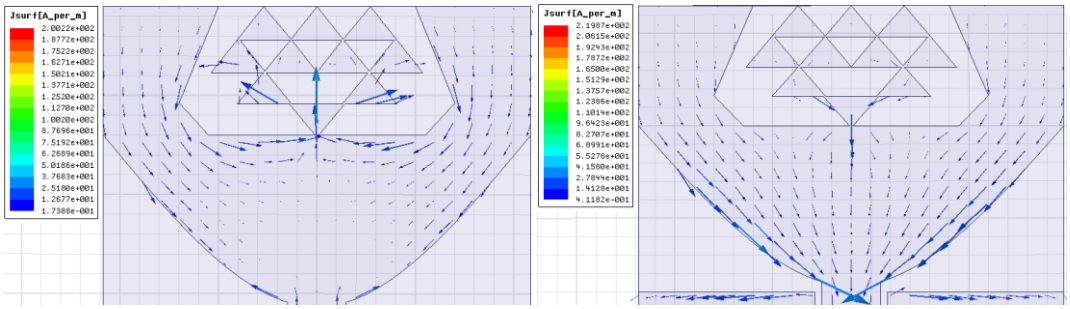

(a) (b)

Figure 3.26 Simulated surface current distributions on the fractal structure of the proposed antenna (a) 5 GHz, (b) 7 GHz.

To further investigate the performance of the antenna, the simulated current distribution in the fractal structure is shown in Figure 3.26. The current is entering from the small triangular part and is distributed on the fractal structure to come outside of the fractal

structure. The current density is changing rapidly at the lower curved part of the radiating patch for different frequencies. So, the fractal is helping to increase impedance bandwidth and radiation of EM wave of the antenna. The electric fields (fringing fields) of the proposed antenna at the frequency of 5 GHz, 7 GHz and 9 GHz are illustrated in Figure 3.27. The cross section view of the antenna shows that the fringing (electric) fields are concentrated with the help of superstrate conductor current. At 5 GHz and 7 GHz, the electric fields are distributed all over the width of the superstrate conductor. But the fringing field density is more in the middle of the conductor at 9 GHz. Therefore, the radiation pattern and gain are improved for the fractal antenna with superstrate conductor.

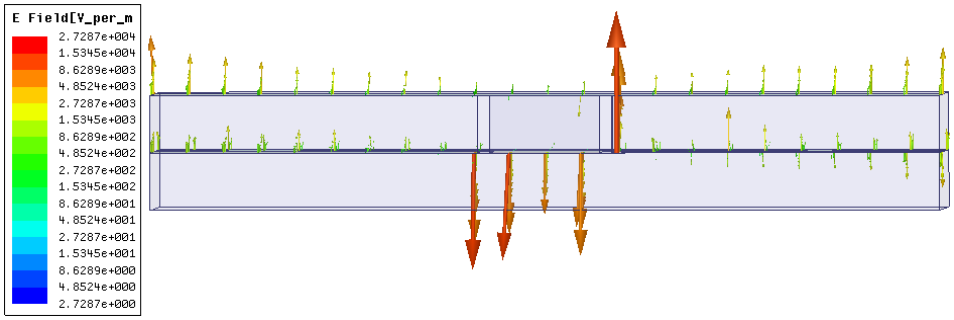

(a)

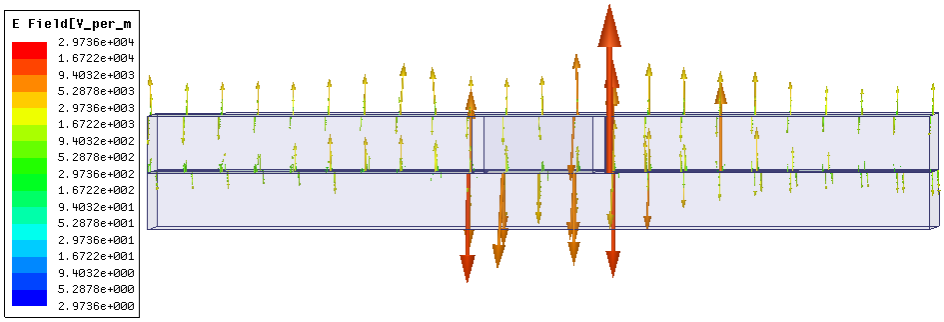

(b)

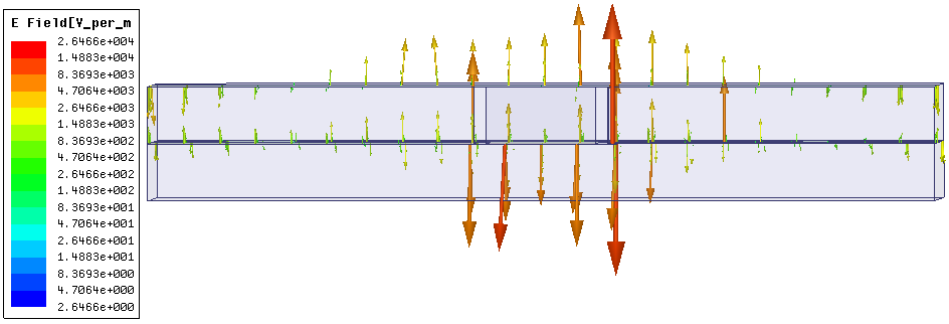

(c)

Figure 3.27 Fringing fields (Electric fields) of the superstrate loaded fractal antenna (a) 5 GHz, (b) 7 GHz, (c) 9 GHz.

3.6 Conclusion

A compact fractal monopole antenna is designed for ultra-wideband application. The monopoles with different profiles are also designed and results are discussed. The radiation pattern exhibits omnidirectional over the entire UWB frequency range (3.1 to 10.6 GHz). The maximum gain of the conventional monopole is increased up to 5.8 dB at 10 GHz with superstrate layer. So, the proposed antenna can be used for UWB communications.

Chapter-4

Gain enhancement of UWB Antenna using Metamaterial

4.1. Introduction

For UWB applications, like electromagnetic warfare (EW) and WLAN etc, new design techniques are developed to implement antennas with different properties. In modern wireless communication systems, the UWB antenna should fit in complex devices and provide a high directivity for longer distance with higher data rates, which means that antenna needs to have high gain, and broader bandwidth. Novel structures or materials that are able to direct or influence the direction and properties of EM wave at microwave and optical frequencies are developed, called as metamaterials.

In the 19th century, Jagadish Chandra Bose has investigated and researched on metamaterial substances. Karl Ferdinand Lindman noticed wave interaction with metallic helices as artificial chiral media. Negative-index materials were first described theoretically by Victor Veselago in 1967 [79]. Winston E. Kock developed a new material which has similar characteristics to metamaterials. Later, the characteristics of artificial dielectrics have been studied by many researchers for lightweight microwave antennas. Metamaterial is also investigated and designed as a microwave radar absorbers in the 1980s and 1990s. In 1999, Pendry demonstrated a split ring resonator based metamaterial [80]. In the year 2000, D. R. Smith et.al. demonstrated a metamaterial experimentally [81]. It is based on a periodic array of interspaced conducting nonmagnetic split ring resonators and continuous wires, that exhibit a frequency region in the microwave regime with simultaneously negative values of effective permittivity and permeability.

In the last decade, several techniques are adopted using metamaterial to enhance the gain of the antenna. D. Li et al proposed and designed a metamaterial unit cell with a low refractive index, which is used as a superstrate to enhance the gain of the antenna [35]. A three layer planar metamaterial structure is placed on the patch antenna. Both simulation and

measurement results show that the broadside gain of the original patch antenna is increased using metamaterial superstrate.

S. Wu et al presented a zero index metamaterial structure for the gain improvement of the tapered slot antenna [83]. The ZIM cell is designed by resonant metal structure and inductor component. By changing the value of inductance, the zero point of permittivity tensor of the ZIM will shift correspondingly. The simulated gain of the ZIM cells loaded TSA is enhanced by 0.9-2.48 dB over the frequency range of 0.575-0.590 GHz. The designed metamaterial structures are dispersive with large material losses and operates in a narrow frequency band.

A. Dhouibi et al designed a low-profile substrate-integrated lens antenna using planar non-resonant metamaterials [84]. A half Maxwell fish-eye (HMFE) lens antenna is placed in a quasi-TEM parallel-plate waveguide with a certain distance for X-band operation. The lens antenna is working over the frequency band from 8 to 12 GHz. Both near and far field plots indicate that the proposed lens antenna is providing a good beam focusing properties. After installation of metamaterial lens in antenna, the size of the whole system becomes too large and proposed lens is not covering UWB frequency range.

In this chapter, the gain of UWB antenna is enhanced further using metamaterial. Here, Luneburg lens design equation is used to implement the metamaterial lens which has beam focusing characteristics, namely, gradient refractive index (GRIN) lens. A near zero index metamaterial concept is applied in the proposed work.

4.2 Metamaterial (MTM)

A metamaterial word has been taken from the Greek word meta, which means beyond, material which is having homogeneous electromagnetic structures. So, metamaterial has unusual properties not available in nature [85]. The microwave metamaterials are fabricated on printed circuit boards by making a metallic structure called unit cell MTM and repeating them in all directions. Such unit cell MTMs are mainly designed with printed resonator or non-resonator metallic structure. Two types of metamaterial structures exist in microwave regime, namely periodic and non-periodic MTM structure. Periodic and non-periodic unit cell MTM structures are considered as equivalent to homogeneous and inhomogeneous medium, respectively. The unit cell MTM is designed by calculating sub-wavelength values

at the operating frequency band. So, it can be described using the effective medium theory. An effective homogeneous structure average cell size p should be much smaller than the guided wavelength λ_g. But the exact cell size is determined based on effective homogeneity limit or effective-homogeneity condition which corresponds to a rule of thumb effectiveness condition. So, microwave engineers often use, $p=\lambda_g/4$, lumped components ($p<\lambda_g/4$) and quasi-lumped components ($\lambda_g/4<p<\lambda_g/2$) and distributed components ($p>\lambda_g/2$) [86]. In case of lumped components, the phase variation of the signal from the input to the output of the component is negligible and the component may be considered as a localized or small size element. In case of distributed component, phase variation along the component cannot be ignored, because the component must be considered as a transmission line section. Thus, MTM has a distributed structure which constitutes lumped elements.

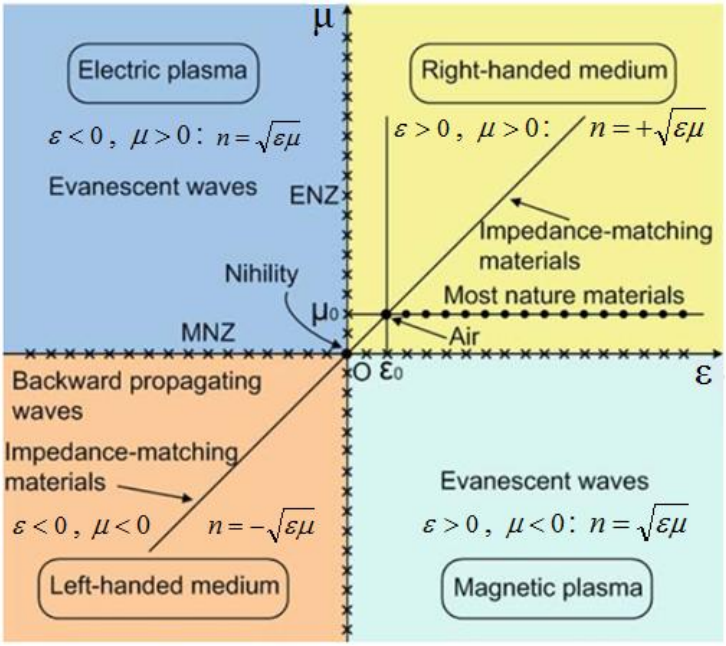

Figure 4.1 All possible properties of isotropic materials in the ε–μ domain.

If the condition of effective-homogeneity is satisfied, the structure behaves as a real material with unusual characteristics that can manipulate electromagnetic waves which depend on the nature of the unit cell. The constitutive parameters are the permittivity (ε) and the permeability (μ), which are related to the refractive index n by

$$n = \pm\sqrt{\varepsilon_r \mu_r} \tag{4.1}$$

where ε_r and μ_r are the relative permittivity and permeability. Four possible signs and properties of isotropic materials in the ε –μ diagram are illustrated in Figure 4.1.

In the first quadrant ($\varepsilon > 0$ and $\mu > 0$) represents right-handed materials (RHM). The second quadrant ($\varepsilon < 0$ and $\mu > 0$) denotes electric plasma, which support evanescent waves. The third quadrant ($\varepsilon < 0$ and $\mu < 0$) is the well-known left-handed materials (LHM), which is supporting a backward propagating wave. A metamaterial word has been taken from the Greek word meta, which means beyond, material which is having homogeneous electromagnetic structures. So, metamaterial has unusual properties not available in nature [85]. The microwave metamaterials are fabricated on printed circuit boards by making a metallic structure called unit cell MTM and repeating them in all directions. Such unit cell MTMs are mainly designed with printed resonator or non-resonator metallic structure. Two types of metamaterial structures exist in microwave regime, namely periodic and non-periodic MTM structure. Periodic and non-periodic unit cell MTM structures are considered as equivalent to homogeneous and inhomogeneous medium, respectively. The unit cell MTM is designed by calculating sub-wavelength values at the operating frequency band.

The selection of MTM properties is also a necessary part to improve the performance of the antenna. MTM antenna can be designed using left handed (LH) and right handed (RH) materials. The phase velocity (v_p), propagation constant (β) and group velocity (v_g) are less than zero for LH material and are greater than zero for RH material. LH material can only provide backward wave radiation. So, RH material is useful for directivity enhancement of the antenna.

Fast-wave i.e. $v_p > c$ (speed of light in air) is supporting leaky-wave antenna structure. In case of $v_p < c$, there will be no radiation in the leaky wave antenna and this condition is suitable for end fire radiation in air i.e. surface wave antenna. In case of surface wave antenna, the directivity can be enhanced by using zero index metamaterial (ZIM) principle. Ideally, the refractive index (n) of ZIM is considered as zero and phase velocity become infinity which is impossible in real life. Hence, materials with near zero or low index metamaterial (NZIM/LIM) are considered to have a refractive index value which varies from 0 to 1. ZIM behaves like a lens with beam focusing property.

In order to design high gain antenna, it is necessary to focus the radiated beam in the direction of end fire radiation. The unit cell metamaterial structures with the following properties are considered:

a) Non-resonant structure unit cell MTM

b) Low material loss

c) UWB frequency band MTM

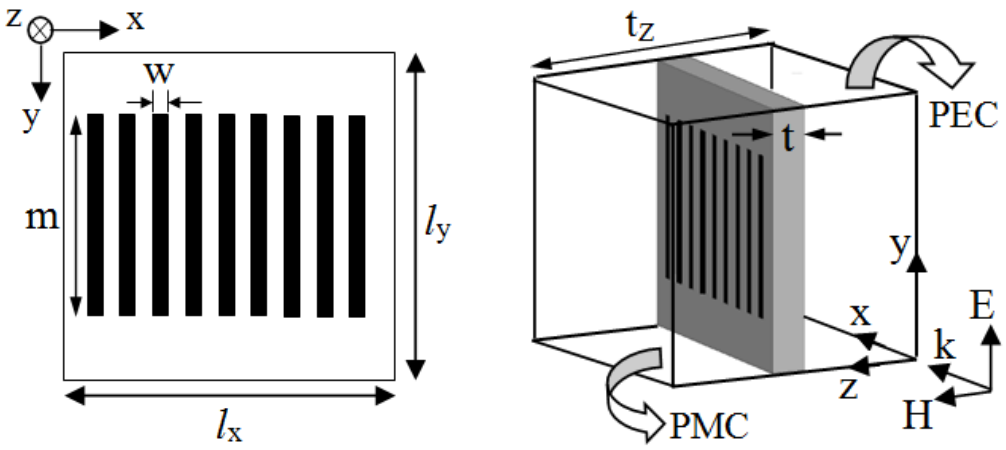

(a) (b)

Figure 4.2 The geometry of the artificial material (a) unit cell, (b) Simulation model. The dimensions of unit cell are $l_x = l_y = 6$ mm, $w = 0.2$ mm, $t = 0.8$ mm and $t_z = 6$ mm.

4.3 GRIN lens metamaterial in monopole antenna

4.3.1 Design GRIN lens

The resonant metamaterial structures are highly dispersive with considerable loss near the resonant frequency, which is not suitable for applications where broad bandwidth and low loss are required. So, non-resonant metamaterial elements provide almost non-dispersive effective constitutive parameters with negligible loss. The proposed material is fabricated on the single side of the dielectric material Roger RO4003 with dielectric constant 3.55, thickness of 0.8 mm. The unit cell metamaterial is designed with non-resonant parallel metallic lines on the substrate as shown in Figure 4.2(a). The dimensions of the unit cell are taken as

$$l_x = l_y = \lambda_0 / 8.3 \qquad (4.2)$$

where, $\lambda_0 = c/f\sqrt{\varepsilon_r}$ at f=6 GHz. The dimension is chosen in terms of free space wavelength (λ_0) indicating that the EM wave will enter in metamaterial through the air.

To extract the values of effective parameter, the scattering object is replaced by a homogeneous medium, i.e. wavelength within the medium becomes large in terms of the unit cell size [87], [88]. To evaluate the scattering performance, the simulation model of the single unit cell is shown in Figure 4.2(b). The perfect electric conductor (PEC) and perfect magnetic conductor (PMC) boundary conditions are also defined. The electric and magnetic polarizations are along the y and z-axes, respectively. The EM wave will propagate along the x-axis.

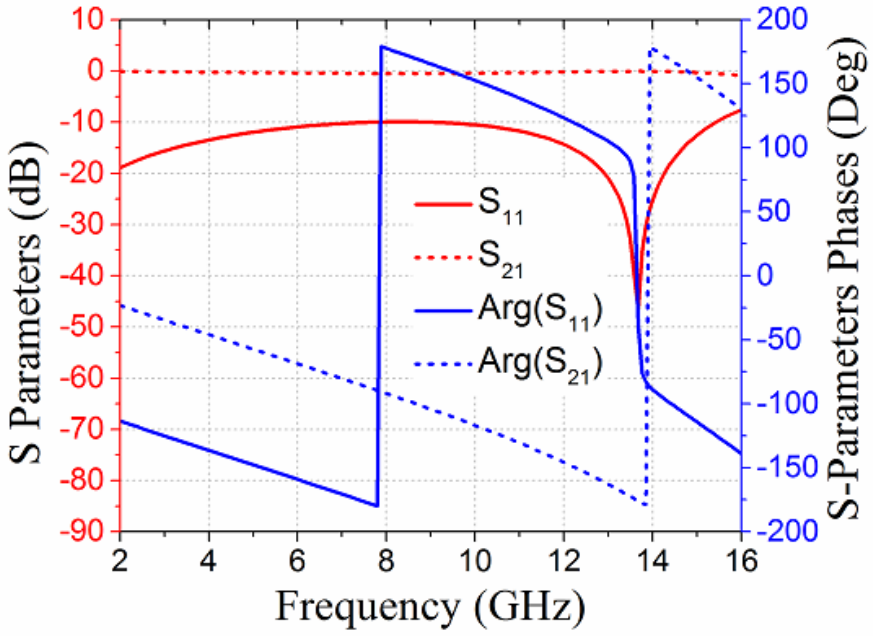

(a)

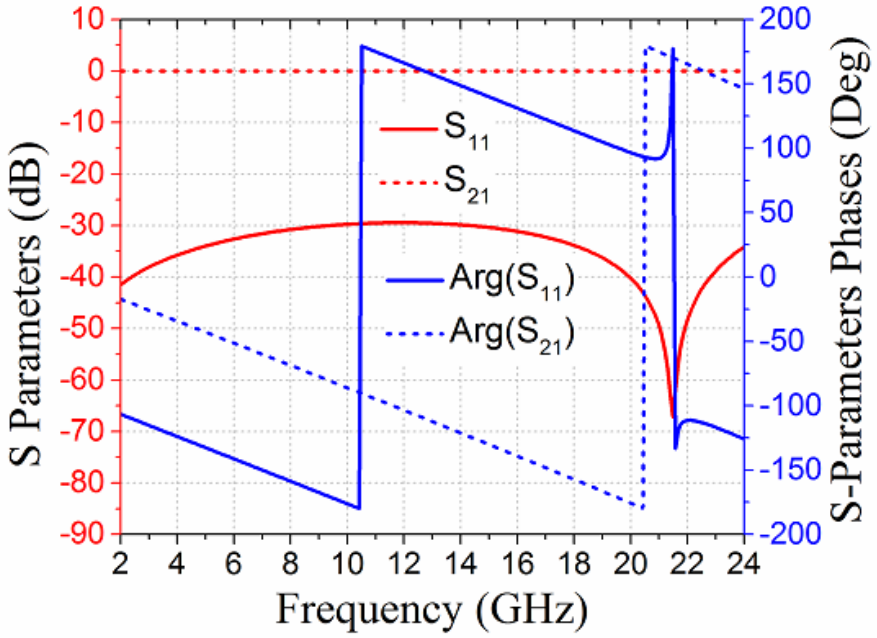

(b)

Figure 4.3 Magnitude (red color) and phase response (blue color) of the scattering parameters for (a) m=4 mm, and (b) m=1.1 mm.

The effective parameters are refractive index (n), permittivity (ε_y) and permeability (μ_z) extracted from the magnitude and phase of the scattering parameters using standard retrieval procedure described in [89], [90]. From the Figure 4.2(a), it can be seen that the length of the parallel metallic line is m. The lowest and highest resonant frequencies are obtained as 14 GHz and 22 GHz by choosing m=4 mm and m=1.1 mm, respectively as shown in Figure 4.3. The corresponding effective permittivity and permeability data are plotted as shown in Figure 4.4(a) and (b), respectively. The resonant frequency of the proposed material is changing with the length of m due to the electrical or current path. At the same time, it can also be observed that effective permittivity, permeability and refractive index values are also changing with the value of m.

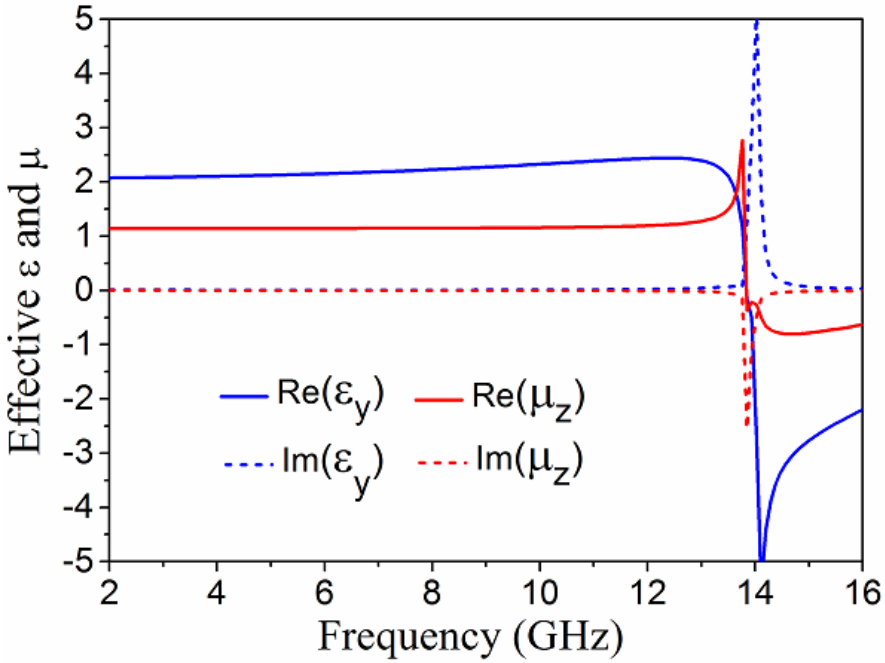
Effective ε and μ
Frequency (GHz)
Re(ε_y)
Re(μ_z)
Im(ε_y)
Im(μ_z)

(a)

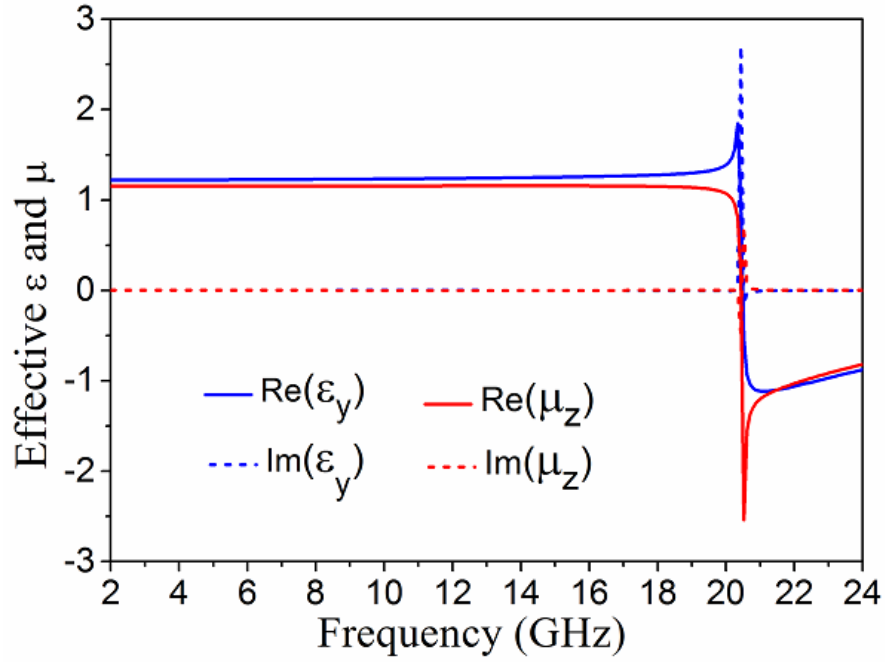
Effective ε and μ
Frequency (GHz)
Re(ε_y)
Re(μ_z)
Im(ε_y)
Im(μ_z)

(b)

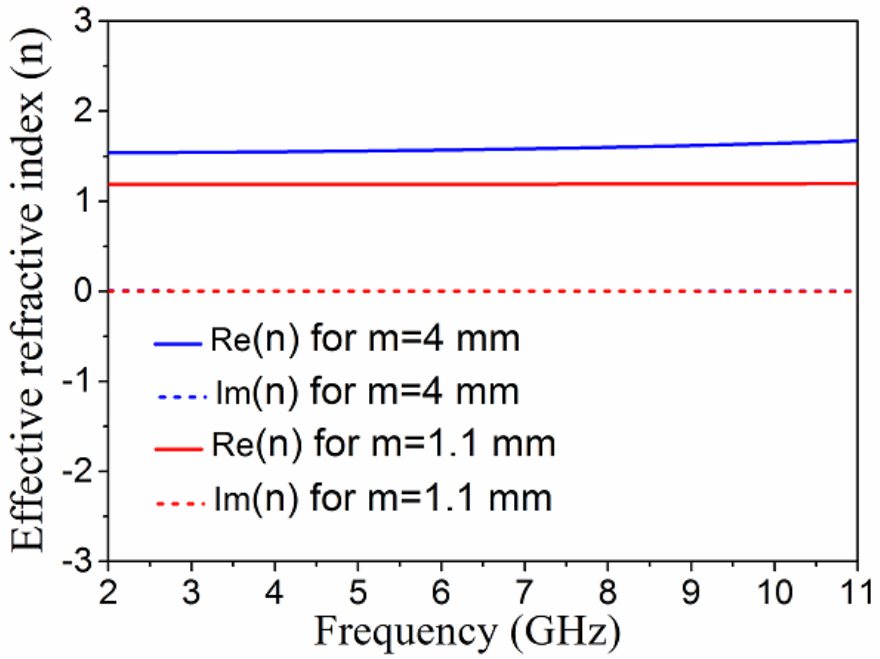

(c)

Figure 4.4. Effective permittivity (ε_y) and permeability (μ_z) of the metamaterial unit cell for (a) *m*=4 mm, and (b) *m*=1.1 mm, (c) Effective refractive index for *m*=4 mm and *m*=1.1 mm.

The effective refractive index values are also plotted and depicted in Figure 4.4(c). It can be noticed that the refractive index is not constant over the frequency band from 2-11 GHz. The variation of the effective refractive index over the frequency band from 2-11 GHz is shown in Table 4.1. It indicates that the refractive index values are also changing with different values of *m*. So, the effective refractive index is calculated by taking the average of the refractive index for a given frequency band at different values of *m* and these average refractive index data are plotted as shown in Figure 4.5.

Table 4.1 Variation of Effective Refractive Index

Frequency range (GHz)	**Parallel-line unit cell length, *m* (mm)**	**Variation of Effective Refractive Index, *n***
2-11	4	1.53–1.67
	3.7	1.47–1.58
	3.4	1.42–1.5
	3.1	1.37–1.42
	2.9	1.34–1.38
	2.7	1.31–1.35
	2.4	1.29–1.32
	2.1	1.25–1.27
	1.8	1.23–1.24
	1.5	1.2–1.22
	1.1	1.18–1.19
	0.5	1.1–1.15

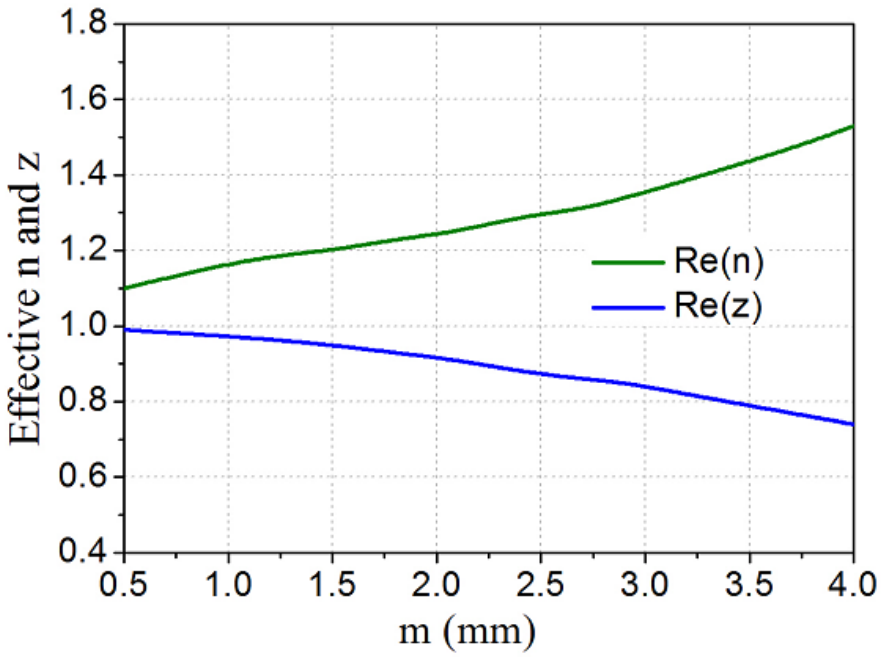

(a)

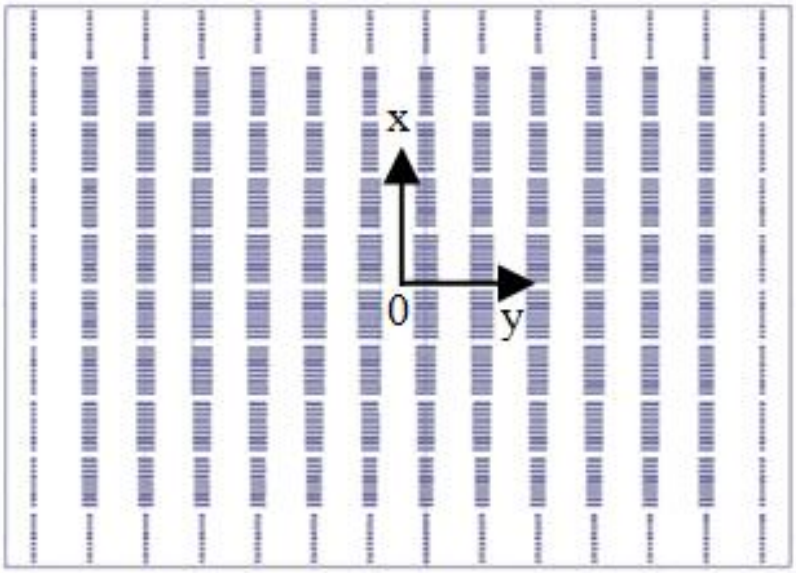

(b)

Figure 4.5 Retrieval results for the parallel line medium, (a) The relationship between the extracted refractive index (*n*) and wave impedance (*z*) on length *m*, (b) The schematic graph of the metallic parallel-lines.

The variation of the effective refractive index and impedance of the unit cell parallel-line metamaterial for the various values of *m* are shown in Figure 4.5(a). From the figure, it is observed that the effective refractive index value becomes low by decreasing the length of the parallel metallic line, *m*. The effective impedance values are near to the unity when the values of *m* are becoming low. The schematic design of the GRIN lens by using parallel-line metamaterial is shown in Figure 4.5(b). The dimension of the GRIN lens is 84×60 mm^2. According to the refractive index values, the arrangement of the metamaterial unit cell in the GRIN lens along the x and y-directions are shown in Figures 4.6(a) and (b), respectively.

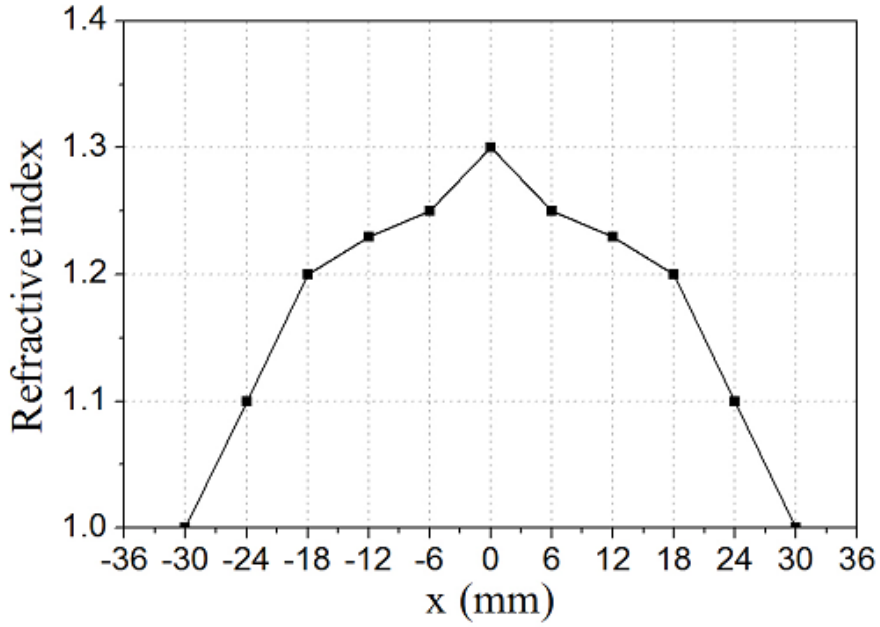

(a)

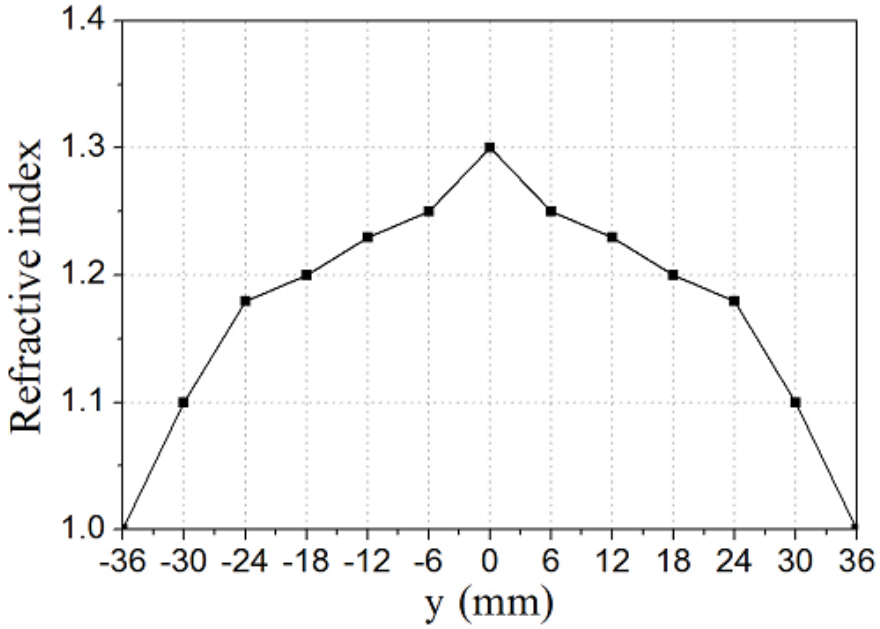

(b)

Figure 4.6 (a) The refractive-index distribution along x-direction, and (b) The refractive-index distribution along y-direction.

4.3.2 GRIN installed monopole antenna

4.3.2.1 Analysis and design of monopole antenna

The geometry of the proposed basic monopole antenna is shown in Figure 4.7(a). The top and bottom conductors are denoted by dark and light gray color. The antenna is designed and etched on the roger RT/duroid 5880 substrate with dielectric constant 2.2 and thickness, h=0.787 mm. The excitation of the antenna is given by 50 Ω microstrip line feed with line width 2 mm and bottom layer consists of the partial ground. The size of the basic monopole is 25×28 mm^2.

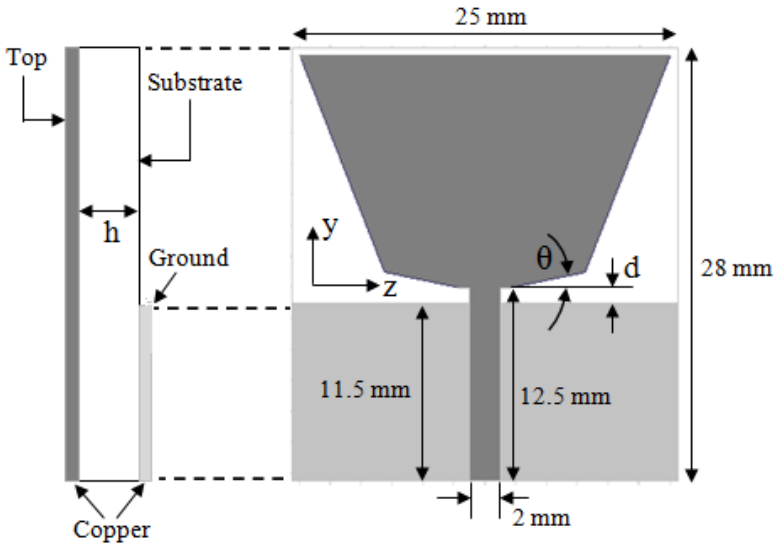

Figure 4.7 Geometry of the basic monopole antenna. Top and side view of the basic monopole.

In the proposed design, the bottom part of the radiating patch is responsible for the variation of the antenna's lowest frequency (f_L). In that place, the polygon structure is designed with an angle (θ) on the radiating patch. The angle θ must vary to fix f_L of the antenna frequency range. The current distribution on the partial ground layer is also responsible for impedance matching of the antenna. Here, the current path of the ground part can be controlled by varying the parameter *d*.

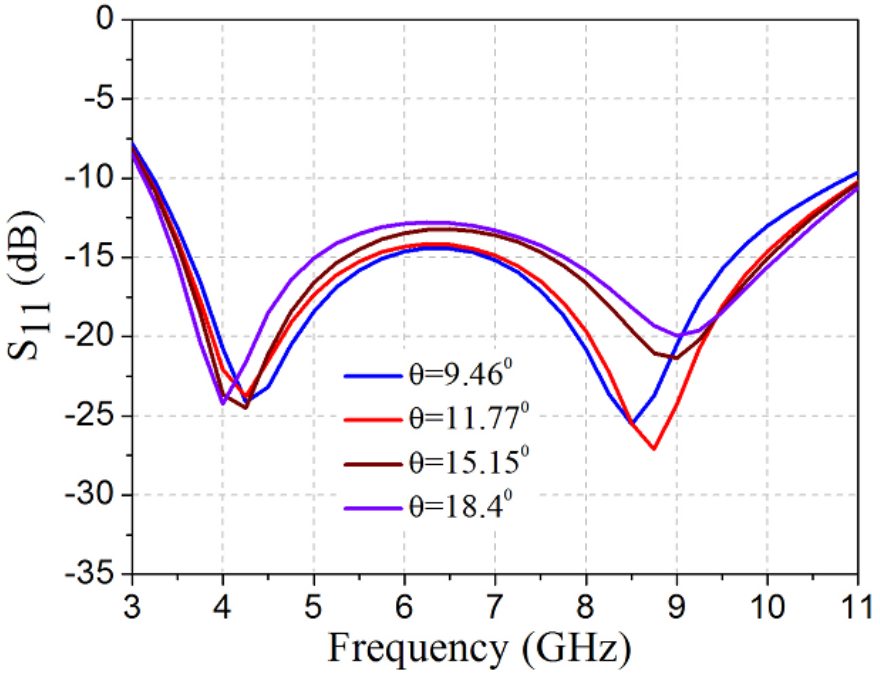

(a)

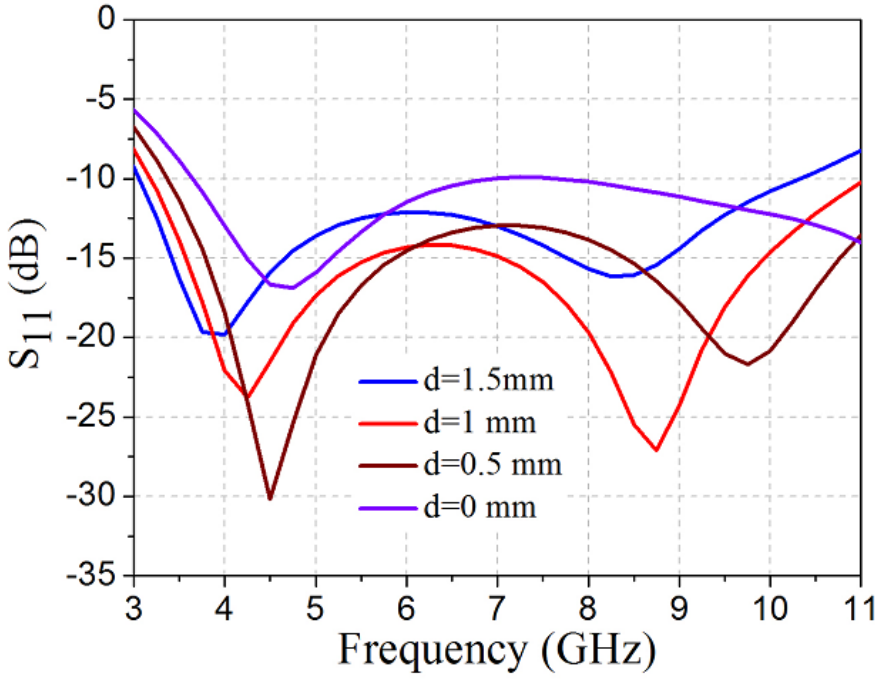

(b)

Figure 4.8 Analysis of monopole antenna, (a) Reflection coefficient (S_{11}) for different value of θ, (b) Reflection coefficient (S_{11}) for different value of d.

The variation of f_L is observed by changing the angle θ. The f_L shifted slightly left side for the increment of θ which is illustrated in Figure 4.8(a). It indicates that the reflection

coefficient is gradually increasing in the middle of the operating frequency band. At $\theta=11.77^0$, the f_L and other frequencies are well maintained over UWB frequency range. The fluctuation of S_{11} for another parameter d at $\theta=11.77^0$ is shown in Figure 4.8(b). It is clear that the lowest frequency f_L is decreasing with increasing the values of *d*. At the same time, the S_{11} is also increasing at high frequencies. The f_L is obtained as 3.1 GHz after optimizing the values of θ and *d* as 11.77^0 and 1 mm, respectively.

To design GRIN antenna, the seven GRIN lenses are placed on the basic monopole antenna as shown in Figure 4.9(a). The antenna and GRIN surfaces are separated by rohacel foams. The distance from the radiation source to the bottom of the GRIN lens is 23 mm. The near-field coupling between the GRIN and the basic monopole is not affected significantly. At the same time, the distance between the corresponding GRIN lens is kept 4 mm ($>l_x/2$) to avoid the destruction of metamaterial properties. The simulated reflection coefficient (S_{11}) of the optimized basic monopole and the GRIN monopole antenna is illustrated in Figure 4.9(b). The f_L is slightly shifted towards the right side.

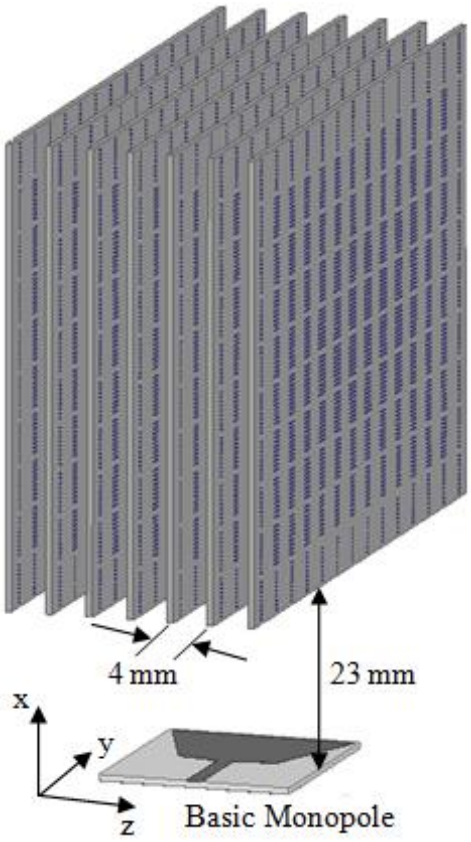

(a)

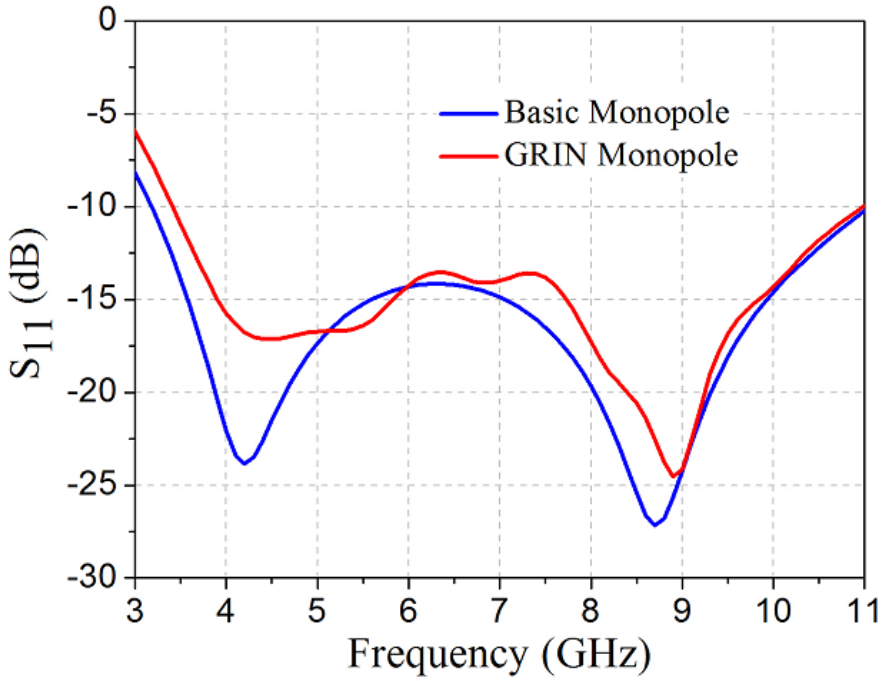

(b)

Figure 4.9 The arrangement of the GRIN with basic monopole, (a) View of GRIN monopole, (b) Simulation result of the reflection coefficient (S_{11}) optimized basic and GRIN monopole.

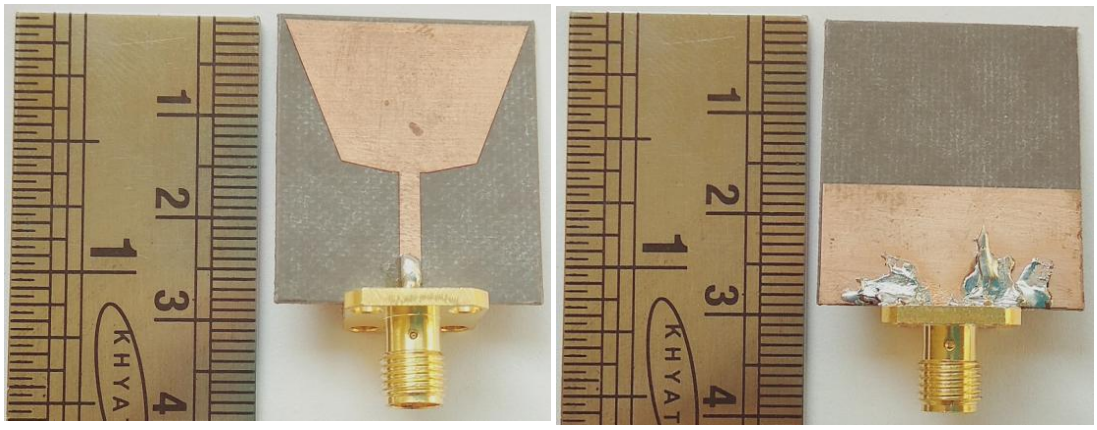

(a) (b)

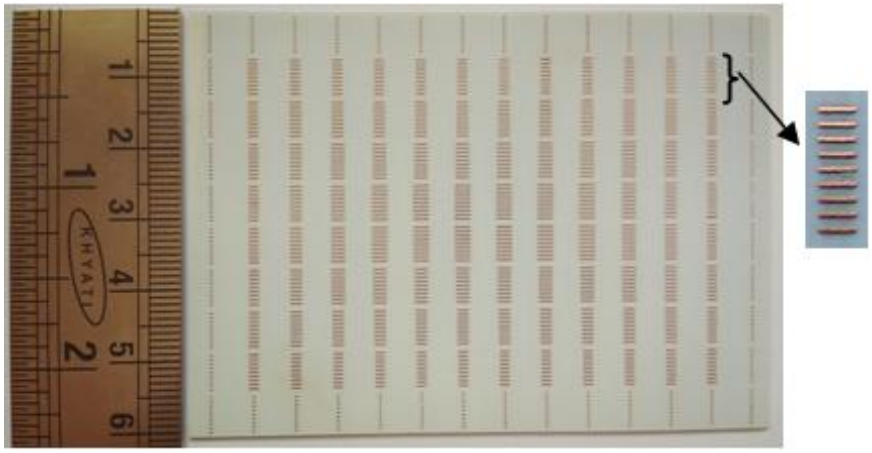

(c)

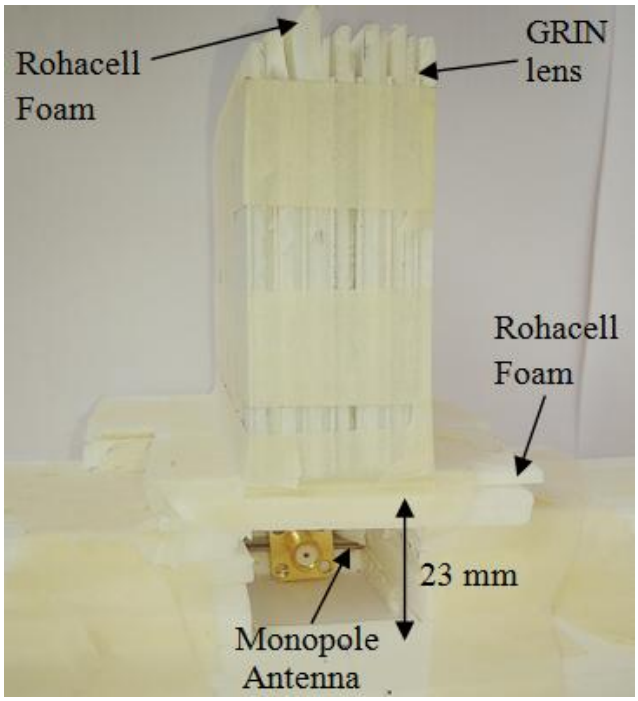

(d)

Figure 4.10 Photograph of the fabricated antennas (a) Top view, (b) Bottom view, (c) GRIN lens, (d) Seven GRIN lens on the antenna.

4.3.2.2 Results and Discussions

The proposed antennas are optimized by simulating a three-dimensional electromagnetic (EM) simulator CST microwave studio 2015. The fabricated prototype of the basic and GRIN monopole antennas are shown in Figure 4.10. The comparison of the performance of proposed GRIN antenna with some existing works in terms of size, operating frequency

band, the peak gain increment are shown in Table 4.2. The proposed GRIN antenna has more compact size compared to the other published works and also working on UWB characteristics.

Table 4.2 Comparison of the performance of the proposed GRIN monopole with similar published work

Reference	**Impedance bandwidth for S_{11}<–10 dB (GHz)**	**Peak Gain increment (dB)**	**Overall dimension (mm^3)**
[42]	3-8	11	-
[93]	6.7-12	9.5	-
[94]	10.5-12.5	-	-
[82]	8.9-10.8	4	215×139×85.8
Proposed structure	3.4-10.6	5.3	170×125×100

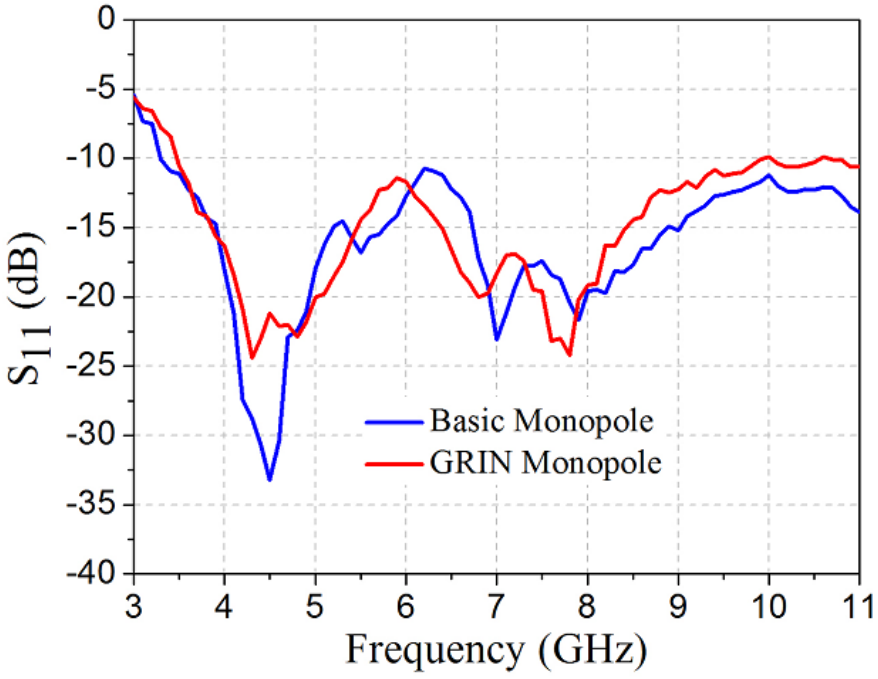

Figure 4.11 Measured reflection coefficient (S_{11}) of the antennas.

The measured reflection coefficients (S_{11}) of the basic and GRIN monopole antennas are plotted in Figure 4.11. It is clearly evident that the S_{11} of the basic and GRIN monopoles are less than –10 dB covering a bandwidth of 3.1-11 GHz and 3.4-11 GHz, respectively. In the case of GRIN antenna, the f_L is 3.4 GHz, and the S_{11} is fluctuating near -10 dB over bandwidth 10-11 GHz. Here, the measurement result of f_L is giving different value, because

the 3D EM software has been taken as an ideal structure filled by air between the objects. But the photograph of GRIN antenna is supported and fixed by using rohacel foams and paper tape.

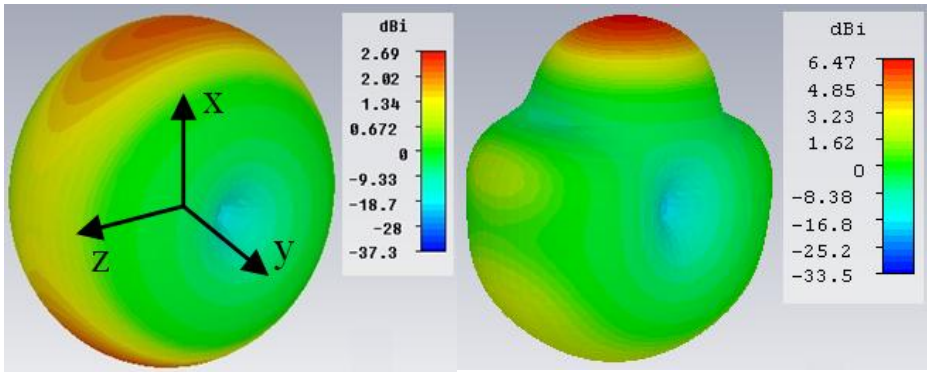

(a1) (a2)

basic monopole GRIN monopole

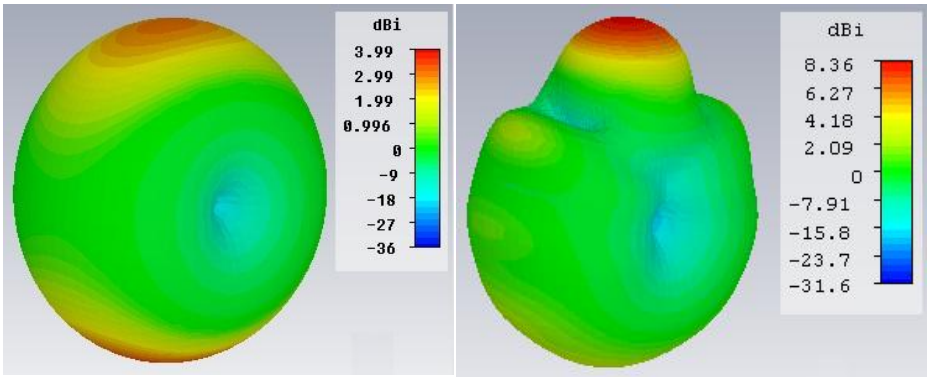

(b1) (b2)

basic monopole GRIN monopole

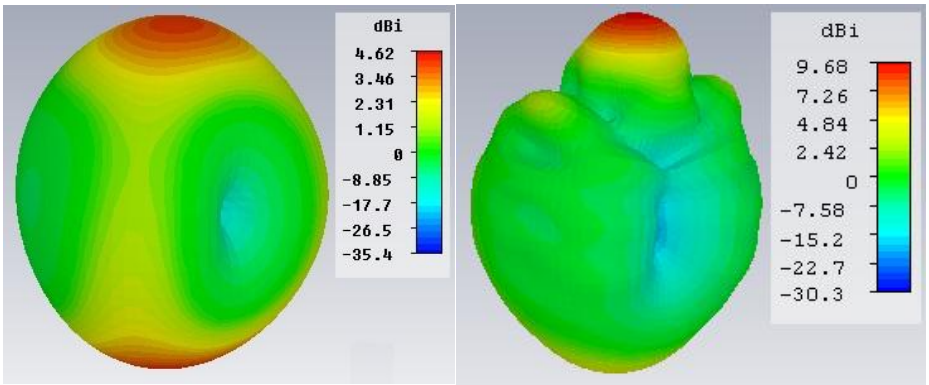

(c1) (c2)

basic monopole GRIN monopole

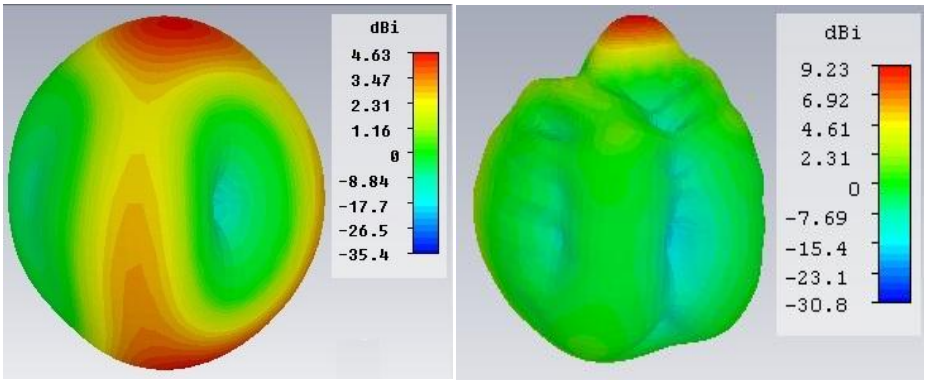

(d1) basic monopole

(d2) GRIN monopole

Figure 4.12 Simulated 3D far-field radiation patterns. For basic monopole at (a1) 4.5 GHz, (b1) 6.2 GHz, (c1) 8 GHz, (d1) 10 GHz and GRIN monopole at (a2) 4.5 GHz, (b2) 6.2 GHz, (c2) 8 GHz, (d2) 10 GHz.

The simulated 3D far-field radiation patterns of the monopole without and with GRIN lenses are illustrated in Figure 4.12. From the figure, it can be seen that a single beam directive and 3D radiation pattern is maximum in the direction of the x-axis at 4.5 GHz, 6.2 GHz, 8 GHz and 10 GHz. The omnidirectional patterns of the basic monopole in xz-plane (H-plane) are transformed to single narrow beam patterns with directive emission.

In order to understand the effect of GRIN, the GRIN monopole is simulated in the 3D EM software HFSS 15. The free-space electric-field distributions with and without the unit cell metamaterial structure of GRIN lens are shown in Figure 4.13. So, it can be observed that the quasi-spherical waves are almost converted into the plane waves in the direction of the x-axis at 9 and 10 GHz by comparing the wavefronts going out with and without unit cell structures in the GRIN lens.

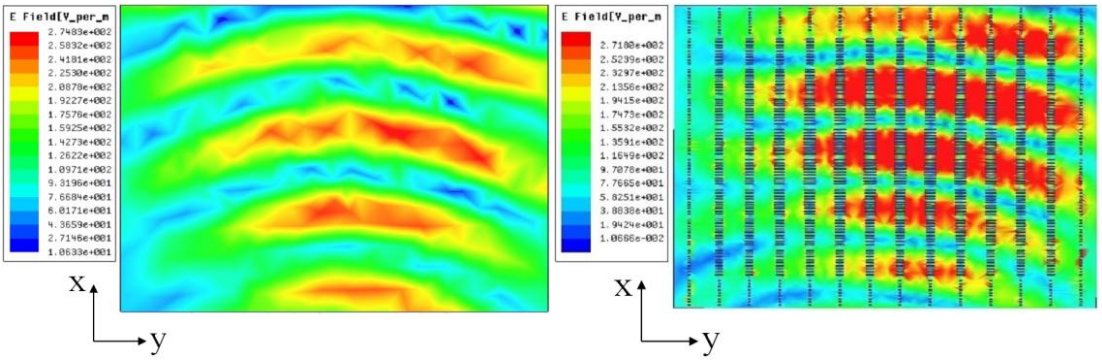

(a1) (a2)

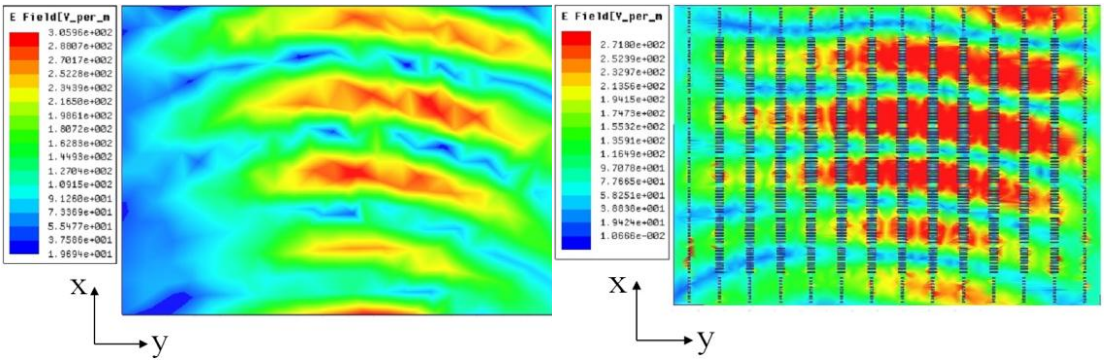

(b1) (b2)

Figure 4.13 Simulated electric-field distributions in free space with and without unit cell metamaterial structure in GRIN lens. Without unit cell structure in GRIN lens at (a1) 9 GHz, (b1) 10 GHz, and with unit cell structure in GRIN lens at (a2) 9 GHz, (b2) 10 GHz.

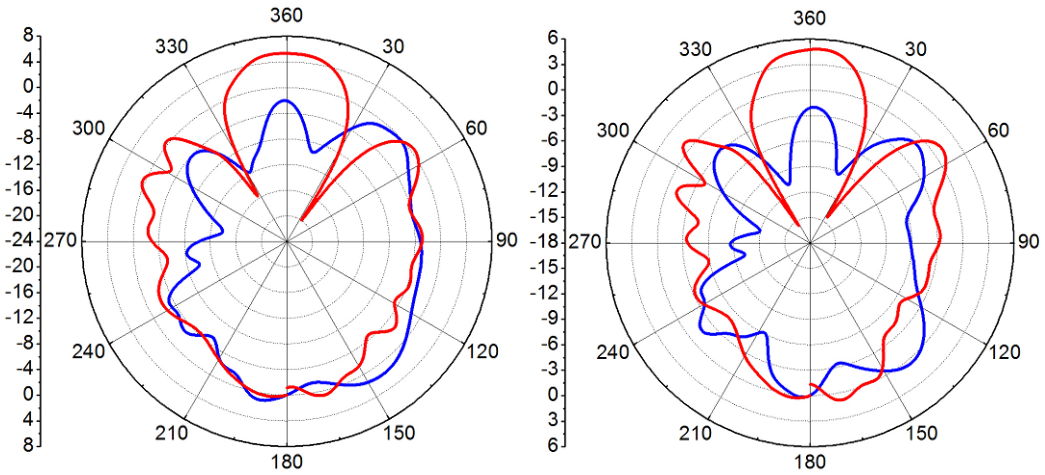

(a) (b)

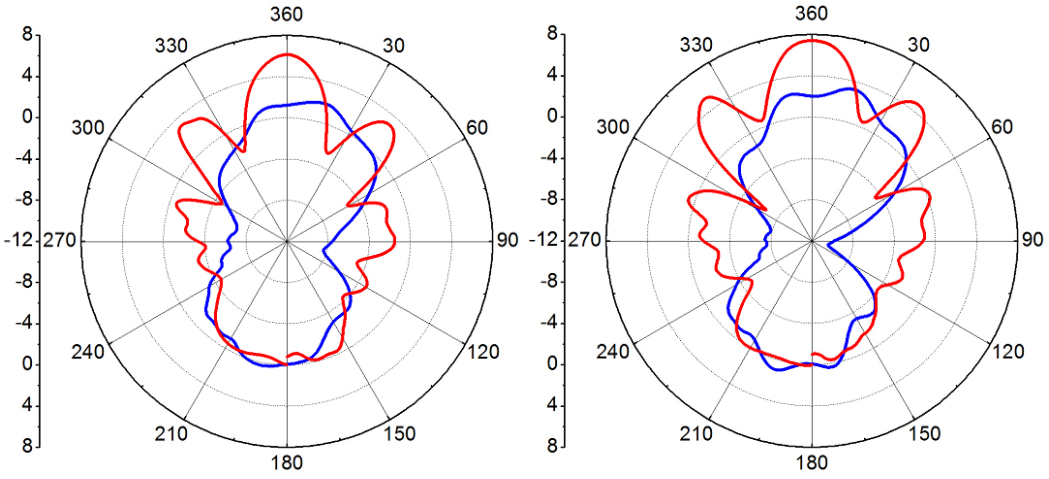

Figure 4.14 Measured H-plane radiation patterns at (a) 4.5 GHz, (b) 6.2 GHz, (c) 8 GHz, (d) 10 GHz The blue and red solid line denotes a basic monopole and GRIN monopole, respectively.

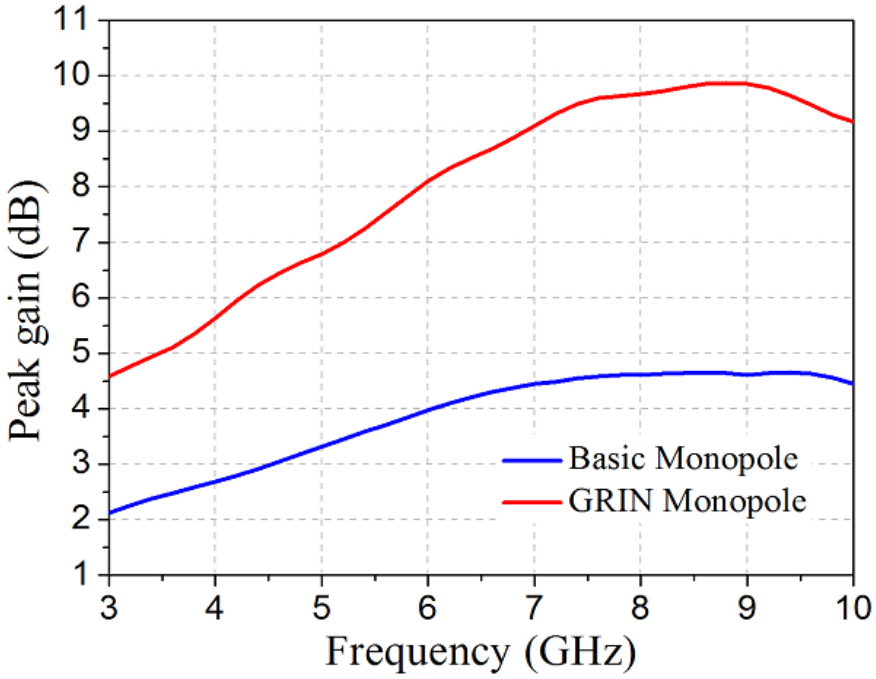

Figure 4.15 Measured gain variation of the basic monopole and GRIN monopole antenna.

The measured H-plane (xz plane) patterns of the antennas are compared at 4.5 GHz, 6.2 GHz, 8 GHz and 10 GHz as shown in Figure 4.14. The measurement results are indicating that the radiation patterns are improved by using a GRIN lens in basic monopole antenna. The measured peak gain of the basic monopole and GRIN monopole antennas in the direction of the x-axis are presented in Figure 4.15. So, it is clear that the peak gain of the basic monopole is increased by 5.3 dB at 8.8 GHz (approximately) due to the effect of GRIN

lens and the gain of GRIN antenna is varying from 4.5-9.8 dB over the frequency band of 3−10 GHz.

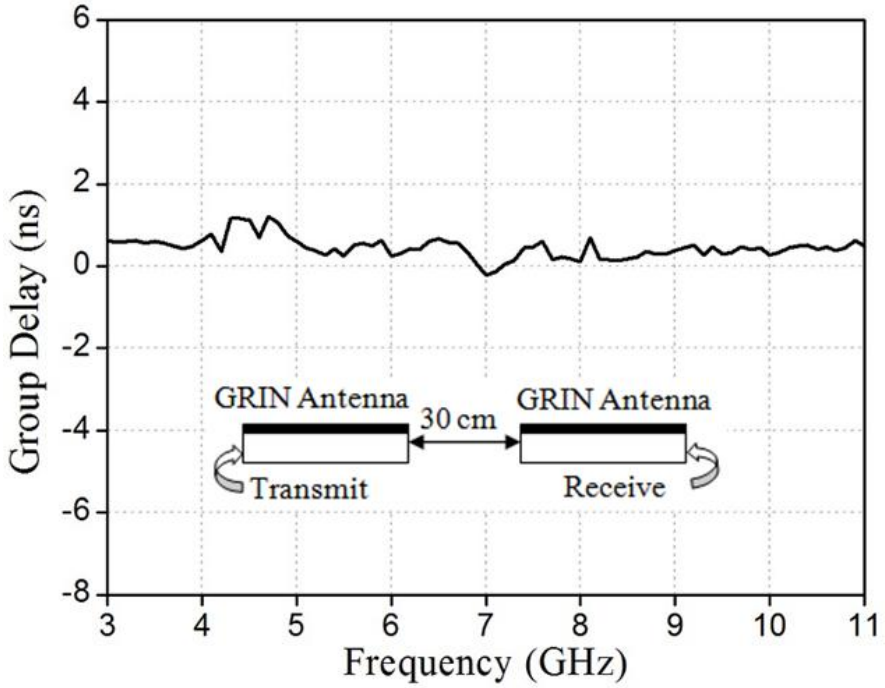

Figure 4.16 Group delay performance of the GRIN monopole antenna

For UWB antenna, the frequency dependent parameters are not sufficient for validating the design. Therefore, the time domain characteristic of the fabricated GRIN monopole is also tested. So, two GRIN antennas are arranged side by side with a distance 30 cm and connected to the ports of the vector network analyzer (VNA). The antenna is giving almost stable group delay performance with a fluctuation approximately ±1.2 ns in the desired band, indicating that a transmitted signal will not be seriously distorted by the proposed antenna as shown in Figure 4.16.

4.4 GRIN installed in tapered slot antenna

4.4.1 Design of tapered slot antenna

The geometry of the basic tapered slot antenna (TSA) structure with top and bottom views are demonstrated in Figure 4.17. It is fabricated on Rogers RO4003 PCB material with relative permittivity as 3.55 and thickness of 0.8 mm. The dimensions of the basic TSA are about 40×46×0.8 mm^3. The microstrip line with impedance transition techniques (50 Ω to 100 Ω) is applied to feed the antenna for impedance matching. The broad and narrow

microstrip line widths are calculated as W_{f2} = 1.7 mm and W_{f1} = 0.8 mm, respectively. The microstrip to slotline transition is realized by etching the slotline on one side of the substrate. An exponential slot radiator is printed on the opposite side of the substrate. The microstrip line crosses below and perpendicular to the slotline. After crossing, the microstrip line is connected to the circular radial stub which acts as a wideband, virtual short circuit.

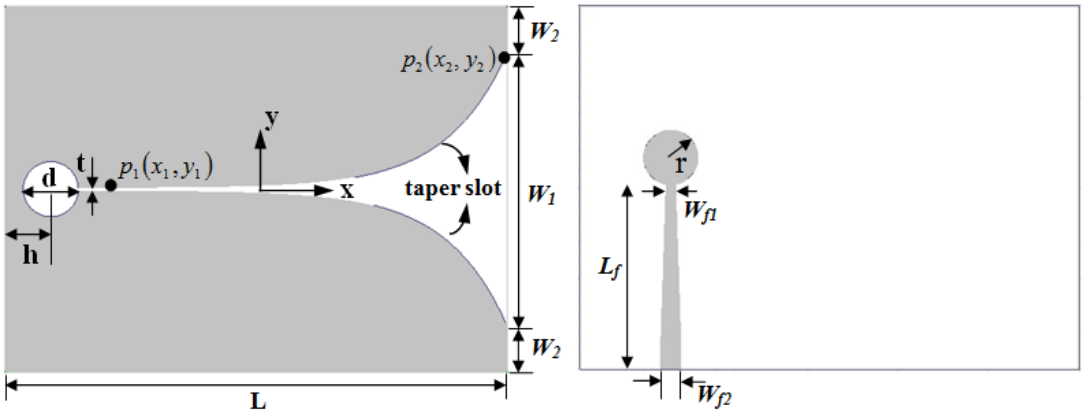

(a) (b)

Figure 4.17 Geometry of the basic TSA antenna, (a) Top view, and (b) Bottom view.

The exponential inner curves on the top surface of the TSA can be described by the following equation,

$$y = \pm\left(c_1 e^{Rx} + c_2\right) \tag{4.3}$$

where, $c_1 = \dfrac{y_2 - y_1}{e^{Rx_2} - e^{Rx_1}}$ and $c_2 = \dfrac{y_1 e^{Rx_2} - y_1 e^{Rx_1}}{e^{Rx_2} - e^{Rx_1}}$

The points $p_1(x_1, \pm y_1)$ and $p_2(x_2, \pm y_2)$ are shown in Figure 4.16(a), where R is the exponential rate that will be able to control the shape of slot. From the equation (4.3), the tapered slot curve varies from 2.5 mm ≤ x ≤ 37.5 mm and 0.1 mm ≤ y ≤ 15 mm on x and y axes, respectively. The optimised dimensions of the basic TSA are shown in Table 4.3.

Table 4.3 Geometrical parameters of the proposed basic TSA

Parameters	Unit (mm)	Parameters	Unit (mm)
L	46	t	0.2
W_1	30	r	2.6
W_2	5	L_f	20.4
h	6	W_{f1}	0.8
d	5	W_{f2}	1.7

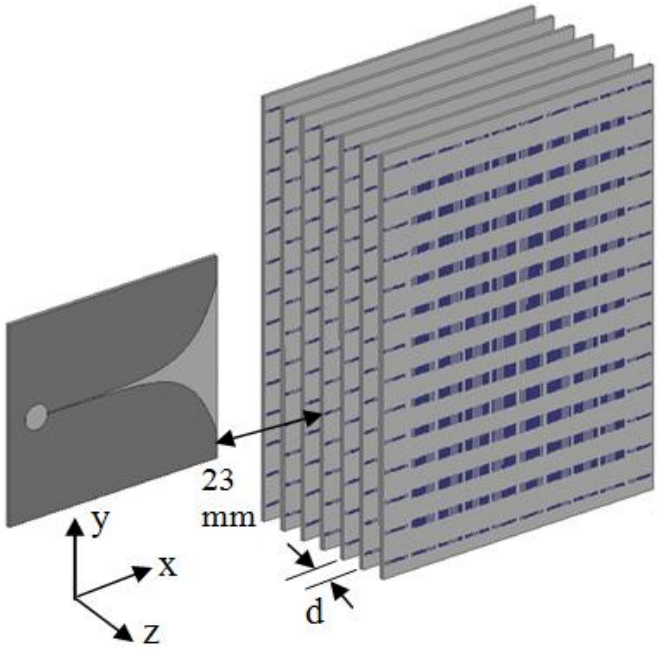

Figure 4.18 Geometrical view and arrangement of the GRIN lens in TSA.

4.4.2 Design and analysis of GRIN lens in TSA

A seven proposed lenses are incorporated in front of the basic TSA as shown in Figure 4.18. The distance from the end fire radiated antenna to the GRIN lens is 23 mm. So, the near-field coupling between the GRIN and the basic TSA will not be affected significantly. To understand the effects of GRIN lens, parametric study has been performed next.

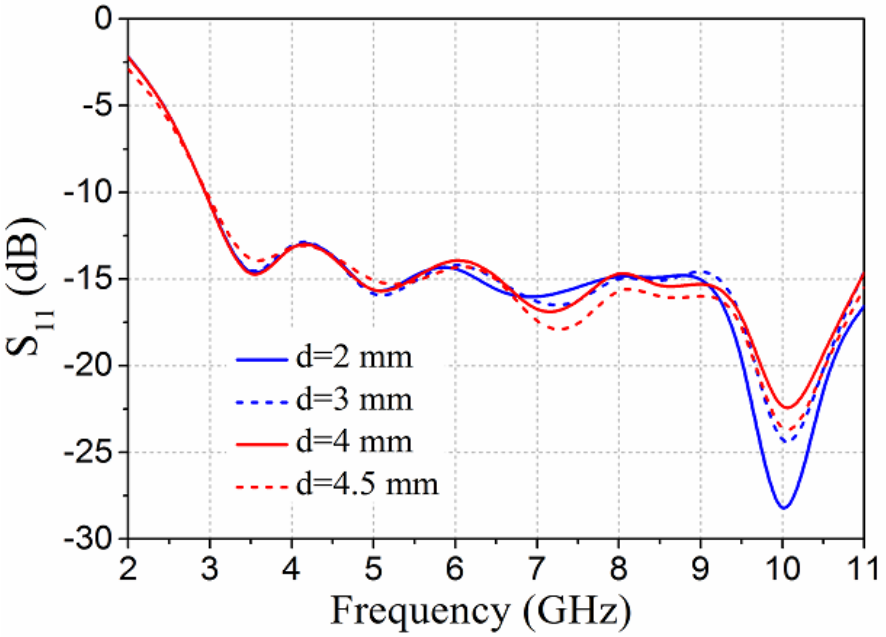

(a)

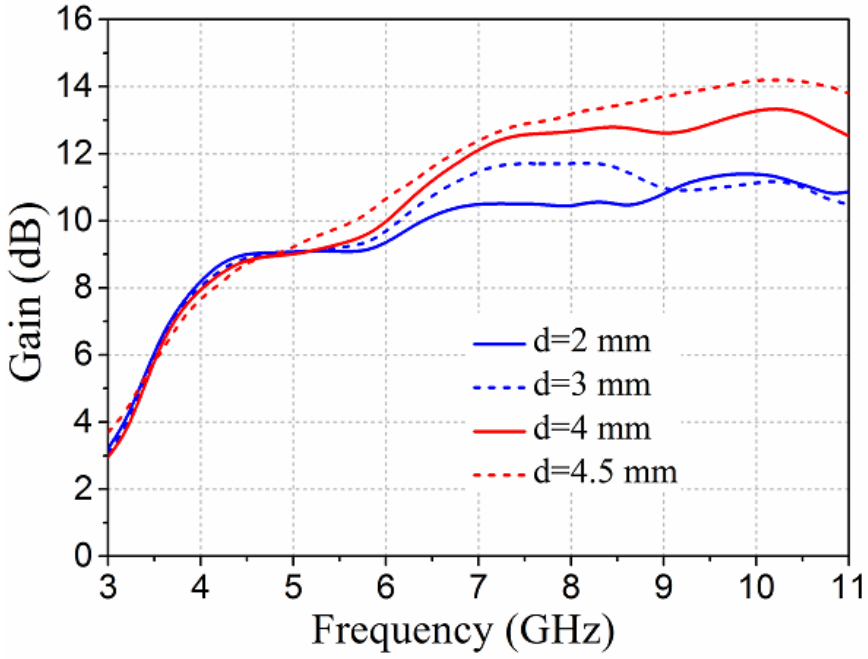

(b)

Figure 4.19 (a) The variation of reflection coefficient (S_{11}) and (b) gain for the distance between GRIN lens are 2 mm,3 mm,4 mm and 4.5 mm.

The distance between GRIN lens (*d*) is playing an important role to create a directive beam of the antenna. Owing to gap *d*, the radiated EM wave can destruct the properties of metamaterial in GRIN lens. To avoid this problem, the GRIN antenna has been analyzed by

simulating at the different values of *d*. The variation of the reflection coefficient is not large for the different values of *d*, as illustrated in Figure 4.19(a). But the gain of the antenna is seriously reduced at the lower values of *d*, as shown in Figure 4.19(b). Due to the short distance between GRIN surfaces, the EM wave is distorted and scattered by the GRIN lens. Therefore, some metamaterial properties of GRIN lens have been lost and radiated beam is not fully focused. Hence, the distance *d* is kept at 4.5 mm ($>l_x/2$) to avoid the destruction of metamaterial properties.

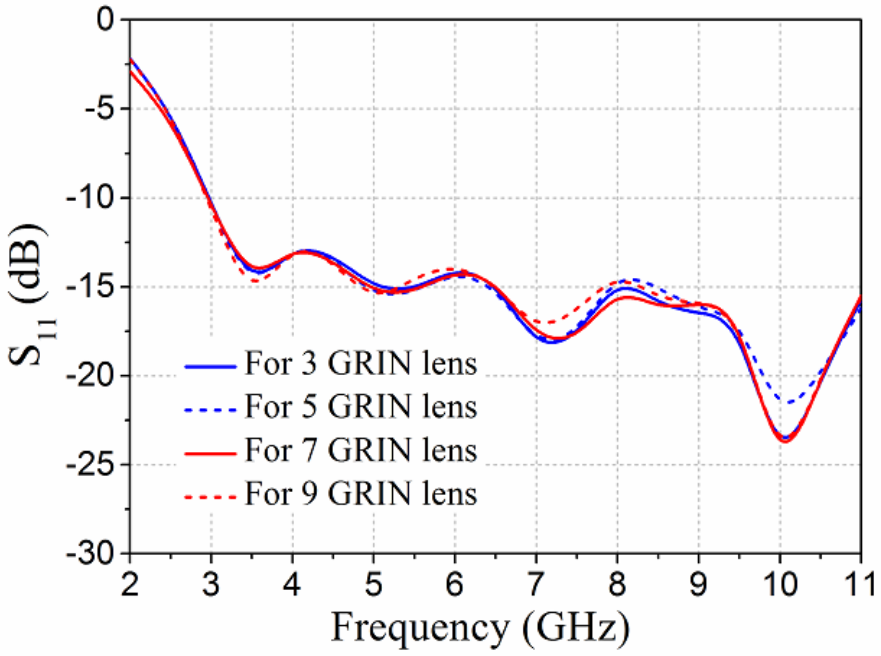

(a)

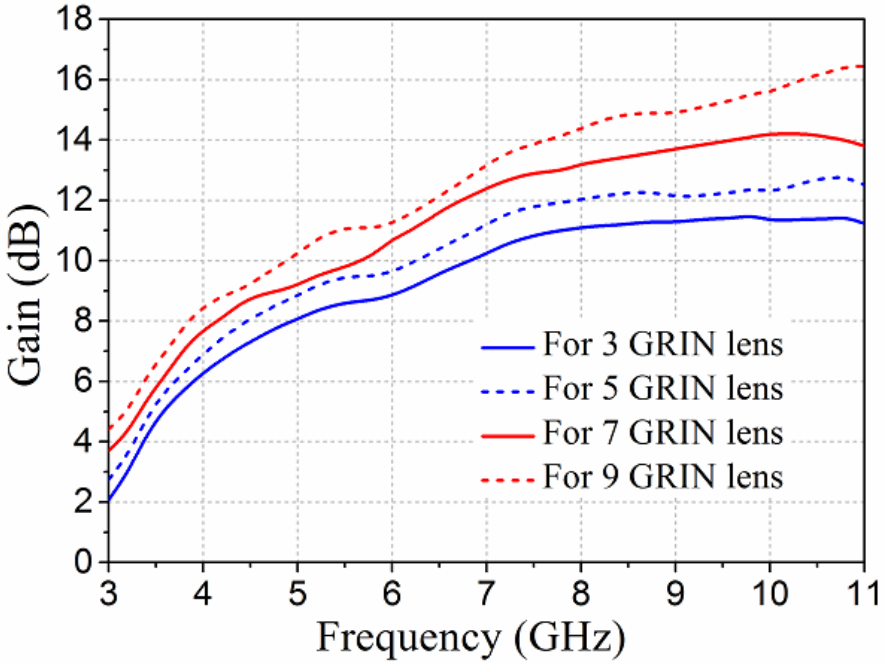

(b)

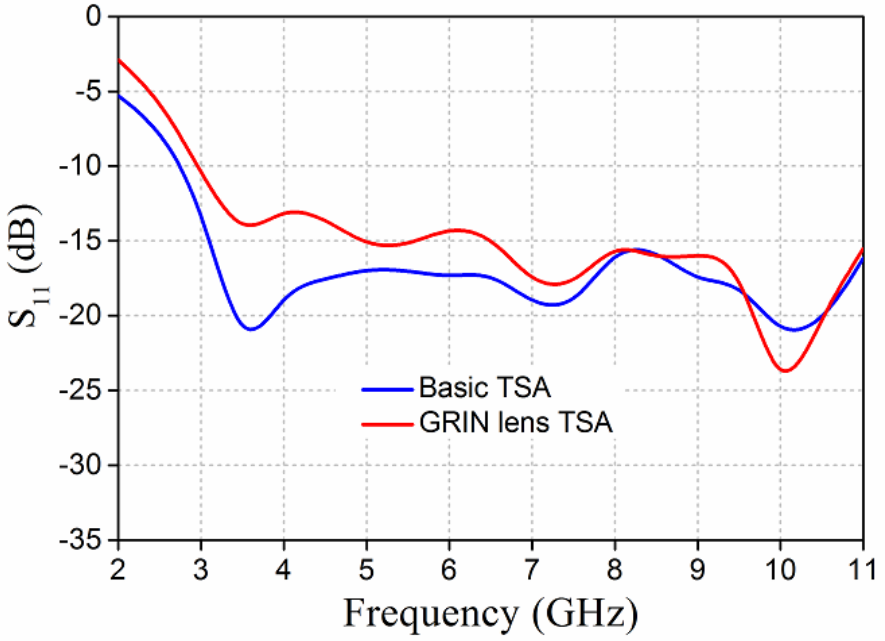

(c)

Figure 4.20 Simulation results of the GRIN antennas for the number of GRIN lens are 3,5,7 and 9. (a) reflection coefficient (S_{11}), (b) gain, and (c) simulated reflection coefficient (S_{11}) of the optimized basic and GRIN TSA

The simulated reflection coefficient (S_{11}) and gain of the antenna for different number of GRIN lenses are depicted in Figure 4.20. The reflection coefficient values are below -10 dB within the frequency band 3 to 11 GHz. It is clear that the reflection coefficient is not significantly affected for the different number of GRIN lenses. On the other side, the gain of the antenna is significantly enhanced when the number of GRIN lenses is increased. The peak gain of the GRIN antenna varies between 4.3 and 16.3 dB (approximately) within the operating frequency band. The simulated S_{11} of the optimized basic and GRIN TSA is shown in Figure 4.20(c).

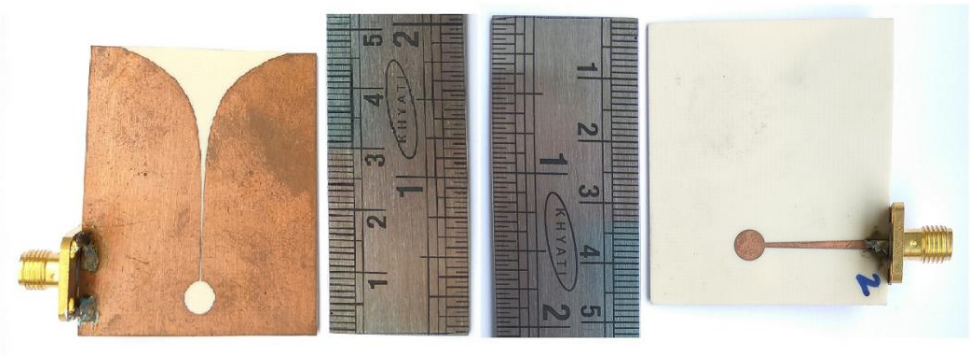

(a) (b)

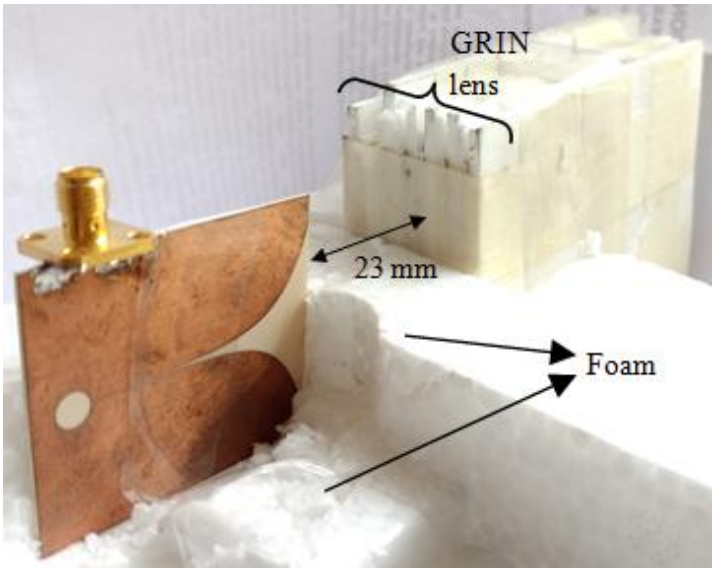

(c)

Figure 4.21 Photograph of the fabricated antennas (a) Top view, (b) Bottom view, (c) GRIN lens, (d) Installation of seven GRIN lens with TSA.

Table 4.4 Proposed GRIN antenna comparison with existed work

Reference	Size (mm^2)	Operating frequency band (GHz)	Peak gain increment (dB)
[42]	170×170	3-8	11
[93]	-	6.7-12	9.5
[94]	-	10.5-12.5	-
[82]	-	8.9-10.8	4.02
[84]	190×130	10.5-12.5	4
[95]	80.5×52	3.5-16	5.8
Proposed work	133×84	3-11	6

4.4.3 Results and Discussions

The fabricated prototype of the basic and GRIN TSA antennas are shown in Figure 4.21. The comparison of the proposed GRIN antenna with some existing works in terms of size, operating frequency band, the peak gain increment is shown in Table 4.4. The proposed GRIN antenna has a compact size compared to the other published works without affecting UWB characteristics.

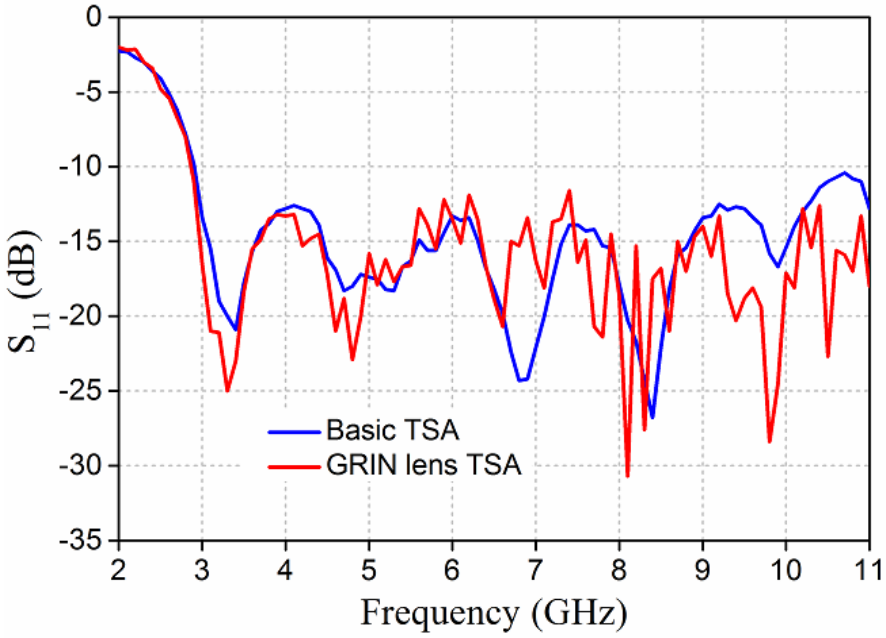

Figure 4.22 Measured reflection coefficient (S_{11}) of the antennas.

The measured reflection coefficient (S_{11}) of the basic and GRIN TSA antennas are shown in Figure 4.22. It can be observed that the S_{11} of the basic and GRIN TSA are less than -10 dB covering a bandwidth of 3-11 GHz. But, the measurement and simulation results of S_{11} are different because the 3D EM software has taken that antenna system as an ideal structure filled by air between the objects. But the GRIN antenna is supported and fixed by using foams. Therefore, the measured data is slightly different from the simulation result.

To understand the effect of GRIN over the radiated beam, the GRIN TSA is simulated in the 3D EM software HFSS 15. The free-space electric-field distributions with and without unit cell metamaterial structure in GRIN lens are depicted in Figure 4.23. So, it can be noticed that the quasi-spherical waves are almost converted into the plane waves in the direction of the x-axis at 9 and 10.5 GHz by comparing the wavefronts. The wavefronts show that the nature of outgoing EM wave through the structure with and without unit cell structures in the GRIN lens. Since the GRIN elements operate far from their resonant frequencies, the loss induced by the sample is low.

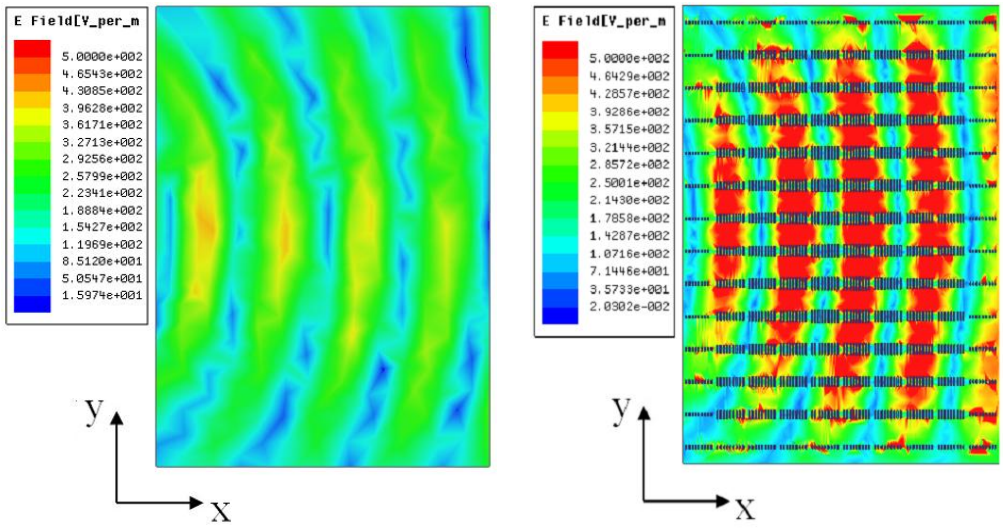

(a1) (a2)

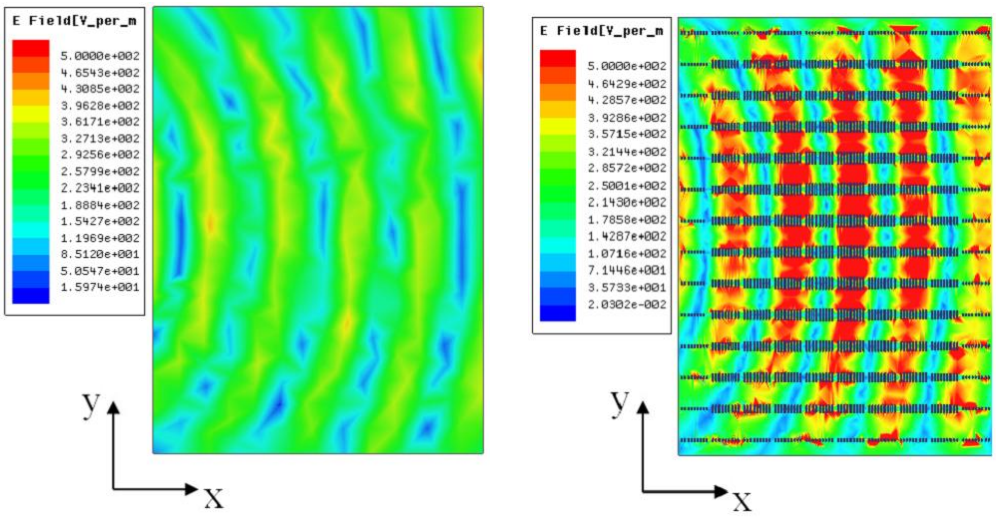

(b1) (b2)

Figure 4.23 Simulated electric-field distributions in free space with and without unit cell metamaterial structure in GRIN lens. Without unit cell structure at (a1) 9 GHz, (b1) 10.5 GHz, and with unit cell structure in GRIN lens at (a2) 9 GHz, and (b2) 10.5 GHz.

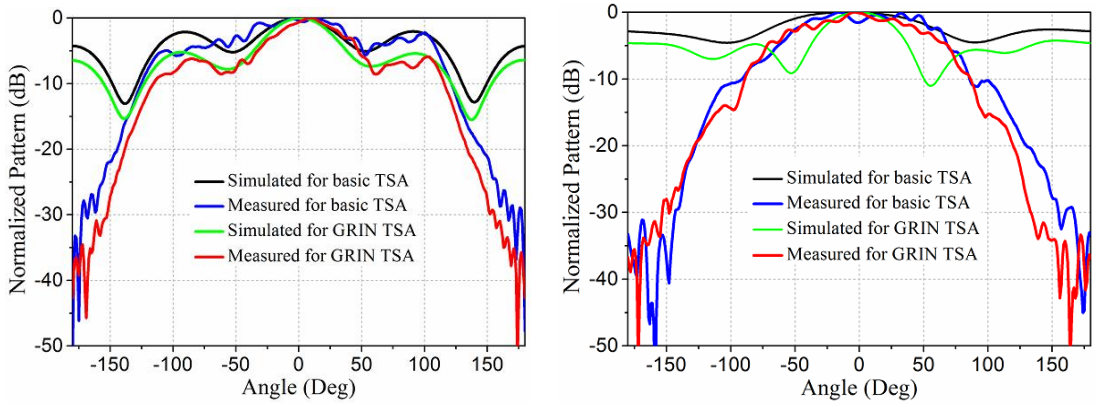

(a) (b)

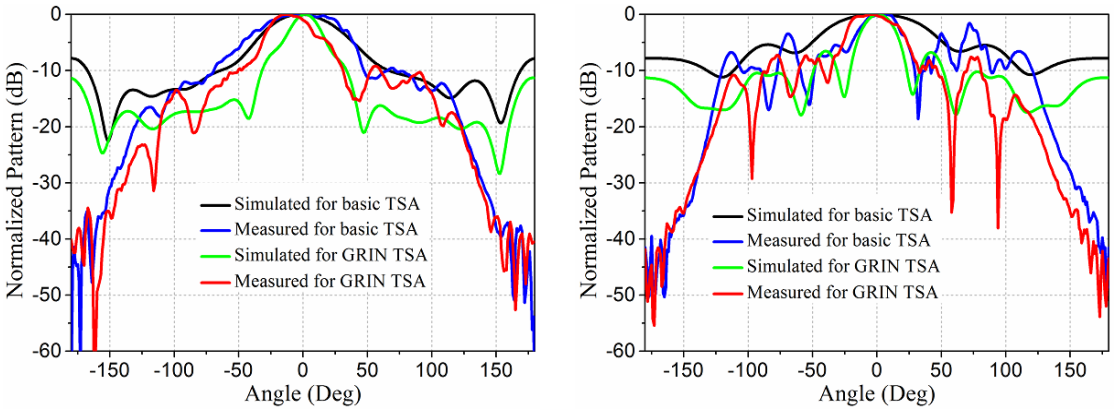

(c) (d)

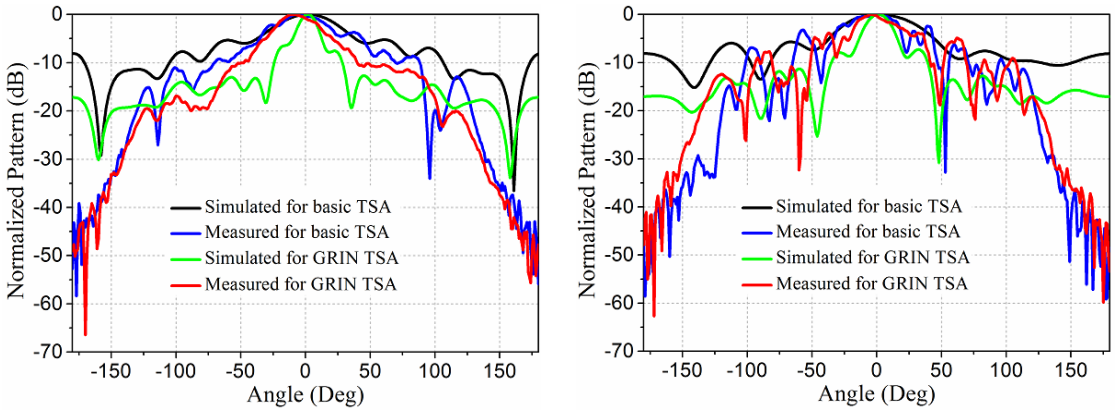

Figure 4.24 Simulated and measured normalized radiation patterns of the basic TSA and GRIN TSA at (a) xy-plane for 3.2 GHz, (b) xz-plane for 3.2 GHz, (c) xy-plane for 8 GHz, (d) xz-plane for 8 GHz, (e) xy-plane for 10.3 GHz, (f) xz-plane for 10.3 GHz. The xy-plane and xz-plane indicating E-plane and H-plane, respectively.

Table 4.5 Half power beam width (HPBW) of the basic TSA and GRIN TSA

Antennas	**HPBW**			
	@3.2 GHz	**@6 GHz**	**@8 GHz**	**@10.3 GHz**
Basic TSA	70	60.5	50	45
GRIN TSA	65.5	56.1	45.4	41.2

The simulated and measured normalized radiation patterns of the antennas in the E-plane (xy-plane) and H-plane (xz plane) are compared at 3.2 GHz, 8 GHz and 10.3 GHz in Figure 4.24. The simulated radiation patterns show that the 3 dB beam widths of the antennas are becoming narrow after using GRIN metamaterial. The measured E-plane radiation pattern achieved a narrow beam width compared to H-plane by using a GRIN lens as shown in Table 4.5. It can be also observed that the side lobes level fluctuations in the H-plane patterns are high for the basic TSA which has been reduced by using GRIN. The simulated and measured gains of the basic TSA and GRIN antennas are obtained in the direction of the x-axis as illustrated in Figure 4.25(a). Due to the effect of GRIN lens , the gain of the basic TSA has been increased by 6 dB at 10 GHz (approximately). The gain of GRIN antenna is varying from 3.7–14 dB over the frequency band of 3−11 GHz.

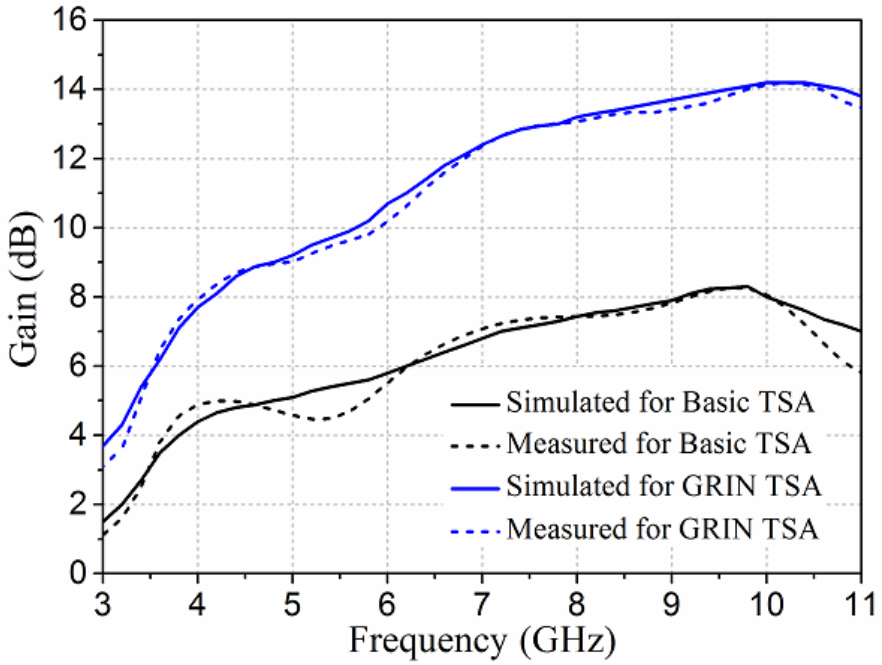
Gain (dB)
Frequency (GHz)
Simulated for Basic TSA
Measured for Basic TSA
Simulated for GRIN TSA
Measured for GRIN TSA

(a)

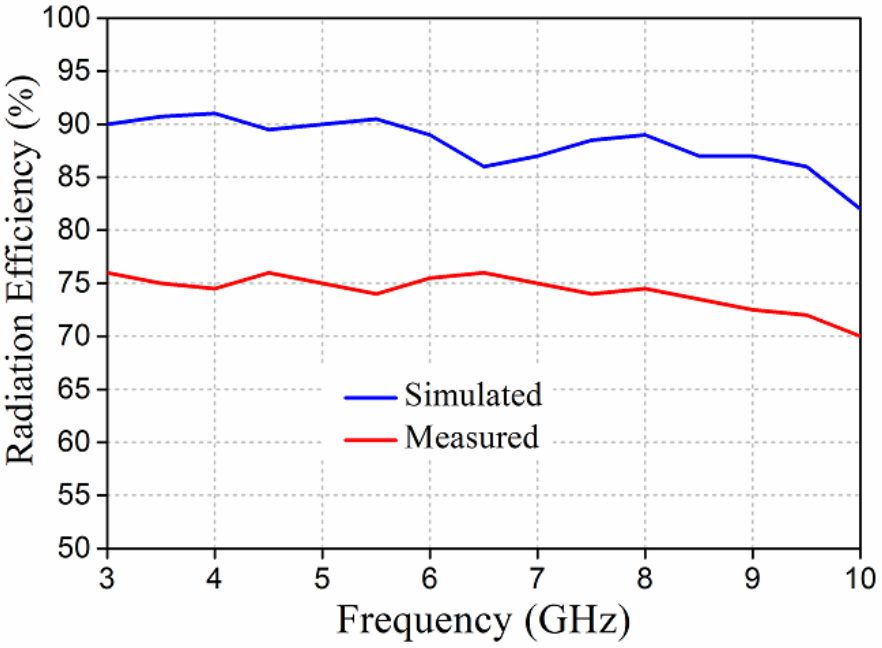
Radiation Efficiency (%)
Frequency (GHz)
Simulated
Measured

(b)

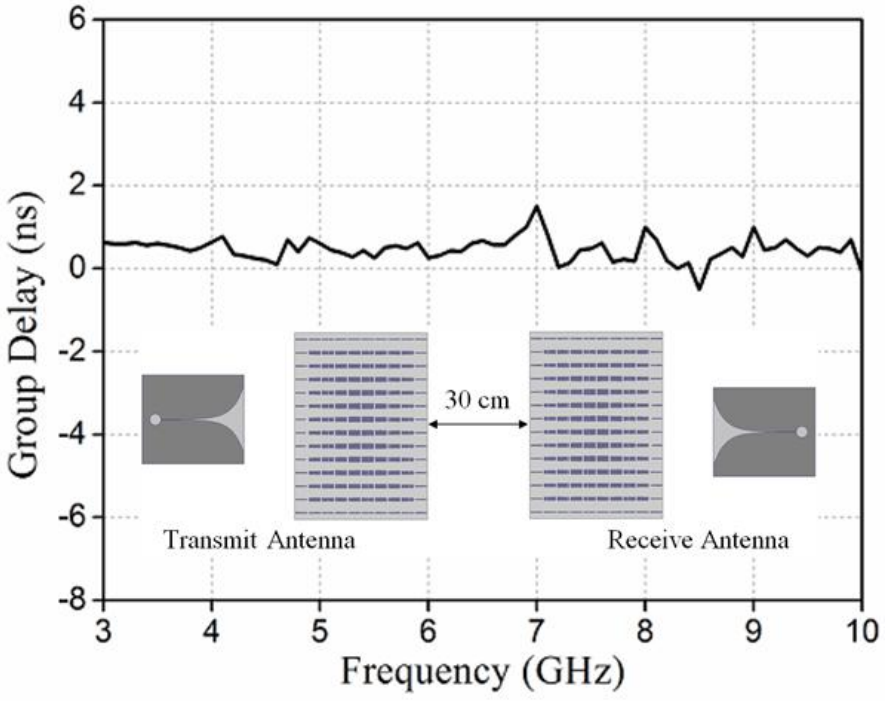

(c)

Figure 4.25 (a) Simulation and measurement results gain of the of the basic TSA and GRIN TSA, (b) variation of measured and calculated radiation efficiency with frequency of the GRIN TSA, and (c) variation of measured group delay of the GRIN TSA.

The calculated and measured results of the radiation efficiency for GRIN TSA are shown in Figure 4.25(b). The aperture efficiency is also calculated with respect to the directivity from the following equation [92],

$$e_{apt} = \frac{D^2 \lambda^2}{4\pi A} \tag{4.4}$$

By calculating from the above equation (4.4), the aperture efficiency is relatively high due to the low area (*A*) of the meta surface lens. The radiation efficiency of the GRIN lens antenna (e_{rad}) is calculated with the antenna realized gain (G) and directivity (D) [93], $e_{rad} = G/D$, which is varying approximately around 85-90% over the operating frequency band. The measured radiation efficiency is varying approximately between 70-75% over the frequency band 3-10 GHz, indicating that the low radiation losses are achieved by the lens. In practical cases, some of the power fed to the antenna terminals is always lost. Moreover, energy is lost in the dielectric material of the antenna and creates unintended heat. Together,

these losses lead to situations where the antenna radiated efficiency in actual operation is always less than the ideal simulation result.

For UWB antenna, the frequency dependent parameters are not sufficient for validating the design. Therefore, the time domain characteristic of the fabricated GRIN monopole is also tested. So, two GRIN antennas are arranged face-to-face with a distance 30 cm and connected to the ports of the vector network analyzer (VNA). The antenna is giving almost stable group delay performance with a fluctuation approximately ±1.2 ns in the desired band, indicating that a transmitted signal will not be seriously distorted by the proposed antenna as shown in Figure 4.25(a).

4.5 MTM physically integrated with TSA

4.5.1 Design of tapered slot antenna

The geometry of the basic tapered slot antenna (TSA) structure with top and bottom views are demonstrated in Figure 4.17. It is fabricated on Rogers RO4003 PCB material with relative permittivity as 3.55 and thickness of 0.8 mm. The microstrip line with impedance transition techniques (50 Ω to 100 Ω) is applied to feed the antenna for impedance matching. The taper section is calculated by the expression which is given below,

$$y = \pm\left(0.02\, e^{0.15x} + 0.07\right) \tag{4.5}$$

where, 0.1 mm ≤ y ≤ 15 mm and 2.5 mm ≤ x ≤ 41.5 mm.

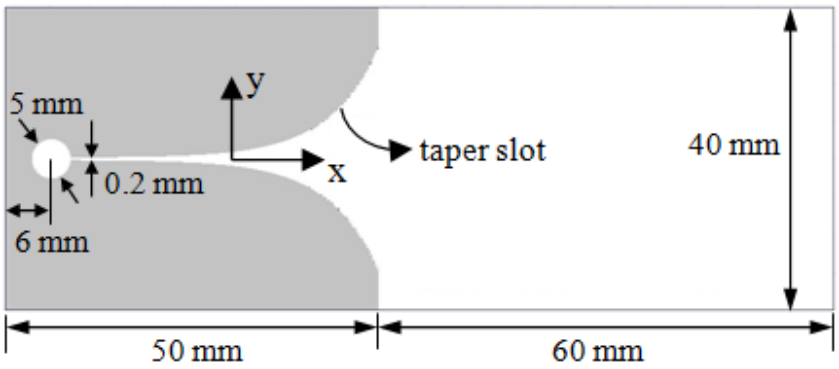

(a)

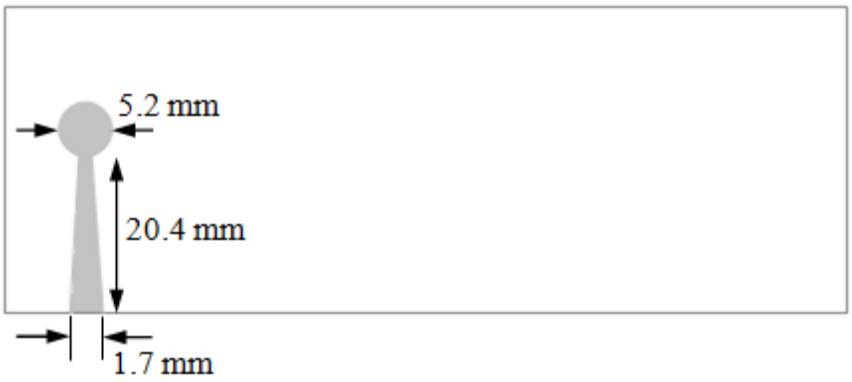

(b)

Figure 4.26 Geometry of the reference TSA, (a) Top view and, (b) Bottom view

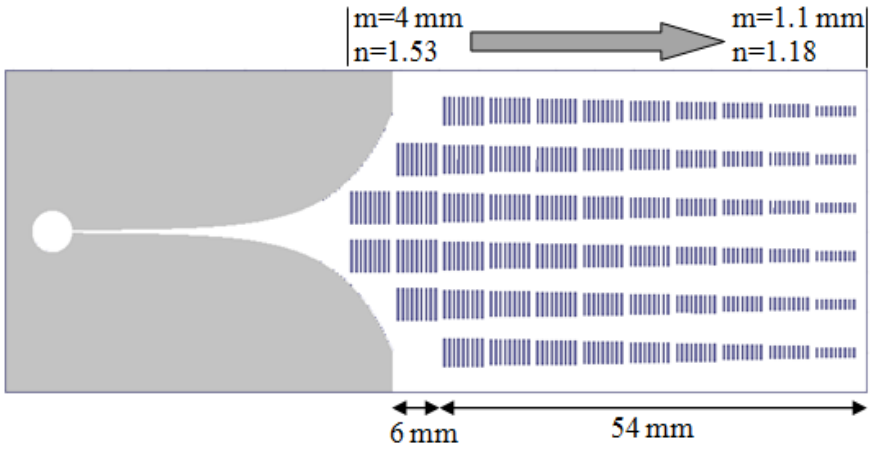

Figure 4.27 Metamaterial GRIN integrated TSA

The proposed metamaterial lens integrated TSA is shown in Figure 4.27. The various refractive index metamaterials are placed in front of the TSA. The phase velocity (v_{ph}) of any medium is inversely proportional to the refractive index of that medium (v_{ph}=c/n, where n=refractive index of the medium). In case of basic TSA, the EM wave is propagating on tapered slot with constant phase velocity and refractive index of antenna substrate ($n_{ant} = \sqrt{\varepsilon_{ant}} = 1.88$). The effective refractive index of the antenna also varies near to 1.8 without using metamaterials. But, the refractive index in the metamaterial area is varying from 1.53 to 1.18 over frequency band 2 to 12 GHz i.e. the MTM refractive index is lowest at the end of the antenna. It is clear that the phase velocity of the EM wave in the proposed metamaterial region is much greater than the antenna substrate. Hence, the radiated beam of the basic TSA will be more directive with narrow beam width, when an EM wave enters the

artificial material region. In this way the proposed material behaves like a beam focusing lens. The variation of refractive index is given in Table 4.1.

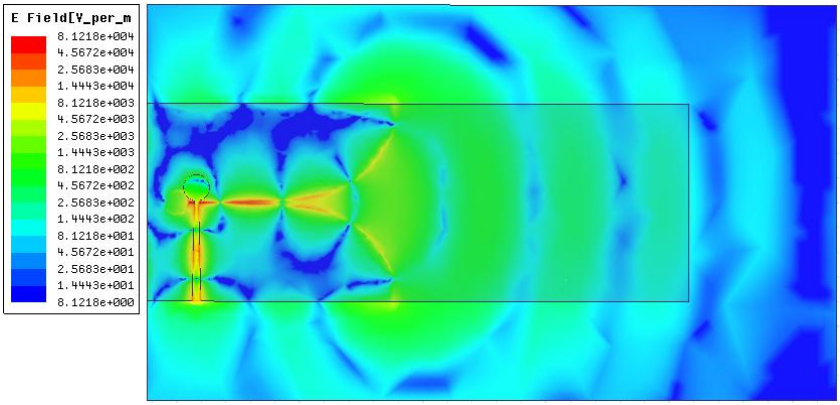

(a)

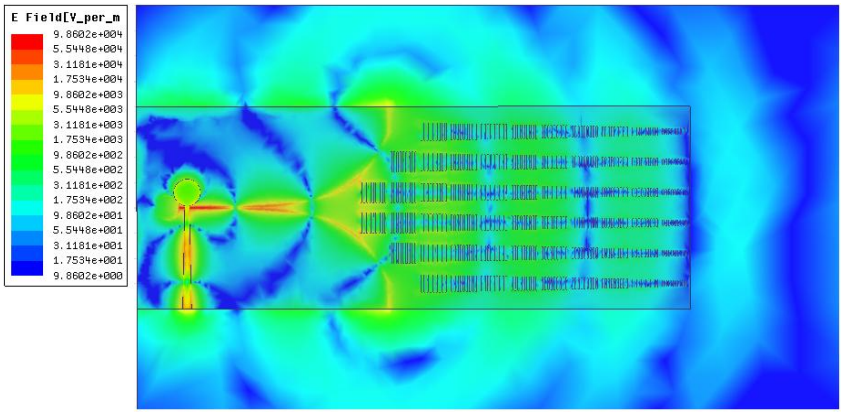

(b)

Figure 4.28 Electric field distributions at 9 GHz, (a) Reference TSA and (b) GRIN TSA.

To understand the effect of metamaterial lens, the GRIN TSA is simulated in the 3D EM software HFSS 15. The electric-field distributions with and without unit cell metamaterial structure in GRIN lens are depicted in Figure 4.28. So, it can be noticed that the lens makes radiated EM wave more uniform than reference antenna in the direction of the x-axis at 9 GHz. The phase velocity of the surface wave is increased at the area of metamaterial lens. Therefore, the beam-width and the side lobe levels are reduced.

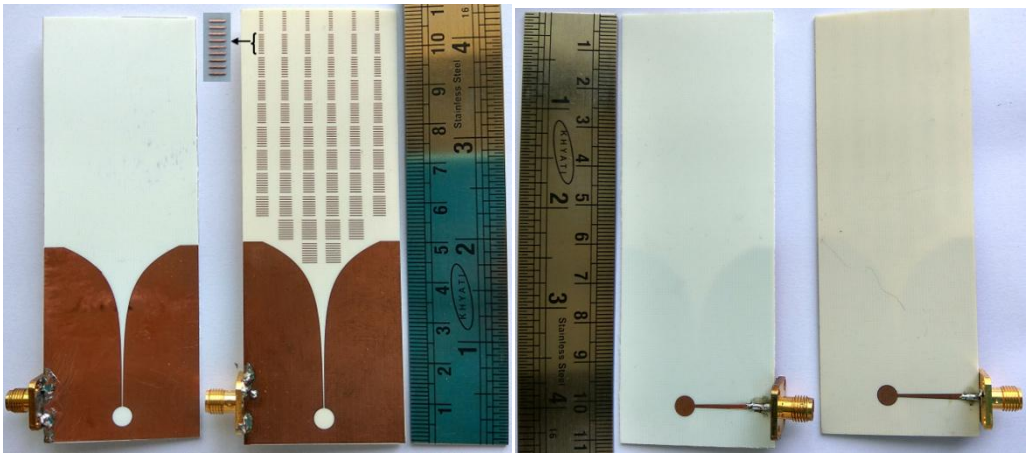

reference TSA GRIN TSA reference TSA GRIN TSA

(a) (b)

Figure 4.29 Photographs of the reference TSA and GRIN lens TSA (a) top view and (b) bottom view.

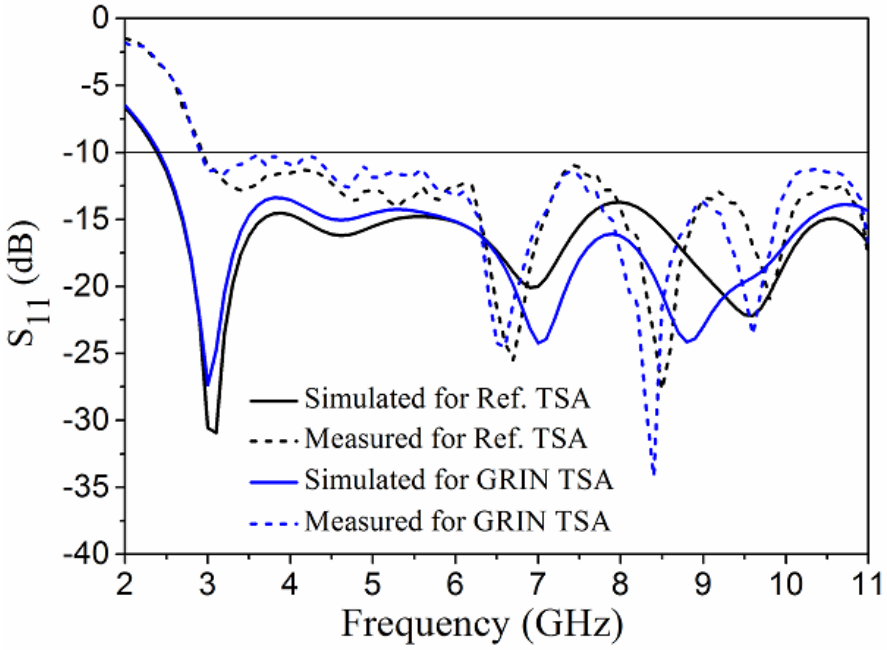

Figure 4.30 Simulated and Measured reflection coefficient of reference and GRIN TSA

4.5.2 Results and Discussions

The fabricated reference and GRIN TSA are shown in Figure 4.29. The simulated and measured reflection coefficients (S_{11}) for both TSA is illustrated in Figure 4.30. The S_{11} of the antennas less than –10 dB for the frequency band 3–11 GHz. Moreover, the S_{11} is varying near –10 dB for the frequency band 3–4.5 GHz.

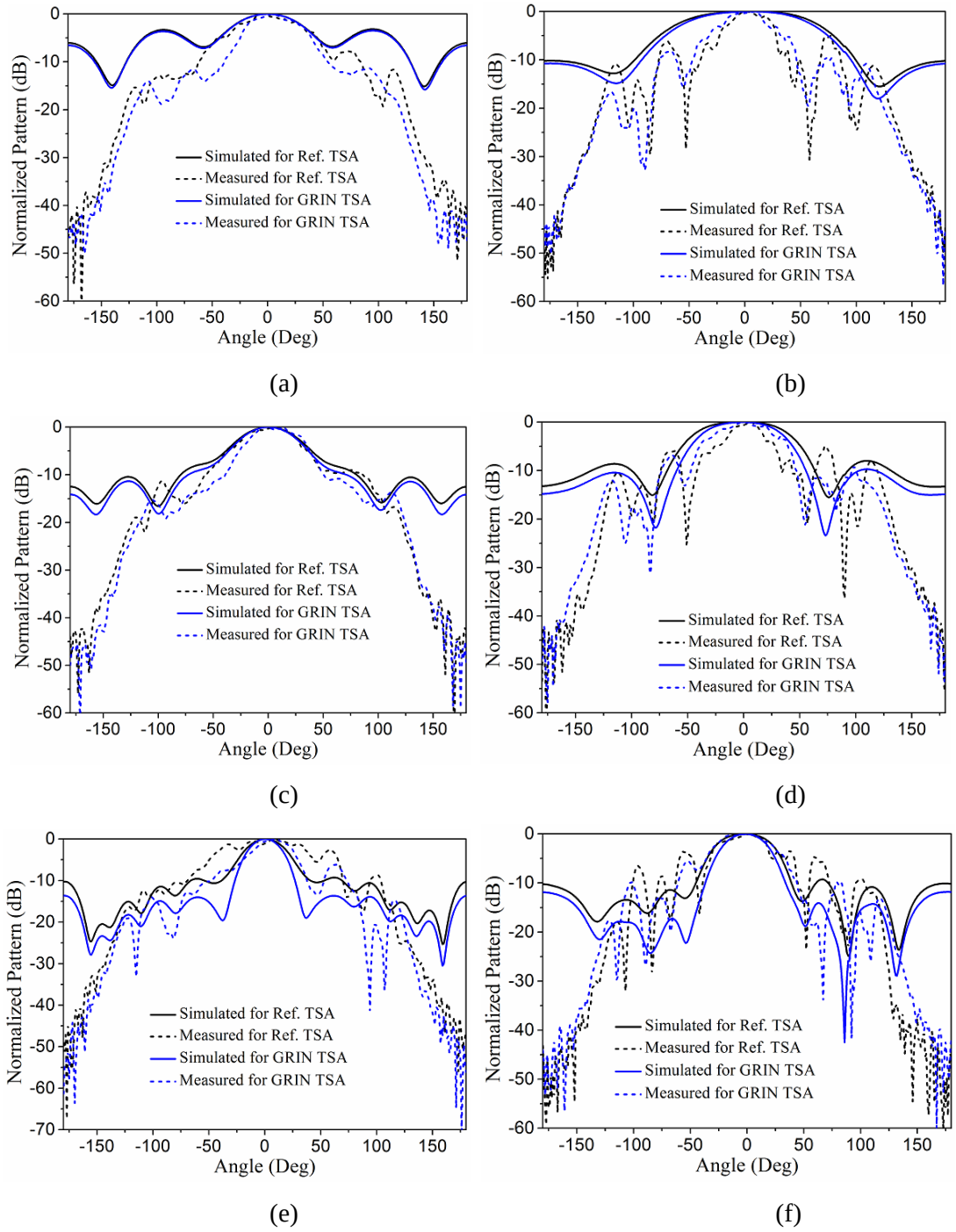

Figure 4.31 Simulated and measured normalized radiation patterns of the reference TSA and GRIN TSA at (a) xy-plane for 3.5 GHz, (b) xz-plane for 3.5 GHz, (c) xy-plane for 6 GHz, (d) xz-plane for 6 GHz, (e) xy-plane for 10 GHz, (f) xz-plane for 10 GHz. The xy-plane and xz-plane denotes E and H-plane, respectively.

The simulated and measured normalized radiation patterns of the antennas are compared at the frequencies of 3.5 GHz, 6 GHz, 8 GHz and 10 GHz in Figure 4.31. The E-plane and H-plane patterns are denotes as xy-plane and xz-plane, respectively. The simulated radiation

patterns show that the 3 dB beam widths of the antennas are becoming narrow after using GRIN metamaterial. The measured E-plane radiation pattern achieved a narrow beam width compared to H-plane by using a GRIN lens. It can be also observed that the side lobes level fluctuations in the H-plane patterns are high for the basic TSA which has been reduced by using GRIN. The simulated and measured gains of the basic TSA and GRIN antennas are obtained in the direction of the x-axis as illustrated in Figure 4.32. The gain of the basic TSA is increased by 2.1 dB at 9.5 GHz using GRIN lens...

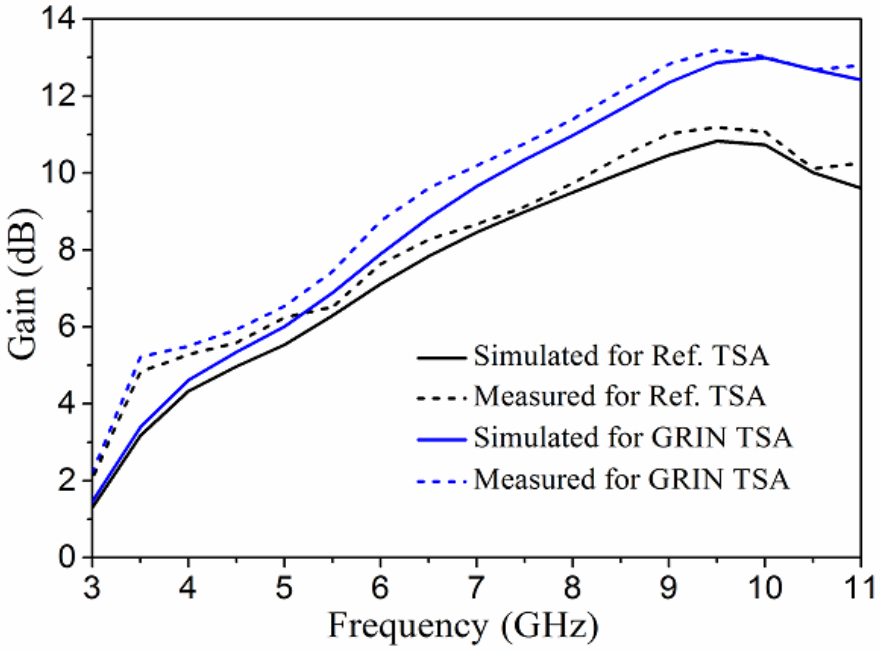

Figure 4.32 Simulated and measured gain of the reference TSA and GRIN TSA at the direction of x axis.

For UWB antenna, the frequency dependent parameters are not sufficient for validating the design. Therefore, the time domain characteristic of the fabricated GRIN monopole is also tested. So, two GRIN antennas are arranged face-to-face with a distance 30 cm and connected to the ports of the vector network analyzer (VNA). The antenna is giving almost stable group delay performance with a fluctuation approximately ±1.2 ns in the desired band, indicating that a transmitted signal will not be seriously distorted by the proposed antenna as shown in Figure 4.33. The proposed antenna is more compact with respect to the references [40], [84] and gain is enhanced compared to the reference [96].

Table 4.6 Comparison between proposed antenna and existing work

Reference	Size (mm^2)	Peak Gain (dB)
[40]	140×80	14
[88]	77×42	12
[84]	190×130	15
[96]	36×36	8
Proposed antenna	110×40	13

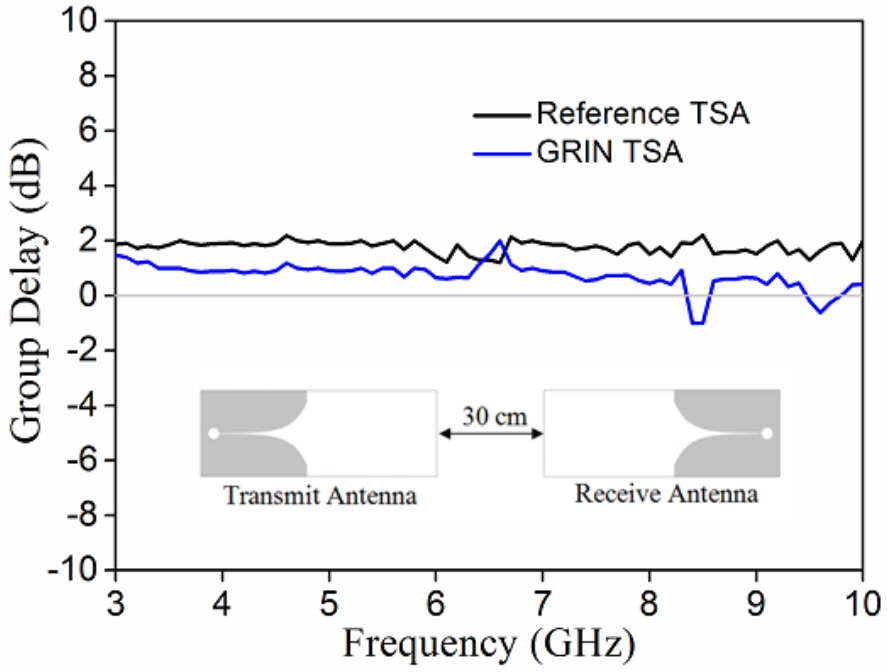

Figure 4.33 Measured group delay performance of the GRIN TSA.

4.6 Conclusions

In this chapter, the directive beam of the printed monopole and TSA antenna is augmented with a broadband GRIN parallel-line metamaterial. The simulation and measurement results of the fabricated antenna are compared. The radiated beam is more directive by using beam focusing lens metamaterial. The efficiency and time domain characteristics are also measured and are observed to be giving satisfactory results. All antennas are compared with the published literature in terms of size, bandwidth and gain.

Hence, the proposed antennas are good candidates for ultra-wideband communication systems.

Chapter-5

Band notch characteristics with artificial material integrated UWB TSA

5.1. Introduction

An ideal UWB antenna is required to transmit without causing interference to the existing services. But some narrow band applications, such as WiMAX, WLAN and ITU bands are existing under UWB frequency band. So, these narrow band services are prone for serious electromagnetic interference (EMI) during UWB communication transmission. These narrow band frequencies are to be notched for a better UWB antenna design.

Lee D. H. et al proposed tapered slot antenna (TSA) with dual band-notched characteristics at 3.5/5.5 GHz for ultra-wideband communication [97]. To realize this, a pair of C-shaped stub is printed beside the feed line. Archimedean spiral-shaped slot is created at the radial stubs of microstrip-slotline transition line. The VSWR spikes within 3.1-4.0 GHz and 5.1-6.2 GHz. But the gain is decreased at high frequencies.

K. A. Alshamaileh et al introduced an ultra-wideband (UWB) antipodal Vivaldi antenna (AVA) with high-Q stopband characteristics using an electromagnetic bandgap (EBG) structure [98]. Two pairs of EBG cells are printed along the antenna feed line to suppress the frequency components at 3.6-3.9 GHz (WiMAX) and 5.6-5.8 GHz (ISM bands) which is verified experimentally. But the gain is positive at the notched frequency band. It means that the radiation is not suppressed significantly at notch frequency.

X. Liu et al applied a complementary split ring resonator (CSRR) on a UWB Vivaldi antenna to eliminate some unwanted narrow band services [99]. The CSRR is placed in several areas of the antenna, namely feeding area, transition-area and the rest of the area, where CSRRs are proved to have little effect on the antenna bandwidth property. A band is rejected within 4.8 to 5.4 GHz and this is verified by measured results. But the gain is decreased at high frequencies due to the harmonic effects of the CSRR resonator.

To overcome this problem, M. Bhaskar et al presented a band notch characteristics (WLAN/WiMAX) on tapered slot ultra-wideband (UWB) Vivaldi antenna [100]. The band-notch operation is achieved at 4.8 GHz with the help of specially designed complementary split ring resonator (CSRR). The CSRR cell is placed near the excitation point of the antenna. But the gain is reduced significantly at high frequencies. So, the gain of the designed antenna is enhanced with the help of anisotropic zero index metamaterial cells. It can be noticed that the gain is 3 dBi at the notch frequency which indicates that the radiation is still present at notch frequency.

D. O. Kim et al proposed a triple-band notched ultra-wideband CPW-fed monopole antenna using meander shaped stubs, the two rectangular complementary split ring resonators (CSRRs) and an inverted U-shaped slot [101]. The meander line stub is added on the top of the radiating patch and the two CSRR slots are created on the feed line. The inverted U slot is placed on the center of the patch. Proposed antenna satisfies the requirement on return loss, -10 dB over the UWB band (3.1- 10.6 GHz) and rejected the WiMAX, IEEE802.11a/n, and ITU 8 GHz band.

Y. C. Lin et al presented an ultra-wideband aperture antenna with extended band-notched designs [102]. The band-notch is obtained using isolated slit, open-end slits and parasitic strips. The band notch is achieved over the frequency band 5-6 GHz.

F. Zhu et al introduced elliptically tapered slot antenna with arc-shaped parasitic strip printed inside the circular slot (balun) [103]. The signal is rejected at 5-6 GHz. But the measured gain is 4 dBi over the operating frequency band and suppressed up to -13 dBi at 5.5 GHz.

In this chapter, the ultra-wideband tapered slot antenna is introduced to band notch WLAN band using SRR slot and gain is enhanced by using artificial material or metamaterial. The ITU band is rejected with the help of electric-field coupled resonator.

5.2 Band Notched Function in UWB Antenna

It is well known that UWB communication systems are very popular for their increased channel capacity and high data rate transmission.

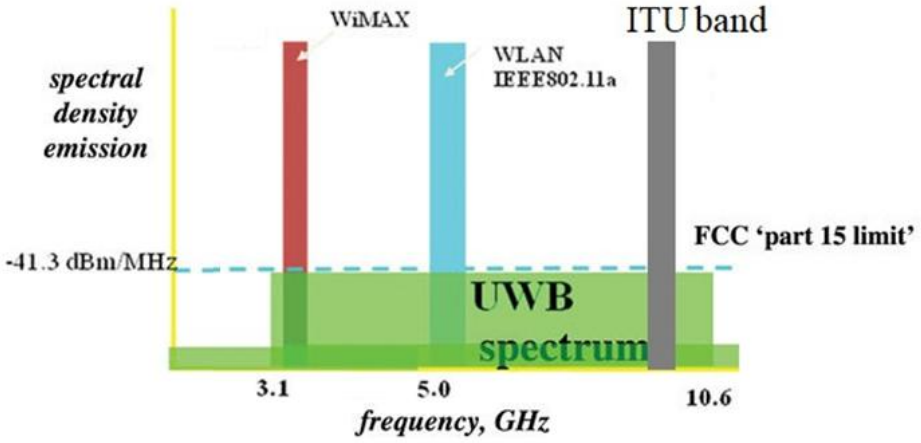

Figure 5.1 Narrow band application within UWB spectrum

Interferences exist with narrow frequency bands (WiMAX at 3.3-3.6 GHz, WLAN at 5.15-5.35 GHZ and 5.725-5.825 GHz, and ITU at 7.9-9.1GHz) within the UWB spectrum, as shown in Figure 5.1. Different methods are available to the notch narrow frequency bands such as bandpass filters. Generally, the band notch has been obtained by adding a bandstop filter. But these techniques have increased the cost and physical size. Hence, resonant structure is designed by inserting slots and slit to remove narrow band in UWB antenna.

The inserting slot method is well known to obtain the frequency band notched function in UWB antenna. Slots are used in different locations in the UWB antenna such as feeding line, radiating elements and ground plane.

5.3 Band notch Tapered slot antenna with artificial material

5.3.1 Design of Tapered slot antenna

The geometry of the basic tapered slot antenna (TSA) structure with top and bottom views are demonstrated in Figure 5.2. It is fabricated on Rogers RO4003 PCB material with relative permittivity as 3.55 and thickness of 0.8 mm. The dimensions of the basic TSA are about 40 × 46 × 0.8 mm^3. The microstrip line with impedance transition techniques (50 Ω to 100 Ω) is applied to feed the antenna for impedance matching. The broad and narrow microstrip line widths are calculated as W_{f2} = 1.7 mm and W_{f1} = 0.8 mm, respectively. The microstrip to slotline transition is realized by etching the slotline on one side of the substrate. An exponential slot radiator is printed on the opposite side of the substrate. The microstrip line crosses below and perpendicular to the slotline. After crossing, the microstrip line is

connected to the circular radial stub which acts as a wideband, virtual short circuit. The exponential inner curves is designed by the following equation,

$$y = \pm\left(c_1 e^{Rx} + c_2\right) \tag{5.1}$$

where $c_1 = \dfrac{y_2 - y_1}{e^{Rx_2} - e^{Rx_1}}$ and $c_2 = \dfrac{y_1 e^{Rx_2} - y_2 e^{Rx_1}}{e^{Rx_2} - e^{Rx_1}}$

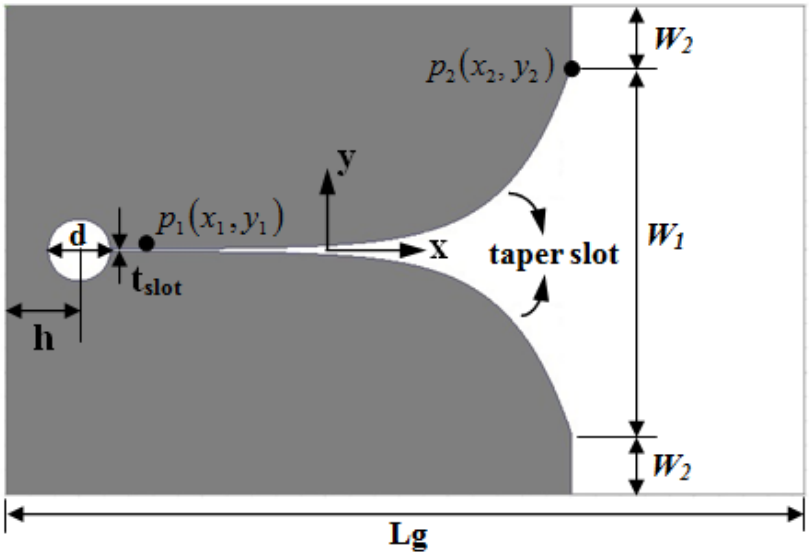

(a)

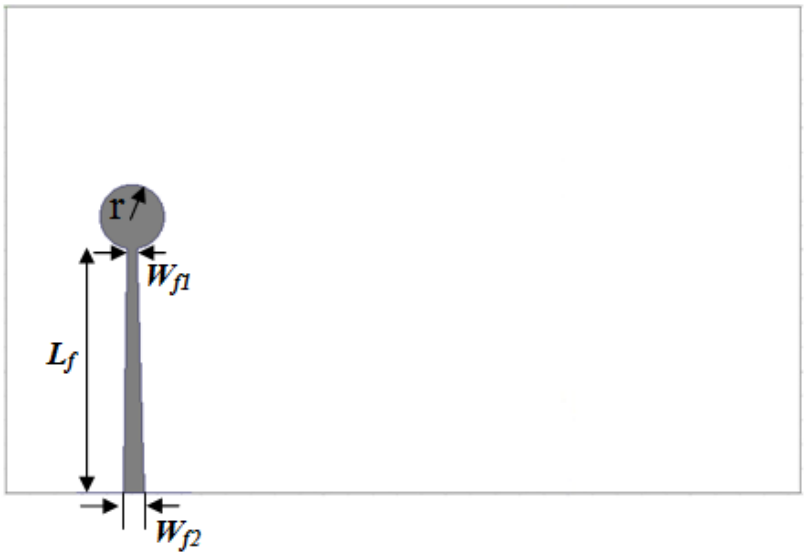

(b)

Figure 5.2 The Geometry of the basic TSA, (a) Top view, (b) Bottom view.

The points $p_1(x_1,\pm y_1)$ and $p_2(x_2,\pm y_2)$ are shown in Figure 5.2(a), where R is the exponential rate which controls the shape of the slot. From the equation (5.1), the ranges of x and y axes of the slot are 2.5 mm $\leq$ x $\leq$ 37.5 mm and 0.1 mm $\leq$ y $\leq$ 15 mm, respectively. The optimized dimensions of the basic TSA are shown in Table 5.1.

Table 5.1 The optimal parameters of the basic TSA

Parameters	**Unit (mm)**	**Parameters**	**Unit (mm)**
Lg	65	t_{slot}	0.2
W_1	30	*r*	2.6
W_2	5	L_f	20.4
h	6	W_{f1}	0.8
d	5	W_{f2}	1.7

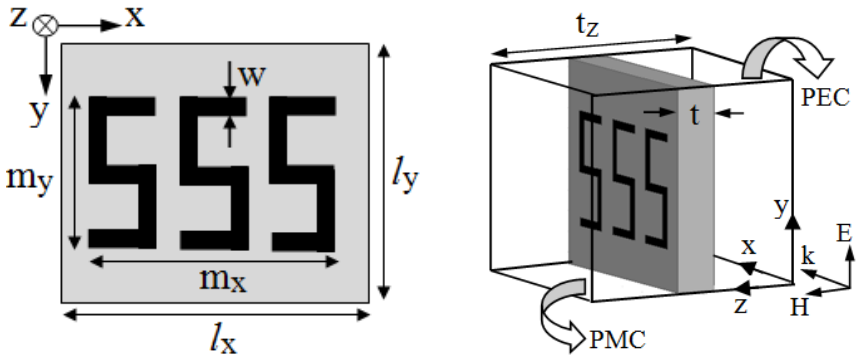

(a) (b)

Figure 5.3 The geometry of unit cell artificial material, (a) Unit cell artificial material (b) The simulation model. The dimensions of parameters are l_x = l_y = 5 mm, m_x = 2.8 mm, m_y = 4 mm and *w* = 0.2 mm, *t* = 0.8 mm and t_z =5 mm.

5.3.2 Design and Characteristics of Broadband Artificial Material

The resonant metamaterial structures are highly dispersive with considerable loss near the resonant frequency, which is not suitable for applications where broad bandwidth and low loss are required. So, non-resonant metamaterial elements provide almost non-dispersive effective constitutive parameters with negligible loss. The proposed material is fabricated on the single side of the dielectric material Roger RO4003 with dielectric constant 3.55, thickness of 0.8 mm. The unit cell metamaterial is designed with non-resonant parallel

metallic lines on the substrate as shown in Figure 4.2(a). The dimensions of the unit cell are taken as

$$l_x = l_y = \lambda_0 / 8.3 \tag{5.2}$$

where, $\lambda_0 = c/f\sqrt{\varepsilon_r}$ at f=6 GHz.

To extract the values of effective parameter, the scattering object is replaced by a homogeneous medium, i.e. wavelength within the medium becomes large in terms of the unit cell size [87], [88]. To evaluate the scattering performance, the simulation model of the single unit cell is shown in Figure 4.2(b). The perfect electric conductor (PEC) and perfect magnetic conductor (PMC) boundary conditions are also defined. The electric and magnetic polarizations are along the y and z-axes, respectively. The EM wave will propagate along the x-axis.

From the effects of electromagnetic properties in the medium, the magnitude and phase response of the scattering parameters are calculated and effective parameters of the propsoed material are extracted from these S-parameters. The proposed artificial material parameters such as effective permittivity (ε_y) and permeability (μ_z) are obtained via retrieval formula as described in [90]. The effective wave impedance (z) and the effective refractive index (n) for the given metamaterial unit cell are obtained from the following equations [90]:

$$z = \pm\sqrt{\frac{(1+S_{11})^2 - S_{21}{}^2}{(1-S_{11})^2 - S_{21}{}^2}} \tag{5.3}$$

$$n = \frac{1}{k_0 d_{eff}}\left\{\mathrm{Im}\left[\ln\left(\frac{S_{21}}{1-S_{11}R_{01}}\right)\right] + 2m\pi - i\,\mathrm{Re}\left[\ln\left(\frac{S_{21}}{1-S_{11}R_{01}}\right)\right]\right\}$$

m=0,1,2,3..... (5.4)

$$\varepsilon_y = n/z \tag{5.5}$$

$$\mu_z = n \times z \tag{5.6}$$

where d_{eff} is the thickness of the virtual homogeneous slab, which replaces the real geometry thickness, k_0 is the free space wave-number of the incident wave and $R_{01} = (z-1)/(z+1)$. Here *m* is an integer related to the branch index of real(*n*) [90].

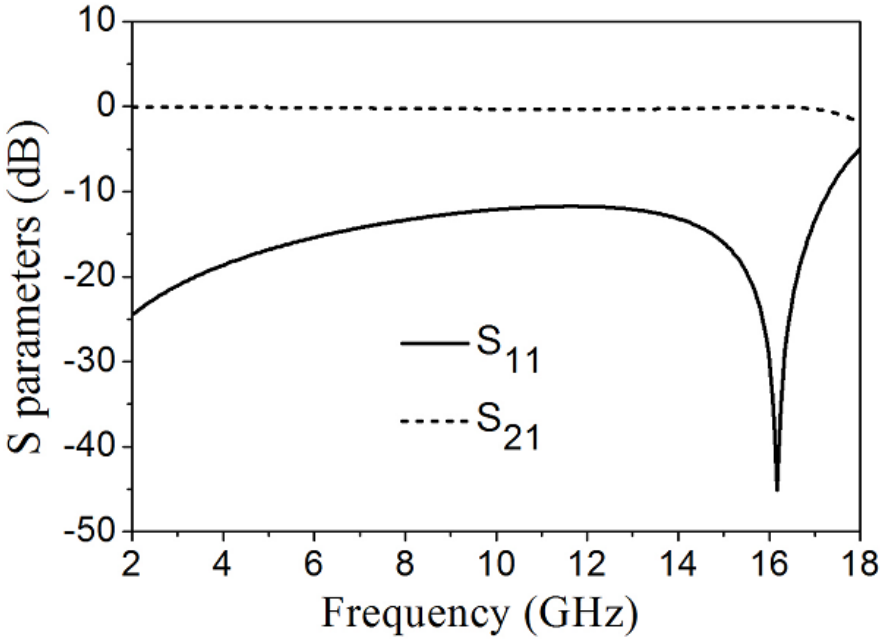

(a)

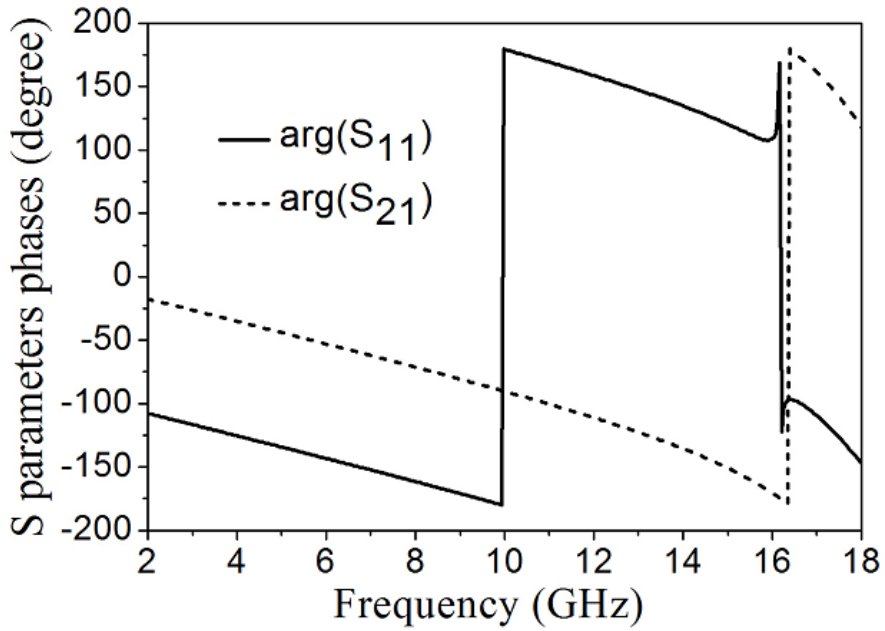

(b)

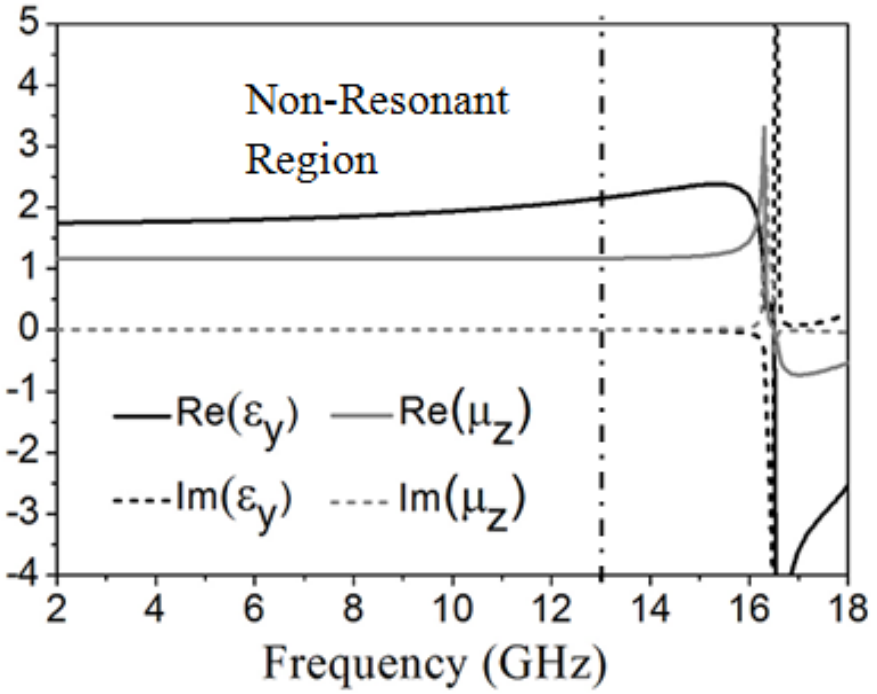

(c)

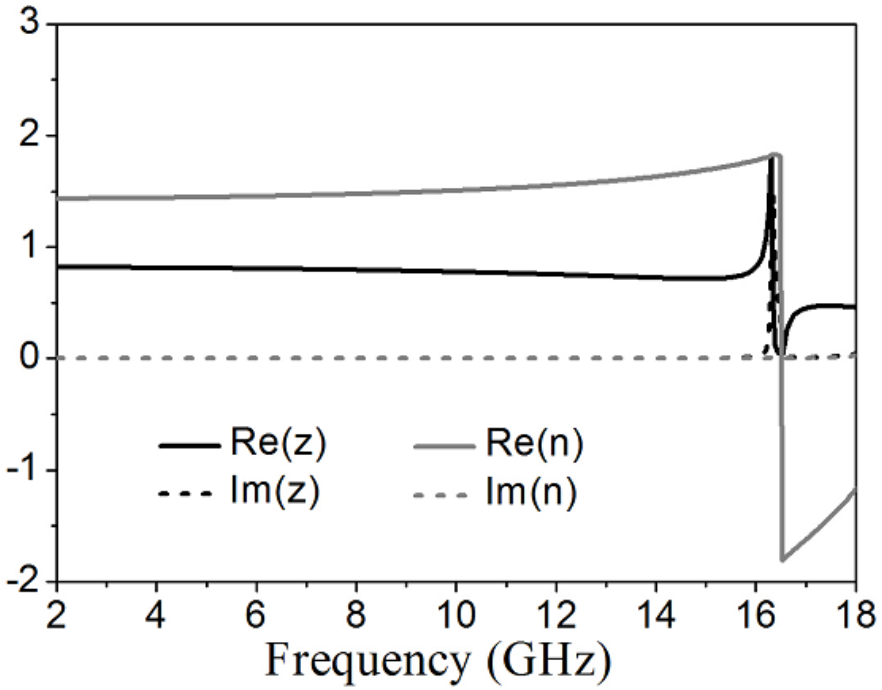

(d)

Figure 5.4 Variation of the parameters of artificial material with respect to frequency, (a) magnitude of scattering parameters, (b) phases of scattering parameters, (c) the effective permittivity (ε_y) and permeability (μ_z), (d) the normalized impedance (z) and effective refractive index (n).

The transmission characteristics of the artificial material are verified by the Ansys HFSS. The magnitude and phase of the scattering parameters of the artificial material are depicted in Figures 5.4(a) and (b), respectively. The reflection coefficient (S_{11}) is less than -10 dB over 2-17 GHz, indicating that the energy can be transmitted through the artificial material within that frequency band. Here, the S-shaped structure is providing longer current path compared to the parallel line non-resonant structure [88]. But the concept of non-resonant metamaterials can be obtained from simple, conducting elements. An electrical resonance occurs for the conductor length due to inductance and capacitance offered by the elements [105]. The resonant frequency of the proposed artificial material occurs at 16 GHz. The proposed material has a non-resonant characteristic over wide frequency band between 2-13 GHz as shown in Figure 5.4(c). The normalized impedance of the artificial material is near to 1 within non-resonant region as illustrated in Figure 5.4(d).

The real and imaginary parts of refractive index are also presented in Figure 5.4(d). The real part of the effective refractive index (n) varies between 1.4-1.5 and imaginary part is near to zero within non-resonant region.

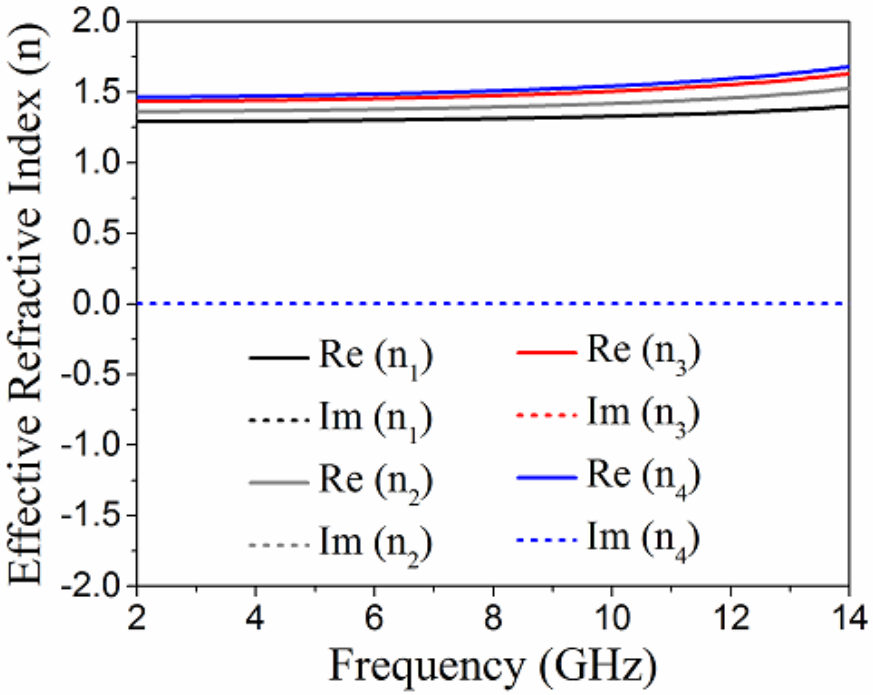

(a)

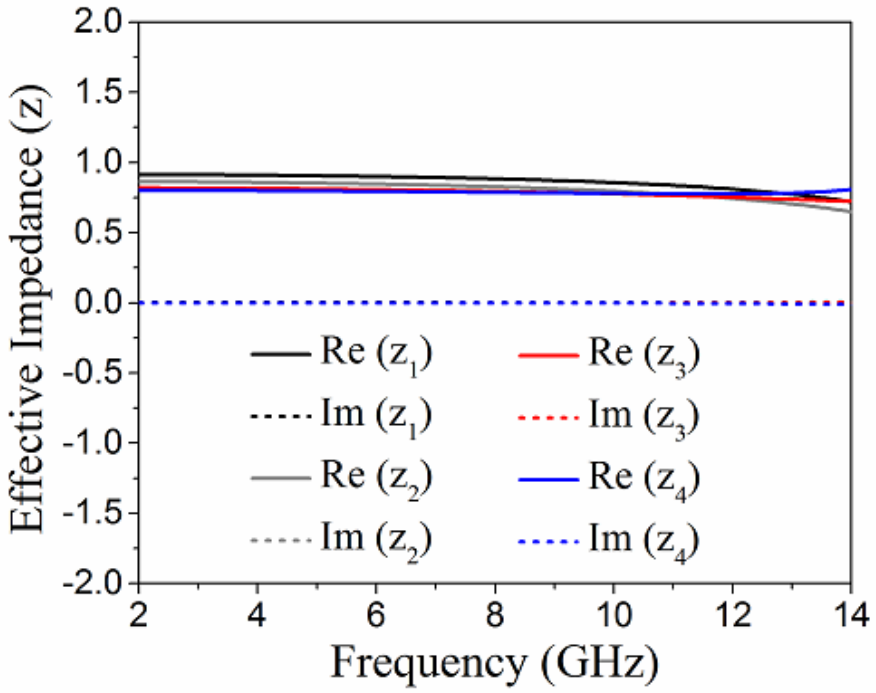
Effective Impedance (z)
Frequency (GHz)
Re (z1)
Im (z1)
Re (z2)
Im (z2)
Re (z3)
Im (z3)
Re (z4)
Im (z4)

(b)

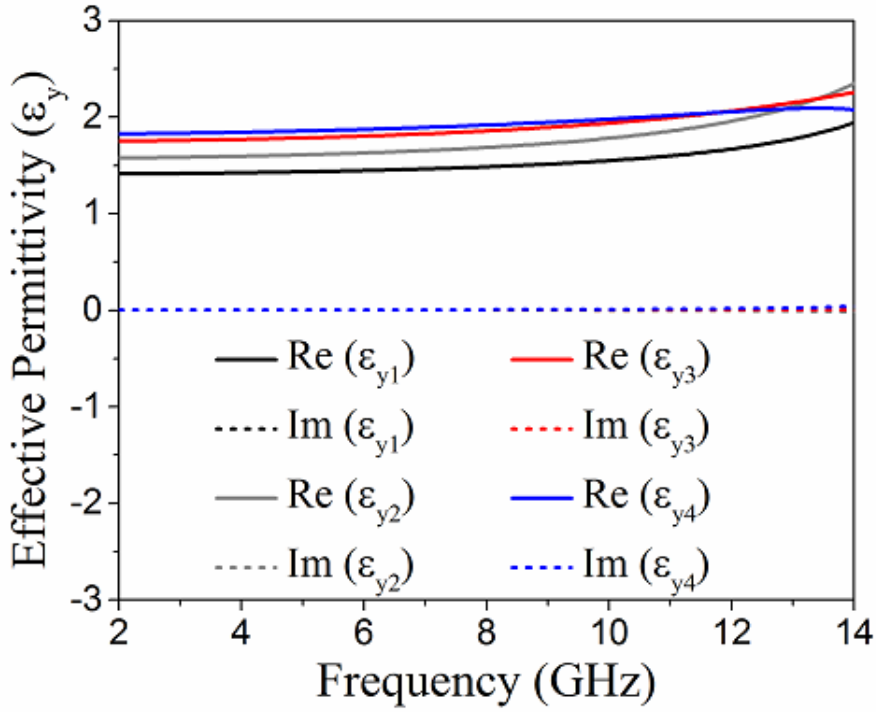
Effective Permittivity (εy)
Frequency (GHz)
Re (εy1)
Im (εy1)
Re (εy2)
Im (εy2)
Re (εy3)
Im (εy3)
Re (εy4)
Im (εy4)

(c)

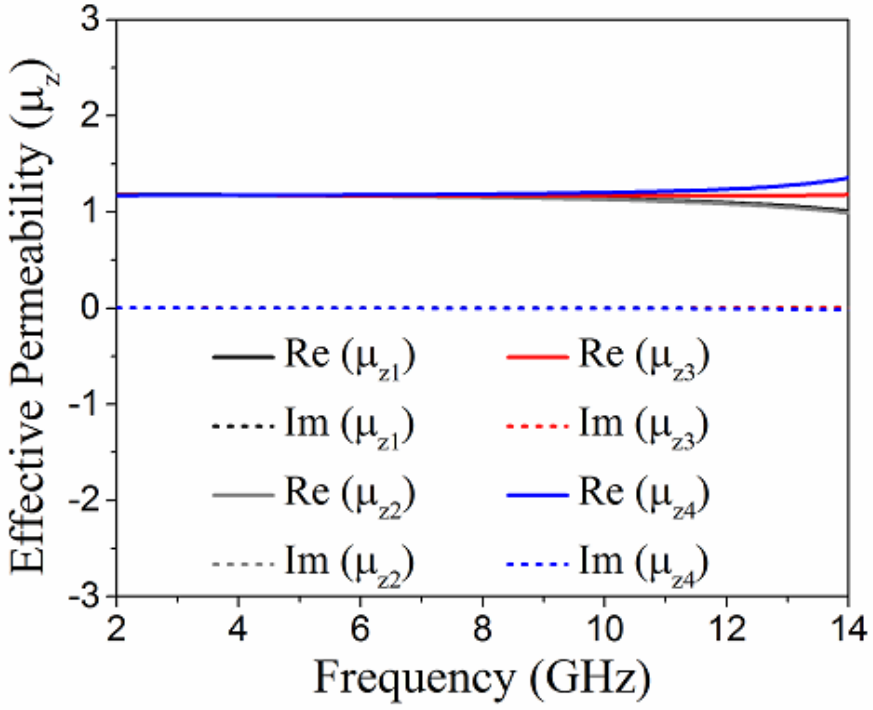

(d)

Figure 5.5 The variation of parameters for the different number of S-shaped structure in the unit cell artificial material with frequency, (a) effective refractive index (n), (b) effective impedance (z), (c) effective permittivity (ε_y), (d) the effective permeability (μ_z).

To understand the effects of the numbers of S structures, the effective parameters for different numbers of S-shaped structures in unit cell are shown in Figures 5.5(a) to (d). The effective refractive index, impedance, permittivity and permeability are denoted as a n_i, z_i, ε_{yi} and μ_{zi}, respectively, where i= 1,2,3,4 i.e. number of S-shapes in unit cell. So, it is clear that the effective refractive index and permittivity are enhanced by increasing the number of S-shape structures in unit cell. But the effective impedance is close to unity by decreasing the number of S-shape structures. Moreover, the effective permeability is almost constant over the frequency band 2-11 GHz.

5.3.3 Analysis and design of SRR Slot in TSA

The SRR is used to create a band notch for the UWB TSA. According to the position of the SRR on the antenna, band notch characteristics will be affected. In case of basic TSA, the operation of the antenna depends on balun, microstrip feeding line. An area near to excitation or input aperture areas of the taper slot is called a transition area. The geometry of

the SRR structure on the radiating patch is depicted in Figure 5.6(a). The length of the substrate is extended up to 19 mm in the modified TSA to accommodate the metamaterial.

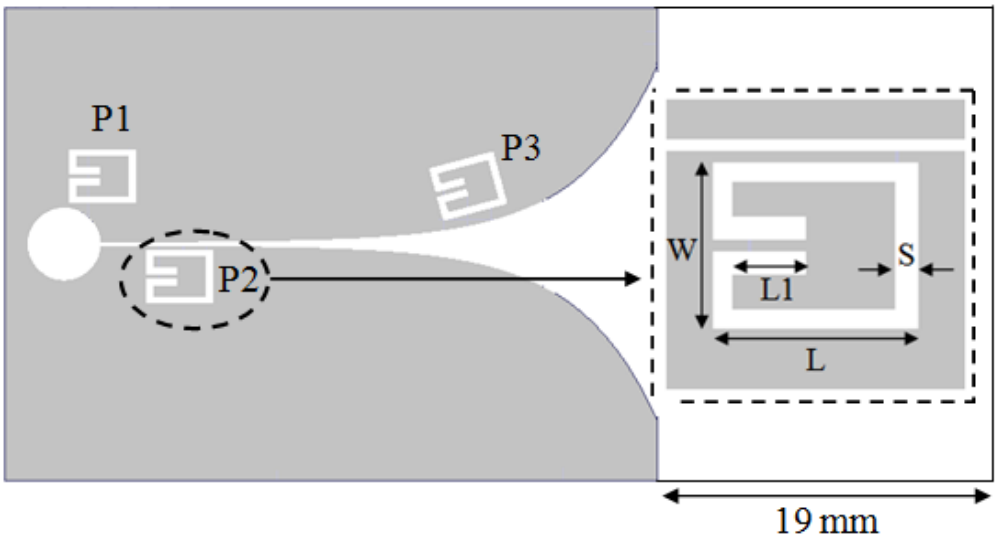

(a)

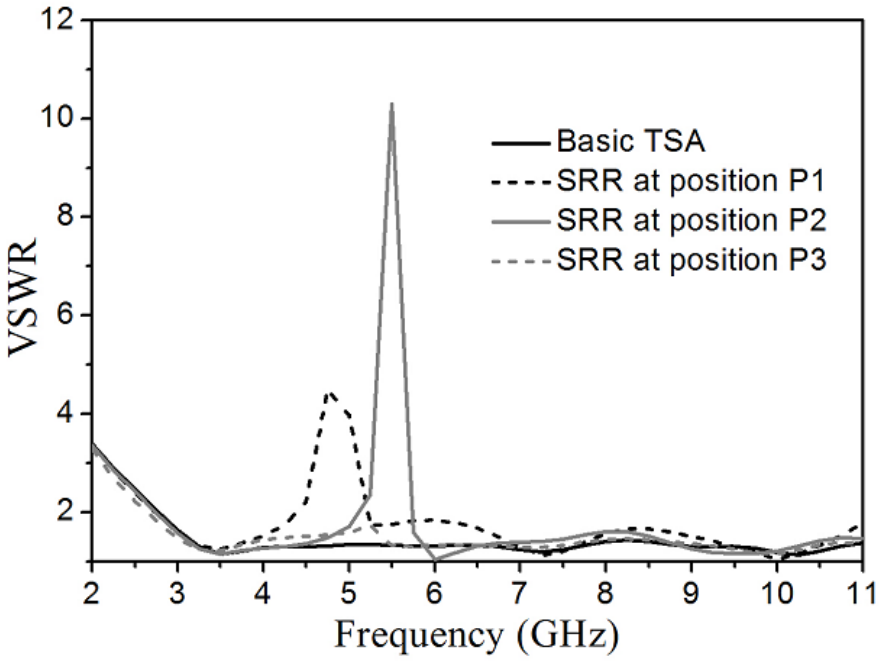

(b)

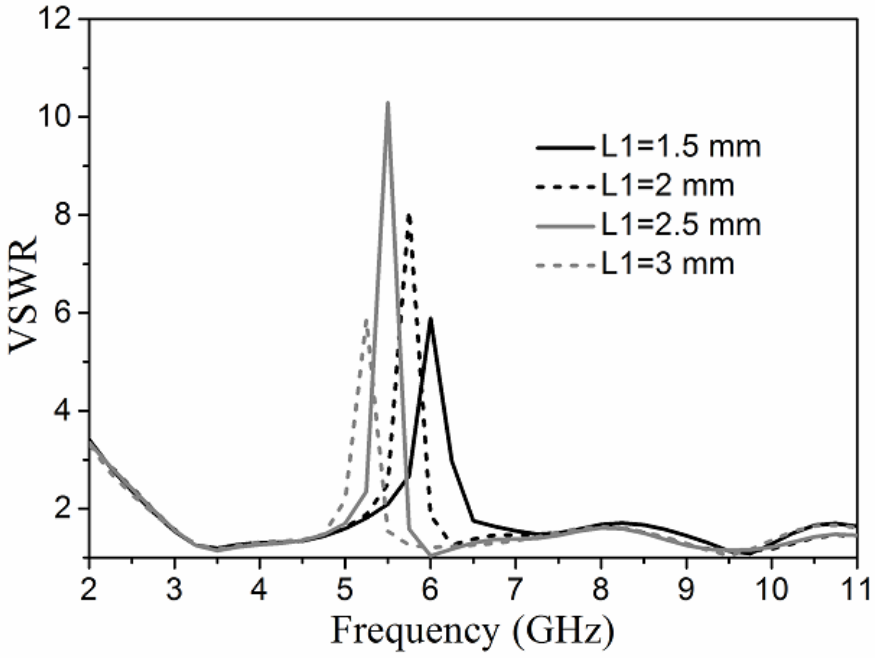

(c)

Figure 5.6 The configuration of SRR slot in basic TSA, (a) Radiating patch with SRR slot in different positions, (b) Corresponding VSWR for SRRs slot in different positions, and (c) Variation of VSWR for the different values of L1. The final dimensions of the SRR unit cell are L=5 mm, L1=2.5 mm, W=3.5 mm, S=0.5 mm.

In order to understand the effects of SRR slot, it is placed at different positions, namely P1, P2 and P3 located in the feeding-area, the transition-area, and the rest area of taper slot, respectively, as shown in Figure 5.6(a). The simulated VSWR of the basic TSA structure where SRR slots are placed at positions P1, P2 and P3 are presented in Figure 5.6(b). It is clear that the basic TSA has a very good impedance matching from 3 to 11 GHz and VSWR spikes at 4.8 GHz, 5.5 GHz for SRR positions P1 and P2, respectively. In case of P3 position, SRR is too far from excitation point. Therefore, the band notch does not work properly. Finally, the WLAN band notch is active, when SRR is etched at the position P2. The electric field is strongly coupled with SRR at the taper slot to create a strong resonance. So, the currents of all working bands are allowed except at the resonant frequency. As a result, a narrow band is suppressed within UWB frequency range. To understand the effects of the current path, the parameter L1 of the SRR slot has been varied as 1.5 mm, 2 mm, 2.5 mm and 3 mm. The VSWR plot is also shown in Figure 5.6(c). It can be seen that the notches are created at 6 GHz, 5.8 GHz, 5.5 GHz and 5.2 GHz for the different values of L1.

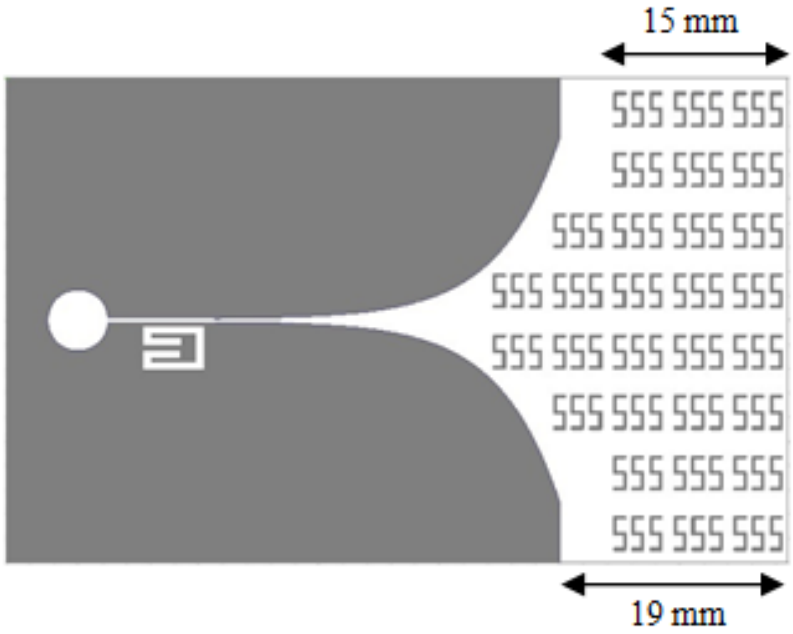

(a)

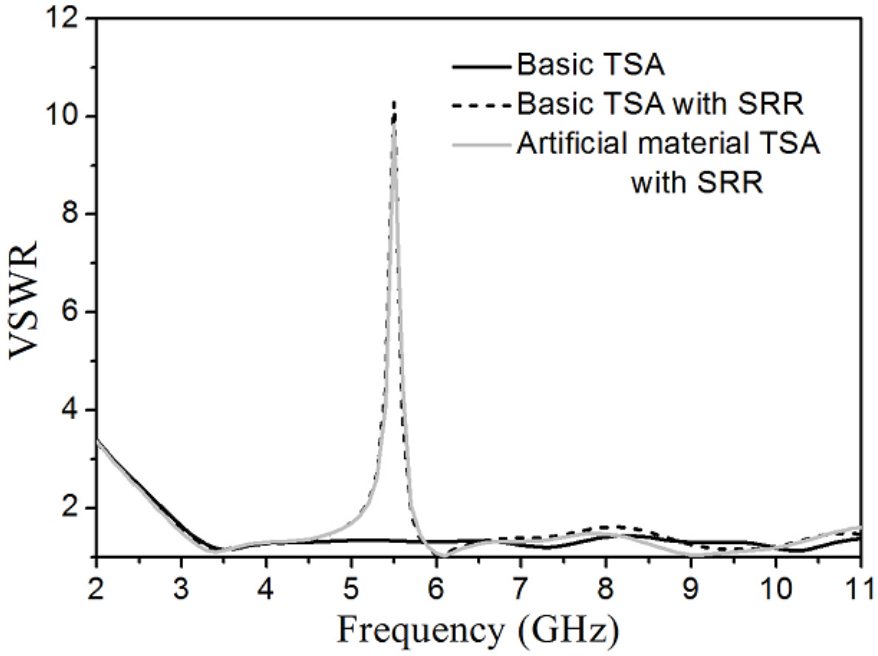

(b)

Figure 5.7 The configuration of artificial material integrated TSA with SRR slot, (a) Artificial material TSA, (b) Comparison of VSWR simulated result for basic TSA, basic TSA with SRR and artificial material TSA with SRR.

5.3.4 Artificial material integrated TSA

In order to understand the effect of artificial material, the proposed material is placed in front of the taper slot area in a periodic fashion. The artificial material loaded TSA with SRR is depicted in Figure 5.7(a). The VSWR comparison of the basic TSA, SRR etched TSA with and without artificial materials is shown in Figure 5.7(b). From this, it is observed that the VSWR is not affected by using artificial material in basic TSA. So, it is considered that the VSWRs for both antennas are notched at the WLAN band. The electric field distribution of the proposed TSA without and with artificial material has been shown in Figures 5.8(a) and (b), respectively. So, it is clear that the electric field intensity of the TSA without artificial material is comparatively lower than that of the artificial material loaded TSA. So, EM wave can travel more distance by using artificial material. The surface current distributions of the artificial material loaded TSA with SRR at position P2 are also shown in Figure 5.8(c). It is clear that the current density is more in the SRR region at 5.5 GHz, it means that the EM wave is suppressed particularly at that frequency.

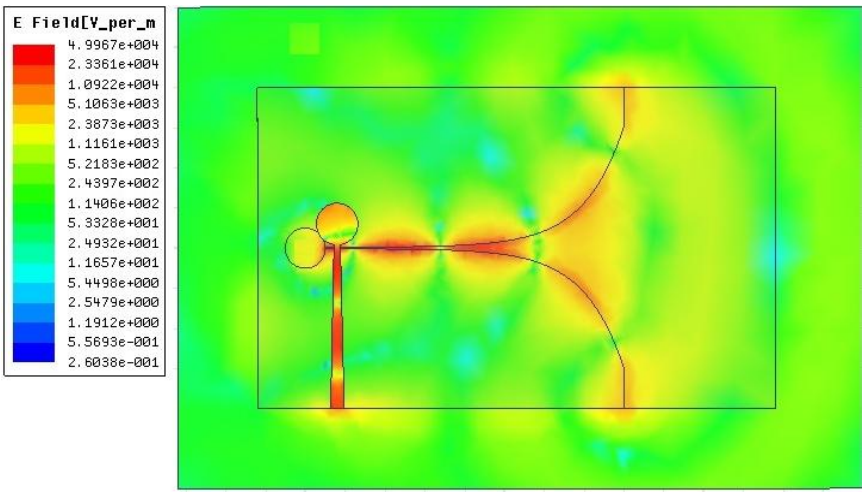

(a)

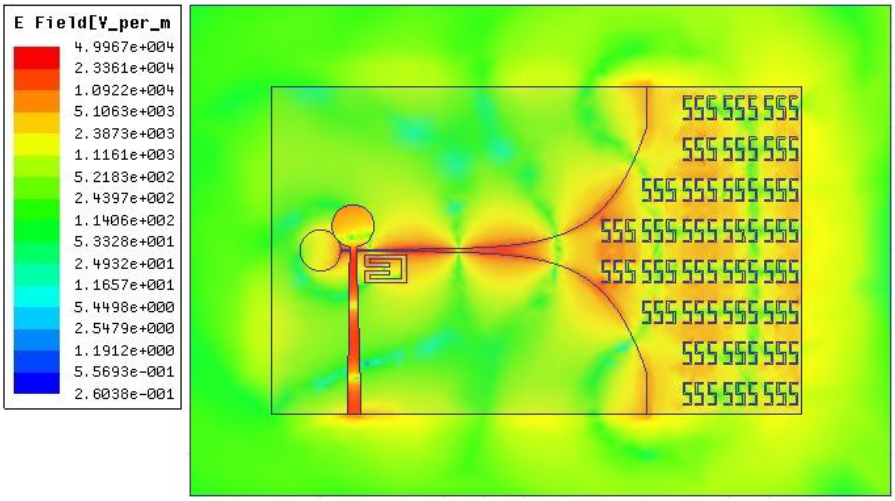

(b)

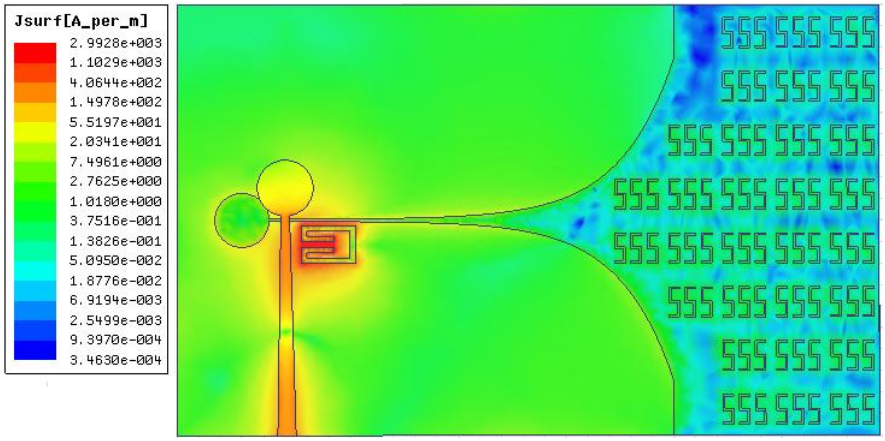

(c)

Figure 5.8 The Field distribution at 10 GHz, (a) Basic TSA, (b) Artificial material cells integrated TSA, and (c) The magnitude of current distribution at 5.5 GHz of the artificial material loaded TSA with SRRs at P2 position.

According to the physics, the phase velocity (v_{ph}) of any medium is inversely proportional to the refractive index of that medium (v_{ph}=c/n, where n=refractive index of the medium). In case of basic TSA, the EM wave is propagating on tapered slot with constant phase velocity and refractive index of antenna substrate ($n_{ant} = \sqrt{\varepsilon_{ant}} = 1.88$) . From the Figure 5.4(d), the simulated effective refractive index of the antenna also varies near to 1.8 without using metamaterials. But, the refractive index in the artificial material area is approximately 1.5 over frequency band 2 to 12 GHz, which is lower than the refractive index of antenna (n_{ant}). It is clear that the phase velocity of the EM wave in the proposed

metamaterial region is much greater than the antenna substrate. Hence, the radiated beam of the basic TSA will be more directive with narrow beam width, when an EM wave enters the artificial material region. In this way the proposed material behaves like a beam focusing lens.

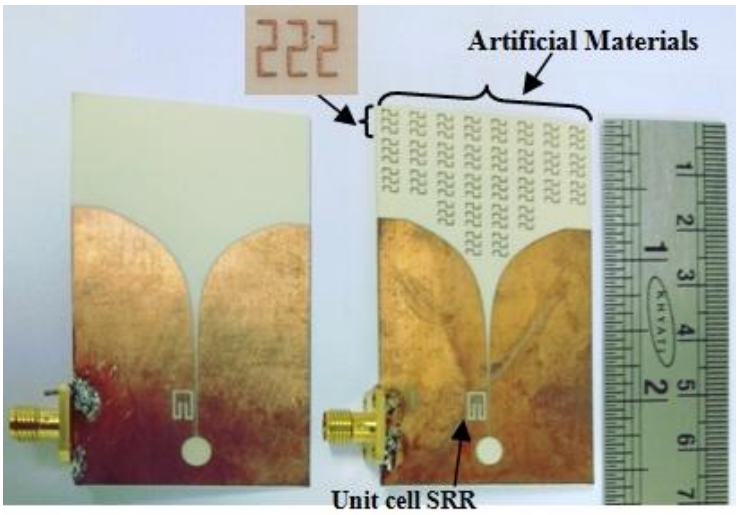

Basic TSA Artificial material TSA with SRR

(a)

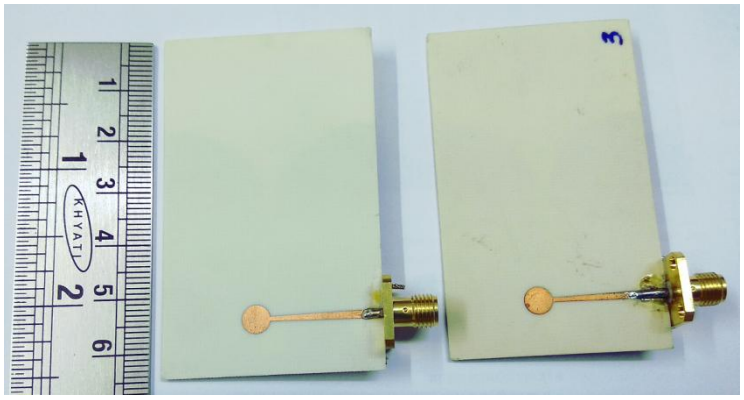

Basic TSA Artificial material TSA with SRR

(b)

Figure 5.9 The Photographs of the fabricated basic TSA and artificial material TSA with SRR, (a) Top view (b) Bottom view.

5.3.5 Results and Discussions

The fabricated prototype of basic TSA and artificial material loaded TSA with SRR slot are shown in Figure 5.9. The proposed antenna is compared with published literature in

terms of size, operating frequency band, peak gain at notch frequency and rejection band application is depicted in Table 5.2. The proposed antenna has better size reduction compared to the existing structures. It can be noticed that the gain level is positive at the notched frequency band in [42]. Therefore, the radiation of the antenna is not suppressed at the notch frequency.

Table 5.2 Comparison between proposed antenna and existed work

Ref.	**Size (mm^2)**	**Operating frequency band (GHz)**	**Gain level at notch frequency (dBi)**	**Peak gain (dBi)**	**Rejected band application**
[99]	80×80	3-12	-2	8	-
[100]	50×50	3.1-10.6	2.6	8.5	WLAN
[40]	80×140	3-14	-	14	-
[88]	42×72	6-19	-	12	-
Proposed work	40×65	3-11	-1.2	11	WLAN

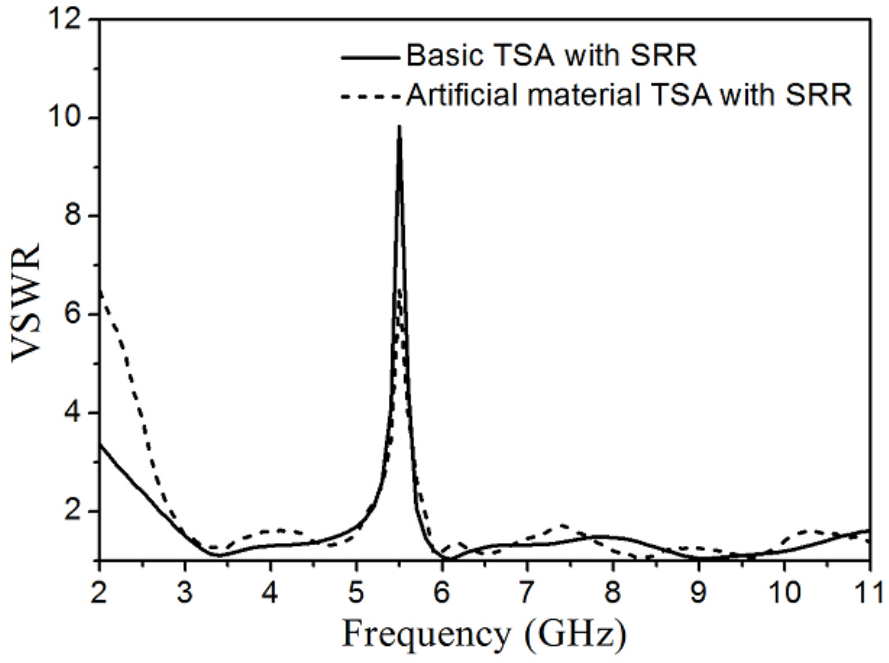

Figure 5.10 The measured VSWR of the basic TSA and artificial material TSA.

The measured VSWRs of basic TSA and artificial material TSA fluctuate at 1.5 over frequency band 3-11 GHz except at 5.1-5.8 GHz as illustrated in Figure 5.10. It can be seen

that the VSWRs of the basic TSA and artificial material TSA are spiking up to 10 and 7 at 5.5 GHz, respectively. The VSWRs of the both antennas overlap at the notch frequency band. So, it is confirmed that the WLAN band is suppressed by using SRR.

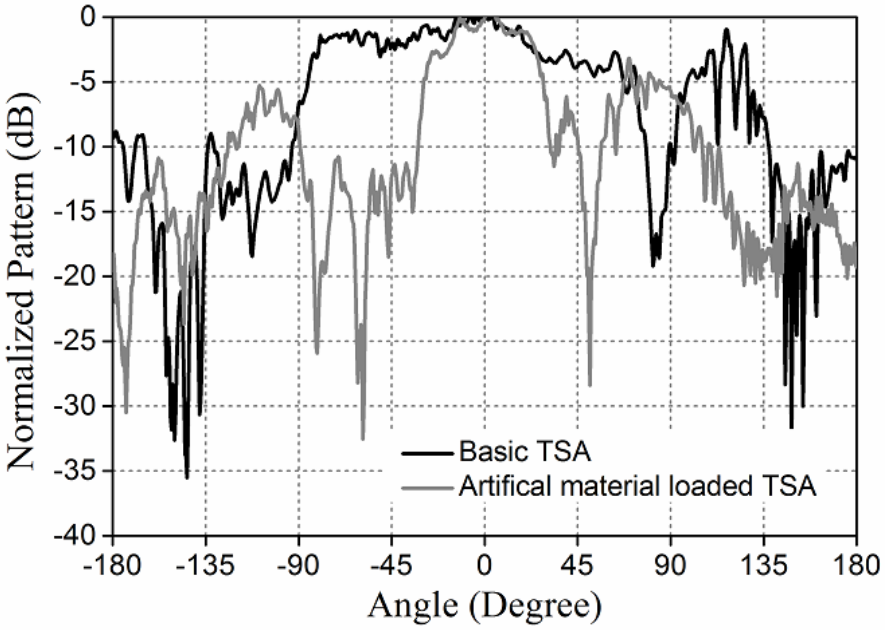

(a)

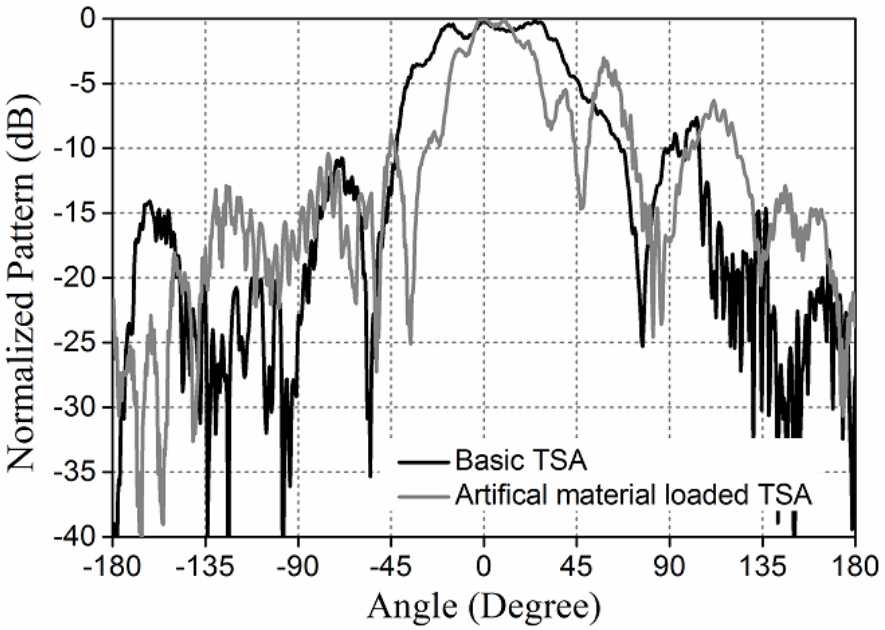

(b)

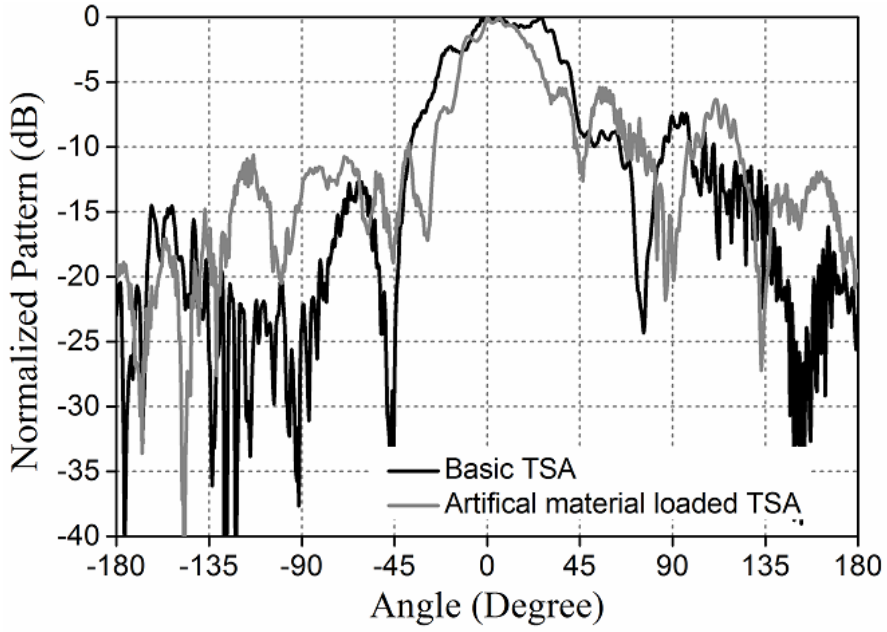

(c)

Figure 5.11 Measured E-plane normalized radiation pattern of basic TSA and artificial material TSA at (a) 6.5 GHz, (b) 8.5 GHz, (c) 10 GHz.

The normalized radiation patterns (E-plane) of the fabricated TSA at 6.5 GHz, 8.5 GHz, and 10 GHz are shown in Figure 5.11. The beam width of the artificial material integrated TSA is much less than basic TSA, which indicates that the pattern becomes more directive. The measurement results of the peak gain with respect to the frequency graph of both the antennas are shown in Figure 5.12(a). Compared to the low frequency region, the measured gain is effectively increased at high frequency side. Hence, it is clear that the maximum gain of the basic TSA is increased from 9.4 to 10.9 dBi at 10 GHz (approximately). Obviously, it can be noticed that the peak gain of the basic TSA and artificial material loaded TSA with SRR slot is decreased up to -4 dBi and -1.2 dBi, repecrtively, at 5.5 GHz.

For UWB antenna, the frequency dependent parameters are not sufficient for validating the design. Therefore, the time domain characteristic of the fabricated GRIN monopole is also tested. So, two GRIN antennas are arranged face-to-face with a distance 30 cm and connected to the ports of the vector network analyzer (VNA). The antenna is giving almost stable group delay performance with a fluctuation approximately ±1.2 ns in the desired band, indicating that a transmitted signal will not be seriously distorted by the proposed antenna as shown in Figure 5.12(b).

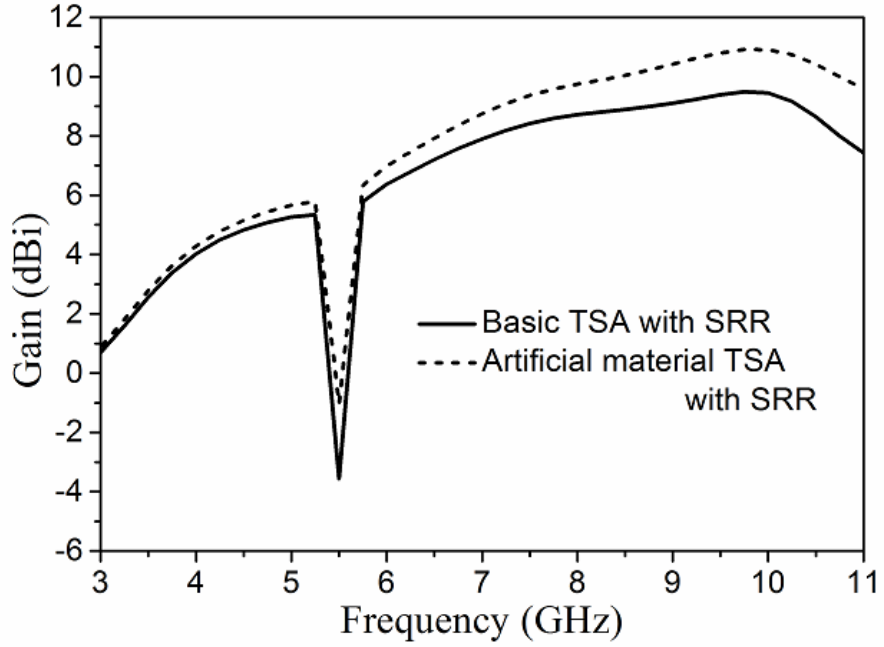

(a)

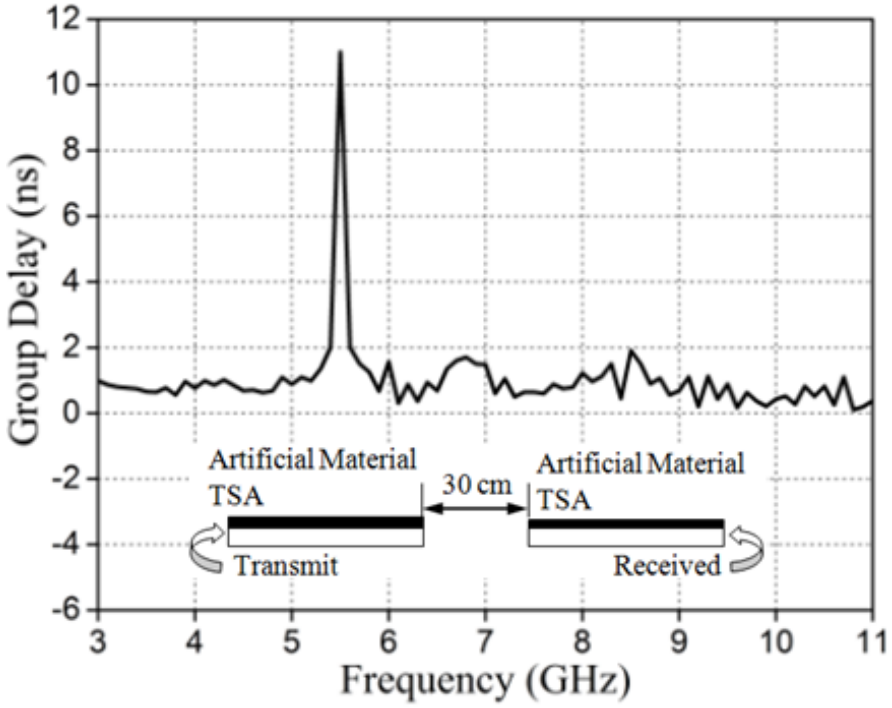

(b)

Figure 5.12 Measured results, (a) Peak gain of basic TSA and artificial material TSA. (b) Group delay for the artificial material TSA with SRR.

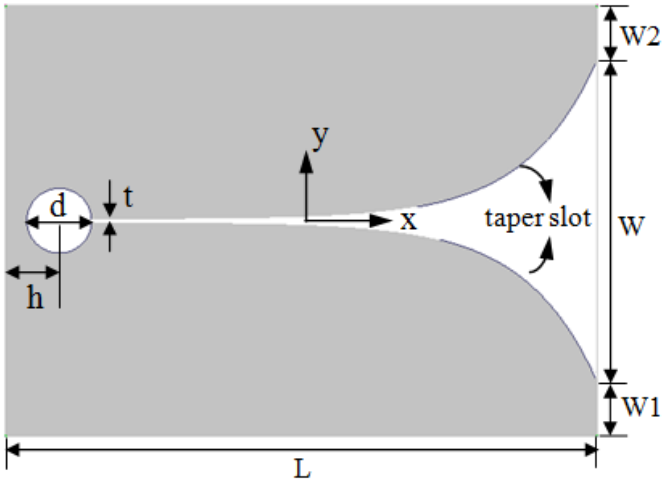

(a)

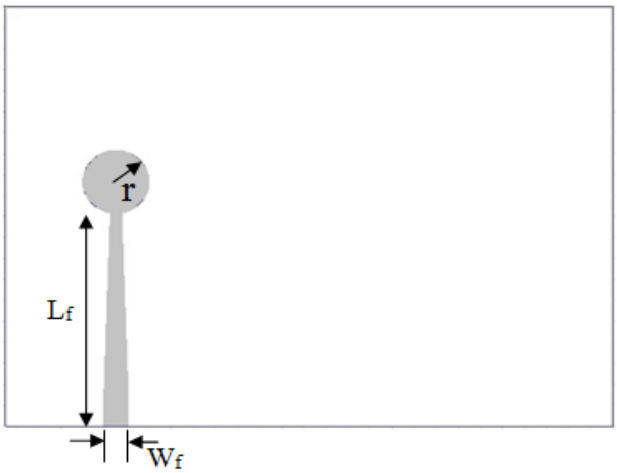

(b)

Figure 5.13 Geometry of basic TSA, (a) Bottom layer and (b) Top layer

5.4 Dual band notched TSA

5.4.1 Design of TSA

The geometry of tapered slot antenna is shown in Figure 5.13. The proposed antenna is fabricated on the RO4003C with relative permittivity 3.55 and thickness 0.8 mm. The total size of the antenna is 55×40×0.8 mm^3. The tapered slot is designed by using the following equations

$$y = \pm\left(0.00824\, e^{0.15x} + 0.087\right) \tag{5.7}$$

where, 0.1 mm ≤ y ≤ 2.5 mm and 0 mm ≤ x ≤ 50 mm.

To improve impedance matching of the TSA, a basic microstrip to slotline transition is realized by etching the slotline on one side of a substrate. On the opposite side of the substrate, a microstrip line crosses perpendicularly to the slotline, that an electromagnetic signal is passed between the two sides. In order to fulfil this operation with negligible power losses, the microstrip line and the slotline have to be orthogonal to each other. In the proposed antenna, microstrip line feed is connected to radial stub and slotline is connected to the circular balun. The microstrip to slotline transition design is shown in Figure 5.13(b). The broad and narrow widths of microstrip line are 1.7 mm and 0.8 mm, respectively.

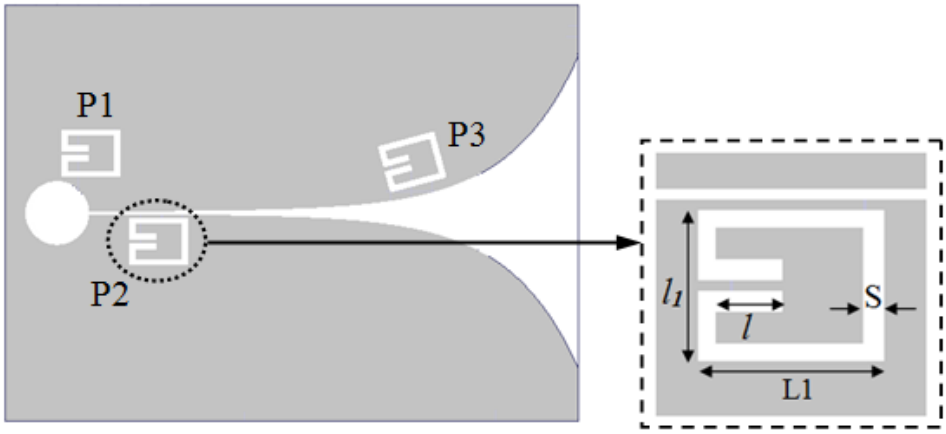

Figure 5.14 Geometry of the single band-notched TSA

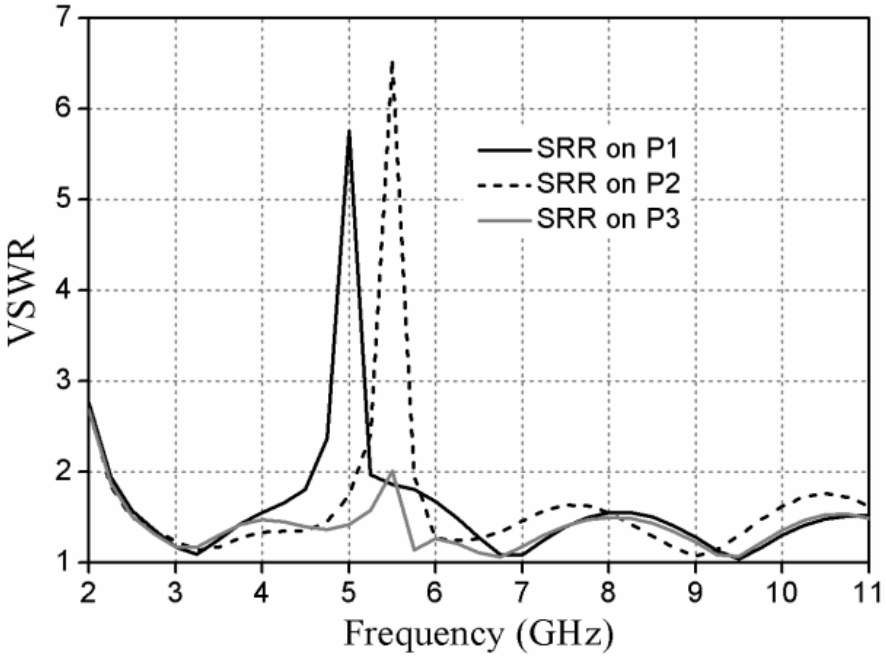

Figure 5.15 Simulated VSWR variation for the SRR slot at position P1, P2 and P3.

5.4.2 Parametric study of band notched TSA

5.4.2.1 Single band notched TSA

Here, the WLAN band notch is created by etching SRR on the bottom part of the TSA. The position SRR slot has a great effect on the band notch property. In case of TSA, the most sensitive part of the antenna is balun, microstrip feeding line and also near to the excitation point. To understand effect of SRR, the SRR slot is created at position P1, P2 and P3 as shown in Figure 5.14. The VSWR has a spike for different position of SRR is illustrated in Figure 5.15. It can be also notice that the VSWR is less effected at position P3. To suppress WLAN application within UWB frequency band, the SRR slot will be more effective at the position P2. SRR is strongly coupled at the taper slot to create a strong resonance. So, the currents of all working bands are allow except at the resonant frequency. As a result, a narrow band is suppressed under UWB frequency range.

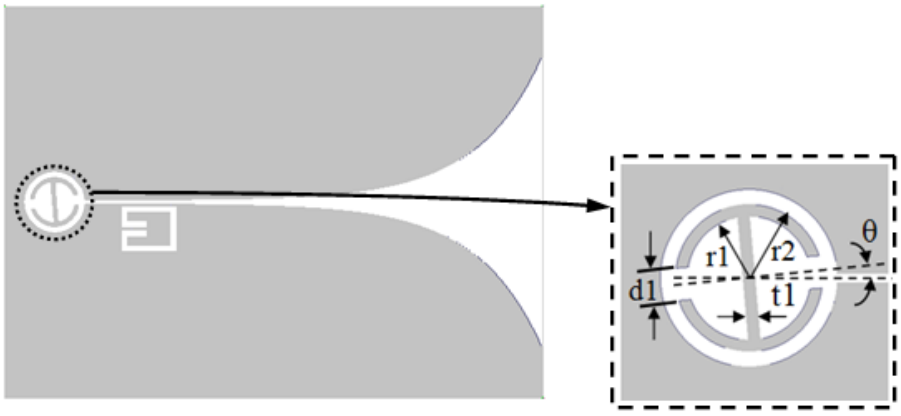

Figure 5.16 Geometry of the proposed TSA

5.4.2.2 Double band notched TSA

In previous section, the SRR slot is used to obtain notch at WLAN band. In this section, the electric-field-coupled (ELC) resonator is placed inside the circular balun as shown in Figure 5.16. ELC resonator parameters are optimized by using three dimensional EM simulator HFSS 15. In order to understand effect of ELC resonator, the ELC resonator is rotate at $\theta=0^0$, 5^0, 10^0. The VSWR has a spike with different angle after rotating the proposed resonator is illustrated in Figure 5.17. The ELC resonator is resonates after scattering with EM wave. It can be seen in Figure 5.17 that the proposed antenna is giving good result at $\theta=5^0$. Therefore, a narrow band is suppressed under UWB frequency range.

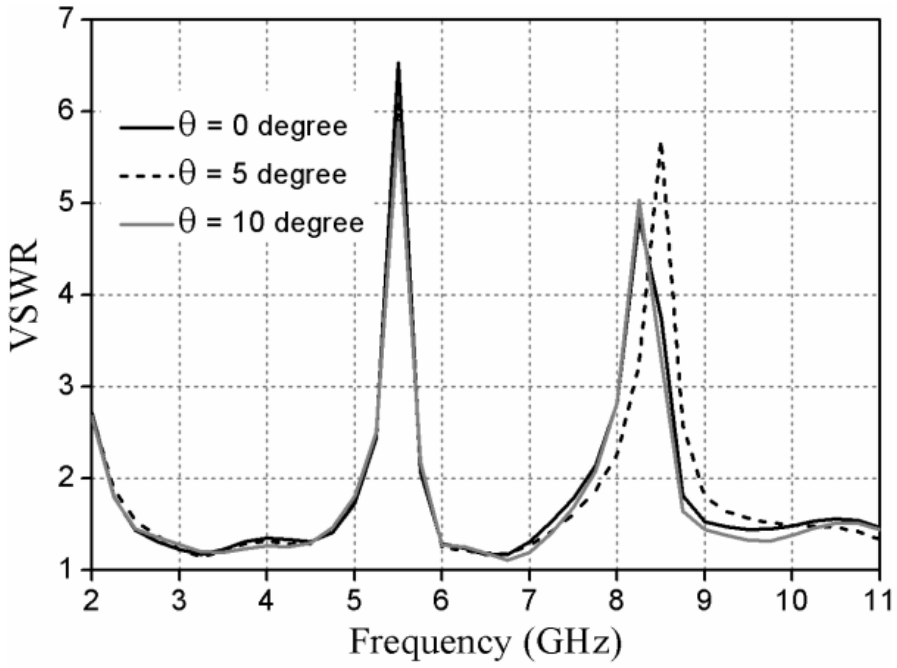

Figure 5.17 Simulated VSWR variation for different angle (θ) of ELC resonator structure inside of the circular balun.

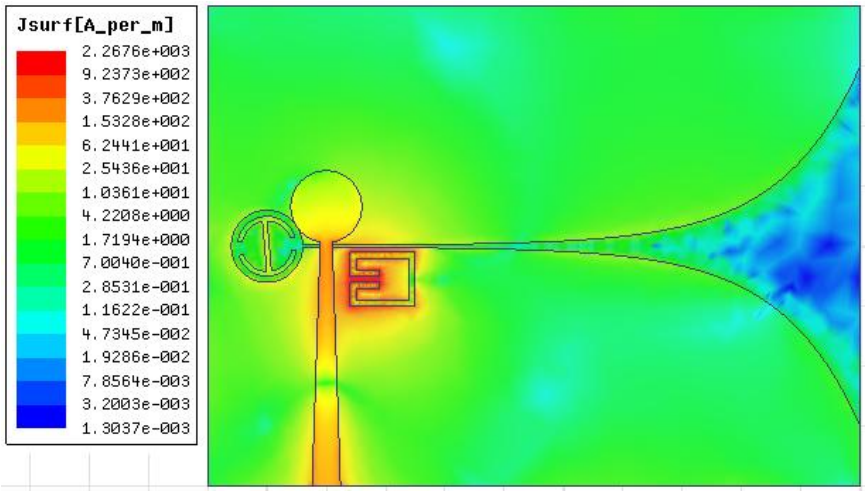

(a)

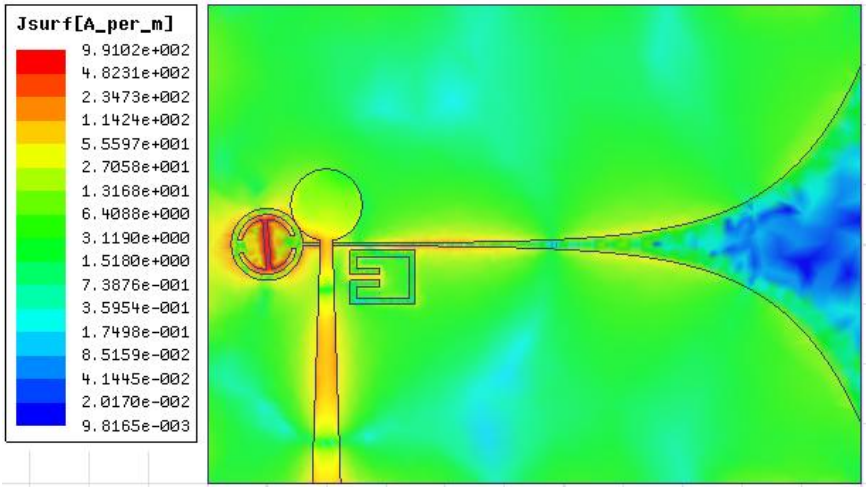

(b)

Figure 5.18 The magnitude of current distribution at 5.5 GHz of the proposed TSA with SRRs at P2 position.

In order to understand the affect of SRR and ELC resonator, the current distribution of the proposed TSA with SRR and ELC resonator is shown in Figure 5.18. It can be observed that the magnitude of current distribution intensity in the SRR is high, depicted in Figure 5.18(a). It means the SRR is strongly couples and resonates to suppress WLAN band. Similarly, the current distribution intensity in the ELC resonator is high, as shown in Figure 5.18(b), which is indicating that the ELC resonator is strongly coupled with EM wave due to the microstrip line feeding. The final optimized dimensions of the proposed antenna are shown in Table 5.3.

Table 5.3 Optimized value of proposed antenna parameters

Parameters	**Unit (mm)**	**Parameters**	**Unit (mm)**
W	40	*S*	0.5
L	55	*l*	2.5
W_f	2.4	l_1	3.5
L_f	20.3	d1	1.1
L1	5	t1	0.4
W1	5	r1	2.1
r	3	r2	2.5
d	6.02	θ	5^0
h	5		

5.4.3 Simulated Results

The simulated VSWR of proposed TSA fluctuating below 1.5 over frequency band 3-11 GHz except 5.1 to 6.1 GHz (WLAN) and 7.8 to 8.9 GHz (ITU), indicating that the good impedance matching are illustrated in Figure 5.19. From the Figure 5.19, it is clear that the VSWR of the proposed TSA is spike up to 6 and 5.5 for WLAN and ITU band, respectively.

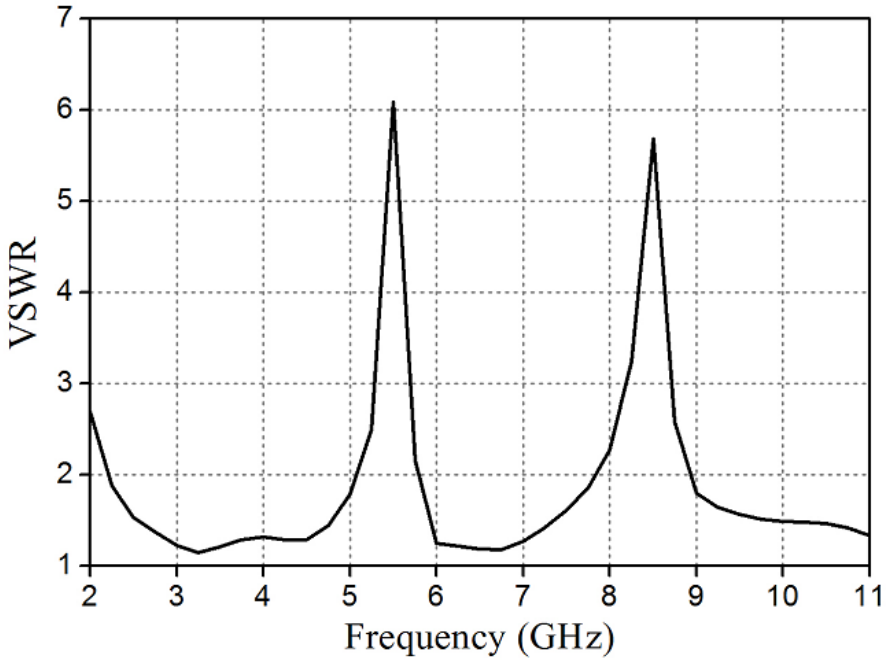

Figure 5.19 Optimized simulated reflection coefficient (S_{11}) of the proposed TSA.

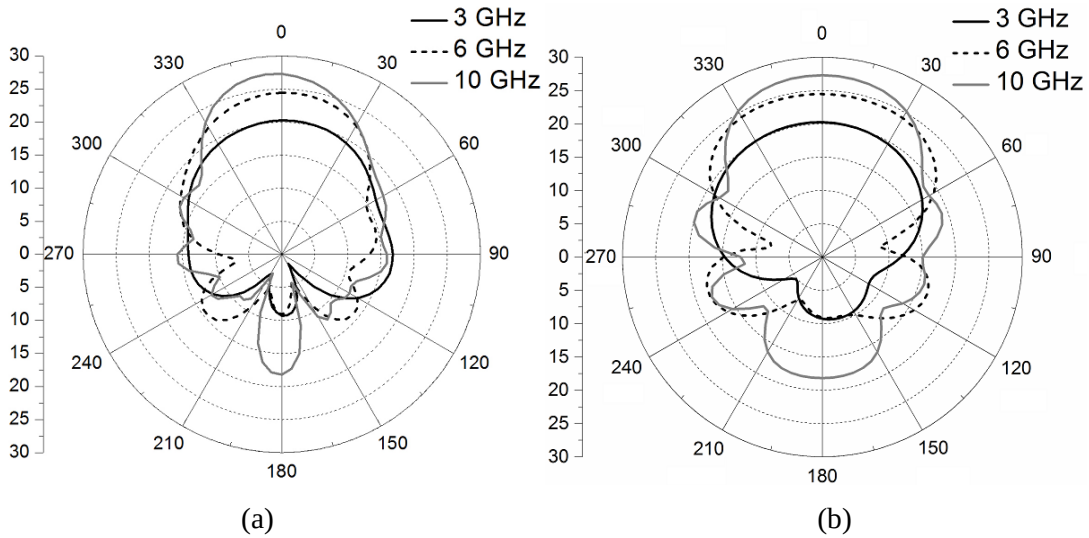

Figure 5.20 Simulated radiation patterns of the proposed TSA at 3 GHz, 6 GHz and 10 GHz, (a) E-plane (xy-plane) and (b) H-plane (xz-plane).

The radiation patterns of the proposed TSA at 3 GHz, 6 GHz, and 10 GHz are shown in Figure 5.20. In the given Figure 5.20, it is observed that the radiation patterns are not affected by using showing ELC resonator and split ring resonator. The peak gain of the simulated proposed antenna with respect to the frequency graph is shown in Figure 5.21. The gain of the TSA is suppressed at the frequency 5.6 GHz and 8.5 GHz to stop the interference with WLAN and ITU band..

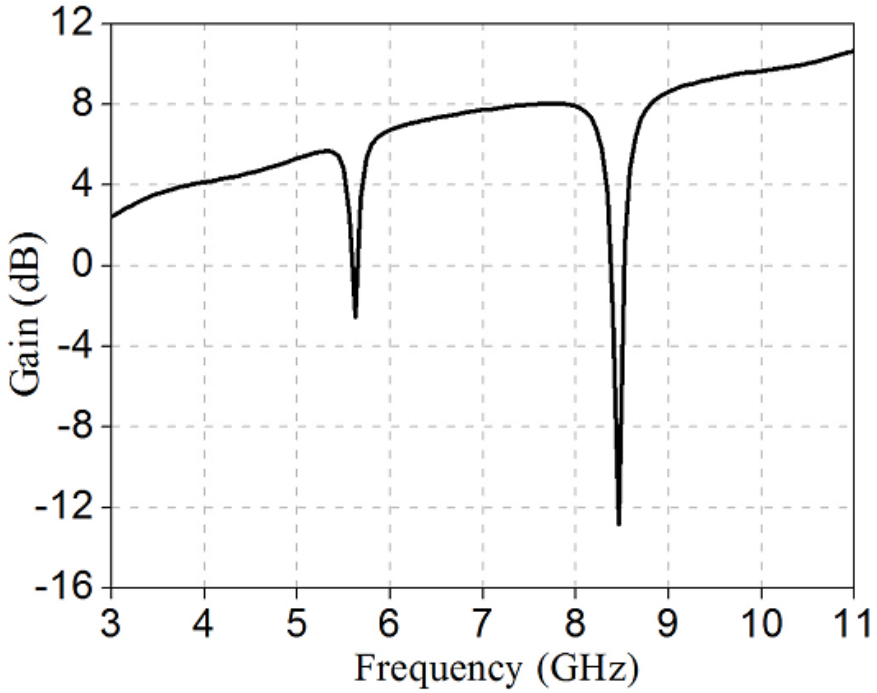

Figure 5.21 Simulated gain for the proposed TSA.

5.5 Conclusion

In this chapter, band notch characteristics are introduced in UWB TSA and artificial material is used to improve the radiation pattern and gain of the antenna. SRR cell is etched on TSA to create resonance at the WLAN band. The WLAN band is rejected at 5.5 GHz. The measured gain of the fabricated antenna is increased by 1.5 dBi with narrow beam width. The electric-field-coupled resonator is located at the balun in TSA and notched for ITU band. Therefore, the proposed antenna can be used for ultra-wideband communication systems with a notch at specific frequency band.

Chapter-6

Conclusions and Scope of Work

6.1 Research findings of the thesis

In this thesis, UWB omnidirectional and directional antennas are investigated with improvement of the radiation pattern, gain and low side lobe level. The band notch is also introduced in directional antenna i.e. tapered slot antenna to mitigate the EM interference with existing technologies. The design of UWB antennas is carefully considered for either for radar, microwave imaging, internet, bluetooth and mobile applications,. So, these parameters are included in terms of the impedance bandwidth, radiation patterns, gain and interference with existing technologies.

Chapter 2 introduced several design techniques of the UWB Vivaldi antennas with different taper profiles and performance is compared. Linear and exponential flare are used in tapered slot antenna. The corrugation is used in TSA to get wider impedance bandwidth. The reflection coefficient is measured and compared with simulated results. The exponential and elliptical taper structures are also applied in unbalanced antipodal Vivaldi antenna. It is also observed that the cross polarization of the unbalanced AVA is high, which is not suitable for UWB application. Hence, corrugated balanced antipodal Vivaldi antenna is designed for the improvement of cross polarization. BAVA has displayed very low cross polarization over the UWB frequency band. All the designed antennas have improved gain compared to existing literature.

The printed omnidirectional antenna or monopole antenna is designed for short range wireless communication. Generally, the gain of the printed monopole is comparatively low. Chapter 3 presents the investigation of monopole with dielectric superstrate for gain enhancement. So, the working distance of the wireless system can be improved. Proposed superstrate is designed with a partial cover conductor on single side of the superstrate with dimension 10×21.5 mm^2. The overall dimension of the fractal monopole antenna with superstrate is $24.5\times21.6\times3.15$ mm^3. The measurement result of the reflection coefficient is

below -10 dB, indicating that the impedance bandwidth is 3.1 to 11 GHz. The measured radiation patterns are also improved and peak gain of the antenna is increased by 1.6 dB with the help of superstrate.

In Chapter 4, artificially designed materials are used to get more gain of the UWB antenna which is called as Metamaterial. Here, metamaterial is designed in such a way that it is working with UWB frequency band. A unit cell metamaterial is designed by fabricating parallel-line structure on the Roger RT/Duroid 4003 substrate. It is observed that the effective refractive index values are varied with the dimensions of the parallel-line structure, m. The effective refractive index value is low and effective impedance values are near to the unity by decreasing the dimension, m. By using these properties, GRIN lens is designed using unit cell metamaterial with the equation of luneburg lens. The refractive index distribution in GRIN lens is very important to reduce the reflection with beam focusing property. The dimension of the GRIN lens is 84×60 mm^2. So, seven GRIN metamaterial lenses are placed above the basic monopole antenna with a separation of 23 mm.

The measured reflection coefficient (S_{11}) of the basic monopole and GRIN monopole are plotted and compared. It is clear that the S_{11} of the basic monopole is less than -10 dB with impedance bandwidth of 3.1-11 GHz. But, GRIN monopole is working over the frequency band from 3.4-11 GHz. In the case of GRIN antenna, the S_{11} is fluctuating near -10 dB over bandwidth 10-11 GHz.

The H-plane (xz plane) patterns of the GRIN monopole are also measured at 4.5 GHz, 6.2 GHz, 8 GHz and 10 GHz. It indicates that the radiation patterns are directive using a GRIN lens in basic monopole antenna. The measured gain of the basic monopole is enhanced across the UWB frequency band due to the GRIN lens and peak gain increases from 4.6 to 9.9 dB at 8.8 GHz (approximately).

The free-space electric-field distributions are also analyzed with and without unit cell metamaterial structure in GRIN lens. It can be observed that the quasi-spherical waves are almost converted into the plane waves at 9 and 10 GHz. GRIN elements are operating far from their resonant frequencies and induced losses are low.

The time domain characteristic of the fabricated GRIN monopole is also tested using a vector network analyzer (VNA). The antenna is giving almost stable group delay

performance with a fluctuation approximately ±1.2 ns in the desired band, indicating that a transmitted signal will not be seriously distorted by the proposed antenna.

The GRIN lens is also tested by installing on the directional antenna i.e. tapered slot antenna. The effects of GRIN lens are analyzed by performing parametric study on a number of GRIN lenses and gap between them. The separation between two GRIN lenses is kept at 4.5 mm to avoid the destruction of metamaterial properties.

The measured reflection coefficient (S_{11}) of the basic and GRIN TSA are less than -10 dB over the bandwidth of 3-11 GHz. The simulated and measured normalized radiation patterns with E-plane (xy-plane) and H-plane (xz plane) are presented at 3.2 GHz, 8 GHz and 10.3 GHz. The measured radiation pattern achieved a narrow beam width using a GRIN lens. Due to the GRIN lens, the gain of the basic TSA has been increased by 6 dB at 10 GHz (approximately). The gain of GRIN TSA is varying from 3.7-14 dB over the frequency band of 3−11 GHz.

The parallel-line unit cell metamaterial is also integrated in front of the tapered slot antenna with different refractive index. By doing these techniques, the radiation pattern becomes more directive with low sidelobe level. The gain of the antenna is also increased.

Certain narrowband applications, such as WiMAX, WLAN and ITU bands exist under UWB frequency band. So, serious electromagnetic interference (EMI) would happen to the UWB communication system. Chapter 5 is devoted to design band notched characteristics on ultra-wideband tapered slot antenna at WLAN band using SRR slot.

To know the effects, the SRR slot is placed at different positions on the TSA, namely P1, P2 and P3. Finally, the WLAN band is actively suppressed at the position P2. The electric field is strongly coupled with SRR at the taper slot to create a strong resonance. So, a narrow band is suppressed within UWB frequency range. Due to the harmonic effects of SRR resonance, the gain may be reduced at high frequencies. Therefore, the S-shaped unit cell metamaterial is designed and integrated in front of the TSA.

The measured VSWR of the proposed TSA is fluctuating at 1.5 over frequency band 3-11 GHz, indicating that the good impedance matching except at 5.1-5.8 GHz. The VSWR is spiking up to 7 at 5.5 GHz. The measured gain of the basic TSA is increased from 9.4 to

10.9 dBi at 10 GHz (approximately) using metamaterial. The gain of the artificial material loaded TSA with SRR slot is decreased up to -1.2 dBi at 5.5 GHz. To suppress the ITU band, the electric-field coupled resonator is placed inside the circular balun of the TSA. So, the VSWR of the proposed TSA spikes up to 5.5 at 8.5 GHz.

At the end of the chapter, all the designed techniques are compared in terms of size, bandwidth and gain.

6.2 Future scope

In the 21st century, the UWB antennas are widely used for commercial and radar applications. Designed and presented UWB antennas in this thesis are good candidates for mass fabrication and applicable in medical imaging, ground-penetrating radar and Speed Monitoring Radar Gun systems. The proposed UWB metamaterial structures are not applied over the antenna array elements. For the future work, the metamaterial can be useful to reduce the coupling in antenna arrays and directivity enhancement purpose, also, a novel broadband compact Metamaterial in nano scale. So, compact nano-scale Metamaterial unit cell can be useful for solar cell application. Implementation of the solar cell antenna using Metamaterial can be the future scope of the present work.

List of Publications

Journal Publications

1. Rahul Singha and D. Vakula. "Compact ultra-wideband fractal monopole antenna with high gain using single layer superstrate," Microwave and Optical Technology Letters, vol. 59, no. 2, pp. 482-488, 2017.
2. Rahul Singha and D. Vakula. "Directive Beam of the Monopole Antenna Using Broadband Gradient Refractive Index Metamaterial for Ultra-Wideband Application," IEEE Access, vol. 5, pp. 9757-9763, 2017.
3. Rahul Singha and D. Vakula, "Gain enhancement of the ultra-wideband tapered slot antenna using broadband gradient refractive index metamaterial," International Journal of RF and Microwave Computer-Aided Engineering, pp. 1-10, 2017 ,e21191.
4. Rahul Singha and D. Vakula, "Artificial Material Integrated Ultra-wideband Tapered Slot Antenna for Gain Enhancement with Band Notch Characteristics," Radioengineering, vol. 27, no. 1, pp. 54-62, 2017.
5. Rahul Singha and D. Vakula, "Low side lobe tapered slot antenna with high gain using gradient refractive index metamaterial for ultra wideband application," Advanced Electromagnetics, vol. 6, no. 4, 2017.

Conference Publications

1. Rahul Singha and D. Vakula, "Corrugated antipodal Vivaldi antenna using spiral shape negative index metamaterial for ultra-wideband application," Signal Processing and Communication Engineering Systems (SPACES), pp. 179-183, 2-3 Jan. 2015.
2. Rahul Singha, D. Vakula and N. V. S. N. Sarma, "Compact concentric ring shaped antenna for ultra-wide band applications," 2nd Radio and Antenna Days of the Indian Ocean (RADIO 2014), pp. 1-4, 7-10 April 2014.
3. Rahul Singha and D. Vakula, "Linear Tapered Slot Vivaldi Antenna with Corrugated Edges for UWB Application," 7th Annual Conference of the Antenna Test & Measurement Society (ATMS), pp. 186-189, 10-12 February 2014.
4. Rahul Singha and D. Vakula, "CPW-fed UWB Antenna with WLAN Band Notch using Circular Dumbbell Slot," 11th International Conference on Microwaves Antenna Propagation & Remote Sensing (ICMARS-2015), pp. 13-15, 15–17th Dec. 2015.

5. Rahul Singha and D. Vakula, “Artificial Material Integrated Tapered Slot Antenna with High Gain for UWB Application,” 10th the Antenna Test & Measurement Society 2017 (ATMS 2017), pp. 138-141, 6-8 Feb, 2017.
6. Rahul Singha and D. Vakula, “Ultra-wideband Tapered Slot Antenna with Dual Band Suppression Characteristics using Electric-field Coupled Resonator and Split Ring Resonator,” IEEE International Conference of Electronics, Communication and Aerospace Technology 2017 (ICECA 2017), pp. 746-749, 20-22 April, 2017.

References

[1] C. G. Christodoulou and P. F. Wahid, Fundamentals of antennas: concepts and applications, vol. 50, SPIE Press, 2001.

[2] T. W. Barret, "History of ultra wideband (UWB) radar & communications: pioneers and innovators," In Progress in Electromagnetics Symposium 2000 (PIERS2000), 2000.

[3] FCC. First report and order, revision of part 15 of the commission's rules regarding ultra-wideband transmission systems. Technical report, Federal Communications Commission, 2002.

[4] C. E. Shannon, "A mathematical theory of communication," Bell Sys. Tech. Jour., vol. 27, July, October, 1948.

[5] Janaswamy, R. and D. H. Schaubert, "Analysis of the tapered slot antenna," IEEE Trans. Antennas Propagat., vol. 35, pp. 1058–1064, Sept. 1987.

[6] A. S. Turk, "Ultra-UWB Vivaldi antenna design for dualsensor adaptive ground-penetrating impulse radar," Microw. Opt. Technol. Lett., vol. 48, no. 5, pp. 834–839, May 2006.

[7] Y. Yang, Y. Wang, and A. Fathy, "Design of compact Vivaldi antenna arrays for UWB see through wall applications," Progress In Electromagnetics Research, vol. 82, pp. 401–418, 2008.

[8] A.M. Abbosh, "Directive antenna for ultrawideband medical imaging systems," Int J Antenna Propag., vol. 2008 (2008).

[9] E. W. Reid, L. Ortiz-Balbuena, A. Ghadiri, and K. Moez, "A 324-element Vivaldi antenna array for radio astronomy instrumentation," IEEE Trans. Antennas Propag., vol. 61, no. 1, pp. 241–249, Jan. 2012.

[10] J. Pourahmadazar, C. Ghobadi, and J. Nourinia, "Novel modified pythagorean tree fractal monopole antennas for UWB applications," IEEE Antennas Wireless Propag. Lett., vol. 10, pp. 484–487, 2011.

[11] M. J. Ammann and M. John, "Optimum design of the printed strip monopole," IEEE Antennas Propag. Mag., vol. 47, no. 6, pp. 59–61, Dec. 2005.

[12] Q. B. Ye, Z. N. Chen, and T. S. P. See, "Ground plane effect on the performance of a butterfly-shaped UWB monopole," in Proc. iWAT, pp. 334–337, Mar. 2008.

[13] Wong, K. L., Tseng, T. C. and Teng, P. L., “Low-profile ultra-wideband antenna for mobile phone applications”, Microwave and Optical Technology Letters, vol. 43, no. 1, pp. 7–9, 2004.

[14] Wong, K. L., Chou, L. C. and Chen, H. T., “Ultra-wideband metal-plate monopole antenna for laptop application”, Microwave and Optical Technology Letters, vol. 43, no 5, pp. 384–386, 2004.

[15] R. Aiello and A. Batra, “Ultra Wideband Systems, Technologies and Applications", Newnes Publication, 2006.

[16] J. D. Taylor, “Ultrawideband Radar: Applications and Design”, CRC Press.

[17] Lui, W. J., C. H. Cheng, and H. B. Zhu, "Experimental investigation on novel tapered microstrip slot antenna for ultra-wideband applications," IET microwaves, antennas & propagation, vol. 1, no. 2, pp. 480-487, 2007.

[18] J. Wu, Z. Zhao, Z. Nie, and Q. Liu, “A printed UWB Vivaldi antenna using stepped connection structure between slotline and tapered patches,” IEEE Trans. Antennas Propag., vol. 13, pp. 698–701, Apr. 2014.

[19] R. Azim, M. T. Islam, and N. Misran, “Compact tapered shape slot antenna for UWB applications,” IEEE Antennas Wireless Propag. Lett., vol. 10, pp. 1190–1193, 2011.

[20] A. Z. Hood, T. Karacolak, and E. Topsakal, “A small antipodal Vivaldi antenna for ultra-wideband applications,” IEEE Antennas Wireless Propag. Lett., vol. 7, pp. 656–660, 2008.

[21] A. M. Abbosh, “Miniaturized microstrip-fed tapered-slot antenna with ultrawideband performance,” IEEE Antennas Wireless Propag. Lett., vol. 8, pp. 690–692, 2009.

[22] F. Jolani, G. Dadashzadeh, M. Naser-Moghadasi, and A. Dadgarpour, “Design and optimization of compact balanced antipodal Vivaldi antenna,” Progr. Electromagn. Res. C, vol. 9, pp. 183–192, 2009.

[23] J. Bai, S. Shi, D. W. Prather,” Modified Compact Antipodal Vivaldi Antenna for 4–50-GHz UWB Application”, IEEE Transactions on Microwave Theory and Techniques, vol. 59, no. 4, pp. 1051-1057, April 2011.

[24] P. Fei, Y.-C. Jiao, W. Hu, and F.-S. Zhang, “A miniaturized antipodal Vivaldi antenna with improved radiation characteristics,” IEEE Antennas Wireless Propag. Lett., vol. 10, pp. 127–130, 2011.

[25] Low, Z. N., J. H. Cheong, and C. L. Law, "Low-cost PCB antenna for UWB applications", IEEE antennas and wireless propagation letters, vol. 4, no. 1, pp. 237-239, 2005.

[26] R. N. Simons, Coplanar Waveguide Circuits, Components, and Systems, John Wiley & Sons, New York, NY, USA, 2001.

[27] Angelopoulos, Evangelos S., Argiris Z. Anastopoulos, Dimitra I. Kaklamani, Antonis A. Alexandridis, Fotis Lazarakis, and Kostas Dangakis, "Circular and elliptical CPW-fed slot and microstrip-fed antennas for ultrawideband applications", IEEE Antennas and Wireless Propagation Letters, vol. 5, no. 1, pp. 294-297, 2006.

[28] Denidni, T. A., and M. A. Habib, "Broadband printed CPW-fed circular slot antenna", Electronics letters, vol. 42, no. 3, pp. 135-136, 2006.

[29] Fallahi H., Atlasbaf Z., “Study of a class of UWB CPW-fed monopole antenna with fractal elements,” IEEE Antennas Wirel. Propag. Lett., vol. 12, pp. 1484–1487, 2013

[30] K. R. Chen, S. Y. D. Sim, J. S. Row, " A Compact Monopole Antenna for Super Wideband Applications," IEEE Antennas and Wireless Propagation Letters, vol. 10, pp. 488-491, 2011.

[31] S. Tripathi, M. Akhilesh and S. Yadav, “Hexagonal Fractal Ultra-Wideband Antenna Using Koch geometry with Bandwidth Enhancement,” IET Microwaves, Antennas & Propagation, vol. 8, pp. 1445-1450, 2014.

[32] M. Ding, R. H. Jin, J. P. Geng, and Q. Wu, “Design of a CPW-fed ultrawide band fractal antenna,” Microw. Opt. Technol. Lett., vol. 49, no. 1, pp. 173–176, Jan. 2007.

[33] Y. Sugio, T. Makimoto, S . Nishimura, and H. Nakanishi, "Analysis for Gain Enhancement of multiple-reflection Line Anterura with Dielechic Plates," Trans. IECE, pp. 80-112, Jan. 1981.

[34] D.R. Jackson and N.G.Alexopoulos, "Gain Enhancement Methods for Printed Circuit Antennas" IEEE Trans. Antennas Propag., vol. 33, no. 9 , pp. 976 -987, Sep. 1985.

[35] D. Li, Z. Szabó, X. Qing, E. P. Li, and Z. N. Chen, “A high gain antenna with an optimized metamaterial inspired superstrate,” IEEE Trans. Antennas Propag., vol. 60, no. 12, pp. 6018–6023, Dec. 2012.

[36] J. Ju, D. Kim, W. J. Lee, and J. I. Choi, “Wideband high-gain antenna using metamaterial superstrate with the zero refractive index,” Microw. Opt. Technol. Lett., vol. 51, no. 8, pp. 1973–1976, Aug. 2009.

[37] H. Attia, L. Yousefi, M. M. Bait-Suwailam, M. S. Boybay, and O. M. Ramahi, “Enhanced-gain microstrip antenna using engineered magnetic superstrates,” IEEE Antenna Wireless Propag. Lett., vol. 8, pp. 1198–1201, 2009.

[38] Shaw T, Bhattacharjee D, and Mitra D., “Gain enhancement of slot antenna using zero index metamaterial superstrate,” Int J RF Microw Comput Aided Eng., 2016;00:e21078.

[39] M. Sun, Z. Chen, and X. Qing, "Gain enhancement of 60-GHz antipodal tapered slot antenna using zero-index metamaterial," IEEE Trans. Antennas Propag., vol. 61, no. 4, pp. 1741-1746, Apr. 2013.

[40] B. Zhou and T. J. Cui, “Directivity enhancement to vivaldi antennas using compactly anisotropic zero-index metamaterials,” IEEE Antennas Wireless Propag. Lett., vol. 10, pp. 326–329, 2011.

[41] Wu, S., Yi, Y., Yu, Z., Huang, X. and Yang, H., “A zero-index metamaterial for gain and directivity enhancement of tapered slot antenna,” Journal of Electromagnetic Waves and Applications, vol. 30, no. 15, pp.1993-2002, 2016.

[42] H.-X. Xu, G.-M. Wang, Z. Tao, and T.-J. Cui, “High-directivity emissions with flexible beam numbers and beam directions using gradient refractive-index fractal metamaterial,” Sci. Rep., vol. 4, p. 5744, 2014.

[43] P. J. Gibson, “The Vivaldi Aerial,” in Proc. 9th Eur. Microw. Conf., pp. 101–105, Sep. 1979.

[44] S. N. Prasad and S. Mahapatra, “A novel MIC slot-line antenna,” in Proc. 9th Eur. Microw. Conf., pp. 120–124, Sep. 1979.

[45] E. Gazit, “Improved design of the vivaldi antenna,” IEE Proceedings, vol. 135, pp. 89–92, 1988 .

[46] J.D.S. Langley, P.S. Hall, and P. Newham, “Balanced antipodal vivaldi antenna for wide bandwidth phased arrays,” IEE Proc. Microw. Antennas Propag., vol. 143, pp. 97–102, 1996.

[47] Yao, Y., W. Chen, B. Huang, Z. Feng, and Z. Zhang, “Analysis and design of tapered slot antenna for ultra-wideband applications,” Tsinghua Science and Technology, vol. 14, no. 1, pp. 1–6, 2009.

[48] M. Gopikrishna, D. D. Krishna, C. K. Aanandan, P. Mohanan, and K. Vasudevan, “Compact linear tapered slot antenna for UWB applications,” Electron. Lett., vol. 44, no. 20, pp. 1174–1175, Sep. 2008.

[49] A. Abbosh, K. Kan, and M. Bialkowski, “A compact UWB planar tapered slot antenna for use in a microwave imaging system,” Microw. Opt. Technol. Lett., vol. 48, no. 11, pp. 2212–2216, 2006

[50] K. Ma, Z. Q. Zhao, J. N. Wu, M. S. Ellis and Z. P. Nie, “A printed Vivaldi Antenna with improved radiation patterns by using two pairs of Eye-Shaped Slots for UWB applications,” Progress In Electromagnetics Research, vol. 148, pp. 63-71, 2014.

[51] I. T. Nasser and T. M. Weller, “A novel method for improving antipodal Vivaldi antenna performance,” IEEE Trans. Antennas Propag., vol. 63, no. 7, pp. 3321–3324, Jul. 2015.

[52] J. J. Lee, S. Livingstone, and R. Koenig, “Performance of a wideband (3–14) GHz dual-pol array,” in IEEE Int. Antennas Propag. Symp. Dig., vol. 1, pp. 551–554, Jun. 2004.

[53] M. W. Elsallal and D. H. Schaubert, "Electronically scanned arrays of dual-polarized, doubly-mirrored balanced antipodal Vivaldi antennas (DmBAVA) based on modular elements," in Proc. IEEE Antennas and Propag. Society Int. Symp., pp. 887-890, Jul. 9-14, 2006.

[54] K.S. Yngvesson, D.H. Schaubert, T.L. Korzeniowski, E.L. Kollberg, T. Thungren and J.F. Johansson, “Endfire Tapered Slot Antennas on Dielectric Substrates,” IEEE Trans. on Antennas and Propag., vol. 33, no. 12, pp. 1392-1399, December 1985.

[55] Hojjat, N., S. Yarasi, S. Safavi-Naeini, and T. Manku, “Design and Analysis of new Fermi-like Tapered Slot Antennas,” IEEE Antennas and Propagation Society International Symposium, vol. 3, pp. 1616-1619, 2000.

[56] J. B. Knorr, “Slotline transitions,” IEEE Transactions on Microwave Theory and Techniques, vol. 22, pp. 548-554, May 1974.

[57] Robinson, G. H. & Allen, J. L., “Slot line application to miniature ferrite devices,” IEEE Transactions on Microwave Theory and Techniques, vol. 17, no. 12, pp. 1079-1101, December 1969.

[58] Hokmabadi, Alireza, Asghar Keshtkar, Alireza Bayat, and Ahmad Keshtkar, "A CPW-fed tapered slot antenna with improved time and frequency domain characteristics," International Journal of Microwave and Wireless Technologies, vol. 9, no. 5, pp. 1185-1190, 2017.

[59] C. Kim and W. Jung, “Ultra-wideband end fire directional tapered slot antenna using CPW to wide-slot transition,” Electron. Lett., vol. 46, no. 17, pp. 1183–1185, 2010.

[60] Honda, S., Ito, M., Seki, H. and Jingo, Y., "A disc manspole with 1:8 impedance bandwidth and omnidirectional radiation pattern" Proceedings of the International symposium of Antennas Propagation. Sapporo, Japan. pp. 1145–114, 1992.

[61] N. P. Agrawall, G. Kumar, and K. P. Ray, “Wide-band planar monopole antennas,” IEEE Trans Antennas Propag., vol. 46, no. 2, pp. 294-295, Feb. 1998.

[62] L. Jianxin, C. C. Chiau, X. Chen, and C. G. Parini, “Study of a printed circular disc monopole antenna for UWB systems,” IEEE Trans. Antennas Propag., vol. 53, no. 11, pp. 3500–3504, Nov. 2005.

[63] Choi SH, Park JK, Kim SK and Park J Y, “A new ultra-wideband antenna for UWB applications,” Microwave and Optical Technology Letters, vol. 40, no. 5, pp. 399 - 401, 2004.

[64] H. V. Ehrenspeck, "The Backfire Antenna, a New Type of Directional Line Source," Proc. IRE , vol. 48, pp. 109-110, January 1960.

[65] Y. Sugio, T. Makimoto, S. Nishimura, and H. Nakanishi, “Analysis for gain enhancement of multiple-reflection line antenna with dielectric plates,” Trans. IECE, pp. 80–112, Jan. 1981.

[66] D. R. Jackson and N. G. Alexopoulos, “Gain enhancement methods for printed-circuit antennas,” IEEE Trans. Antennas Propag., vol. 33, no. 9, pp. 976–987, Sep. 1985.

[67] C. S. Lin, S. S. Zhong, J. H. Shi, and Y. Wang, “Gain enhancement technique for microstrip antennas,” in Proc. IEEE Antennas Propag., vol. 36, pp. 905–910, Jul. 1988.

[68] Dubost G and Zisler S., "Antennas a Large Bande", Masson, New York, pp. 128–129, 1976.

[69] Garg, R., Bhartia, P., Bahl, I. and Ittipiboon, A., Microstrip Antenna Design Handbook, Artech House, Boston, 2000.

[70] Liang JX, Chiau CC, Chen, XD and Parini CG, "Study of a printed circular disc monopole antenna for UWB systems," IEEE Transactions on Antennas and Propagation , vol. 53, no. 11, pp. 3500-3504, 2005.

[71] B. L. Ooi, G. Zhao, M. S. Leong, K. M. Chua, and C. W. L. Albert, “Wideband LTCC CPW-fed two-layered monopole antenna,” Electron. Lett., vol. 41, no. 16, pp. 9–10, Aug. 2005.

[72] L. Lizzi, R. Azaro, G. Oliveri, and A. Massa, “Printed UWB Antenna Operating Over Multiple Mobile Wireless Standards,” IEEE Antennas and Wireless Propagation Letters, vol. 10, pp. 1429-1432, 2011.

[73] J. J. Kim, T. Yoon, J. Kim, and J. Choi, “Design of an ultra wide-band printed monopole antenna using FDTD and genetic algorithm,” IEEE Microw. Wireless Compon. Lett., vol. 15, no. 6, pp. 395–397, Jun. 2005.

[74] Z. N. Low, J. H. Cheong, and C. L. Law, “Low-cost PCB antenna for UWB applications,” IEEE Antennas Wireless Propag. Lett., vol. 4, pp. 237–239, 2005.

[75] N. P. Agrawall, G. Kumar, and K. P. Ray, “Wide-band planar monopole antennas,” IEEE Trans Antennas Propag., vol. 46, no. 2, pp. 294-295, Feb. 1998.

[76] X. Chen, Z. Luo, Z. Zheng, P. Feng, and K. Huang, “Effective reflective characteristics of superstrates and their effects on the resonant cavity antenna,” IEEE Trans Antennas Propag, vol. 63, pp. 1572–1580, 2015.

[77] F. Meng and S.K. Sharma, “A dual-band high-gain resonant cavity antenna with a single layer superstrate,” IEEE Trans Antennas Propag, vol. 63, pp. 2320–2325, 2015.

[78] H. Bukhari and K. Sarabandi, “Ultra-wide band printed slot antenna with graded index superstrate,” IEEE Trans Antennas Propag, vol. 61, pp. 5278–5282, 2013.

[79] V. G. Veselago, “The electrodynamics of substances with simultaneously negative values of ε and μ,” Sov. Phys. Usp, vol. 10, no. 4, pp. 509-514, Jan.-Feb.1968.

[80] J. B. Pendry, A. J. Holden, D. J. Robins, W. J. Stewart, “Magnetism from conductors and enhanced nonlinear phenomena,” IEEE Trans. on Microwave Theory and Tech., vol. 47, no. 11, pp. 2075-2084, Nov. 1999.

[81] D. R. Smith, W. J. Padilla, D. C. Vier, S. C. Nemat-Nasser, S. Schultz, “Composite medium with simultaneously negative permeability and permittivity,” Phys. Rev. Lett., vol. 84, no. 18, pp. 4184-4187, May 2000.

[82] F. Y. Meng, Y. L. Lv, K. Zhang, Q. Wu, and L. W. Li, “A detached zero index metamaterial lens for antenna gain enhancement,” Prog. Electromagn. Res., vol. 132, pp. 463–478, 2012.

[83] Wu S., Yi Y., Yu Z., Huang X. and Yang H., “A zero-index metamaterial for gain and directivity enhancement of tapered slot antenna,” J. Electromagn. Waves, vol. 30, no. 15, pp. 1993–2002, 2016.

[84] A. Dhouibi, S. Burokur, A. de Lustrac, and A. Priou, “Low-profile substrate-integrated lens antenna using metamaterials,” IEEE Antennas Wireless Propag. Lett., vol. 12, pp. 43–46, Jan. 2013.

[85] R. S. Kshetrimayum, "A brief Intro to metamaterials," IEEE potentials, vol. 23, no. 5, pp. 44-46, Jan 2005.

[86] J. S. G. Hong, M. J. Lancaster. Microstrip Filters for RF/Microwave Applications, Wiley-Interscience, 2001.

[87] R. Liu, T. J. Cui, D. Huang, B. Zhao, and D. R. Smith, ‘‘Description and explanation of electromagnetic behaviors in artificial metamaterials based on effective medium theory,’’ Phys. Rev. E, Stat. Phys. Plasmas Fluids Relat. Interdiscip. Top., vol. 76, p. 026606, Aug. 2007.

[88] L. Chen, Z. Lei, R. Yang, J. Fan, and X. Shi, ‘‘A broadband artificial material for gain enhancement of antipodal tapered slot antenna,’’ IEEE Trans. Antennas Propag., vol. 63, no. 1, pp. 395–400, Jan. 2015.

[89] D. R. Smith, D. C. Vier, T. Koschny, and C. M. Soukoulis, ‘‘Electromagnetic parameter retrieval from inhomogeneous metamaterials,’’ Phys. Rev. E, Stat. Phys. Plasmas Fluids Relat. Interdiscip. Top., vol. 71, pp. 036617- 1–036617-11, Mar. 2005.

[90] X. Chen, T. M. Grzegorczyk, B. I. Wu, J. Pacheco, and J. A. Kong, “Robust method to retrieve the constitutive effective parameters of metamaterials,” Phys. Rev. E, Stat. Phys. Plasmas Fluids Relat. Interdiscip. Top., vol. 70, Feb. 2004.

[91] B. Schuppert, “Microstrip/slotline transitions: Modeling and experimental investigation,” IEEE Trans. Microw. Theory Tech., vol. 36, pp. 1272–1282, Aug. 1988.

[92] C. Pfeiffer and A. Grbic, “Planar lens antennas of subwavelength thickness: collimating leaky-waves with metasurfaces”, IEEE Trans. Antennas Propag., vol.63, no.7, pp. 3248-3253, July 2015.

[93] E. Erfani, M. Niroo-Jazi, and S. Tatu, ‘‘A high-gain broadband gradient refractive index metasurface lens antenna,’’ IEEE Trans. Antennas Propag., vol. 64, no. 5, pp. 1968–1973, May 2016.

[94] H. B. Molina and J. Hesselbarth, ‘‘Microwave dielectric stepped-index flat lens antenna,’’ Int. J. Microw. Wireless Technol., vol. 9, pp. 1103–1109, Jun. 2017.

[95] X. X. Li, G. Liu, Y. M. Zhang, L. Sang, and G. Q. Lv, “A compact multi-layer phase correcting lens to improve directive radiation of Vivaldi antenna,” Int. J. RF Micro. Comput.-Aided Eng., vol. 27, no. 7, 2017, Art. no. e21109.

[96] K. Ma, Z. Q. Zhao, J. N. Wu, M. S. Ellis and Z. P. Nie, "A printed Vivaldi Antenna with improved radiation patterns by using two pairs of Eye-Shaped Slots for UWB applications," Progress In Electromagnetics Research, vol. 148, pp. 63-71, 2014.

[97] Lee, D. H., H. Y. Yang, and Y.-K. Cho, “Ultra-wideband tapered slot antenna with dual bandnotched characteristics,” IET Microwave Antennas Propagation, vol. 8, no. 1, pp. 29–38, 2014.

[98] K. A. Alshamaileh, M. J. Almalkawi, and V. K. Devabhaktuni, “Dual band-notched microstrip-fed vivaldi antenna utilizing compact EBG structures,” Int. J. Antennas Propag., vol. 2015, Feb. 2015, Art. no. 439832.

[99] X. Liu, Z. Lei, R. Yang, J. Zhang, L. Chen, and X. Kong, “The band notch sensitivity of Vivaldi antenna towards CSRRs,” Prog Electromagn Res Lett, vol. 43, pp. 125–135, 2013.

[100] Bhaskar, M., E. Johari, Z. Akhter, and M. J. Akhta, “Gain enhancement of the Vivaldi antenna with band notch characteristics using zero-index metamaterial,” Microw. Opt. Technol. Lett., vol. 58, no. 1, pp. 233–238, January 2016.

[101] D. O. Kim and C.Y.Kim, “CPW-fed ultra wideband antenna with triple-band notch function,” Electronics Letters, vol. 46, 2010.

[102] Y. C. Lin and K. J. Hung, “Compact ultrawideband rectangular aperture antenna and band-notched designs,” IEEE Trans. Antennas Propag., vol. 54, pp. 3075–3081, Nov. 2006.

[103] F. Zhu, S. Gao, A. T. S. Ho, R. A. Abd-Alhameed, C. H. See, J. Li, and J. Xu, “Miniaturized tapered slot antenna with signal rejection in 5–6-GHz band using a balun,” IEEE Antennas Wireless Propag. Lett., vol. 11, pp. 507–510, 2012.

[104] X. Chen, T. M. Grzegorczyk, B. I. Wu, J. Pacheco, and J. A. Kong, “Robust method to retrieve the constitutive effective parameters of metamaterials,” Phys. Rev. E, Stat. Phys. Plasmas Fluids Relat. Interdiscip. Top., vol. 70, Feb. 2004, Art. ID 016608.

[105] R. Liu, Q. Cheng, J. Y. Chin, J. J. Mock, T. J. Cui, and D. R. Smith, “Broadband gradient index microwave quasi-optical elements based on non-resonant metamaterials,” Opt. Express, vol. 17, no. 23, pp. 21030–21041, Nov. 2009